A Study on the Electromechanical/Dielectric Response of Poly(ethylene oxide)-Nanocrystalline-Cellulose Composites and Polyvinylidene Fluoride Electroactive Polymers

by

Patrick Sullivan Bass

A dissertation submitted to the Graduate Faculty of
Auburn University
in partial fulfillment of the Degree of
Doctor of Philosophy

Auburn, Alabama
May 7, 2016

Keywords: electroactive polymer, poly(ethylene oxide), nanocrystalline cellulose, polyvinylidene fluoride

Copyright 2016 by Patrick Bass

Approved by

Zhongyang Cheng, Co-chair, Professor of Materials Engineering
Maobing Tu, Co-chair, Professor of Forestry
Dong-Joo Kim, Professor of Materials Engineering
Barton Prorok, Professor of Materials Engineering
Majid Beidaghi, Assistant Professor of Materials Engineering

Abstract

The study of electroactive polymers (EAPs) has garnered a lot of attention over the past two decades for their ability to generate large electromechanical actuation responses without the need for any moving parts, external motors or servos. These types of materials are lightweight, they can be formed into almost any shape, and they operate simply through the application of an external electric field. They have possible applications in robotics, prosthetics, microfluidics, etc., making them an exciting material that can be utilized in a broad range of applications. Ionic polymer metallic composite (IPMC) are EAPs that function based off of the motion of ions through a parent polymer matrix. The inherent size difference between the transiting ions generates localized volume changes between the two sides of the polymer film resulting in an observed bending response. Though, there has been a large amount of research focused on these actuators, there are still fundamental questions with respect to their operation that have yet to be answered. The following dissertation proposes new methodologies for tackling some of these questions. Research initiatives focused on the creation and synthesis of environmentally friendly and biodegradable green IPMCs, modeling the time-dependent electromechanical response for use with a variety of IPMCs, developing a remote sensing capability for monitoring IPMC actuation using changes in their dielectric properties, investigating whether IPMCs could be used as energy storage devices, and finally, identifying a new and unique two-phased IPMC bending response that could possibly pave the way for different and exciting areas of application and research.

As such, a series of experiments were conducted to understand and model the electromechanical performance and dielectric response of EAPs made of biodegradable poly(ethylene oxide) with nanocrystalline cellulose used as a mechanical-stiffening filler, as well as with non-biodegradable polyvinylidene fluoride films. Through the investigation of the experimental results, the work herein will provide insight into the actuation and dielectric behavior of IPMC EAPs. Intrinsic research into the nature of the dielectric properties of materials will also be conducted. In all, and through vetting the results against others' models and methods, a broadened understanding of these types of materials and their resulting characteristics is obtained.

Table of Contents

List of Figures

List of Tables

Chapter 1: Introduction and Research Objectives

1.1 Fundamentals of Electroactive Polymers (EAPs), their Background and Significance

Electroactive polymers (EAPs), also named as artificial muscles, are a newly developed type of polymeric materials exhibiting giant electromechanical response.[1, 2] Electroactive polymers (EAPs) have gained a lot of attention over the past two decades for their ability to generate large electromechanical actuation without the need for any moving parts, external motors or servos.[2] These polymer systems are able to change their size or shape under an applied electric field. This biomimetic functionality enables these types of materials to have possible applications in robotics, biotechnology, mechatronics, prosthetics, micro-valves, and the like. They are also of interest due to their light weight, large actuation performance, fracture tolerance, and they can be made into almost any shape.[1] These characteristics open up a great number of possible applications. Early research into EAPs first emerged in 1880 where experiments were conducted with a rubber strip that was fixed at one end and had a weight attached to the free end. Under an applied electric field it was found to elongate and then return to its original form when the field was removed.[3] It was not until the turn of the millennium that the study of EAPs was popularized and in-depth research into EAPs began when Yoseph Bar-Cohen issued a challenge to the science community to create an EAP hand to compete against a human in an arm-wrestling contest.[4] Even after over a decade since this challenge, we are still expanding our fundamental knowledge of these types of materials and it is through the enhancement of our current understanding of how and why these types of materials act the way they do that will drive what future uses EAPs can be utilized for. This work strives to explain some of the mysteries that EAP research presents with the goal of furthering our knowledge of the inner workings of these systems.

EAPs represent manmade actuators that can closely mimic the electrical and physical response of natural muscles and are thus termed “artificial muscles.”[5] Natural, biological muscles operate due to ionic flux within the muscle tissue which is caused by the brain sending nerve impulses (electric signals) to the synapses located on a specific muscle.[6] With a response time of about 1 ms, these signals provide enough of an electric potential to change the shape of the voltage-sensitive channels in the terminal cisternae of the sarcoplasmic reticulum (SR). This process causes the release of large numbers of calcium (Ca^{2+}) ions. These ions then flow into the muscle tissue where there are parallel thick (myosin) and thin filaments (comprised of troponin, actin, and tropomyosin). The Ca^{2+} combines with the troponin along the thin filament, removing

the blocking action of the tropomyosin to the actin active sites. When this occurs, the actin active sites are free to interact with the myosin heads along the thick filament. The result of this cyclic process is that the thick filament pulls the thin filament across it resulting in an overall contraction of the target muscle. Expansion occurs when the brain no longer sends signals to the muscles and the Ca^{2+} ions return to the terminal cisterna of the SR. The development of EAPs also bridges the area of prosthetics and implants, making it possible for these "artificial muscles" to directly replace biological muscles.[5]

It has been reported that the net energy density for biological muscle is 0.2 - 40 J/kg.[2] Thus, the goal of EAP research is to meet or exceed this reference point, especially in the case where they could be used for prosthetics. EAPs studied to date can be classified into two categories: electronic (*e*-EAP) and ionic (*i*-EAP), depending on the mechanism of the electromechanical response.[2]

1.1.1 Electronic EAPs

The actuation response of *e*-EAPs is based on the parent polymer system's inherent piezoelectric, electrostrictive or other electrostatic response characteristics.[7] The electromechanical response observed in e-EAPs can originate from an electrostrictive effect,[8] the Maxwell-stress (i.e. electrostatic force) effect,[9, 10] and the re-orientation of dipoles.[11] The *e*-EAPs are usually good electrical insulators that can stand with a high electric field. They exhibit a fast electromechanical response with a linear strain and a response time from μs to ns and their strain response is well defined by the electric field applied on it. Therefore, the electromechanical response of an *e*-EAP is usually characterized by the relationship between the electric induced strain and the electric field applied on.[11, 12] However, *e*-EAPs require a very high driving electric field (> 100 MV/m).[11]

Regarding the electromechanical response, there are two types of *e*-EAP actuation mechanisms: electrostriction and Maxwell stress. For *e*-EAPs based on the electrostriction, such as irradiated P(VDF-TrFE)[13] and polyvinylidene fluoride (PVDF)-based copolymers[12] and terpolymers,[14] a linear electromechanical strain response of about 5% to 10% has been observed with an elastic modulus of about 10^2 to 10^3 MPa.[11] For the *e*-EAPs based on the Maxwell stress effect, a linear electromechanical strain of more than 100% has been observed in dielectric elastomers with a very low Young's modulus (i.e. a few to 20 MPa).[11] Although the *e*-EAPs exhibit a large linear strain, the displacement obtained from the linear strain is still too small to be

directly used in many applications. Therefore, various designs have been introduced to amplify the displacement generated by the linear strain.[15, 16]

Table 1 showcases several examples of *e*-EAPs and their comparative parameters ranging from maximum strain, to applied electric field, to work/energy density, and dielectric properties. For most cases, a large electric field is required for actuation, which is also accompanied by a large strain response. One of the widely used approaches to amplify the displacement is the cantilever structure (i.e. unimorph), in which at least two layers are required to be bound together. Therefore, the linear strain along the length direction generated in one layer is converted into a bending actuation of the unimorph. When the *e*-EAPs are used to develop unimorphs, new issues related to binding layer arise.

1.1.2 Ionic EAPs

i-EAPs are the most popularly studied type of EAPs and are generally comprised of a polymeric membrane layer, doped with an ionic salt, and coated with a conducting surface electrode.[17] As such, this type of EAP will be the focus of the research presented in this dissertation. Regarding the actuation of *i*-EAPs, which include ionic polymer-metal composites (IPMCs),[17] conducting polymers,[18] hydrogels,[19] etc., when an electric field is applied on it, the ions in the polymer are forced to move so that the distribution of the ions changes with time,[1, 2] which leads to the accumulation of cations and anions onto different electrodes.[2] That is, under an electric field, the charge carriers move in the polymer matrix, which results in a re-distribution of the charge carriers, such as the accumulation of the charge carriers to the electrodes. Due to the difference in the size between different types of the charge carriers, the re-distribution or accumulation of the charge carriers and the resulting electrostatic pressure differential culminates in a bending actuation with a large displacement in a simple thin film.[1, 20] This is an advantage of *i*-EAPs over *e*-EAPs for the actuator applications.

Figure 1 provides a general representation of how *i*-EAPs conduct their bending actuation. Typically, an ionic salt is dissolved into a polymer system providing both positive (cations – blue) and negative (anions – green) charge carriers. These ions are randomly distributed throughout the polymer matrix before any external electric field is applied (the hash-marked areas). Once an external voltage is applied to the sample via metalized surface electrodes, the ions migrate to their respective electrodes. The resulting pressure difference generated due to the size disparity between the ions creates a differential expansion within the matrix which results in the observed

macroscopic bending actuation. It is this ionic flux, which results in a bending actuation, that makes ionic EAPs more similar to the excitation response seen in natural muscles and the reasoning behind these films being called "artificial muscles."

Compared to *e*-EAPs, *i*-EAPs require a very low electric field (<1 MV/m) or a low driving voltage (10^0 to 10^1 V over a thickness from tens to hundreds of micrometers), but exhibit a slow electromechanical response with a response time from seconds to minutes.[2] As with the *e*-EAPs, **Table 1** displays a series of examples for *i*-EAPs and their various properties relative to *e*-EAPs. Though their strain response is generally lower than *e*-EAPs, the required electric field needed for them to actuate is much less which leads to a wide variety of options for picking an EAP based off of the needs for a specific application. Additionally, **Figure 2** illustrates a graphical comparison between the two types of EAPs. Plotting work density versus applied electric field was chosen because these two parameters encompass many of the properties shown in **Table 1** and they provide a way of directly comparing the various examples of EAPs through their material properties (Young's modulus), sample synthesis characteristics (sample thickness), actuation performance (strain), and the actuating environment (applied voltage). From the figure, it can be seen that *e*-EAPs require a large applied electric field, but exhibit a large volumetric work density while *i*-EAPs generally require a low applied electric field and show a comparatively low work density. Also, work density (J/m^3) was chosen over energy density (J/kg) since this was more widely published in the literature and since film density was not readily available in all articles for converting from one parameter to another.

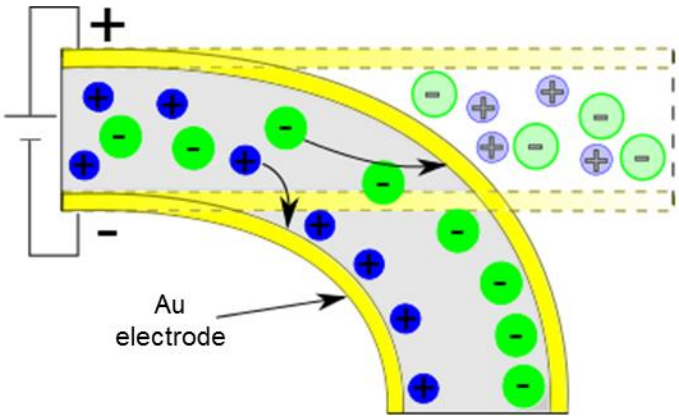

Figure 1: *i*-EAP electromechanical response generated from ionic diffusion

Various *i*-EAPs, such as ionic gels,[21] ionomeric polymer-metal composites (IPMCs),[17] conductive polymers,[22] and, graphite-polymer composites[23] have been studied/developed. The electromechanical performance of *i*-EAPs varies over a broad range. Some

i-EAPs have a high Young's modulus, but exhibit a small electromechanical strain response, while others exhibit a large electromechanical strain, but have a very small Young's modulus. For example, hydrogels have a very low Young's modulus of about 10^1 kPa[21] with a strain of about 4%;[24] composite of graphite oxide and P(VDF-CTFE) has a Young's modulus of about 10^1 MPa with a strain that can be up to more than 50%.[23] On the other hand, *i*-EAPs made from plant cellulose, a natural and biodegradable polymer, has a Young's modulus of about 9 GPa, but only exhibits an electromechanical strain of about 0.038%.[25]

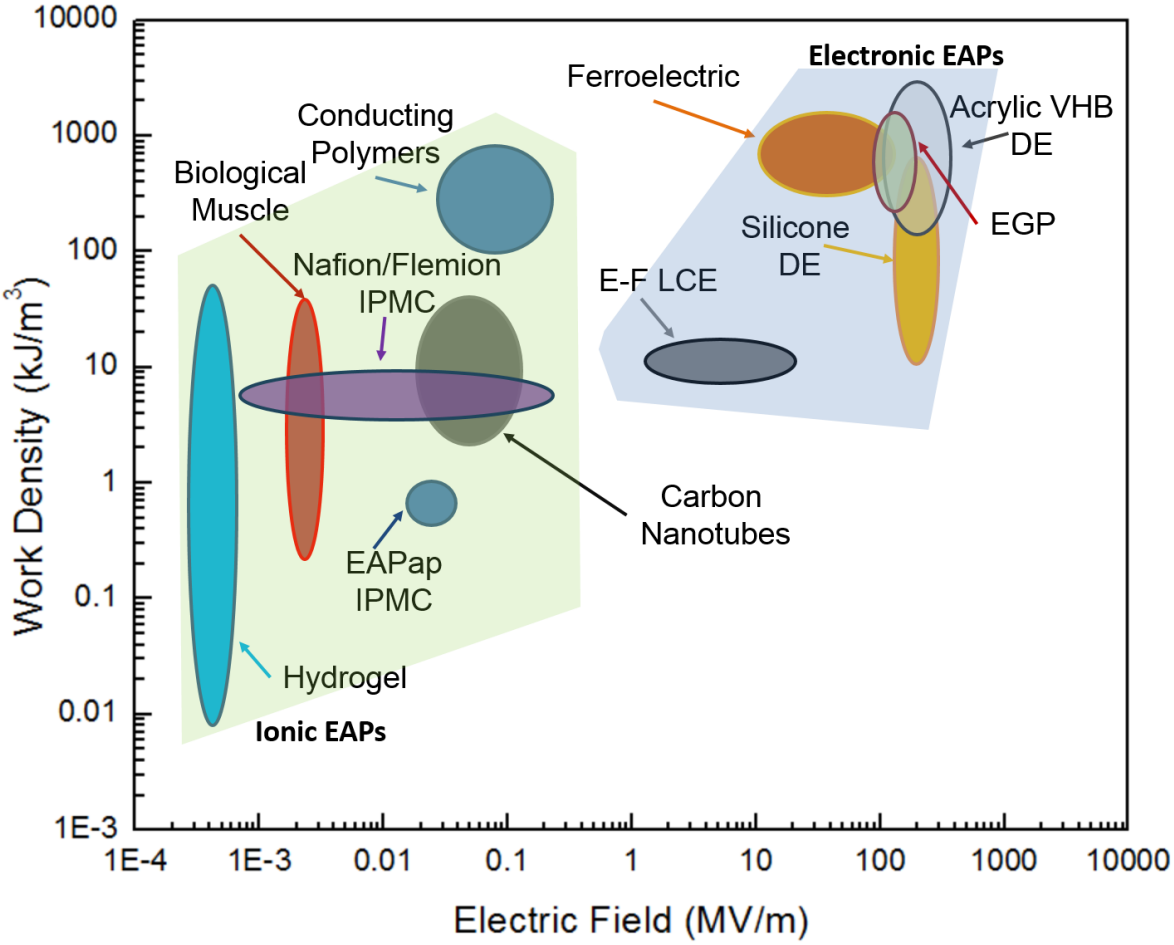

Figure 2: EAP comparison concerning the applied electric field and the corresponding work density measured for each specific type of actuator

Table 1: Electroactive Polymer Parameter Comparison

		Type	Material	Max. Strain %	Voltage (VDC)	Electric Field (MV/m)	Young's Modulus (MPa)	Work Density (kJ/m³)	Energy Density (J/kg)	Cation	Response Time (s) ‡	e' 1kHz	D at 1kHz	Density (g/cm³)	Thickness (µm)
		Biological Muscle	Mammalian Skeletal Muscle[2, 20, 71-75]	20	0.1	0.002	200	0.2 - 40	0.2-40	Na^+ or Ca^{2+}	1-5 ms, eye blink: 0.1-0.4 ms	300	--	1.037	50
Electronic EAPs	1	Ferroelectric	PVDF-TrFE[68-70]	3.5-7	>1000	13-150	400-1200	320->1000	170-535†	--	5.00E-6	4E+4	7.5	1.870-2	0.1
	2	Dielectric Elastomer (DE)	Silicone[61-68]	120	>1000	110-350	0.1-1	10-750	9-680†	--	3.52E-4	3	--	1.1	100
			Acrylic VHB 4910[61]	380	>1000	125-440	1-3	150-3400	155-3540†	--	5.11E-3	4.8	--	0.96	100
	3	Electrostrictive Graft Polymers	[59, 60]	3-8	--	100-200	550	250-1800	--	--	1.00E+1	11	--	--	--
	4	Liquid Crystal Elastomers (LCE)	Thermal[56-58]	19-45	--	--	0.3-4	3-56	--	--	1.2-3.2	--	--	--	100
			Electric-Field (EF)[54, 55]	2-4	0.11	1.5-25	100	20	--	--	4.00E-3	5	--	--	0.075
Ionic EAPs	1	Ionic Gels	Hydrogel[49-53]	4-10	1-10	0.00025-0.0006	0.01	0.006-50	--	Na^+	1.00E+2	8-60	--	--	1000-5000
	2	Conducting Polymers	Polypyrrole/ Polyaniline[35-48]	2-12	1.2-10	0.03-0.25*	200-800	100	--	--	1-2	2-100	3E-3-1.0	--	40
	3	Carbon Nanotubes	[32-34]	0.2-1	1-30	100-3000*	1-10 GPa	2-40	--	--	0.053-0.33	--	--	--	0.01
	4	Ionic Polymer Metal Composites (IPMC)	Nafion/ Flemion[26-31]	0.5-3.3	1-7	0.0005-0.233*	50-100	5.5	33-66†	Li^+ or Na^+	0.15-1	16-110	--	1.5	30-2000
			Electroactive Paper (EAPap)[25]	0.038	--	0.23	9 GPa	0.65	0.84	Na^+	--	--	--	0.77	30
			PEO-NCC (H_2SO_4) Composites	0.11-1.5	4	0.073-0.133	130-315	0.13 - 3.5	0.11-3.1†	Li^+	1.0E+2	400-1000	15-26	1.14	50-60
			PEO-NCC (HCl) Composites	0.08-0.84	4	0.057-0.092	176-501	0.09-4.72	8.0E-2-4.15	Li^+	1.0E+2	--	--	1.15-1.26	50-60
			PEO (no NCC)	0.31-0.97	4	0.073-0.133	93-312	1.3-4.4	1.2-3.8	Li^+	1.0E+2	400-2000	9.2	1.15-1.26	30-60
			PVDF	0.39	4	0.125	476	3.66	2.52	Co^{2+}	1.0E+1	5E+4	3.2	1.45	32

*V/h, †WD/Density, ‡s- rate%/ strain%

In summary, *e*-EAPs generally experience linear actuation, with a fast response time, and a high Young's modulus, but have a limited displacement and require a large driving voltage. Meanwhile *i*-EAPs showcase a bending actuation, with very large displacements, and require only a small driving voltage, but have a relatively slow response time and a low Young's modulus. As such, in an effort to improve *i*-EAP properties, such as: displacement, response time, and Young's modulus, some focus of this dissertation will explore changes in ionic salt concentration, applied voltage, and filler content to these respective areas.

The goal of this study was to fabricate EAPs that involved a simple synthesis process with a straightforward actuation mechanism with regards to the measuring/characterization process, therefore *i*-EAPs were selected over *e*-EAPs. In addition, since *i*-EAPs will be the main-focus of this dissertation, with minimal mention of *e*-EAPs hereafter, *i*-EAPs will be referred to as simply EAPs for the remainder of the report unless otherwise explicitly stated.

1.1.3 General Overview of Research Initiative

As will explored in greater detail in the coming sections, there are a series of goals that were explored and will be presented in this dissertation. Special attention will be focused on *i*-EAPs and one of the research focuses is to propose the creation of biodegradable, *i*-EAPs. Typical *i*-EAP synthesis utilizes caustic materials that can be hazardous to both humans and the environment, wherein the push to make EAPs, in general, to be faster, stronger, and better has placed an oversight onto the lifecycle impact these materials can have on their environment. This study will explore the use of alternative, *green* materials which can perform similar functionalities, but that pose a minimal environmental risk. Another drive of this report was also to characterize the actuation behavior of the *i*-EAPs created and to assert newly formed empirical relationships to describe their motion. As will be seen, many models have been proposed for describing *i*-EAP actuation, with accompanying advantages and disadvantages. In this dissertation, two models will be proposed which more accurately represent the time-dependent response of these materials, thus enabling a better understanding of how these materials operate while providing a compact fitting form for easy use in engineering design. Additionally, this dissertation will explore an indirect method of monitoring *i*-EAP actuation based on changes in their dielectric properties when they deform under an applied electric field. This methodology presents a new avenue for *i*-EAP monitoring that is based on the material response and is not reliant on traditional observation techniques like photographs, video or laser vibrometry. Finally, new areas of application for the *i*-

EAPs developed in this study will be explored, such as energy storage devices where it was found that these films can have charging/discharging profiles that are similar to both batteries and capacitors, making for a unique material. Also, a unique, two-phased bending response will be explored wherein a traditional e-EAP can be made to experience both the characteristic bending response of i-EAPs followed by a linear extension response that is synonymous with e-EAP actuation. This dissertation presents novel solutions and explanations behind some of the questions regarding the *i*-EAP actuation phenomenon with the hope of furthering our understanding in this area and for creating new avenues of EAP research.

1.1.4 Typical EAP Materials and Their Fabrication (Nafion and Flemion)

The most commonly studied and commercially available EAP is called Nafion (perfluorinated sulfonic acid) and it is made by DuPont.[76-78] It can be purchased as a powder or as prefabricated sheets, which then can be cut into a desired shape. It has been used in applications such as proton conducting membranes for fuel cells, batteries, electrochemical energy storage systems, chlor-alkali cells, water electrolyzers, etc.[79] It is the predominant EAP due to its actuation performance, response time, and for being relatively inexpensive. It can achieve electromechanical strains upwards of 2% at ±3 V DC[80] with response times of under 4 s[81] and energy densities reaching 7 Wh/kg.[82] Nafion has been researched heavily as an EAP,[83-85] however, one of its drawbacks is that it is not biodegradable or recyclable.[86, 87]

Nafion is made by copolymerizing perfluorinated vinyl ether with tetrafluoroethylene (TFE).[79] This is typically done by dissolving perfluorosulfonic acid (PFSA) dispersions with TFE copolymer into either dimethylacetamide (DMAc)[88] or dimethylformamide (DMF)[89] and stirring the solutions for 6 h at 80 ^{o}C. The solutions are then solution cast at temperatures between 80-120 ^{o}C for up to 12 h to create the final ionic membrane. Both DMAc and DMF are organic solvents and are carcinogenic. TFE, commonly known as Teflon, has also been found to be possibly carcinogenic, wherein tests conducted on rats found tumors at the site of application, but TFE is not currently classified as to its carcinogenicity to humans.[90] Both TFE and PFSA can pose a health hazard during the casting or hot pressing processes; “polymer fume fever” can occur where a temporary flu-like illness can occur for 24-48 h and is associated with the decomposition of fluoropolymers.[91] Again, Nafion is a readily available material that produces excellent EAP performance, but it is rather complicated to synthesize, it or its constituents are not

biodegradable, and the chemicals and materials associated with its synthesis pose possible health hazards and handling precautions are necessary.

Flemion (perfluorinated carboxylic acid), made by Asahi Glass Co., is very similar in chemical makeup to Nafion and is also a popular ionic EAP.[78, 83, 92] Synthesis processing is also similar to that of Nafion in that Flemion is a copolymer of TFE and perfluorinated vinyl ether with a carboxylic acid group side chain. Flemion comonomers are created by conducting a pyrolysis process on oxidized compounds in oleum, which start from TFE and iodine and combining them with hexafluoropropylene oxide.[93] Oleum is a synonym for sulfuric acid and is extremely hazardous.[94] It can cause severe skin burns and eye damage and can be fatal if inhaled. Iodine is also a toxic chemical and can cause skin irritation, serious eye irritation, it may cause respiratory irritation, and can cause damage to the thyroid with prolonged exposure.[95] Iodine is very toxic to the environment and has acute aquatic toxicity. Polar solvents used with Flemion synthesis range from ethylene glycol, to crown ethers and various forms of 1-ethyl-3-methylimidazolium tetrafluoroborate BMI-BF_4.[78, 92] Ethylene glycol, commonly known as antifreeze, can cause kidney damage and death if swallowed.[96] BMI-BF_4 is toxic to both humans and the environment with long lasting effects.[97] Flemion, like Nafion, is also a perfluorinated polymer and likewise is not recyclable nor biodegradable.

For the development of other types of EAPs, such as the conducting polymer, polypyrrole (PPy), the polymer matrices themselves are nonhazardous. However, when combined with other chemicals to make functional smart materials, the additional chemicals tend to be hazardous or environmentally harmful. PPy actuators have been created using dodecylbenzensulfonate DBS as a dopant.[98] PPy itself is nontoxic,[99] but DBS is harmful is swallowed, can cause serious eye damage, and is acutely toxic to aquatic life. PPy can be dissolved in water, but PPy-based conducting polymers research also use solvents such as dimethyl sulphoxide (DMSO), DMF, and pyridine.[100] DMSO and Pyridine are both carcinogenic, are not biodegradable, are combustible, and can cause birth defects.[101, 102] As stated earlier, DMF is carcinogenic.

Silicone is a common material used in the creation of dielectric elastomers (an electronic EAP).[103-105] Elastomers are created from a silicone elastomer dispersion in xylene. This solution is flammable, can affect the nervous system, cause skin and eye irritation, and can adversely affect the kidneys and liver.[106] Its synthesis spawns from a three-step process:[107] 1) chlorosilane synthesis, 2) chlorosilane hydrolysis, and 3) polymerization and polycondensation.

As mentioned, the final solution for creating silicone elastomers is hazardous; likewise, the chlorosilane synthesis step involves the condensation of methanol with hydrochloric acid HCl. Methanol is highly flammable and can cause damage to organs while also being toxic to aquatic life.[108] HCl is corrosive to the skin, can cause serious eye damage, and is toxic to fish.[109]

As a counter to the negative aspects of Nafion, Flemion, and other EAP-based materials, the development of the EAPs focused on for this study are biodegradable, environmentally friendly, and very simple to make. Essentially, the process utilized herein is that the polymer of choice, poly(ethylene oxide) (PEO), is dissolved in water along with a specified ionic salt, is magnetically stirred for a period of time, and then solution cast at low temperatures. Once the electrodes are sputtered to either side, the films can then be cut to the desired sample size for use. The *green* nature of and its applicability to EAP research will be discussed at length in the proceeding sections.

1.1.5 Current Actuation Monitoring Methods

1.1.5.1 Laser Vibrometry Analysis

An optical analysis process or methodology, like taking still photographs or video is the predominant method for characterizing EAP actuation. The measurement of sample tip deflection using a laser vibrometer is another such optical-based monitoring process used to measure EAP actuations. Laser displacement measuring systems are typically used for recording EAP parameters that occur over small deflections or fast actuation frequencies and is used for monitoring both electronic and ionic EAPs.[110] In this setup, the laser vibrometer is mounted with the laser being reflected off of the sample electrode surface and back to the device photo detector.[111] Using this monitoring process, micro deflections of the samples can be measured from 0.1 Hz to 200 Hz or higher at sensitivities of less than 100 μm for recorded deflections.[80, 112] This monitoring process, though very precise, has operating limitations, namely for bending actuators. Here, if the films were to actuate past the line of sight of the laser, then the film will have effectively disappeared and no more usable data can be obtained unless the sample returns to the laser's viewing area.

1.1.5.2 Optical Imagery Analysis

The other traditional optical analysis method for EAPs is through the use of a digital camera or recording device. Generally, when this setup is chosen for bending actuators, the camera is mounted with its lens perpendicular to the thickness plane of the samples.[110, 113, 114] This

method enables the recording of the EAP bending throughout the entirety of the experiment, either through a continuous video recording or via photographs taken at set time intervals. From this technique, EAP properties, such as displacement, speed, frequency, etc. can be measured, with a sensitivity defined off of how fast the images or video can be taken and the resolution of and between images. Due to the small thicknesses of the EAP actuators, however, obtaining a sufficient focus on the samples during actuation can be challenging, so small perturbations and deflections can sometimes be difficult to discern. However, this method enables the monitoring of the sample bending for however long the external electric field is applied. As such, this was the method chosen during this study to observe the EAPs.

1.1.5.3 Capacitive Sensing

Another actuation monitoring technique is to measure changes in capacitance during actuation. This method is typically utilized for monitoring the actuation behavior of dielectric elastomers (DE).[115] These materials are, as mentioned, electronic EAPs and when a voltage is applied to them, they undergo a large volume change due to Maxwell stresses. A dielectric elastomer film is layered between two compliant electrodes and the film is then modeled as a simple parallel plate capacitor. Upon excitation, the elastomer film thickness contracts along the electric field direction and its electrode area expands. The operating principle behind this monitoring method is that when the DE's thickness and area are both changing during actuation, there is an accompanying change in the measured capacitance, indicating that there is a one-to-one relationship between the changes in these two parameters. In the study cited, for between 0-3 kV of applied voltage, there was an approximate difference of 2-3 V measured for the output voltage, making it possible to measure actuator displacement through direct changes in capacitance. Capacitance for parallel plate capacitors is defined as **Eq. (1.1)**:

$$C = \varepsilon_0 \varepsilon_r \frac{A}{h} \tag{1.1}$$

where, ε_0 is the permittivity of free space (which does not change with applied voltage), ε_r, is the elastomer's dielectric constant, A is the electrode area, and h is the sample thickness. Clearly, as the sample thickness decreases, a corresponding increase in capacitance will occur.

To develop a *'self-sensing'* monitoring process, wherein actuation could be monitored through changes in sample capacitance versus using additional monitoring equipment, the researchers placed an external resistor (R) between the DE actuator and the ground in the circuit, enabling the measurement of the changes. Capacitive reactance can be calculated using:

$$X_C = \frac{1}{\omega C} \tag{1.2}$$

where, ω is the angular frequency of an applied AC electric field. The recorded change in voltage (from the input to the output voltage) due to sample deformation can thus be calculated using:

$$V_{output} = \frac{R}{R + X_C} V_{input} \tag{1.3}$$

To effectively utilize these equations to monitor changes in actuation displacement, two voltages were applied to the samples; an actuation voltage (2.2-3.0 kV DC) and a sensing voltage (300 V_{pp} AC at 100 Hz). As the DE actuates, the amplitude of the measured output voltage was found to be proportional to the sample's displacement. In addition, with increasing DC voltage, there is an increased phase shift for the measured output voltage, which, as mentioned, can be related back to the capacitance changes incurred due to the sample actuation. This method proved effective for measuring displacements due to changes in capacitance and was shown to be a better method for conducting such methods compared to a laser sensor setup that Jung et. al used to compare the results of their study. This method also eliminated the need for external measuring equipment, like lasers, which is a step forward as far as commercial applications are concerned. Similarly, ionic EAPs generally use an optical analysis system for monitoring actuation behavior, which can prove to be intrusive. However, as with the example cited in this section, the study presented in this report will explore the use of a capacitance measuring technique that utilizes AC dielectric readings and will relate the recorded data to the observed electromechanical performance. As with the self-sensing technique described for DEs, a novel approach for conducting self-sensing with ionic EAPs will be described herein with the goal of creating a new monitoring methodology for this type of EAP system.

1.1.6 Current Electromechanical Actuation Models

As new applications and uses for IPMCs arise, the importance for understanding and predicting how they actuate and their actuation mechanism has grown. IPMC actuation behavior is typically described in qualitative terms, stating that "…initially the moving rate was very slow and it became fast, and saturated with time."[116] This general description of the three modes of actuation (slow, steady, and saturated) is then followed by a quantitative analysis on a specific area, like maximum strain or response time. The processes behind the three modes is intuitive and involves the separation of charge carriers within the polymer matrix due to ionic motion; actuation is *slow* just after initial excitation due to most of the ions being distributed randomly throughout

the polymer matrix with only a small amount contributing to actuation, then as time progresses the rate of ions accumulating at the polymer-electrode interface occurs at a *steady* rate and the actuation is linear, with respect to time, then finally, as the number of remaining ions within the matrix begins to be depleted, due to there only being a finite amount of mobile ions within the polymer matrix, the actuation reaches its maximum value and is *saturated*.

As a result of the slow, steady, saturated response observed for IPMC materials, their actuation profile is highly nonlinear. For engineering design concerning these actuators, there has been a large focus in this area to learn more. The process for quantifying the time-dependent behavior, as a whole, has thus become a major area of interest with studying IPMC films and has generated many models. Models have fallen into three areas: 1) white box, where the underlying physical mechanisms, believed to account for the various physical and chemical processes going on within the EAP, are taken into consideration.[117, 118] Unfortunately, these processes are not very well understood and the resulting analysis has returned conflicting views of the root cause behind the bending.[117, 119] Additionally, equations generated from these models are typically difficult to correlate to experimental data and become impractical;[120, 121] This method typically utilizes complex equations, like the Nernst-Planck model,[120] (as described with **Eq. (1.4)**) which provide a detailed description on how the flux of ions contribute to actuation, but contain parameters that may be difficult to obtain or require experimentally determined properties. 2) Black box models, where the opposite approach is taken and empirically derived models are formed based primarily off of experimental data with little consideration to the underlying mechanisms.[122, 123] Finally, 3) gray box models, which act to bridge the two types of models using some physical laws, but combined with empirically derived parameters when the mechanisms in question are too complicated or not understood well enough to be obtained through derivation.[124-126]

This section will provide examples for the current state of research for modeling the time-dependent nature of IPMC actuation. An analysis of the advantages and disadvantages of these models will be given. For the models that readily lend themselves for use, a brief comparative analysis will be done showcasing how these models fit a set of experimental data while also comparing these results with one of the models developed in this dissertation.

1.1.5.1 White Box Models

As stated, physics-based (or white-box) models strive to characterize the behavior of IPMC actuation by delving into the physical and chemical mechanisms taking place within the material. Early work concerning physical models was conducted by Tadokoro in 2000.[119] Here, he proposed that the accumulation of water molecules trapped within the matrix were dragged toward the negative electrode by mobile cations as they quickly migrated to the cathode under an applied electric field. This accumulation of water molecules within the matrix caused an expansion and contraction between the two electrodes resulting in the observed bending actuation. The model created consisted of a series of partial-differential equations that included parameters that were not well known or measurable. Tadokoro reported positive agreement between experimental and simulated tip displacement.

Nemat-Nasser and Li, in 2000, also proposed a physical model for IPMC actuation, but used a micromechanics approach.[117] This approach proposes that clusters form in the polymer matrix from the side chains of the polymers and can become saturated with water. As with the Tadokoro model, under an applied electric field, the mobile cations transit towards the cathode. However, bending actuation is generated due to stresses formed along the polymer backbone from localized charge imbalances within the matrix. These imbalances create electrostatic forces that induce a bending curvature within the polymer. Nemat-Nasser and Li determined it was these localized electrostatic forces that caused the bending and that the transportation of water within the matrix caused only a secondary effect. They tested this theory with an actuator in air and in water with their simulation also showing good results. This conclusion is interesting because Nemat-Nasser and Li's physical interpretation to the cause of the IPMC actuation is in stark contrast to the Tadokoro model, yet both models agreed with experimental results. Consequently, the physics behind understanding and applying both models will need to be reinvestigated if either one proves to be correct.

Another example of a physical model is represented by the below relationship which describes the Nernst-Planck model, used for describing the diffusion and convection of charges and the migration of particles under an applied electric field.[127]

$$\frac{\delta C}{\delta t} + \nabla\left(-D\nabla C - \frac{zDFC}{RT}\nabla\Phi\right) = -\bar{u}\cdot\nabla C \tag{1.4}$$

Here, *C* is the concentration of charged particles, *D* is the diffusion constant, *z* is the valence number, *F* is the Faraday constant, Φ is the electric potential, *R* is the universal gas constant, and u is the ionic velocity. When a voltage is applied to the system, all free cations will start transiting to their attracting electrode. The combination of this relationship with Newton's Second law and the Rayleigh damping model yields a complex model that was shown to fit experimental results for their Nafion films very well.[128] As such, parameters such as the concentration gradient, the diffusion coefficient and ionic velocities may be difficult to obtain without experimental parameters and thus making this a difficult model to use with experimental results. Additionally, the author's did not explicitly detail their final actuation model in the study for accomplishing a comparative study.

The application of physical models to IPMC actuation is a challenging one. The underlying physical and chemical processes that are responsible for the IPMC actuation have not yet been fully realized or precisely identified, leaving somewhat of a gap in our present understanding. Additionally, the governing physical equations can be quite complex and values for the parameters within these equations can be difficult to measure, inhibiting their use.[121]

1.1.5.2 Black-Box Models

As mentioned, black-box models employ empirical methods for identifying the system behaves with minimal consideration to the underlying physical processes. Physical models do well with understanding the mechanisms behind IPMC actuation, but simpler black or gray-box models are very useful for utilizing the actuation phenomenon in engineering design.

An attempt to characterize the tip displacement of IPMC actuators was first developed by Kanno et al. in 1994.[122, 129, 130] Here they developed a black box model, considering the IPMC as a bending cantilever beam with one fixed end. The model they developed is shown as **Eq. (1.5)**.

$$Y(t) = Ae^{-\alpha t} + Be^{-\beta t} + Ce^{-\gamma t} + De^{-\epsilon t} + E \tag{1.5}$$

Here, A, B, C, D, E and $\alpha, \beta, \gamma, \epsilon$ are constants determined through observing the tip behavior of their actuator at various voltages and fitting the relationship to the tip displacement, in conjunction with a least squares algorithm to determine the values for the constants. As such, it was a cumbersome process for accurately determining the values for the nine separate fitting parameters.

A simple black-box model was developed by Montazami and is based on the normalized electromechanical strain of multilayer Nafion IPMCs.[131] It is the simplest of models, requiring only two fitting parameters. In their study on the strain, response time, and curvature of Nafion-based IPMCs they put forth **Eq. (1.6)** to fit their normalized strain data.

$$s(t) = s_{max}\left(1 - e^{-t/\tau}\right) \tag{1.6}$$

Here, the time-dependent strain *s* is represented by the maximum strain s_{max} and a time constant τ relating to the bending moment of the film. Similarly to the Arrhenius-based model proposed in this study, the Montazami model only has two parameters to fit, making for an easy-to-use model. As stated, IPMC actuation follows a slow, steady, then saturated bending response due to the flux of ions within the matrix; the Montazami model does well with representing the steady and saturated portions of the actuation, but cannot be used to describe the initial-time dependent or slow response of the films (when $t \to 0$). The disparity between the Montazami model and the model proposed herein when fitted against a sample of experimental data will be discussed later in this section.

In an effort to include more physical parameters to the black box model, Xiao and Bhattacharya incorporated the below first-order differential equation.[123]

$$\frac{dK}{dt} = \frac{1}{\tau}(K_v V - K) \tag{1.7}$$

This relationship was used to describe the induced curvature in the IPMC where *K* is the induced curvature, K_v is the maximum induced curvature per unit applied voltage, *V* is the applied voltage, and τ is a time constant. Solving this equation yields **Eq. (1.8)** where *C* is a constant of integration.

$$K(t) = K_v V + Ce^{-t/\tau} \tag{1.8}$$

This time-dependent representation of the Xiao-Bhattacharya model makes it possible to fit the experimental data. This model encompasses four fitting terms, making it somewhat more complex than the Montazami model, however, it is found that this model agrees with the experimental data better than the Montazami model, but as with the Montazami model, the Xiao-Bhattacharya model is somewhat lacking for the initial, slow actuation response.

With the goal of incorporating beam theory into IPMC black models, Chen developed **Eq. (1.15)** for the out-of-plane deflection of the tip of the IPMC.[132]

$$w(t) = \frac{L^3 F(t)}{3YI} \tag{1.9}$$

Here, L is the length of the IPMC, Y is the Young's modulus, I is the moment of inertia of the beam ($I = wh^3/12$, where w is the width of the beam and h is half its thickness) estimated as a rectangular plate with an axis of rotation along the short end of the film, and *F(t)* is an external, time varying force applied at the end of the beam. Three film parameters are thus needed along with the *F(t)* profile acting on the film, which again, makes it more complex than the Montazami model and the compact model presented in this dissertation. In Chen's report, there is no mention of how the external force changes with respect to time, nor does it describe how the excitation electric field is applied to the film, but it assumes that it happens at the non-fixed end of the IPMC. In this dissertation, the *F(t)* will be represented as both a linear and Arrhenius relationship to see how well, or how poorly, it can characterize a sampling of the recorded experimental data if the time-dependent external force profile is known. The application of this deflection model is somewhat unrealistic since IPMC actuation occurs due to the externally applied electric field (the electrostatic force) acting along the entirety of the surface of the actuator, not just at the tip.

For engineering purposes, a large part of research going into modeling the actuation response of IPMCs uses finite-element analysis,[133] assuming that the IPMCs materials have a uniform composition. This methodology is more of a black or gray box method and utilizes mostly experimental data to characterize the IPMC response, but does not necessarily take into consideration the underlying physics involved. Since a close-packed form of these types of models is generally not available, a finite-element analysis model was not included in this analysis.

In addition, most of the prescribed models were based off of Nafion films where the anion is fixed to the polymer matrix. This results in only the cation moving through the matrix. For polymer systems where both the cation and anion are mobile, these models will have to be adjusted due to the size disparity between ions accounting for varied accumulation times at their respective electrodes.

1.1.5.3 Gray-Box Models

Gray-box models for IPMC actuation act as an alternative to the complex physical models and the more simplified black-box models. These models leverage well-established and easily-modeled physical laws and combine them with empirical parameters to cover areas that may be overly complex or not well understood.

De Gennes considered the electromechanical response of IPMCs has also been considered from a thermodynamics perspective.[134] He proposed a linear, gray-box that utilized the Onsager

formulation where the motion of the cation and solvent were considered with the anion fixed within the matrix. The motion of the cations was described in terms of the current density, *J*, whereas the motion of the solvent was detailed using a term for flux, *M.* Under static conditions, these particles can be described using the below two equations:

$$J = \kappa E - L_{12}\nabla p \tag{1.10}$$

$$M = L_{21}E - K\nabla p \tag{1.11}$$

Here, κ is the membrane conductance and *K* is the Darcy coefficient, *E* is the applied electric field, $-\nabla p$ is a pressure gradient, and $L_{12} = L_{21} = L$ is a cross coefficient with units of (m/s)(V/m) represent the electromechanical transduction. De Gennes reasoned that the water molecules trapped within the polymer matrix were dragged by the mobile ions to the electrode-matrix interface and were the reason for the induced curvature. Though these equations are compact, they are only valid for static, steady-state conditions and those where the actuator only experiences small deflections. Additionally, the transport of water molecules described in the study has not been linked to the IPMC actuation and there was no published fitting with experimental data.

IPMCs have also been described through representing the motion of the charge carriers within the polymer matrix with an equivalent circuit model.[125] Here, since IPMCs are both inherently resistive and capacitive, the films could be modeled as a parallel capacitor and resistor in series with a second capacitor and resistor with a third resistor between the two pairings. The electrodes on either side of the IPMC are represented by the capacitor/resistor combo and the matrix material is the third resistor which signifies the ease of flow of ions through the matrix. Assuming that both electrodes were fabricated similarly, the capacitance and resistance in the pairings could be set equal to each other. This analysis results in an equation for how charge builds up at either of the two electrode-polymer interfaces with respect to time (**Eq. (1.12)**) and also an equation relating that charge with the electromechanical stresses incurred by the IPMCs due to the ionic flux (**Eq. (1.13)**), with an experimentally determined proportionality constant c_1.

$$Q(t) = V\frac{R_1C_1}{2R_1 + R_2}\left[1 - e^{-\left(\frac{2R_1+R_2}{R_1C_1R_2}\right)t}\right] \tag{1.12}$$

$$Q \cong c_1\sigma \tag{1.13}$$

This concept was utilized by Jain for Nafion-based IPMCs, wherein he considered the IPMC as a uniform cantilever beam subjected to an input voltage which imparts an overall bending moment in the film.[135] Using Kirchhoff's laws for RC circuits, the IPMC was modeled as a

resistor in parallel with a second resistor and parallel plate capacitor. A circuit diagram describing how Jain modeled the IPMC is shown in **Figure 3.a**. Assuming that the individual resistor has a comparatively low resistance to the one in series with the capacitor, the charge distribution can be related both to the input voltage and to the induced bending moment generated in the film. Combining these two relationships yields a model for the tip-displacement angle of the IPMC as a function of time. In its compact form, the relationship is denoted by **Eq. (1.14)**.

$$\theta(t) = \frac{K}{b-a}e^{-at} + \frac{K}{a-b}e^{-bt} \tag{1.14}$$

Here, K relates to the gain and IPMC capacitance, and a and b are a function of a time constant, which characterizes the bending moment generation, and the RC time constant of the modeled, in-series resistor and capacitance (K, a>0, and b>0). When applying this model to experimental data, it was found that for $t = 0, \frac{K}{b-a} + \frac{K}{a-b} = 0$.

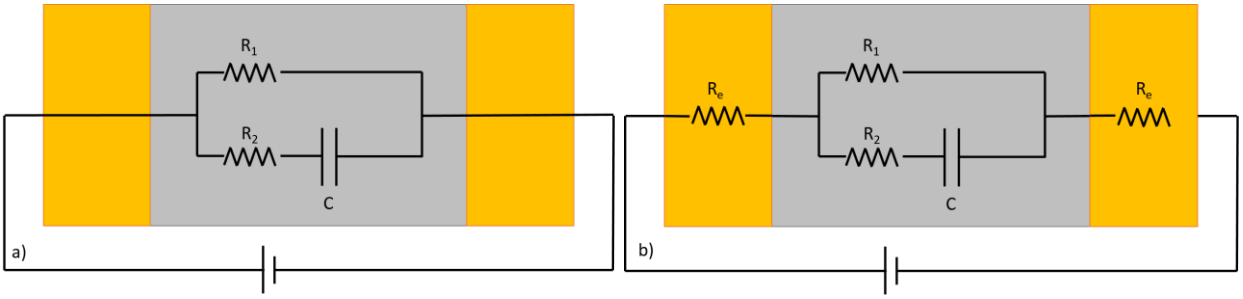

Figure 3: Circuit model comparison for IPMC actuators utilizing the a) Jain and b) Shi models

Shi extends the idea put forth by Jain a step further by considering the resistance of the two electrodes (R_e) in contact with the bulk IPMC material (R_1, R_2, and C), which was also Nafion.[136, 137] In this case two resistors on either side of the bulk circuit described by the Jain model were included. The relationship developed by Shi for tip displacement is, thus, similar to that proposed by Jain and is represented by **Eq. (1.15)**.

$$\delta(t) = B\left(\frac{a_0 - a}{a^2}e^{-at} + \frac{a_0}{a}t + \frac{a - a_0}{a^2}\right) \tag{1.15}$$

Here, a and a_0 were determined to be $a = \frac{1}{R_2 C}$ and $a_0 = \frac{1}{R_1 C}$ and B was a constant of integration found during taking the inverse Laplace of the relationship developed for the input voltage and the tip deflection. The improved upon circuit diagram for how Shi incorporated the electrodes into his model versus Jain is shown in **Figure 3.b**. When applying this model to experimental data, it was found that for $t = 0, \frac{a_0 - a}{a^2} + \frac{a - a_0}{a^2} = 0$.

Both the Jain and Shi models will be compared later in this study to showcase their applicability to accurately describe the IPMC bending phenomenon and how well they do it versus models presented in this study. For both models, when $t \to 0$, both $\theta(t)$ and $\delta(t) \to 0$; they reach similar saturation values when compared against experimental data. Also, the two models have only three fitting parameters, making them simple and compact for use. However, both models do not accurately address the *slow* portion of the actuation process (**Figure 4**) and therefore, they do not fully fit/represent the experimental data.

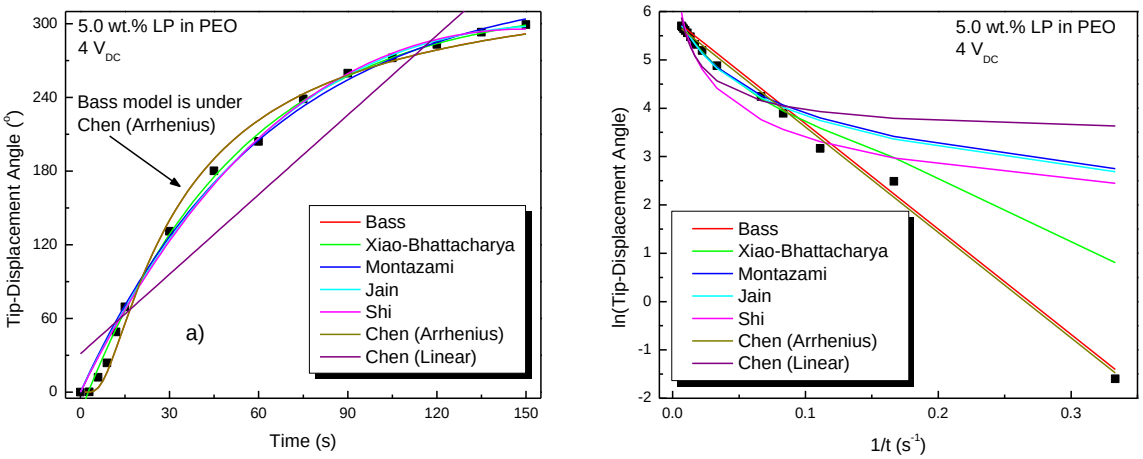

Figure 4: Application of various tip-displacement models to the a) nonlinear and b) linear experimental data for PEO with 5.0 wt.% LP

A comparison of how well the Montazami, Jain, Shi, Xiao-Bhattacharya, and Chen models, along with the Arrhenius-based model (Bass) presented herein, with how well they fit a sampling of experimental data generated in this study is shown in **Figure 4**. **Figure 4** showcases a set of experimental data for a PEO-based IPMC with 5.0 wt.% LP. Through inspection of **Figure 4.a** it can be seen that the majority of the models fit the experimental data fairly well from times greater than roughly 10 s. However, as can be seen from **Figure 4.b**, when the natural log of the experimental data is plotted against 1/t, for smaller time increments only the Arrhenius-based model presented here and the Chen model that uses an Arrhenius function for *F(t)* fit the data the closest. The Xiao-Bhattacharya model also does a good job with matching the experimental data for most of the fitting curve. The slow section of the slow, steady, saturated actuation progression for IPMCs appears to be difficult to match for the majority of the displayed models. A note of mention again for the Chen model is that Chen did not mention how the applied force in his model changed with time, just that it was applied at the end of the IPMC film. As such, the Chen model was employed with a linear and Arrhenius force representation. It is quite evident that when the

linear representation of the applied force is used that the fitting is very poor, while when the Arrhenius-based force representation is used, that the model fits very well. In reality, an applied tip force with either of these force profiles is unlikely, but that the intended force profile alluded to by Chen is likely somewhere in between. Taking this into consideration leads to the conclusion that the Arrhenius-based model developed in this study most closely resembles that of the measured experimental data. This model will further be shown to accurately fit not just the PEO-based and PVDF-based IPMCs developed for this study, but also can be used with describing the actuation of IPMCs including Nafion, Flemion, and the conducting polymer polypyrrole, making it a possible universal model, as well as one that can be easily interpreted when the data is plotted in its linear representation shown in **Figure 4**. Comparisons of how well these models fit IPMC actuation data from externally published articles will be presented in Chapter 3. As such, it will be shown that the model presented in this dissertation more closely resemble the experimental data and thus, the IPMCs themselves.

The complexity and/or lack of direct correlation to the gathered experimental data for the other models presented in this section preclude their inclusion in that analysis. However, their significance in adding depth to our knowledge of how and why IPMC actuators behave the way they due demand their acknowledgement in this report.

1.2 Motivation

The study of EAPs, including characterizing their performance and studying their behavior, is an exciting field of research. The goal of this report was to further our fundamental understanding of these types of materials and to extend our knowledge of the types of materials that can be used as EAPs. One research aim was to create biodegradable EAPs, as an alternative to the commercially available Nafion and Flemion, which did not harm the environment once they were no longer needed and their lifecycle was complete. Once the synthesis of this '*green'* polymer system was developed and refined, a systematic investigation of their bending performance was conducted to develop a model that could predict the actuators response and provide insight into physical properties of these actuators that would not otherwise be possible to obtain. Once this electromechanical model was developed, it was of interest to find a way that the actuation performance of the EAPs could be monitored without the need of a bulky optical system with the goal of creating a remote monitoring capability. A fundamental investigation of the time-dependent changes in dielectric properties of the EAP films was therefore conducted as they

underwent their bending. Through linking the changing dielectric signature and the dynamic mechanical responses, the first steps of finding a way to remotely monitor the EAP performance were taken. Additionally, changes in the films' dielectric properties translated to changes in capacitance, therefore it became of interest to study the synthesized EAPs as possible energy-storage devices. Finally, as more and more dielectric data was compiled for these films, the opportunity arose to do a fundamental analysis on this data and to investigate possible links between the EAP's conductivity and its permittivity.

The proposed contribution of this dissertation is five-fold; first to introduce the development of environmentally friendly composite EAPs that can act as alternatives to the current, non-recyclable EAP technologies; second, to create a new way to both predict and analyze the synthesized EAP's electromechanical actuation; third, to develop a more physics based approach to describe the electromechanical actuation; fourth, to link this electromechanical model with the material's dielectric properties for the development of a novel monitoring method that can reduce or eliminate the actuation monitoring hardware, thus increasing possible applications for these EAPs while providing a fundamental analysis on the direct relationship between a material's real permittivity and its conductivity which could pave the way for new scientific research and understanding; fifth, to create new materials for energy storage devices. Each of these research objectives aims at increasing our knowledge and understanding of the underlying physical processes that make the function of EAP materials possible, while also furthering current EAP research by creating EAPs from new materials.

1.2.1 Research Objectives

1.2.1.1 Objective I – Development and Analysis of Biodegradable/Green EAP

The initial objective in this study was to not only create a smart material with excellent performance characteristics, but was also, a material whose principal components were biodegradable and environmentally friendly. With the field of EAP study beginning to mature, commercial IPMC EAPs, such as Nafion (sold by DuPont) and Flemion (a carboxylate version of Nafion,[138] sold by Asahi Glass), are now widely available. As previously mentioned, these products have excellent actuating performance characteristics. Granted, these are exemplary materials for EAP research and application, but, from a lifecycle perspective, what is to come of these actuators once their use is no longer wanted/required? As previously mentioned, neither Nafion nor Flemion are biodegradable or recyclable, so when they are discarded, they will

invariably have a negative impact on the environment. Thus, the first objective, in part, was to choose a green EAP matrix material for study as a possible IPMC alternative to these products. Polymer system selection involved a literature review, resulting in the use of two parent polymer matrix materials: plant cellulose and poly(ethylene oxide) (PEO). Each of these materials have had some initial EAP studies conducted, enabling a viable starting point for their evaluation.

1.2.1.1.1 Material Selection

The first option explored for an EAP material for use in this research was electroactive paper. Cellulose is the most abundant natural polymer on Earth and is used in a wide variety of applications, ranging from paper, pharmaceuticals, foods, and textiles.[25] The cellulose molecule is comprised of repeating glucose molecules that form in alternating crystalline and amorphous regions along the cellulose fiber.[139] Hydrogen bonding between cellulose molecules creates a monoclinic crystalline structure.[140] The use of cellulose as smart materials first gained traction in 2002.[141] Here, several paper samples (hardwood, softwood, bacterial cellulose, etc.) using different types of doping chemicals (ethylene glycol, glycerin, and DL-Threitol) were tested to study their performance characteristics. The paper used was inherently environmentally friendly, biodegradable, and ultra-lightweight, so their potential use in this study was clear. Silver and gold were used as electrodes and tip displacements around 0.1 mm at 5 Hz were recorded. Research continued with this type of EAP and later, cellophane films made from cotton cellulose and saturated with sodium hydroxide.[25] These materials had recorded tip displacements of 4.0 mm at 4 Hz with a resulting energy density calculated to be 0.84 J/kg.[25] This value was based off of the tip displacement and the sample's Young's modulus, which was measured as being between 4.3-7.1 GPa. The high Young's modulus of the cellulose chains made this an interesting candidate for this study, but its low actuation performance hindered it from being selected as the primary-polymer matrix.

Poly(ethylene oxide) (PEO), a well-known solid-polymer electrolyte,[142, 143] is a lesser-known biodegradable EAP. PEO is a semi-crystalline polymer[144] and its lamella structure is responsible for creating its large degree of crystallinity as spherulites.[144] It is a polar polymer, arising from the atomic oxygen along the polymer backbone, which enables it to readily dissolve ionic salts into its matrix.[145] This characteristic enables PEO to facilitate the migration of both cations and anions through its matrix.[146, 147] Ionic mobility through the polymer matrix is related to the ability of the PEO chains to move and be rearranged in conjunction with how strong

the interaction is between the mobile cation and the oxygen atoms along the PEO backbone.[148] PEO has also been approved by FDA to be used in drug delivery systems.[149-151] PEO has also had longtime use with human applications such as: ointments due to its ability to wash off with water; suppositories where the softness of the device is controlled by the molecular weight of the PEO; formulating pharmaceuticals and drug coatings for controlled release of medication; in cosmetics like creams, lotions, and powders and styling gel like CARBOWAX®.[152] With the ability of PEO to dissolve ionic salts, its biodegradability, and with it being relatively inexpensive, PEO makes for an excellent candidate for further EAP research.

In most of the current EAP research utilizing PEO, it is typically added to other polymer matrices to enhance ionic mobility within the composite structure, due to its electrolyte properties. That is, PEO has been mixed with different polymers, such as poly(ethylene glycol) (PEG),[153] cotton cellulose,[116, 154] and conducting polymers like poly(3,4 ethylene-dioxythiophene)[22, 155] for increased actuation performance. When PEO was used as the primary matrix polymer for EAPs, PEO was doped with lithium perchlorate (LP), which results in a lowered Young's modulus for the PEO based EAP.[153] Bending strains of greater than 1% with tip displacements of approximately 13 mm were recorded as a result of this approach.

With PEO being capable of diffusing both anions and cations through its matrix, and with it being capable of large bending displacements, it was decided that this would be the parent-polymer matrix for this EAP research. Also, with cellulose having such excellent mechanical properties, it was further decided that the cellulose would be used as a filler material to create PEO-NCC composites that could combine the excellent characteristics of both materials. When ionic salts are added to the PEO matrix, its crystallinity decreases and it becomes softer and more difficult to handle.[156] To counteract this softening, a special kind of cellulose was added to increase the composite stiffness. The cellulose can be reduced to nano size, through an acid hydrolysis process, wherein the amorphous regions within the cellulose fiber strands are eliminated. This results in nanocrystalline rods that can be dispersed in the PEO solution. As will be discussed, these rods have excellent mechanical characteristics and when combined with the PEO to form a composite, they form films that are stronger than the parent PEO matrix and, in some cases, their inclusion can improve actuation performance. For these reasons, the combination of PEO and NCC to make EAPs was chosen, instead of studying one over the other.

In this study, composites of PEO with nanocrystalline cellulose (NCC) were developed as a biodegradable EAP. NCC is a biomass derivative comprised of the crystalline regions of plant cellulose fibers, making it a green, renewable material. A sulfuric acid hydrolysis process was used to eliminate the amorphous regions of the parent cellulose fiber, leaving crystalline rods with exceptional mechanical properties.[157] The crystalline regions of the cellulose films can have one of two crystalline structures; Iα has a P_1 triclinic structure and Iβ has a $P2_1$ monoclinic structure.[158] Iα is typically found in algae, whereas Iβ is dominant in most other plant materials. The Iα structure can be irreversibly changed to an Iβ structure. These rods have a Young's modulus of 110-220 GPa for NCC rods that were a few hundred nanometers in length and a few tens of nanometers in diameter.[159, 160] Therefore, it is expected that adding NCC, the Young's modulus can be enhanced, which is confirmed by the proceeding experimental results. More interestingly, it is experimentally found that the electromechanical strain response of PEO can be enhanced by adding NCC. The NCC molecule is shown in **Figure 5.a**. It can be seen that there are three hydroxyl groups surrounding a 5-carbon, 1-oxygen member ring. A small fraction of these hydroxyl groups are replaced by sulfate groups during the hydrolysis process. The structure of a cellulose chain is shown in **Figure 5.b**, where there is a clear delineation between the crystalline and amorphous regions. During the acid hydrolysis process, the amorphous regions are eliminated at a faster rate compared to the crystalline regions. The strong hydrogen bonding between the cellulose molecules in the crystalline region makes them more resistant to enzymatic hydrolysis,[161] and it is this lowered rate of elimination for the crystalline regions that is responsible for the creation of the NCC rods. The resulting crystalline rods are shown in **Figure 5.c**. As will be discussed later in this study, it is believed that the combination of the stiffness of the NCC chains and the contribution of the sulfate ions to the actuation are responsible for the enhanced actuation performance.

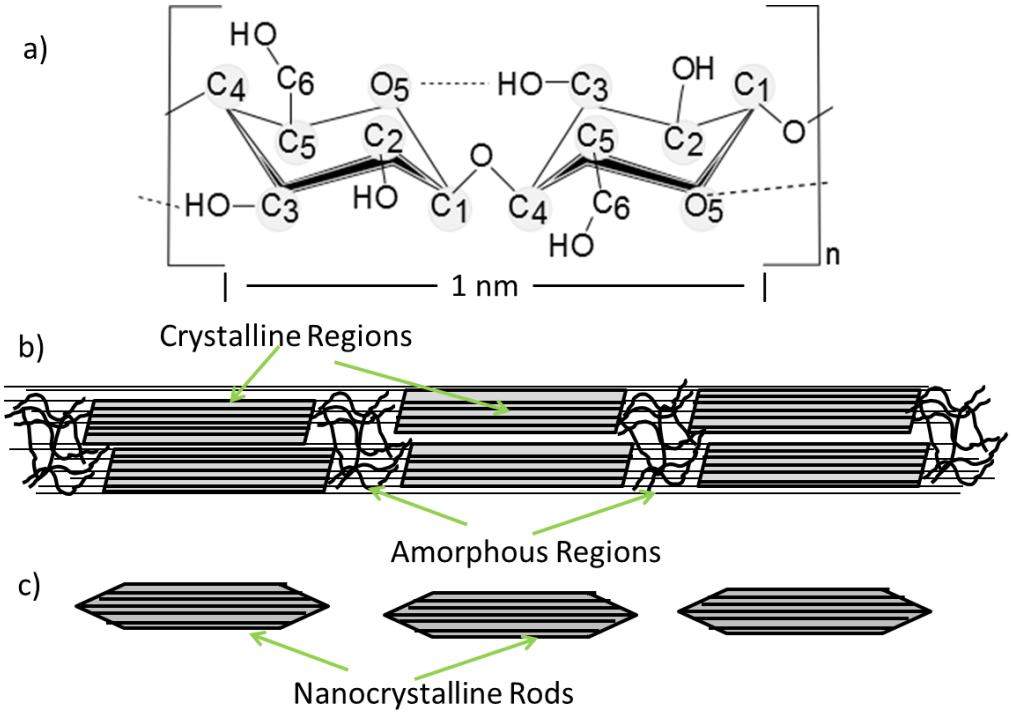

Figure 5: a) Cellulose molecule, b) representation of cellulose fiber, c) resulting nanocrystalline rods after sulfuric acid hydrolysis process

1.2.1.1.1 Time-Dependent Electromechanical Actuation Modeling

The actuation phenomenon showcased by ionic polymer-metallic composites was found to follow a three-phase actuation process: slow, steady, and saturated. Under an applied electric field, there is an initial slow actuation performance. As time increases, there is a ramp up in the bending and the actuators have a constant deflection. With further increases in time, the actuation begins to slow and saturate to a near-maximum value. This process is illustrated in **Figure 6**. Since ionic EAPs actuate based on the flux of ions through their host polymer matrix, this process can be described based on this ionic motion. When the external 4 V DC is first applied, the ions are accelerated from their initial, randomly distributed locations and begin transiting towards their attracting electrode. Here, the number of ions reaching their respective electrode is low with their effect on actuation being minimal. As the ions begin to accumulate at the electrodes, there is a period of constant actuation as a continual flux of ions reaches the electrode surface. Finally, when the ions moving within the matrix begins to be depleted, the electromechanical actuation reaches saturation point as the majority of the ions are now at the electrode interface. The generalized strain response (or tip displacement) associated with this bending process is illustrated in **Figure 7** where

the differing actuation processes are separated into their described areas [i) slow, lag response, ii) steady, constant actuation, and iii) saturated performance].

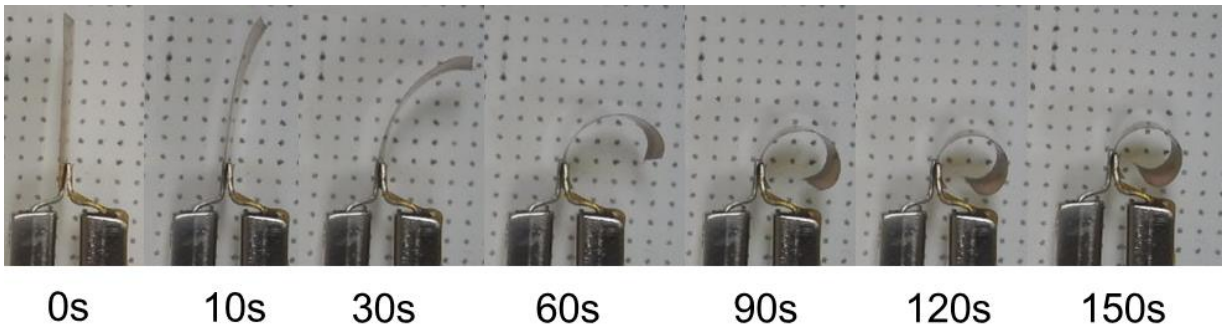

Figure 6: Typical PEO EAP electromechanical actuation response

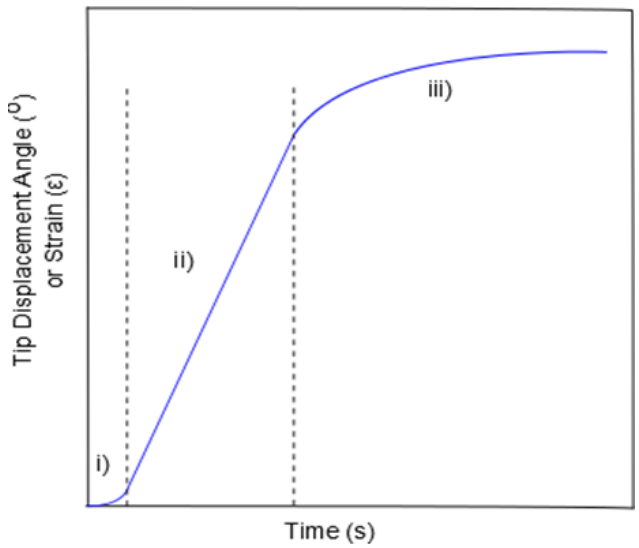

Figure 7: Generalized Arrhenius behavior for the EAP strain and tip displacement response

The slow, steady, saturated electromechanical response for IPMCs, was found for both the PEO and PVDF-based composites studied in this report. Furthermore, upon further inspection, they were found to follow an Arrhenius-like response with respect to time. The second objective of this report, therefore, introduces the development of a simple and intuitive black-box method for quickly characterizing actuator bending performance, while also providing a mechanism wherein the nonlinear IPMC actuation response can be presented as a linear regression. The applicability of this model was found to extend across multiple IPMC response characteristics, namely: tip-displacement angle, strain, and radius of curvature for the bending films.

The discovery of this Arrhenius behavior for this type of EAP provides insight into not only monitoring the strain behavior of the samples but it provides a way to characterize the material properties of the films that may not have been possible otherwise. The simple model proposed herein both fits the empirically derived data for the electromechanical performance and can be coupled with the Stokes Einstein model, thus providing the potential for this relationship to become a powerful gray-box model. The Stokes Einstein model is used to describe the motion of charged particles in a viscous medium that are subjected to an external electric field. This novel approach makes it possible to calculate the EAP's apparent viscosity, apparent ionic diffusion coefficient, and ionic velocity. In this study, two polymer systems with various ionic salts were used. PEO was used for its environmentally friendly characteristics and for its well established use as a solid-polymer electrolyte capable of readily dissolving ionic salts for use as mobile charge carriers. PVDF EAP films were also synthesized and were created to compare experimental results with the PEO composites to validate the introduced electromechanical model, which was empirically derived from the PEO actuation response. As will be discussed further in the next section and then in far more detail later on, the development of this model can be linked to the time-dependent changes in dielectric properties of the sample. It is this link that enables an indirect method of actuation monitoring.

1.2.1.2 Objective II – Development of Charge-Distribution Actuation Model

As will be further explored in subsequent chapters, the creation of the Arrhenius-based actuation model utilizes a simple function form and results in a fitting curve that only requires two fitting parameters. The possible far-reaching use of the Arrhenius-based model spurned interest in the underlying physical processes causing actuation for IPMCs. A second, gray-box model, was developed in parallel, and focused on the motion of ions through the solid-polymer electrolyte matrix. Assuming the ions moved at a constant drift velocity through the solid-polymer electrolyte matrix resulted[162] in a model that closely corroborated both the experimental data as well as the initially proposed actuation model. Specifically, this charge-distribution model was focused on how the accumulation of both the cations and anions at their respective electrode-matrix interfaces effected the strain on either side of the matrix, which resulted in the observed bending actuation. Current understanding of IPMC actuation focuses primarily on the cation motion within the matrix and assumes that the anion is stationary.[1, 163, 164] These models consider a rigidly fixed anion with a mobile cation. The mobile cation thus causes an expansion within the matrix as it

accumulates at the anode. It has been introduced that there is motion occurring for both the anion and cation in Nafion-based IPMCs containing 1-ethyl-3-methylimidazolium (EMI^+) and tetrafluorborate (BF_4^-).[165] Wherein actuation is the combination of the accumulation of the cations at the anode and then for the anions at the cathode. This report indicated that the faster moving cations, due to their size difference compared to the anions, reached their respective electrode faster. This led to the actuator initially bending towards the anode side of the film. As time went on, the larger anions would then begin to accumulate at the cathode surface leading to a transition of the bending of the IPMC from the anode to the cathode surface. A subsequent contraction would then occur at the cathode side of the sample. The researchers in the Nafion study looked at the actuation response of the anions independently as a black-box circuit model.

The model to be presented in this thesis takes this idea a step further and looks at how the overall time-dependent response of IPMC is affected by the distribution of anions and cations within the matrix and their redistribution as they accumulate at the electrode surface. It is assumed that both sides of the film experience expansion, instead of having one side expand while the other contracts. This idea behind EAP actuation is similar to the way that bimetallic systems bend for a given temperature gradient due to dissimilar coefficients of thermal expansion for the two metals. Bending occurs due to one metal expanding further than the other with changes in temperature. The success gained between this charge-distribution model as well as the Arrhenius-based model along with their applicability across multiple polymer systems lends credence for the use of the simple Arrhenius model to be used for quick analysis of IPMC EAPs, with the follow-on use of the second model for a more detailed analysis.

1.2.1.3 Objective III – Development of a Dielectric Monitoring Model

As mentioned, the traditional analysis method for monitoring EAP actuation has dealt with optical imagery or laser range finding. Both of these methods have their advantages, but come with an inherent disadvantage in that their monitoring requires a bulky monitoring system. This type of system may be acceptable for laboratory research, but in real world applications, this added equipment becomes a limiting factor. These optical analysis techniques directly monitor the samples actuation and, as described in the previous section, can be used to indirectly determine the underlying physical properties of the EAP system. The fourth objective in this study is to introduce a new methodology that takes an opposite approach to the traditional methods, in that, the process for this method is to directly monitor the changes in the samples material properties

which then leads to indirectly being able to monitor the sample's bending actuation. The proposed method involves applying a small AC field on top of the much larger DC electric field. The AC field is small enough wherein it does not impede the actuation due to the larger DC field, but it enables the monitoring of the frequency-dependent dielectric properties of the samples and how they change the longer the DC field is applied. Ionic EAPs operate based off of ionic flux within the polymer matrix and it is the time-dependent nature of this flux as they move through the matrix and reach their attracting electrode that provides a dielectric signature that can be broken up into the constituent parts for the transiting anion and cation.

Through using the well-established Cole-Cole model, which is used to describe the frequency-dependent response of non-interacting dipoles under the influence of an applied AC electric field, the ionic relaxation time can be determined. In this study, the non-interacting dipoles were defined to be the moving anion and cation arising from the dopant ionic salt used. This relaxation time correlates to the time it would take for the oscillating ions to return to a randomly oriented state once the applied electric field has been removed. For the tested EAPs, this value was found to not be a constant. It changed as a result of the applied DC electric field being administered to the samples for an extended period of time. The longer the DC field is applied, the longer the relaxation time (i.e., the longer it took for the ions to return to a randomly oriented state). When the value for this parameter was traced for the entirety of the experiment, it was found to follow a similar Arrhenius behavior to that of the electromechanical response.

It was the discovery of this Arrhenius response that shaped the third objective of this study. Along with developing and vetting two new actuation-based electromechanical actuation models, a dielectric response model is presented which tracks the changes in the ionic relaxation times in order to provide an indirect method of observing the films actuation. With this proposed method, the film's changing dielectric signature provides a way to monitor the film's physical actuation response without the need for a camera or a laser system. Through linking these two behaviors, it can be possible to remotely monitor the films actuation by solely reading its dielectric measurements.

1.2.1.4 Objective IV: Development of Ionic Conductive Material as an Energy Storage Device

The final objective of this report aims at looking into IPMC electroactive polymers as artificial muscles. As discussed previously, IPMCs operate based on the flux of ions through the

polymer matrix and actuation due to the accumulation of these ions at their respective matrix-electrode interface. The structure of IPMCs is similar to that of capacitors wherein a dielectric material is encapsulated between two conducting surfaces. The building up of charge carriers, in this case ions, at the electrode surfaces under an applied electric field acts to charge the capacitor with a total charge being proportional to the applied electric potential and capacitance of the device. Turning off the external power to the capacitor enables it to discharge and provide energy for a given application.

Capacitors are typically charged under constant voltage and the increase in charge generally follows **Eq. (1.16)**. The current through a capacitor/resistor circuit decreases during charging and follows **Eq. (1.17)**. During the discharging of the capacitor, the charge in the capacitor follows **Eq. (1.18)** and the current follows **Eq. (1.19)**.

$$q(t) = C\Delta V\left(1 - e^{-t/RC}\right) = Q_{max}\left(1 - e^{-t/RC}\right) \tag{1.16}$$

$$I = \frac{dq}{dt} = \frac{\Delta V}{R} e^{-t/RC} \tag{1.17}$$

$$q(t) = C\Delta V\left(1 - e^{-t/RC}\right) = q_i e^{-t/RC} \tag{1.18}$$

$$I = \frac{dq}{dt} = -\frac{Q_i}{RC} e^{-t/RC} \tag{1.19}$$

Here, q is charge, C is capacitance, ΔV is voltage, R is resistance, and I is current.

Batteries, on the other hand, are typically charged in three stages.[166, 167] First a constant current is applied until the battery reaches a set voltage limit; this is called bulk charging. Under a constant current, the potential difference across the battery tends to increase linearly with time, according to Ohm's law, as the internal resistance increases. This stage will typically charge a battery to 80-90% of its total charge. When the target voltage is obtained, the second stage, or absorption charge, begins and the current begins to drop as the battery reaches its saturation voltage. The current will decrease, as internal resistance again rises, until the battery is fully charged. The second stage will charge the battery up to roughly 95% total charge. The third stage of battery charging involves dropping the applied voltage to a lower level to charge the battery to 100% and to maintain the state-of-charge condition. The discharging of batteries will have a somewhat linear drop in cell voltage vs. time.

For the PEO-based IPMCs studied in this report, it was found that they had characteristics of both capacitors and batteries when it came to charge and discharging cycles. Therefore, this topic looks to shed light on the possible applications of PEO-based IPMCs as energy storage

devices. This capacitor/battery functionality would offer a new type of material application in this arena. 5.0 wt.% LP PEO-based IPMCs were studied and the results on their charging and discharging cycles are compared and analyzed.

1.2.1.5 Objective V: Discovery of a Completely New Electromechanical Coupling Effect

In addition to the PEO films, which will be extensively studied in this report, PVDF-based EAPs were also produced for comparison and study. Interestingly, it was found through this study that ferroelectric PVDF films can be forced to generate both the linear and nonlinear, bending actuation responses, resulting in a new area of EAP response and research. The behavior for materials like PVDF used in ferroelectric, electronic EAPs generates a linear actuation response due to conformal changes along the polymer backbone, wherein a predominantly cis-trans polymer chain reorients into a predominantly trans-trans chain as a response to an applied electric field.[7, 11] The electric dipole polarization of this polymer is reversible and can be changed under an applied electric field. The performance for PVDF films is a linear piezoelectric response. As described, ionic EAPs operate due to the flux of ions within their matrix. PVDF films developed here were infused with the ionic salt cobalt perchlorate so as to perform a bending actuation like ionic EAPs. However, after saturation bending actuation of the films, it was found that the films began bending in the opposite direction. This counter actuation is believed to be the result of large, localized electric fields within the PVDF matrix that cause the conformal changing along the PVDF backbone. This in turn creates a secondary, linear actuation phase of the films. The discovery of this type of actuation response opens the door for very interesting applications of these EAP films wherein complex material deformation can occur within a single uniform film. An introductory assessment of this phenomenon will be conducted for this objective and leave open the door for future research and study.

Chapter 1 References

1. Bar-Cohen, Y. and Q. Zhang, *Electroactive polymer actuators and sensors.* MRS bulletin, 2008. **33**(03): p. 173-181.
2. Bar-Cohen, Y., *Y. Electroactive Polymer (EAP) Actuators as Artificial Musles: Reality, Potential, and Challenges*. 2004, Bellingham: SPIE Press.
3. Roentgen, W., *About the changes in shape and volume of dielectrics caused by electricity.* Section III in G. Wiedemann (Ed.), Annual Physics and Chemistry Series, 1880. **11**: p. 771-786.
4. Bar-Cohen, Y., *WorldWide ElectroActive Polymers.* Artificial Muscles) Newsletter, 1999. **7**(2): p. 1-16.

5. Bar-Cohen, Y., *Actuation of biologically inspired intelligent robotics using artificial muscles.* Industrial Robot: An International Journal, 2003. **30**(4): p. 331-337.
6. Marieb, E.N. and K. Hoehn, *Human anatomy & physiology*. 2007: Pearson Education.
7. Carpi, F., et al., *Electroactive polymer actuators as artificial muscles: are they ready for bioinspired applications?* Bioinspiration & biomimetics, 2011. **6**(4): p. 045006.
8. Zhang, Q., V. Bharti, and X. Zhao, *Giant electrostriction and relaxor ferroelectric behavior in electron-irradiated poly (vinylidene fluoride-trifluoroethylene) copolymer.* Science, 1998. **280**(5372): p. 2101-2104.
9. Pelrine, R., et al., *High-speed electrically actuated elastomers with strain greater than 100%.* Science, 2000. **287**(5454): p. 836-839.
10. Zhang, Q., et al., *An all-organic composite actuator material with a high dielectric constant.* Nature, 2002. **419**(6904): p. 284-287.
11. Cheng, Z. and Q. Zhang, *Field-activated electroactive polymers.* MRS bulletin, 2008. **33**(03): p. 183-187.
12. Li, Z., Y. Wang, and Z.-Y. Cheng, *Electromechanical properties of poly (vinylidene-fluoride-chlorotrifluoroethylene) copolymer.* Applied physics letters, 2006. **88**(6): p. 062904.
13. Cheng, Z.-Y., et al., *Transverse strain responses in the electrostrictive poly (vinylidene fluoride–trifluorethylene) copolymer.* Applied physics letters, 1999. **74**(13): p. 1901-1903.
14. Xu, H., et al., *Ferroelectric and electromechanical properties of poly (vinylidene-fluoride–trifluoroethylene–chlorotrifluoroethylene) terpolymer.* Applied Physics Letters, 2001. **78**(16): p. 2360-2362.
15. Xu, T.-B., Z.-Y. Cheng, and Q. Zhang, *High-performance micromachined unimorph actuators based on electrostrictive poly (vinylidene fluoride–trifluoroethylene) copolymer.* Applied physics letters, 2002. **80**(6): p. 1082-1084.
16. Cheng, Z., et al., *Design, fabrication, and performance of a flextensional transducer based on electrostrictive polyvinylidene fluoride-trifluoroethylene copolymer.* Ultrasonics, Ferroelectrics and Frequency Control, IEEE Transactions on, 2002. **49**(9): p. 1312-1320.
17. Shahinpoor, M., *Ionic polymer–conductor composites as biomimetic sensors, robotic actuators and artificial muscles—a review.* Electrochimica Acta, 2003. **48**(14): p. 2343-2353.
18. Jager, E.W., E. Smela, and O. Inganäs, *Microfabricating conjugated polymer actuators.* Science, 2000. **290**(5496): p. 1540-1545.
19. Carpi, F. and E. Smela, *Biomedical Applications of Electroactive Polymer Actuators*. 2009: John Wiley & Sons.
20. Madden, J.D., et al., *Artificial muscle technology: physical principles and naval prospects.* Oceanic Engineering, IEEE Journal of, 2004. **29**(3): p. 706-728.
21. Xia, L.-W., et al., *Nano-structured smart hydrogels with rapid response and high elasticity.* Nature communications, 2013. **4**.
22. Ikushima, K., et al., *PEDOT/PSS bending actuators for autofocus micro lens applications.* Synthetic Metals, 2010. **160**(17): p. 1877-1883.
23. Ghaffari, M., et al., *Aligned Nano-Porous Microwave Exfoliated Graphite Oxide Ionic Actuators with High Strain and Elastic Energy Density.* Advanced Materials, 2013. **25**(43): p. 6277-6283.

24. Ha, E.-J., et al., *Electroactive hydrogel comprising poly (methyl 2-acetamido acrylate) for an artificial actuator.* Journal of Applied Physics, 2013. **114**(5): p. 054701.
25. Kim, J., S. Yun, and Z. Ounaies, *Discovery of cellulose as a smart material.* Macromolecules, 2006. **39**(12): p. 4202-4206.
26. Akle, B.J., et al., *Direct assembly process: a novel fabrication technique for large strain ionic polymer transducers.* Journal of Materials Science, 2007. **42**(16): p. 7031-7041.
27. Nemat-Nasser, S. and Y. Wu, *Comparative experimental study of ionic polymer–metal composites with different backbone ionomers and in various cation forms.* Journal of Applied Physics, 2003. **93**(9): p. 5255-5267.
28. Shahinpoor, M. and K.J. Kim, *Ionic polymer-metal composites: I. Fundamentals.* Smart materials and structures, 2001. **10**(4): p. 819.
29. Noh, T.-G., et al., *Electrochemical characterization of polymer actuator with large interfacial area.* Electrochimica acta, 2002. **47**(13): p. 2341-2346.
30. Kim, K.J. and M. Shahinpoor, *Ionic polymer–metal composites: II. Manufacturing techniques.* Smart Materials and Structures, 2003. **12**(1): p. 65.
31. Bergamasco, M., F. Salsedo, and P. Dario. *A linear SMA motor as direct-drive robotic actuator*. in *Robotics and Automation, 1989. Proceedings., 1989 IEEE International Conference on*. 1989. IEEE.
32. Baughman, R.H., et al., *Carbon nanotube actuators.* Science, 1999. **284**(5418): p. 1340-1344.
33. Barisci, J.N., G.G. Wallace, and R.H. Baughman, *Electrochemical Characterization of Single-Walled Carbon Nanotube Electrodes.* Journal of the electrochemical society, 2000. **147**(12): p. 4580-4583.
34. Barisci, J.N., et al., *Increased actuation rate of electromechanical carbon nanotube actuators using potential pulses with resistance compensation.* Smart materials and structures, 2003. **12**(4): p. 549.
35. Stoyanov, H., et al., *Molecular composites with enhanced energy density for electroactive polymers.* Journal of Materials Chemistry, 2010. **20**(35): p. 7558-7564.
36. Baughman, R., *Conducting polymer artificial muscles.* Synthetic metals, 1996. **78**(3): p. 339-353.
37. Herod, T.E. and J.B. Schlenoff, *Doping-induced strain in polyaniline: stretchoelectrochemistry.* Chemistry of Materials, 1993. **5**(7): p. 951-955.
38. Madden, J., et al. *Load and time dependence of displacement in a conducting polymer actuator*. in *Materials Research Society Symposium Proceedings*. 2002. Warrendale, Pa.; Materials Research Society; 1999.
39. Madden, J.D., P.G. Madden, and I.W. Hunter. *Conducting polymer actuators as engineering materials*. in *SPIE's 9th Annual International Symposium on Smart Structures and Materials*. 2002. International Society for Optics and Photonics.
40. Mazzoldi, A., A. Della Santa, and D. De Rossi, *Conducting polymer actuators: Properties and modeling*, in *Polymer sensors and actuators*. 2000, Springer. p. 207-244.
41. Madden, J.D., et al., *Conducting polymer actuator*. 2001, Google Patents.
42. Madden, J.D., P.G. Madden, and I.W. Hunter. *Polypyrrole actuators: modeling and performance*. in *SPIE's 8th Annual International Symposium on Smart Structures and Materials*. 2001. International Society for Optics and Photonics.
43. Ding, J., et al., *High performance conducting polymer actuators utilising a tubular geometry and helical wire interconnects.* Synthetic Metals, 2003. **138**(3): p. 391-398.

44. Yamaura, M., T. Hagiwara, and K. Iwata, *Enhancement of electrical conductivity of polypyrrole film by stretching: Counter ion effect.* Synthetic Metals, 1988. **26**(3): p. 209-224.
45. Wallace, G., et al., *Ionic liquids and helical interconnects: Bringing the electronic braille screen closer to reality.* EAP Actuators and Devices, SPIE, 2003: p. 5051-44.
46. Madden, J.D., et al., *Fast contracting polypyrrole actuators.* Synthetic Metals, 2000. **113**(1): p. 185-192.
47. Bay, L., et al., *A conducting polymer artificial muscle with 12% linear strain.* Advanced materials, 2003. **15**(4): p. 310-313.
48. Anquetil, P.A., et al. *Thiophene-based conducting polymer molecular actuators*. in *SPIE's 9th Annual International Symposium on Smart Structures and Materials*. 2002. International Society for Optics and Photonics.
49. O'Grady, M.L., P.-l. Kuo, and K.K. Parker, *Optimization of electroactive hydrogel actuators.* ACS applied materials & interfaces, 2009. **2**(2): p. 343-346.
50. Kim, S.J., et al., *Behavior in electric fields of smart hydrogels with potential application as bio-inspired actuators.* Smart materials and structures, 2005. **14**(4): p. 511.
51. Kim, S.J., et al., *Shape change characteristics of polymer hydrogel based on polyacrylic acid/poly (vinyl sulfonic acid) in electric fields.* Sensors and Actuators A: Physical, 2004. **115**(1): p. 146-150.
52. Calvert, P., *Gel sensors and actuators.* MRS bulletin, 2008. **33**(03): p. 207-212.
53. Pissis, P. and A. Kyritsis, *Electrical conductivity studies in hydrogels.* Solid State Ionics, 1997. **97**(1): p. 105-113.
54. Lehmann, W., et al., *Giant lateral electrostriction in ferroelectric liquid-crystalline elastomers.* Nature, 2001. **410**(6827): p. 447-450.
55. Huang, C., Q. Zhang, and A. Jakli, *Nematic Anisotropic Liquid-Crystal Gels—Self-Assembled Nanocomposites with High Electromechanical Response.* Advanced Functional Materials, 2003. **13**(7): p. 525-529.
56. Shenoy, D.K., et al., *Carbon coated liquid crystal elastomer film for artificial muscle applications.* Sensors and Actuators A: Physical, 2002. **96**(2): p. 184-188.
57. Thomsen, D.L., et al., *Liquid crystal elastomers with mechanical properties of a muscle.* Macromolecules, 2001. **34**(17): p. 5868-5875.
58. Finkelmann, H. and M. Shahinpoor. *Electrically controllable liquid crystal elastomer-graphite composite artifical muscles*. in *SPIE's 9th Annual International Symposium on Smart Structures and Materials*. 2002. International Society for Optics and Photonics.
59. Su, J., J. Harrison, and T. St Clair. *Novel polymeric elastomers for actuation*. in *Applications of Ferroelectrics, 2000. ISAF 2000. Proceedings of the 2000 12th IEEE International Symposium on*. 2000. IEEE.
60. Wang, Y., et al., *Deformation mechanisms of electrostrictive graft elastomer.* Smart materials and structures, 2004. **13**(6): p. 1407.
61. Kornbluh, R.D., et al. *Ultrahigh strain response of field-actuated elastomeric polymers*. in *SPIE's 7th Annual International Symposium on Smart Structures and Materials*. 2000. International Society for Optics and Photonics.
62. Pei, Q., et al. *Multifunctional electroelastomer roll actuators and their application for biomimetic walking robots*. in *Smart Structures and Materials*. 2003. International Society for Optics and Photonics.
63. Ashley, S., *Artificial muscles.* Scientific American, 2003. **289**(4): p. 52-59.

64. Kofod, G., *Dielectric elastomer actuators.* Chemistry, 2001.
65. Sommer-Larsen, P., et al. *Performance of dielectric elastomer actuators and materials*. in *SPIE's 9th Annual International Symposium on Smart Structures and Materials*. 2002. International Society for Optics and Photonics.
66. Pelrine, R., et al. *Dielectric elastomer artificial muscle actuators: toward biomimetic motion*. in *SPIE's 9th Annual International Symposium on Smart Structures and Materials*. 2002. International Society for Optics and Photonics.
67. Wingert, A., et al. *Hyper-redundant robot manipulators actuated by optimized binary-dielectric polymers*. in *SPIE's 9th Annual International Symposium on Smart Structures and Materials*. 2002. International Society for Optics and Photonics.
68. Cheng, Z.-Y., et al. *P (VDF-TrFE)-based electrostrictive co/ter-polymers and their device performance*. in *SPIE's 8th Annual International Symposium on Smart Structures and Materials*. 2001. International Society for Optics and Photonics.
69. Cheng, Z.-Y., et al., *Electrostrictive poly (vinylidene fluoride-trifluoroethylene) copolymers.* Sensors and Actuators A: Physical, 2001. **90**(1): p. 138-147.
70. Xia, F., et al. *Poly (vinylidene-fluoride-trifluoroethylene) based high-performance electroactive polymers*. in *Smart Structures and Materials*. 2003. International Society for Optics and Photonics.
71. Hopkins, P.M., *Skeletal muscle physiology.* Continuing Education in Anaesthesia, Critical Care & Pain, 2006. **6**(1): p. 1-6.
72. Duck, F.A., *Physical properties of tissues: a comprehensive reference book*. 1990: Academic Press.
73. Wood, A.W., *Physiology, Biophysics, and Biomedical Engineering*. 2012: CRC Press.
74. Bijlani, R., *Fundamentals Physiology A Textbook for Nursing Students*. 2001: JAYPEE BROTHERS PUBLISHERS.
75. Brodal, P., F. Ingjer, and L. Hermansen, *Capillary supply of skeletal muscle fibers in untrained and endurance-trained men.* Am J Physiol, 1977. **232**(6): p. H705-H712.
76. Park, I.-S., et al., *Physical principles of ionic polymer–metal composites as electroactive actuators and sensors.* MRS bulletin, 2008. **33**(03): p. 190-195.
77. Bar-Cohen, Y., et al. *Characterization of the electromechanical properties of Ionomeric Polymer-Metal Composite (IPMC)*. in *SPIE's 9th Annual International Symposium on Smart Structures and Materials*. 2002. International Society for Optics and Photonics.
78. Wang, J., et al., *A Flemion-based actuator with ionic liquid as solvent.* Smart Materials and Structures, 2007. **16**(2): p. S214.
79. Mauritz, K.A. and R.B. Moore, *State of understanding of Nafion.* Chemical reviews, 2004. **104**(10): p. 4535-4586.
80. Akle, B.J., M.D. Bennett, and D.J. Leo, *High-strain ionomeric–ionic liquid electroactive actuators.* Sensors and Actuators A: Physical, 2006. **126**(1): p. 173-181.
81. Paquette, J.W. and K.J. Kim, *Ionomeric electroactive polymer artificial muscle for naval applications.* Oceanic Engineering, IEEE Journal of, 2004. **29**(3): p. 729-737.
82. Lufrano, F. and P. Staiti, *Conductivity and capacitance properties of a supercapacitor based on Nafion electrolyte in a nonaqueous system.* Electrochemical and solid-state letters, 2004. **7**(11): p. A447-A450.
83. Bar-Cohen, Y. and S.P. Leary. *Electroactive polymers (EAP) charaterization methods*. in *SPIE's 7th Annual International Symposium on Smart Structures and Materials*. 2000b. International Society for Optics and Photonics.

84. Liu, Y., et al. *Ionic Electroactive Polymer Actuators with Aligned Carbon Nanotube/Nafion Nanocomposite Electrodes*. in *MRS Proceedings*. 2011. Cambridge Univ Press.
85. Anand, S., et al., *Energy harvesting using ionic electro-active polymer thin films with Ag-based electrodes.* Smart Materials and Structures, 2010. **19**(4): p. 045026.
86. *Safe handling and use of perfluorosulfonic acid products*. 2009.
87. *Material Safety Data Sheet - Nafion PFSA Membranes*. 2011.
88. Jung, J.-H., et al., *Electro-active graphene–Nafion actuators.* Carbon, 2011. **49**(4): p. 1279-1289.
89. Lian, Y., et al., *Enhanced electromechanical performance of graphite oxide-nafion nanocomposite actuator*. The Journal of Physical Chemistry C, 2010. **114**(21): p. 9659-9663.
90. Sigma-Aldrich, *Poly(tetrafluoroethylene) MSDS*. 2014. p. 1-7.
91. PlasticsEurope, *Guide for the Safe Handling of Fluoropolymer Resins*. 2005.
92. Nemat-Nasser, S. and S. Zamani. *Experimental Study of nafion-and flemion-based ionic polymer metal composites (Ipmcs) with ethylene glycol as solvent*. in *Smart Structures and Materials*. 2003. International Society for Optics and Photonics.
93. Okazoe, T., et al., *Synthesis of perfluorinated carboxylic acid membrane monomers by utilizing liquid-phase direct fluorination.* Journal of fluorine chemistry, 2005. **126**(4): p. 519-525.
94. Sigma-Aldrich, *Sulfuric acid, fuming.* Sigma Aldrich, 2015. **MSDS No. 435597 [Online]**.
95. Sigma-Aldrich, *Iodine.* Sigma Aldrich, 2015. **MSDS No. 326143 [Online]**.
96. Sigma-Aldrich, *Ethylene glycol.* Sigma Aldrich, 2015. **MSDS No. 324558 [Online]**.
97. Fluka, *1-Ethyl-3-methylimidazolium tetrafluoroborate.* Sigma Aldrich, 2014. **MSDS No. 04365 [Online]**.
98. Christophersen, M., B. Shapiro, and E. Smela, *Characterization and modeling of PPy bilayer microactuators: Part 1. Curvature.* Sensors and Actuators B: Chemical, 2006. **115**(2): p. 596-609.
99. Aldrich, *Polypyrrole.* Sigma Aldrich, 2014. **MSDS No. 482552 [Online]**.
100. Ansari, R., *Polypyrrole conducting electroactive polymers: synthesis and stability studies.* Journal of Chemistry, 2006. **3**(4): p. 186-201.
101. Sigma-Aldrich, *Dimethyl Sulphoxide.* Sigma Aldrich, 2015. **MSDS No. D5879 [Online]**.
102. Sigma-Aldrich, *Pyridine.* Sigma Aldrich, 2015. **MSDS No. 270970 [Online]**.
103. Kofod, G. and P. Sommer-Larsen, *Silicone dielectric elastomer actuators: Finite-elasticity model of actuation.* Sensors and Actuators A: Physical, 2005. **122**(2): p. 273-283.
104. O'Halloran, A., F. O'Malley, and P. McHugh, *A review on dielectric elastomer actuators, technology, applications, and challenges.* Journal of Applied Physics, 2008. **104**(7): p. 071101.
105. Pelrine, R., et al. *Dielectric elastomers: Generator mode fundamentals and applications*. in *SPIE's 8th Annual International Symposium on Smart Structures and Materials*. 2001. International Society for Optics and Photonics.
106. Corporation, A.S., *Dimetyle Silicone Elastomer Dispersion in Xylene.* Applied Silicone Corporation, 2006. **MSDS No. 1330-20-7 [Online]**.

107. Colas, A., *Silicones: Preparation, Properties, and Performance.* Dow Corning, Life Sciences, 2005.
108. Sigma-Aldrich, *Methanol.* Sigma Aldrich, 2015. **MSDS No. 322415 [Online]**.
109. Sigma-Aldrich, *Hydrochloric Acid.* Sigma Aldrich, 2014. **MSDS No. 339253 [Online]**.
110. Tsiakmakis, K., et al. *Measuring Motion Parameters of Ionic Polymer-Metal Composites (IPMC) Actuators with a CCD Camera*. in *Instrumentation and Measurement Technology Conference Proceedings, 2007. IMTC 2007. IEEE*. 2007. IEEE.
111. Breaban, F., et al., *LASER SCANNING VIBROMETRY APPLIED TO NONDESTRUCTIVE TESTING OF ELECTRO-ACTIVE POLYMERS.* University" Politehnica" of Bucharest Scientific Bulletin, Series D: Mechanical Engineering, 2011. **73**(2): p. 171-180.
112. Yun, S., J. Kim, and C. Song, *Performance of Electro-active paper actuators with thickness variation.* Sensors and Actuators A: Physical, 2007. **133**(1): p. 225-230.
113. Bao, X., et al., *Characterization of bending EAP beams.* 2004.
114. Bar-Cohen, Y., S. Sherrit, and S.-S. Lih. *Characterization of the electromechanical properties of EAP materials*. in *SPIE's 8th Annual International Symposium on Smart Structures and Materials*. 2001. International Society for Optics and Photonics.
115. Jung, K., K.J. Kim, and H.R. Choi, *A self-sensing dielectric elastomer actuator.* Sensors and Actuators A: Physical, 2008. **143**(2): p. 343-351.
116. Mahadeva, S.K., S. Yun, and J. Kim, *Dry Electroactive Paper Actuator Based on Cellulose/Poly (Ethylene Oxide)—Poly (Ethylene Glycol) MicroComposite.* Journal of Intelligent Material Systems and Structures, 2009a. **20**(10): p. 1141-1146.
117. Nemat-Nasser, S. and J.Y. Li, *Electromechanical response of ionic polymer-metal composites.* Journal of Applied Physics, 2000. **87**(7): p. 3321-3331.
118. Farinholt, K.M., *Modeling and characterization of ionic polymer transducers for sensing and actuation*. 2005, Virginia Polytechnic Institute and State University.
119. Tadokoro, S., et al. *Modeling of Nafion-Pt composite actuators (ICPF) by ionic motion*. in *SPIE's 7th Annual International Symposium on Smart Structures and Materials*. 2000. International Society for Optics and Photonics.
120. Pugal, D., K.J. Kim, and A. Aabloo, *An explicit physics-based model of ionic polymer-metal composite actuators.* Journal of Applied Physics, 2011. **110**(8): p. 084904.
121. Cha, Y., M. Aureli, and M. Porfiri, *A physics-based model of the electrical impedance of ionic polymer metal composites.* Journal of Applied Physics, 2012. **111**(12): p. 124901.
122. Kanno, R., et al. *Characteristics and modeling of ICPF actuator*. in *Proceedings of the Japan-USA symposium on flexible automation*. 1994.
123. Xiao, Y. and K. Bhattacharya. *Modeling electromechanical properties of ionic polymers*. in *SPIE's 8th Annual International Symposium on Smart Structures and Materials*. 2001. International Society for Optics and Photonics.
124. Brunetto, P., et al., *A model of ionic polymer–metal composite actuators in underwater operations.* Smart Materials and Structures, 2008. **17**(2): p. 025029.
125. Paquette, J.W., et al., *An equivalent circuit model for ionic polymer-metal composites and their performance improvement by a clay-based polymer nano-composite technique.* Journal of Intelligent Material Systems and Structures, 2003. **14**(10): p. 633-642.
126. Newbury, K.M. and D.J. Leo, *Linear electromechanical model of ionic polymer transducers-part I: model development.* Journal of Intelligent Material Systems and Structures, 2003. **14**(6): p. 333-342.

127. Kim, K., et al. *Ionic polymer-metal composite: an emerging smart material*. in *World Forum on Smart Materials and Smart Structures Technology: Proceedings of SMSST'07, World Forum on Smart Materials and Smart Structures Technology (SMSST'07), China, 22-27 May, 2007*. 2008. CRC Press.
128. Pugal, D., *Model of self-oscillating ionic polymer-metal composite bending actuator*. 2009, Thesis. Tartu University.
129. Kanno, R., et al. *Dynamic model of ICPF (ionic conducting polymer film) actuator*. in *Systems, Man and Cybernetics, 1995. Intelligent Systems for the 21st Century., IEEE International Conference on*. 1995. IEEE.
130. Kanno, R., et al. *Modeling of ICPF (ionic conducting polymer film) actuator-modeling of electrical characteristics*. in *Industrial Electronics, Control, and Instrumentation, 1995., Proceedings of the 1995 IEEE IECON 21st International Conference on*. 1995. IEEE.
131. Montazami, R., et al., *Thickness dependence of curvature, strain, and response time in ionic electroactive polymer actuators fabricated via layer-by-layer assembly.* Journal of Applied Physics, 2011. **109**(10): p. 104301.
132. Chen, Z., et al., *A dynamic model for ionic polymer–metal composite sensors.* Smart Materials and Structures, 2007. **16**(4): p. 1477.
133. Yim, W., J. Lee, and K.J. Kim, *An artificial muscle actuator for biomimetic underwater propulsors.* Bioinspiration & biomimetics, 2007. **2**(2): p. S31.
134. De Gennes, P., et al., *Mechanoelectric effects in ionic gels.* EPL (Europhysics Letters), 2000. **50**(4): p. 513.
135. Jain, P., et al., *Two IPMC fingers based micro gripper for handling.* International Journal of Advanced Robotic Systems, 2011. **8**(1): p. 1-9.
136. Shi, L., S. Guo, and K. Asaka. *Modeling and experiments of IPMC actuators for the position precision of underwater legged microrobots*. in *Automation and Logistics (ICAL), 2012 IEEE International Conference on*. 2012. IEEE.
137. Shi, L., et al., *A novel soft biomimetic microrobot with two motion attitudes.* Sensors, 2012. **12**(12): p. 16732-16758.
138. Yoshida, N., et al., *Characterization of Flemion® membranes for PEFC.* Electrochimica Acta, 1998. **43**(24): p. 3749-3754.
139. O'SULLIVAN, A.C., *Cellulose: the structure slowly unravels.* Cellulose, 1997. **4**(3): p. 173-207.
140. Wertz, J.-L., O. Bédué, and J.P. Mercier, *Cellulose science and technology*. 2010: Epfl Press.
141. Kim, J. and Y.B. Seo, *Electro-active paper actuators.* Smart Materials and Structures, 2002. **11**(3): p. 355.
142. Fergus, J.W., *Ceramic and polymeric solid electrolytes for lithium-ion batteries.* Journal of Power Sources, 2010. **195**(15): p. 4554-4569.
143. MacGlashan, G.S., Y.G. Andreev, and P.G. Bruce, *Structure of the polymer electrolyte poly (ethylene oxide) 6: LiAsF6.* Nature, 1999. **398**(6730): p. 792-794.
144. Huang, Y.P. and E.M. Woo, *Effects of entrapment on spherulite morphology and growth kinetics in poly (ethylene oxide)/epoxy networks.* Polymer, 2001. **42**(15): p. 6493-6502.
145. Bruce, P. and C. Vincent, *Structure of an amorphous polymer electrolyte, poly (ethylene oxide) 3: LiCF3SO3.* Chemical Communications, 1997(2): p. 157-158.
146. Gadjourova, Z., et al., *Ionic conductivity in crystalline polymer electrolytes.* Nature, 2001. **412**(6846): p. 520-523.

147. Hayamizu, K., et al., *NMR studies on poly (ethylene oxide)-based polymer electrolytes with different cross-linking doped with LiN (SO2CF3) 2. Restricted diffusion of the polymer and lithium ion and time-dependent diffusion of the anion.* Macromolecules, 2003. **36**(8): p. 2785-2792.
148. Kovac, M., M. Gaberscek, and S. Pejovnik, *Influence of humidity on microstructure and electrical characteristics of (PEO-plasticiser) nLiAl (SO3Cl) 4 polymer electrolytes.* Solid state ionics, 2000. **131**(3-4): p. 323-327.
149. Kumari, A., S.K. Yadav, and S.C. Yadav, *Biodegradable polymeric nanoparticles based drug delivery systems.* Colloids and Surfaces B: Biointerfaces, 2010. **75**(1): p. 1-18.
150. Gombotz, W.R., et al., *Protein adsorption to poly (ethylene oxide) surfaces.* Journal of biomedical materials research, 1991. **25**(12): p. 1547-1562.
151. Cohn, D., et al., *Biodegradable poly (ethylene oxide)/poly (ϵ-caprolactone) multiblock copolymers.* Journal of biomedical materials research, 2002. **59**(2): p. 273-281.
152. Bailey, F.J., *Poly (ethylene oxide)*. 2012: Elsevier.
153. Shahinpoor, M. and K.J. Kim, *Solid-state soft actuator exhibiting large electromechanical effect.* Applied Physics Letters, 2002. **80**(18): p. 3445-3447.
154. Mahadeva, S.K., et al., *Effect of poly (ethylene oxide)-poly (ethylene glycol) addition on actuation behavior of cellulose electroactive paper.* Journal of applied polymer science, 2009b. **114**(2): p. 847-852.
155. Plesse, C., et al., *Polyethylene oxide–polytetrahydrofurane–PEDOT conducting interpenetrating polymer networks for high speed actuators.* Smart Materials and Structures, 2011. **20**(12): p. 124002.
156. Zhang, Y., et al., *Effects of lithium perchlorate on poly (ethylene oxide) spherulite morphology and spherulite growth kinetics.* Journal of Applied Polymer Science, 2012. **123**(4): p. 1935-1943.
157. Hubbe, M.A., et al., *Cellulosic nanocomposites: a review.* BioResources, 2008. **3**(3): p. 929-980.
158. Poletto, M., V. Pistor, and A.J. Zattera, *Structural characteristics and thermal properties of native cellulose.* Cellulose-fundamental aspects. Ed. Van de Ven, T. and Gdbout, L. InTech, 2013: p. 45-68.
159. Šturcová, A., G.R. Davies, and S.J. Eichhorn, *Elastic modulus and stress-transfer properties of tunicate cellulose whiskers.* Biomacromolecules, 2005. **6**(2): p. 1055-1061.
160. Iwamoto, S., et al., *Elastic modulus of single cellulose microfibrils from tunicate measured by atomic force microscopy.* Biomacromolecules, 2009. **10**(9): p. 2571-2576.
161. Nishiyama, Y., P. Langan, and H. Chanzy, *Crystal structure and hydrogen-bonding system in cellulose Iβ from synchrotron X-ray and neutron fiber diffraction.* Journal of the American Chemical Society, 2002. **124**(31): p. 9074-9082.
162. Tropea, C., A.L. Yarin, and J.F. Foss, *Springer handbook of experimental fluid mechanics*. Vol. 1. 2007: Springer.
163. Yim, W., et al. *Dynamic modeling of segmented ionic polymer metal composite (IPMC) actuator*. in *Intelligent Robots and Systems, 2006 IEEE/RSJ International Conference on*. 2006. IEEE.
164. Lughmani, W.A., et al., *Modeling of bending behavior of IPMC beams using concentrated ion boundary layer.* International Journal of Precision Engineering and Manufacturing, 2009. **10**(5): p. 131-139.

165. Liu, Y., et al., *Ion transport and storage of ionic liquids in ionic polymer conductor network composites.* Applied Physics Letters, 2010. **96**(22): p. 223503.
166. Simpson, C., *Battery Charging*, in *www.ti.com*, N. Semiconductor, Editor. 2011, Texas Instruments: Texas Instruments.
167. Corporation, D., *Battery Charging Basics and Charging Algorithm Fundamentals*, in *Deltran Corporation*. 2002, Battery Tender: www.batterytender.com.

Chapter 2: Experimental Setup and Procedure

2.0 Research Methodology and Measurement Process

For achieving the proposed research objectives, the details of the research approach and methodology used are presented here. Through conducting the proposed study, a broader understanding of the actuation mechanisms concerning EAP behavior, from both the electromechanical and dielectric perspectives will be accomplished. Upon selection of PEO as the primary polymer matrix for this study, due to its biodegradability and environmental friendliness, the effect of ionic salt and NCC concentration on actuation performance was conducted for the PEO films. The amount of each constituent and the effect it had on performance was systematically studied and analyzed. For a comparative analysis, PVDF EAP films were also synthesized with the ionic salt, CoPH, added to its matrix. NCC was not added to these samples due to compatibility issues that arose when mixing the NCC suspension to the PVDF solution.

For all EAP samples, an optical and dielectric analysis was conducted, enabling near-real time observations and characterization of these smart materials. Additionally, surface morphology was studied using scanning electron microscopy and crystallinity determinations were conducted using differential scanning calorimetry.

For each specified ionic salt and NCC concentration, for a given polymer matrix, solutions were cast onto glass slides. The final films were cut into rectangular samples with equal dimensions. Where possible, for electromechanical actuation testing, three samples from each film were actuated twice, resulting in a total of approximately nine tests for a given sample set. Dielectric measurements were also recorded during each actuation run at 10 s intervals to be averaged across all tests. For the PEO samples, results indicated that the actuation testing was repeatable, reproducible, and reversible. However, for the PVDF samples, testing indicated that under voltage, the gold electrodes appeared to diffuse into the PVDF matrix during actuation. Therefore, successive testing of individual PVDF samples was limited.

2.1 Material Preparation

PEO powder ($M_V \sim 100{,}00$), lithium perchlorate (LP), and cobalt perchlorate (CoPH) were obtained from Sigma-Aldrich. Polyvinylidene Fluoride (PVDF) powder was obtained from Solvay. The perchlorate salts provided the mobile (ex: Li+) cations and ClO_4^- anions for diffusion in the polymer matrix.

2.1.1 Poly(ethylene oxide) Sample Preparation

PEO-based solutions were created using 0.3 g of total mass (PEO and ionic salt) which was dissolved into 12.5 mL of deionized (DI) water. The ionic salt was added at concentrations of 0.0, 1.0, 2.5, and 5.0 wt.%; the samples became softer with increasing salt concentration and increases past 5.0 wt.% yielded samples that were difficult to handle. For the PEO, only composites with LP were created. Attempts to add CoPH to PEO-based films resulted in samples that tended to rapidly deteriorate under ambient conditions. It was found that the ratio of 0.3 g of PEO to 12.5 ml DI water was just enough to create a clear, homogeneous solution. Solutions were magnetically stirred 12 hours and then sonicated in a Cole-Parmer 8891 ultrasonic cleaner for 90 minutes to remove any PEO clusters that had formed during the mixing process. Cluster formations in PEO solutions have been well studied[1-3] and are caused from interactions of the end groups (OH or OCH_3) that are attached to either side of the PEO backbone.[1] The OH groups show a larger tendency for dissolving in water compared to the OCH_3 groups. Upon agitation through the stirring process, the OCH_3 group can become attracted to and stick to the oxygen atoms in neighboring PEO chains, forming clusters. Ultrasonic vibrations were used[3] to break this weak bonding and enable the OCH_3 end group to tentatively dissolve in the water, creating the final solution.

For solution casting the PEO-based films, 2.54x7.62 cm glass slides were placed into a 65 ^{o}C preheated oven where 5mL of solution was cast onto the slides using a Fisherbrand 100-1000μL Finnpipette. This temperature was chosen due to it being the designated melting temperature of the PEO by Sigma-Aldrich. The solutions were kept in the oven for approximately 90 minutes. Once dry, the films were immediately removed from the oven and rapidly cooled on a freezer pack for 5 minutes. After cooling, they were peeled from the glass, covered with a second glass slide, and then annealed at 55 ^{o}C for 4-6 h to alleviate any residual stresses that were imposed on the films during the peeling process. The films tended to curl upon peeling and this annealing step was conducted to flatten the samples back out. Approximately 20 nm of gold was then sputtered onto both sides of the films, using a Pelco SC-6 sputter coater, for use as electrodes. Free-standing film thickness measurements were obtained by using a Mitutoyo 543-252 Absolute Digimatic Indicator with a 1 μm resolution. Five measurements were taken along individual sample lengths and then averaged with a calculated value of 54.5 ± 5.0 μm across the majority of the prepared composites. The composite films were cut into a rectangle shape (19.1×6.35 mm), which was used as the actuator.

A portion of the testing in this study looked at testing PEO-based films with varying thicknesses. To create thinner films, samples were prepared with 3 and 4 ml of solution cast onto glass slides instead of the usual 5 ml. This resulted in film thicknesses of 32 ± 2.0 µm and 45 ± 3.0 µm, respectively. For preparing thicker films, a 12.5 ml solution was evaporated down to 6.25 ml, resulting in films with thicknesses of 103 ± 5.0 µm.

2.1.2 Polyvinylidene Fluoride Sample Preparation

PVDF sample preparation was similar to making the PEO composites. 0.3g of total mass (or PVDF powder and ionic salt) were added to 10 mL of the organic solvent dimethylformamide (DMF) and magnetically stirred for 12 hours. Samples tested contained CoPH; attempts at creating samples with LP resulted in films with poor uniformity with the LP not readily dispersing in the final, dried film. Salt concentrations were added at 0.0, 1.0, 2.5, 5.0, 7.5, 10, 12.5, and 15.0 wt.% and magnetically stirred for 12 hours, yielding a light pink solution. The PVDF matrix was able to absorb a larger amount of ionic salt without becoming noticeably softer compared to similar salt increases with the PEO samples. 2.54x7.62 cm glass slides were placed into a preheated oven at 50 ^{o}C where 3 ml of the PVDF-salt solution was cast and left to dry for approximately 2 hours. There was minimal curling in the films after peeling, so the annealing step was disregarded. Approximately 20 nm of gold was similarly sputtered onto both surfaces of the films, to act as electrodes. Samples were cut into 19.1x6.35 mm rectangles. Thickness measurements yielded average thicknesses across all PVDF samples of 31.5 ± 3.7 µm. NCC was not added to the PVDF samples due to the PVDF samples being synthesized to validate the fitting models developed from the PEO composite analysis. The resulting salt-matrix structures for both the PEO-NCC composites and the PVDF films were similar to that shown in **Figure 1**.

2.1.3 Nanocrystalline Cellulose Preparation/Incorporation into PEO Composites

The NCC used in the PEO composites was obtained from the Forest Products Lab and Center for Bioenergy and Bioproducts at Auburn University. It originally began as a microcrystalline cellulose material (Avicel PH-101) purchased from Sigma Aldrich. The Avicel initially comes from wood chips that were ground and pretreated to remove hemicellulose, lignin and other matrix materials from the structure, leaving only purified cellulose fibers. From here, the crystalline portions of the cellulose were isolated through an acid hydrolysis process.[4] Sulfuric acid was added to a mixture of cellulose and deionized water and left to react with the cellulose in the solution for a set amount of time. The use of sulfuric acid has a two-fold result where it not

only removes the amorphous regions from the cellulose fibers, but it also leaves a negative surface charge (SO_3^- attaches to some of the NCC hydroxyl groups) on the NCC rod which makes it more stable and better dispersed in the water suspension.[5] The solution is then diluted with large amounts of deionized water to stop the reaction, and centrifuged to remove any remaining sulfuric acid and particles from the solution. The remaining suspension contains a given concentration of NCC with a controlled length, depending on the amount of time the sulfuric acid is left to react. NCC rods in this study were found to be cylindrical in shape with dimensions ranging from a few hundred nm in length and 20-50 nm in diameter. **Figure 8.a.** shows an example of a typical NCC rod found in the synthesized NCC suspension. Of note, however, is that if the sulfuric acid were left to react with the cellulose, the molecule would be completely destroyed. This indicates that through this process, the properties of the NCC can be controlled. For this study, a repeated process was conducted wherein the same general sized NCC rods were synthesized.

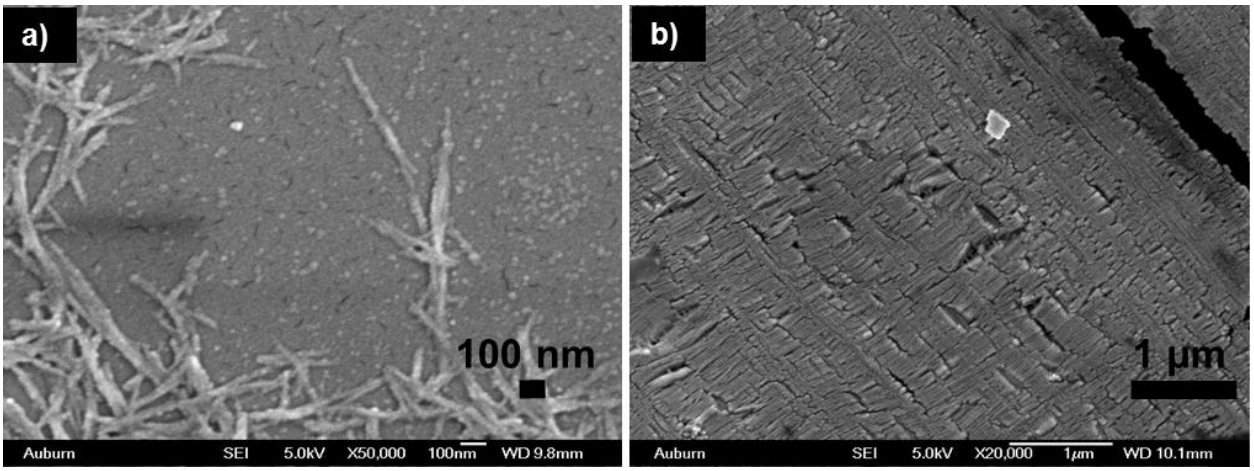

Figure 8: Scanning electron micrograph of: a) individual NCC rods and b) patterned surface of PEO matrix with 7.5 vol.% NCC added

The experiments presented in this thesis used a 35 mg/mL NCC suspension concentration with a 0.8 wt.% S content (roughly 2.0 wt.% SO_3^- concentration). NCC was added to the PEO-salt solution in concentrations of 0.0, 0.5, 1.0, 1.5, 2.5, 5.0, and 7.5 vol.% before being magnetically stirred. The previously mentioned sonication step for placing solutions in an ultrasonic bath for 90 minutes is also used to more readily disperse the NCC into the solution. The effect of the NCC addition can be seen in **Figure 8.b.**, where 7.5 vol.% NCC was added to the PEO-salt matrix. The patterned surface shows that there is clear interplay between the NCC rods and the polymer matrix. The NCC rods are chains of cellulose molecules bundled together in specific crystalline structures and held together via the hydrogen bonding of their hydroxyl groups to the oxygen atoms in the

adjoining cellulose molecules.[6] In the NCC-PEO EAP composites, the hydroxyl groups on the outer surface of the NCC rods undergo hydrogen bonding with the oxygen atoms along the PEO chain,[7] generating the structures seen in the figure. As will be discussed, this influence of the NCC on the PEO structure plays a role in the composite stiffness and overall ionic mobility within the polymer matrix, and thus the level of electromechanical bending actuation.

2.2 Characterization and Measurement

This section outlines the general testing procedures for both the PEO and PVDF-based films. References will be made to the testing equipment utilized, their settings along with the parameters with which the individual experiments were conducted. Further details on the experiments and procedures may be found in following chapter breakouts.

2.2.1 Actuation Excitation Overview and Procedure

During bending actuation experiments, EAP samples were generally tested under an applied 4 V DC. PEO-based samples were held under this applied field for approximately 2.5 min under ambient conditions, while for PVDF films, due to their faster performance, the applied voltage was held for 30-60 s at a time. As mentioned, three to six separate samples from each salt/NCC concentration were tested twice with their electromechanical actuation results being averaged. Initial testing, with non-NCC PEO-based EAPs, ranged applied voltages from 3-10 V DC. They were left at this voltage for some time until the EAPs reached their saturation actuation. It was found that at 4 V DC, the samples could reach similar saturated bending actuation as with them being tested at 10 V DC (~360^{o} tip displacement angle rotation, as shown in **Figure 9.b.**). This indicated that the maximum strain is independent of applied voltage, but that it is a function of the amount of available charge carriers in the matrix (shown via increase in actuation from **Figure 9.a.** to **Figure 9.b.**). Expectedly, the 10 V DC trials reached their maximum electromechanical actuation faster than at 4 V DC. Though the higher voltage resulted in a faster response time, the lower voltage enabled a closer study of the samples during the experiments with results found that may have been missed under faster actuation. It was also established that the samples would reach near their maximum bending actuation in roughly 2.5 min. Therefore, this time and 4 V DC were chosen for use in much of the remainder of this report for both the PEO and PVDF samples.

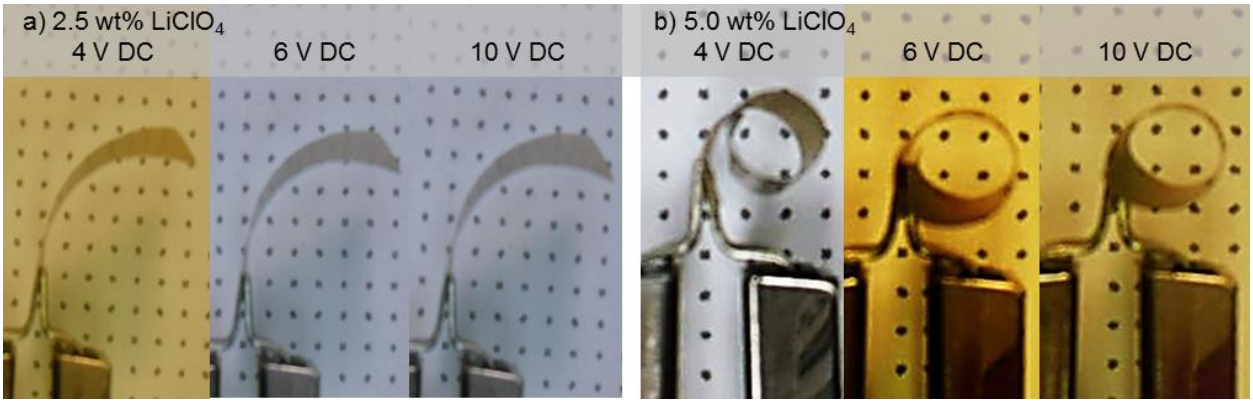

Figure 9: Saturation actuation for PEO EAPs at various voltages with: a) 2.5 wt.% LP with 0.0 vol.% NCC and b) 5.0 wt.% LP with 0.0 vol.% NCC

2.2.2 Characterization of Sample Dielectric Properties

Along with supplying the driving electric field for actuation testing, capacitance and impedance data were obtained from an Agilent 4294A Impedance Analyzer with the samples being secured for testing via an Agilent 16334A Test Fixture for initial testing and later with an in-house constructed sample holder. As stated, samples were generally held under 4 V DC, provided by the impedance analyzer, for 30 s to 2.5 min. (**Figure 10** shows the experimental setup).

To measure frequency-dependent dielectric properties of the samples, a small AC electric field was administered by the impedance analyzer at an oscillating level of 100 mV with a testing frequency range of 100 Hz to 1 MHz. Measurements were taken in Cp~D mode where the films were treated as a capacitor and the parallel-plate capacitance (Cp) was measured simultaneously with the sample loss (D).

Dielectric measurements were also taken in real-time during actuation excitation where the impedance analyzer imparted the 4 V DC bias onto the samples go generate the macroscopic bending actuation. The same, low, 100 mV AC field was also applied enabling a continuous reading of how the dielectric properties of the films varied with time under external excitation. The AC field is much smaller than the applied DC voltage, and hence wise, does not interfere with the bending actuation. Each frequency sweep took approximately 10 s to transit the targeted frequency range. A modified Excel macro was used to pull data continuously from the impedance analyzer during testing. Samples were returned to their starting orientation between timed tests using -4V DC. For each type of sample, three to six samples were chosen and their mechanical and electrical responses were measured twice per sample and then averaged.

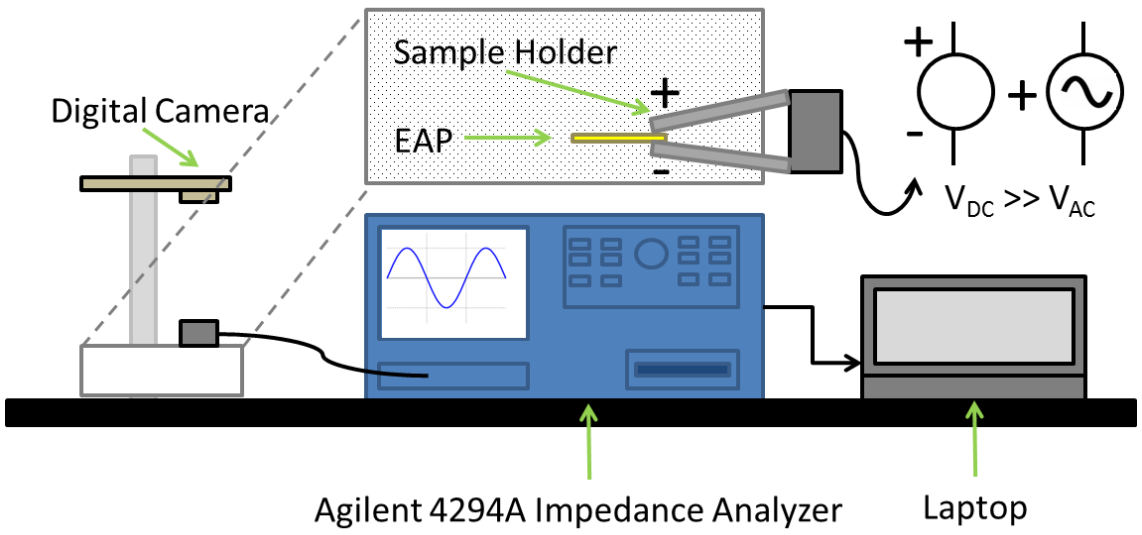

Figure 10: Experimental equipment setup diagram

Similar low-frequency dielectric testing was conducted using a Solartron SI 1260 Impedance/Gain-Phase Analyzer. Impedance measurements were taken for frequencies ranging from 0.1 Hz to 1 MHz and compared to the previously discussed impedance data. Here, a single sample from each sample set was tested, with the measurements covering similar frequencies being directly comparable to the dielectric readings taken with the Agilent 4294A Impedance Analyzer.

For sample testing that required varying temperatures, a temperature profile similar to that of **Figure 11** was used. Target temperatures were maintained for a minimum of ten minutes before dielectric or actuation measurements were taken. This enabled the system, oven chamber, and samples to reach the given temperature. Additionally, if multiple measurements were taken at a given temperature (i.e., multiple actuations were conducted at a single temperature), five minutes were waited between successive tests to ensure that any internal heating that occurred within the samples had dissipated. Temperature-dependent dielectric measurements were taken from -60 ^{o}C to 60 ^{o}C at 10 oC increments. Temperature-dependent actuation testing was conducted for temperatures ranging from 0 ^{o}C to 50 ^{o}C.

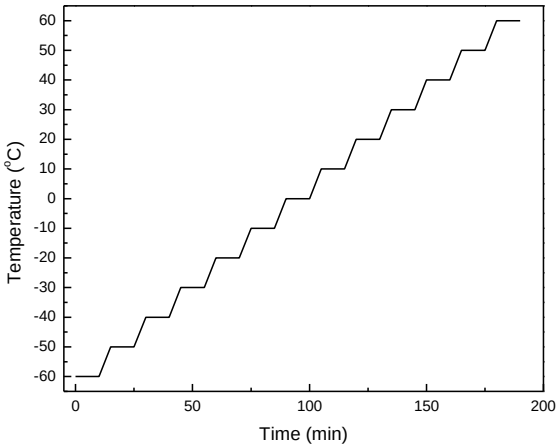

Figure 11: Sample temperature profile

Additionally, humidity was controlled during testing using an AC-9901 air pump. Air was pushed through a saturated magnesium-chloride salt solution and then into the testing chamber. The incorporation of this device enabled a fairly constant humidity within the testing chamber that ranged between 20-30%. PEO is a known material used for humidity sensors,[8] so it was important to maintain a consistent humidity throughout testing so as to mitigate unintended environmental influences on testing results.

2.2.3 Optical Analysis Procedure

Traditional methods of monitoring EAP actuation rely on external, optical monitoring equipment, characterizing actuation through imagery analysis using cameras, lasers, etc. This equipment can be bulky, making the process of monitoring the actuator inhibit possible applications that it can be used for. To combat this, a process for monitoring actuation through analyzing the changes in the EAP's dielectric properties will be introduced in the next section. However, in order to link the dielectric behavior to the electromechanical response, a new way of analyzing the actuation data using the traditional optical monitoring process should be conducted.

Due to the previously described limitations of the laser rangefinder setup, an optical analysis using a digital camera mounted with the thickness dimension facing the camera was chosen for this study. Using this method, it was possible to track sample actuation throughout its entire progression as the film went through its bending progression in response to an applied DC electric field which was held on the sample for a predetermined period of time. From here, the goal was to calculate the level of strain induced by the sample as it actuated and to model this strain response as a function of time. The samples were imaged edge-on to the camera, enabling accurate

capture of the actuation and to track the mechanical bending actuation for the entirety of the experiment.

Bending actuation was captured with a digital camera with images/videos taken at set time intervals. The experimental setup is, again, showcased in **Figure 10**. The grid of points behind the sample was used to quantify the actuation process; each point is separated by 0.5 cm. Image and video analysis was conducted using a freeware software program called Tracker. The images were taken of the actuators at set time intervals to best capture the actuation and translate that into quantifiable results. **Figure 6** shows a typical bending profile for a PEO EAP. During the first 15 s, the actuation is relatively slow and therefore, more images are taken during this interval than in successive 15 s increments. As experimentation progressed, the capturing of still images during testing was replace with recording videos. A digital camera capable of taking images at 30 frames per second was used to capture the bending performance.

2.2.4 Elastic Modulus and Elastic Strain Energy Density Determination

Elastic modulus determination was carried out with a TA Instruments RSA3 Dynamic Mechanical Analysis device, with the results averaged across five samples per salt/NCC concentration. Samples were clamped at 20 cNm torque and loaded under a constant longitudinal extension of 0.05 mm/s until fracture. The elastic modulus was calculated from the slope of the resulting stress-strain curve (**Figure 12**).

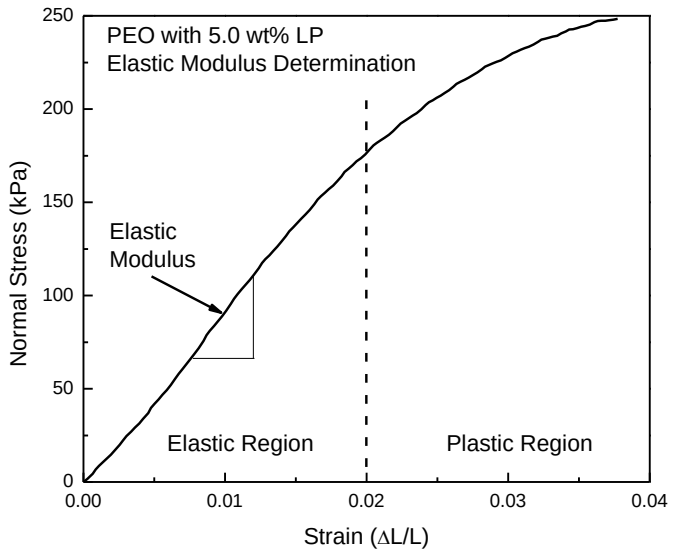

Figure 12: Sample data set for elastic modulus determination (PEO with 5.0 wt.% LP and 0.0 vol.% NCC)

As described, the elastic modulus of the films was determined from the slope of the stress-strain curve obtained while continually stretching the samples until they fractured. For actuation applications, an EAP is characterized by two critical parameters: maximum elastic energy density W_m and blocking force F_b. The W_m represents the maximum mechanical energy that can be generated by the EAP under an electric field, while the F_b reflects the maximum force/stress generated by the EAP. For a polymer with the linear elasticity, the W_m or the elastic potential energy per unit volume can be written as[9]:

$$W_m = \frac{1}{2} Y * s_m^2 \tag{2.10}$$

and the F_b can be written as:

$$F_b \propto Y * s_m \tag{2.11}$$

where, Y and s_m are the elastic modulus (i.e. Young's modulus) of the EAP and the maximum mechanical strain induced in the EAP by the electric field, respectively. Therefore, it is highly desirable to have a higher Y and a higher s_m for an EAP (note: the units for W_m are J/m^3, which is the work density, as shown in **Table 1**; to convert to energy density, with units of J/kg, the work density needs to be divided by the sample's density). Additionally, the maximum displacement observed in an actuator is also critical from the real application point of view. The maximum displacement is dependent on the maximum strain of the EAP and the device design. These two equations imply a balance between two forces within the polymer matrix: 1) the electrostatic force generated by the flux of the anions and cations stacking up at their respective electrodes and 2) the elasticity inherent to the polymer matrix itself. The electrostatic force is responsible for the observed actuation performance; the amount of strain produced in the sample, while the samples' elasticity counteracts this force. At maximum strain, these two forces are balanced and equal and the sample's overall elastic strain energy can be calculated. The W_m for a selection of the PEO-NCC composites with LP are displayed in Chapter 3. These results will be refined and analyzed with respect to PEO-NCC composites with LP and various concentrations of NCC filler, and finally compared to PVDF films with added LP/CoPH salts.

2.2.5 Scanning Electron Microscopy, Differential Scanning Calorimetry, and Energy Density Equipment

Scanning electron microscopy (SEM) analysis was conducted using a JEOL JSM-7000F Field Emission Scanning Electron Microscope. Differential scanning calorimetry testing was conducted using a TA Instruments 2910 device. Here samples masses were measured between 8-

10 mg and placed in an aluminum pan where they were heated over the desired temperature range at an increase of 10 ^{o}C/min. Energy storage testing was conducted using a constant current of 1 mA generated from an Agilent E2612A DC power supply.

2.3 Data Analysis Calculations

This section provides an overview of the process that was conducted for obtaining some of the fundamental values used in the analysis of the PEO and PVDF-based EAPs throughout the duration of this study. These calculations are critical to the analysis conducted in this report so it is of importance to discuss their procedure and outcome here as their use and relevance will be ubiquitous in the coming chapters.

2.3.1 Determination of Electromechanical Strain, Tip-Displacement Angle, and Radius of Curvature

During actuation, the tip of the EAP was tracked relative to the grid points behind it, returning an (x,y) coordinate for each successive image (later in experimentation, the tip of the film was tracked automatically using the previously mentioned Tracker freeware). The bending actuation of the composite films under a constant DC electric field showed a near-perfect circular curve, as shown in **Figure 13.a**. Therefore, these actuators were modeled as a segment of constant arc length (*a*) located on a contracting circle. **Figure 13.b-c** show the completion of the characteristic circle for PEO EAPs with 5.0 wt.% LP/0.0 vol.% NCC and 5.0 wt.% LP/1.5 vol.% NCC, respectively.

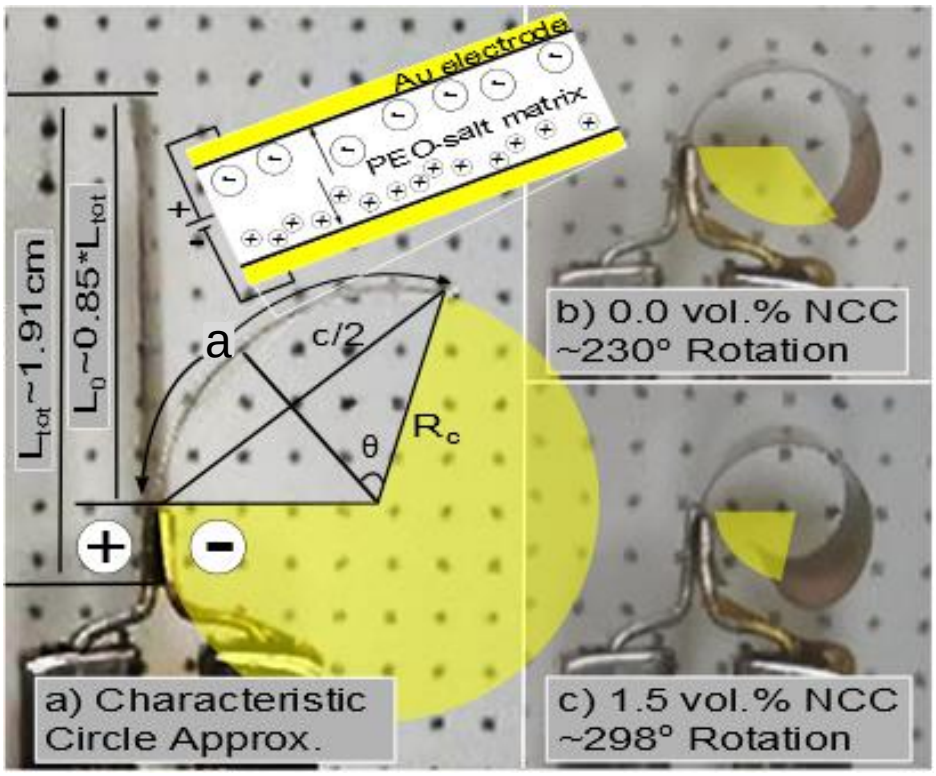

Figure 13: EAP bending geometry for a) characteristic circle approximation, b) saturation actuation for 5.0 wt.% LP with 0.0 vol.% NCC, and c) saturation actuation for 5.0 wt.% LP with 1.5 vol.% NCC composites

A perfectly straight film would represent an infinite circle and as their bending progressed, the circle would contract with an ever decreasing radius of curvature (R_c). The idealized progression of the IPMC throughout its actuation process is shown in **Figure 14**. Here, the idealized tip-displacement angle for an IPMC is illustrated as it reaches various 30^o increments in its actuation. Again, the IPMC is treated as a segment of constant length on a contracting circle. This implies that a characteristic circle can be represented, with a varying radius of curvature, for the film as it actuates. The figure shows the characteristic circle segments for three angles: 30^o, 120^o, and 330^o. It is evident that the radius of curvature decreases with increasing tip-displacement angle. Also, as an example with 120^o, the tip displacement angle can also be determined by applying a tangent line to the tip of the film. This leads to a manual measurement way to capture the IPMC tip-displacement angle.

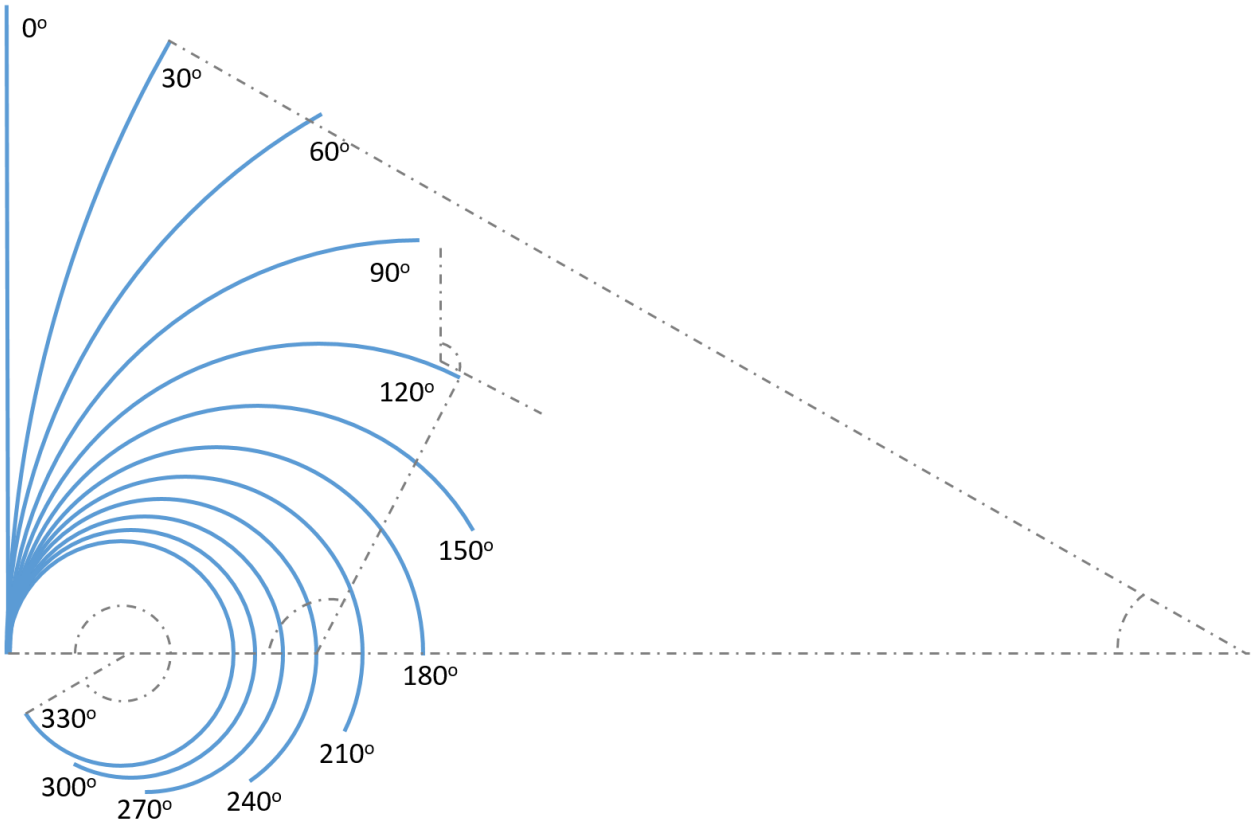

Figure 14: Progression of IPMC tip-displacement angle θ

The assumption of the films being that of a segment of constant arc on a contracting circle results in only two pieces of information being available about the geometry of the film with respect to this assumption: the length of the film (which is the arc length (a)) and the chord. The tip coordinates, from the base of the film to its tip, provided the chord (c) value for the time-dependent characteristic circle, defining the clamped location of the film as (0,0). From the geometry of the circle, the equations which can be used to calculate R_c are shown below as **Eq. (2.1)** and **Eq. (2.2)**, where θ is the angle subtended by the chord on the circle (the tip-deflection angle of the EAP relative to the origin). Unfortunately, there is no direct algebraic way to calculate R_c based solely on a and c, so to calculate this value with the eventual goal of determining the sample strain behavior, a numerical solution method is necessary.

$$a = R_c\theta \tag{2.1}$$

$$c = 2R_c \sin\frac{\theta}{2} \tag{2.2}$$

Newton's Method, which uses an iterative process to numerically solve for the roots of a given parent equation to arrive at a solution for the target variable,[10] was chosen to numerically

solve for θ. This could then be used to solve for R_c using **Eq. (2.1)**, and then ultimately to calculate strain. It takes the form:

$$x_{n+1} = x_n - \frac{f(x_n)}{f'(x_n)} \tag{2.3}$$

where, x_n represents an initial guess for the targeted value, x_{n+1} is the next calculated approximation, $f(x_n)$ is the parent function, and $f'(x_n)$ is its derivative. To obtain the parent function, which in this case will target solving for the tip-deflection angle θ, and its derivative **Eq. (2.1)** and **Eq. (2.2)** will be used as the starting point. They can be combined, yielding:

$$c = \frac{2a}{\theta}\sin\frac{\theta}{2} \tag{2.4}$$

which takes the form:

$$\frac{c}{a} = \frac{\sin x}{x} \tag{2.5}$$

where, $x = \frac{\theta}{2}$. Rearranging this equation into the desired form for its roots yields:

$$\sin x - \frac{c}{a}x = 0 \rightarrow\ f(x_n) = \sin x - \frac{c}{a}x \tag{2.6}$$

taking the derivative returns:

$$f'(x_n) = 0 = \cos x - \frac{c}{a} \tag{2.7}$$

Inserting **Eq. (2.6)** and **Eq. (2.7)** into **Eq. (2.3)** forms the numerical approach for finding the angle, θ from **Eq. (2.1)**.

$$x_{n+1} = x_n - \frac{\sin x_n - \frac{c}{a}x_n}{\cos x_n - \frac{c}{a}} \tag{2.8}$$

After an initial guess for the angle between 0 and 2π, iterating **Eq. (2.8)** converges towards the final angle approximation. Multiplying the result by 2 returns the entire angle subtended by the arc length and chord which when substituted into **Eq. (2.3)** returns the radius of curvature R_c. Strain can be calculated using **Eq. (2.9)**, where *s* is the strain and *h* is the sample thickness.[11] It is clear that strain is inversely proportional to the radius of curvature, which intuitively makes sense, since the larger the curl, the smaller the radius of curvature, and thus greater expected strain.

$$s = \frac{h}{2R_c} \tag{2.9}$$

This relationship is used in **Figure 19.b**, from Chapter 3, where the calculated tip-displacement angle profile for a sampling of films is provided and in **Figure 19.a**, where the corresponding

strain behavior is shown. As discussed previously and tied directly to the EAP actuation response, there is an evident lag, constant strain, and saturated behavior found that is showcased by the time-dependent strain response. This phenomenon will be analyzed further in the proceeding sections.

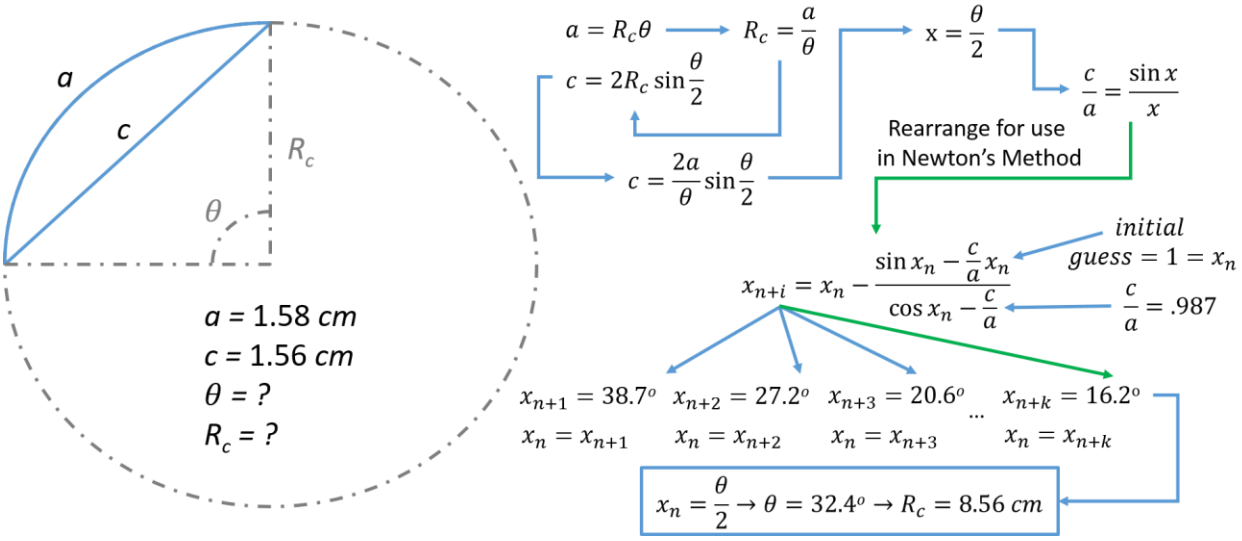

Figure 15: Newton's Method example using experimental data from a PEO film with 5.0 wt.% LP

A sample process for calculating the tip-displacement angle θ and the radius of curvature R_c is shown in **Figure 15**. Here, actual experimental data for the arc length (length of the actuating film) *a* and the chord (distance from the base to the tip of the sample) *c* are given. The film is represented by the solid segment of the circle shown and the characteristic circle for the actuator at this specific point in the actuation process is represented by the dashed circle. Again, for the images and videos taken, the only information known for the film is its length and chord, so the tip-displacement angle and radius of curvature must be determined. Since there are no algebraic relationships that can do this at hand, Newton's Method was chosen to calculate these parameters. The equation manipulation described above is illustrated and the iterative solution process is shown after an initial guess (in this case, 1 rad) is provided (of note, is that after each iteration, the angle is given in radians; this has been converted to degrees here). After five iterations, the final angle value is arrived at with a 0.56% difference from the angle value obtained in the fourth iteration.

2.3.1 Dielectric Calculations, Analysis and Cole-Cole Plots

As described in Chapter 3, in addition to recording the bending actuation of the EAP films via an optical monitoring system, a new methodology will be proposed in this study to quantify this process. In this respect, frequency-dependent dielectric measurements across a set frequency

range were taken at predetermined intervals to track the time dependent changes in these readings. Again, the samples actuated due to the applied 4 V DC while the dielectric readings were taken through the addition of a small 100 mV AC field (**Figure 10)**. A representative composite plot of the data recorded for a 2.5 minute test is shown in **Figure 16**. **Figure 16.a.** shows the changes in the real dielectric constant of the material, while **Figure 16.b.** displays how the loss response changes under the applied DC load. It is evident that the relaxation peak in **Figure 16.b.** shifts its frequency location as time goes on. This peak signifies the maximum applied AC field frequency that the oscillating ions within the PEO matrix can match;[12] above this frequency, the ions will still vibrate, but at a lower-than-applied frequency. **Figure 16.b** clearly illustrates that this peak shifts to lower frequencies, with respect to time, under the large driving DC voltage. Similar responses have been recorded for each of the salt and NCC concentrations and with multiple samples for each of these respective composite constituents. This indicates that there is a clear and repeatable response that can be readily measured for analysis. Chapter 5 will further discuss the analysis of this response in detail.

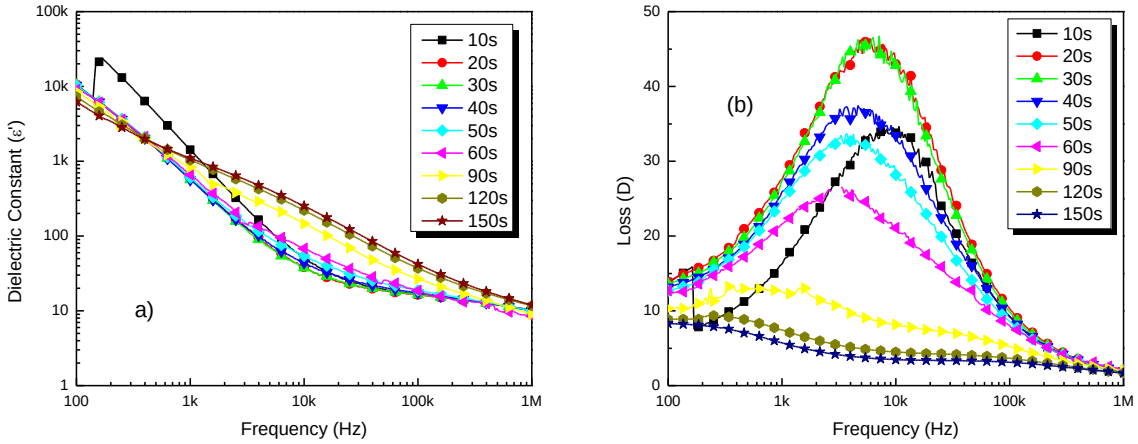

Figure 16: Time-dependent dielectric response for PEO-NCC composites with 5.0 wt.% LP and 1.5 vol.% NCC showing a) real dielectric constant and b) dielectric loss

As mentioned, **Figure 16.a-b** shows how a 5.0 wt.% LP in PEO film's frequency-dependent dielectric properties changes with respect to time when subjected to an additional, larger DC field and will be further addressed later in the study. As for now, the focus will be on some of the basic calculations and fittings employed for interpreting the dielectric data to better understand the physical meaning behind the gathered experimental data.

Under an alternating electric field, a materials complex permittivity can be described by **Eq. (2.10).**

$$\varepsilon^* = \varepsilon' - i\varepsilon'' \quad (2.10)$$

Here, $\varepsilon'$and ε''represent the materials real and imaginary permittivity, respectively. The real portion of the permittivity indicates how much energy from an external electric field is stored in the material while the imaginary portion indicates how dissipative or lossy a material is. When using the impedance analyzer to measure a materials dielectric properties, it is set to Cp~D mode, where again, the films are modeled as a parallel-plate capacitor and thus, the real portion of the material's capacitance and its' loss are recorded. This enables the real permittivity ε' to be determined from converting the capacitance, using **Eq. (1.1)** along with the geometry of the film. **Figure 17.a** is the result of this calculation.

$$C = \varepsilon_0 \varepsilon' \frac{A}{h} \quad (1.1)$$

The material's loss *D* is a composite of the material's real and imaginary response and is described by **Eq. (2.11)**. It represents the ratio of a material's ability to dissipate versus store energy in response to the applied AC frequency.[13] Again, the time dependent changes of this property for a PEO-based IPMC are shown in **Figure 17.b**.

$$D = \tan\delta = \frac{\varepsilon''}{\varepsilon'} \quad (2.11)$$

The material's imaginary permittivity response is a function of the material's dielectric loss and conductivity, as described by **Eq. (2.12)**.

$$\varepsilon'' = \varepsilon''_{rd} + \frac{\sigma_{AC}}{\omega \varepsilon_0} \quad (2.12)$$

Here, $\sigma_{AC}$is the frequency-dependent conductivity, ω is the angular frequency ($\omega = 2\pi f$), and $\varepsilon_0$is the permittivity of free space. ε''_{rd} represents the dielectric loss of the material. A film's AC conductivity can be calculated by solving this equation directly for σ_{AC}. If $\sigma_{AC}$is plotted versus frequency, then a film's DC conductivity ($f \approx 0\ Hz$) can be approximated if the generated curve does not vary much with respect to the applied frequency for the low frequency region.

The dielectric data can be further explored by plotting the material's imaginary permittivity versus its' real permittivity. This is called the Cole-Cole plot. It can be used to calculate the static permittivity ε_0 for when the applied frequency is very low, the permittivity for a very high frequencies ε_∞, and the relaxation time τ_0.[14] For an ideal dielectric material, a plot of ε''versus ε'would yield a semicircle with the center of the circle located on the ε' axis. For a non-ideal dielectric material, deviations from the semicircle plot indicate losses within the material possibly due to ionic conductivity. As an example, the real and imaginary permittivity, loss, and Cole-Cole

plot are shone in **Figure 17.a-d** for a PEO film without any LP salt. The applied AC frequency ranges from 0.1 Hz to 1 MHz. The slope in **Figure 17.c** was found to be -0.816, indicating the predominance of DC conductance in this region[15]. A flatter slope would indicate lower losses within the dielectric material at low frequencies.

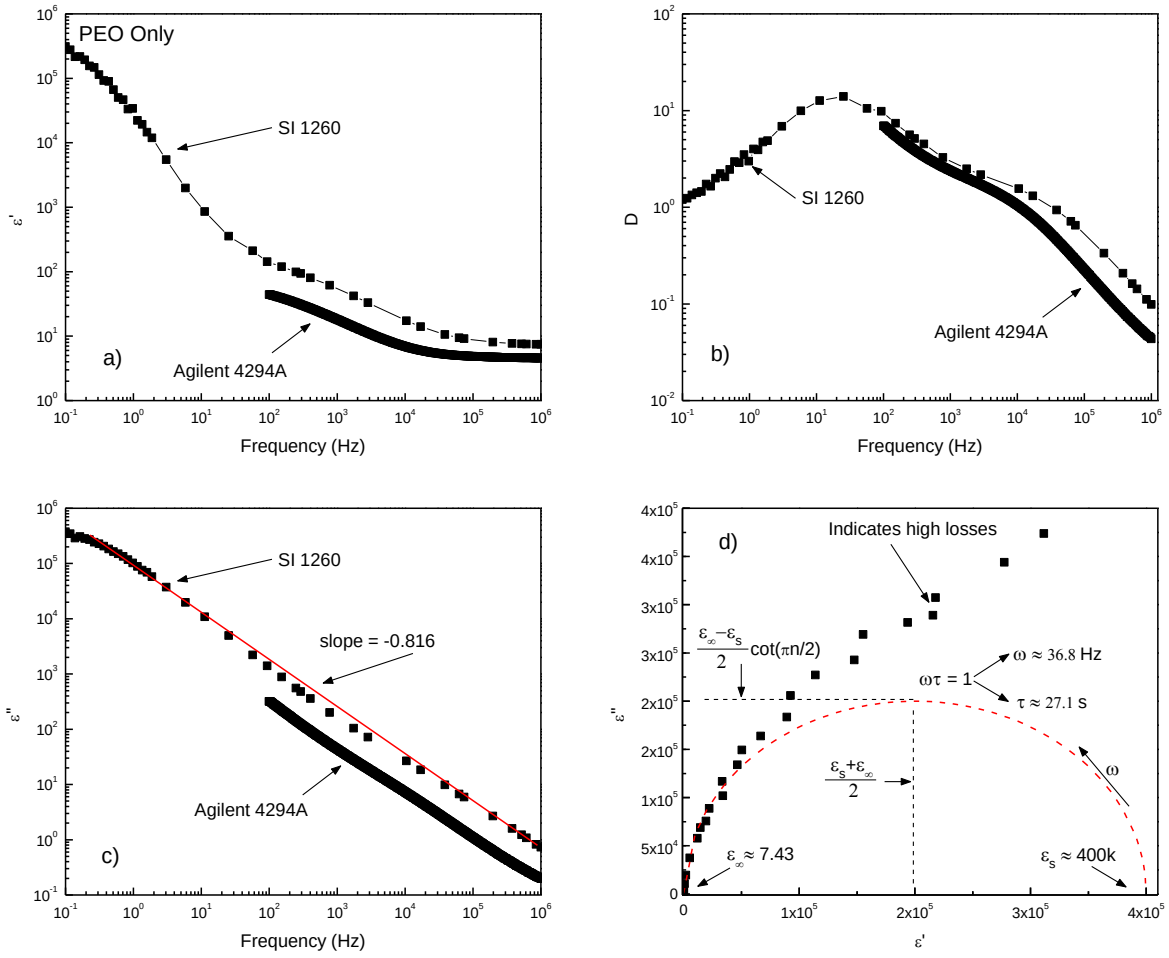

Figure 17: Example of dielectric calculations for a film of only PEO showcasing the a) real permittivity, b) loss, c) imaginary permittivity, and d) Cole-Cole plot (note: dielectric measurements from both the SI 1260 and Agilent 4294A impedance analyzers are shown for comparison)

The maximum of the semicircle for the Cole-Cole plot (**Figure 17.d**) indicates where the angular frequency ω and the relaxation time $\boldsymbol{\tau}$ (the time it takes for the dipoles or charge carriers within a material to reorient under an alternating electric field) equal 1. This offers a graphical way to obtain these parameters. In this example, the PEO film is clearly not ideal, with a large tail extending from an initial arc which can be represented by the plotted semicircle. The permittivities ε_0 and ε_∞ were found to be approximately 400k and 7.43, respectively, with a relaxation time of

27.1 s, and where n was approximated as 1, indicating a singular relaxation process within the material.

The semicircle itself in **Figure 17.d** is a curve generated by the Cole-Cole relaxation model. A Cole-Cole relaxation process is a model that accounts for polar dielectric materials that have more than one relaxation time when submitted to an alternating electric field.[14] The empirical relationship created by Cole-Cole is shown in **Eq. (2.13).**

$$\varepsilon^*(\omega) = \varepsilon_\infty + \frac{\varepsilon_0 - \varepsilon_\infty}{1 + (i\omega\tau_0)^{1-\alpha}} \tag{2.13}$$

Here, the α term can be between 0 and 1 and refers to how broad the distribution of relaxation times is. A value of 0 indicates that there is only one relaxation time for the given dielectric material (Debye relaxation). This relationship can be manipulated into a form representing the equation of a circle,[14, 16] as shown by **Eq. (2.14)**, where $n = 1 - \alpha$.

$$\left(\varepsilon' - \frac{\varepsilon_0 + \varepsilon_\infty}{2}\right)^2 + \left[\varepsilon'' + \frac{\varepsilon_0 - \varepsilon_\infty}{2}\cot(n\pi/2)\right]^2 = \left[\frac{\varepsilon_0 - \varepsilon_\infty}{2}\csc(n\pi/2)\right]^2 \tag{2.14}$$

The center of the circle is located at:

$$\left(\frac{\varepsilon_0 + \varepsilon_\infty}{2}, \frac{\varepsilon_\infty - \varepsilon_0}{2}\cot(n\pi/2)\right) \tag{2.15}$$

In addition, the radius of the circle can be determined by:

$$r = \frac{\varepsilon_0 - \varepsilon_\infty}{2}\cot(n\pi/2) \tag{2.16}$$

The closer the ε_0 and ε_∞ permittivities are, the lower the loss within the dielectric and a lower dependence on applied frequency.[17] Therefore, a material with low loss and small frequency dependence would have the smallest semicircle possible.

As mentioned, the employment of the dielectric relationships referenced in this section will be applied in the analysis of the experimentally recorded data. Since the analysis of the data later in the study will be of importance, it was vital to discuss how these calculations would take place in this section so as to focus the discussion on the idea at hand.

Chapter 2 References

1. Hammouda, B., D.L. Ho, and S. Kline, *Insight into clustering in poly(ethylene oxide).* Marcomolecules, 2004. **37**: p. 6932-6937.
2. Ho, D.L., B. Hammouda, and S.R. Kline, *Clustering of poly(ethylene oxide) in water revisited.* Journal of Polymer Science, 2002. **41**: p. 135-138.
3. Morariu, S. and M. Bercea, *Clustering in poly(oxyethylene) aqueous solutions.* Academia Ramana, 2011. **56**(5): p. 545-551.
4. Elazzouzi-Hafraoui, S., et al., *The shape and size distribution of crystalline nanoparticles prepared by acid hydrolysis of native cellulose.* Biomacromolecules, 2008. **9**(1): p. 57-65.

5. Hubbe, M.A., et al., *Cellulosic nanocomposites: a review.* Bioresources, 2008. **55**: p. 929-980.
6. Samir, M.A.S.A., F. Alloin, and A. Dufresne, *review of recent research into cellulosic whiskers, their properties and their application in nanocomposite field.* Biomacromolecules, 2005. **6**: p. 612-626.
7. Mahadeva, S.K., et al., *Effect of poly(ethylene oxide)-poly(ethylene glycol) addition on actuation behavior of cellulose electroactive paper.* Journal of Applied Polymer Science, 2009. **114**: p. 847-852.
8. Harsányi, G., *Polymer films in sensor applications: a review of present uses and future possibilities.* Sensor Review, 2000. **20**(2): p. 98-105.
9. Ragavan, V., *Materials Science and Engineering–A first course*. 2006, Prentice Hall of India, New Delhi.
10. Atkinson, K.E., *An Introduction to Numerical Analysis*. 1978, New York, NY: Wiley.
11. Zhang, Q., et al., *An all-organic composite actuator material with a high dielectric constant.* Nature, 2002. **419**(6904): p. 284-287.
12. Gupta, S., *Krishan's Engineering Physics Vol-2*. Krishna Prakashan Media.
13. Havriliak, S. and S.J. Havriliak, *Dielectric and mechanical relaxation in materials: analysis, interpretation, and application to polymers*. 1997: Hanser New York.
14. Raju, G.G., *Dielectrics in electric fields*. Vol. 19. 2003: CRC Press.
15. NACEUR, H., A. MEGRICHE, and M. EL MAAOUI, *Frequency-dependant dielectric characteristics and conductivity behavior of Sr1− x (Na0. 5Bi0. 5) xBi2Nb2O9 (x= 0.0, 0.2, 0.5, 0.8 and 1.0) ceramics.* Oriental Journal of Chemistry, 2013. **29**(3): p. 937-944.
16. Wei, Y.Z. and S. Sridhar, *A new graphical representation for dielectric data.* The Journal of chemical physics, 1993. **99**(4): p. 3119-3124.
17. Ahmad, Z., *Polymeric dielectric materials.* by Silaghi MA. InTech, Rijeka, 2012: p. 3-26.

Chapter 3: Development and Analysis of a Biodegradable/Green EAPs

3.0 Overview

As stated in Chapter 1, a large drive for this study was to create a smart material that was environmentally friendly, biodegradable, and one that did not use harsh chemicals with its synthesis. PEO was thus chosen to be the primary polymer matrix of study for this report. The ionic salt of choice for this polymer was chosen to be lithium perchlorate, which is readily dissolved into the PEO matrix due to the atomic oxygen along the PEO backbone. Under excitation, the dissociated ions travel to their respective electrodes, which in turn generates the overall observed bending actuation response. Henceforth, biodegradable IPMC EAPs were synthesized and tested under various testing parameters. This section provides a characterization of the PEO films and an in-depth analysis of the actuation behavior of the films and how they compare with other similar IPMC EAPs.

As stated in Chapter 2, films were synthesized with 1.0, 2.5, and 5.0 wt.% LP with final samples having dimensions of 1.9 cm x 0.62 cm with an average thickness of 54.5 ± 5 μm for PEO-based 5 ml of solution cast onto a glass substrate. As will be seen in the proceeding sections, the increase in salt concentration was accompanied by a decrease in stiffness, i.e. Young's Modulus. To circumvent this decline, a biodegradable, green stiffening material was sought after. NCC, when added to the PEO matrix, was found to increase film stiffness while also increasing the electromechanical response. Concentrations of NCC added to the PEO films were 0.5, 1.0, 1.5, 2.5, 5.0, and 7.5 vol.% NCC suspension. The increase in actuation performance was found to be due to the sulfate space charge which replaces some of the hydroxyl groups along the NCC backbone during the sulfuric acid hydrolysis process. This sulfate ion acts to more readily disperse the NCC chains in the water suspension. This space charge is also known to be labile in alkaline solutions and will readily dissolve in the presence of ionic salts. The performance between this type of NCC imbedded in the PEO and that of NCC without the sulfate space charge are compared.

3.1 Young's Modulus Determination

The Young's modulus for a given sample was determined through calculating the slope of the stress strain curve in the initial, linear region, as described in Chapter 2. This property will be used to calculate the film's energy density, which provides a means for comparison with other EAP materials. For the PEO-NCC composites with LP as the ionic salt, the compiled results of this testing is shown in **Figure 18**. It can be seen that there is a generally linear decrease (-6.0 MPa

per wt.% LP) in the elastic region with increasing salt concentration. 5.0 wt.% LP was chosen as the primary salt concentration for this research, and at that concentration, there was found to be a linear increase in Young's modulus with increasing NCC content at a rate of about 30 MPa per vol.% NCC. This relationship clearly illustrates the strong interaction between the PEO matrix and NCC filler. Of note is the 1.5 vol.% NCC concentration, where it was determined that the Young's modulus was found to be approximately 133 MPa. The benefits of this concentration are explicitly described in other sections, so it is important to mark that this PEO-NCC composite had a 20% increase in stiffness compared to non-NCC films.

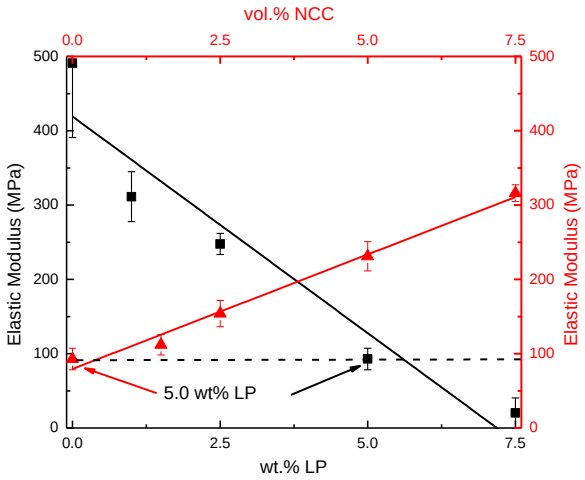

Figure 18: Elastic modulus trending for increasing LP concentrations (black curve) and increasing NCC vol.% (red curve)

The Young's Modulus and elastic energy densities data for all of the PEO-based films tested in this study are listed in **Table 2**. As can be seen from the table, the Young's Modulus for the HCl-based NCC also increases with increasing NCC content. However, there is not the corresponding actuation boost as seen with the sulfuric-acid based NCC. Of note with the table, the energy densities are calculated with the fitted maximum strain for the bending actuation performance, which the fitting process will be detailed later in this chapter. A free standing film for the hydrochloric-acid based NCC was not obtainable, so its value is not included in this table.

Table 2: Young's Modulus and energy density data for various IPMC composites

	wt.% LP	vol.% NCC	Y_m (MPa)	W (kJ/m^3)	W (J/kg)
PEO	0.0	0.0	491	--	--
	1.0	0.0	311	1.49	1.31
	2.5	0.0	248	3.23	2.83
	5.0	0.0	92.9	4.36	3.83
	7.5	0.0	20.1	--	--
NCC-H_2SO_4	5.0	1.0	135	5.54	4.87
	5.0	1.5	112	12.1	10.6
	5.0	2.5	154	8.64	7.59
	5.0	5.0	231	2.08	1.82
	5.0	7.5	316	0.198	0.174
NCC-HCl	5.0	1.0	176	0.296	0.260
	5.0	2.5	339	2.90	2.55
	5.0	5.0	454	1.01	0.886
	5.0	7.5	501	0.198	0.174
PVDF	15.0	0.0	476	3.66	2.52
NCC-H_2SO_4	--	--	7760	--	--

3.2 Actuation Performance (Strain and Tip-Angle Displacement)

The actuation performance of PEO-based EAP films will be discussed at great length in the proceeding sections and chapters. Therefore, this section will discuss a brief set of experimental data without any fitting parameters associated with it. The addition of ionic salt to the PEO matrix results in films with greater actuation performance. This is due to the availability of more mobile charge carriers to add to the electromechanical actuation. However, as discussed in the previous section, the increased performance comes at the cost of mechanical stiffness, which may influence possible applications for these films. **Figure 19.a-b** shows the time dependent strain response and the tip-displacement angle behavior for various PEO-based IPMCs with increasing LP and NCC content. It is clearly evident that with increasing LP concentrations, the actuation performance increases. In addition, it can be seen that with initial increase in NCC content, there is an increase in the electromechanical response. As will be discussed in further detail in the proceeding chapter, this is due to the sulfate space charge which adds to the mobile ions available to generate the actuation response. When adding 1.0 vol.% to the 5.0 wt.% LP PEO films, the response is fairly similar to the non-NCC films. However, with the small increase in NCC content to 1.5 vol.%, there is a large jump in strain and tip-displacement behavior. For comparison sake, the tip-displacement angle was chosen as the parameter of choice for the majority of the figures shown in this report,

this was done because the strains experienced by the films were low and due to the tip-displacement angle being a more tangible parameter to follow and describe. Again, this concept will be discussed in greater detail later, but its recognition serves the purpose of providing an example of the electromechanical actuation performance that these biodegradable EAPs are capable of. The inserts in **Figure 19.b** relate what the observed actuator performance was in relation to the displayed data and is applicable for both the strain and tip-displacement angle figures. Also, a similar plot could be constructed featuring the time-dependent nature of the radius of curvature for these films, if treated as a segment of constant arc length on a contracting circle, where if the radius of curvature data was normalized with respect to the length of the films (i.e. the arc length), then that would return the tip-displacement angle. As can be seen, there are three modes to the data presented in this figure; slow, steady, and saturated. The modeling of this behavior will be the main focus of the following two chapters. The fitted parameters for this figure are also in the next chapter.

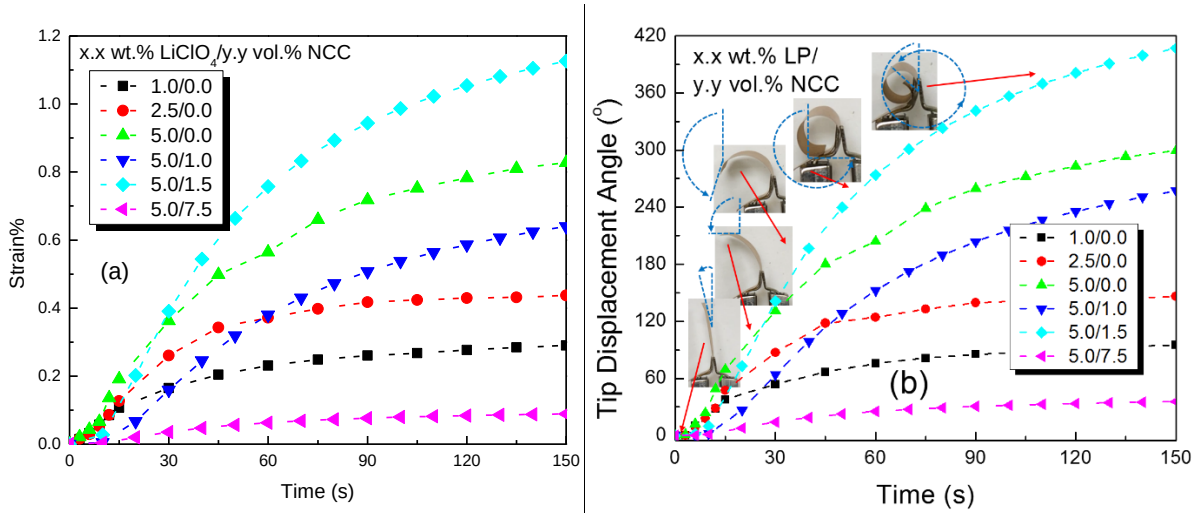

Figure 19: a) Strain and b) tip-displacement angle electromechanical actuation response of PEO-based IPMC composites

3.3 Energy Density

The calculations related to energy density are described in other sections in this report. Therefore, this section will primarily discuss the results of these calculations and compares the films developed in this study with other types of EAPs. **Figure 2** from Chapter 1 displayed the energy density versus increasing applied electric field for a group of various EAPS, both ionic and electronic. **Figure 20** updates this figure with the work done from this study. It now includes the behavior from the PEO IPMCs with LP, but no NCC, the PEO-NCC composites (both for the sulfuric acid based and HCl-based composites), as well as for PVDF-based films that were also

fabricated for this study for comparison sake and will be discussed later. It is clear that the PEO-based films have a comparable performance to that of animal muscle, to varying degrees, but require a larger driving voltage. In this comparison, they are also comparable to Nafion in terms of energy density using the fitted maximum energy density. The response time for the Nafion films is upwards of two orders of magnitude higher (**Table 1**), but depending on the application, this could be good or bad. The data for **Figure 20**, from the PEO-based and PVDF IPMCs are located in **Table 1**.

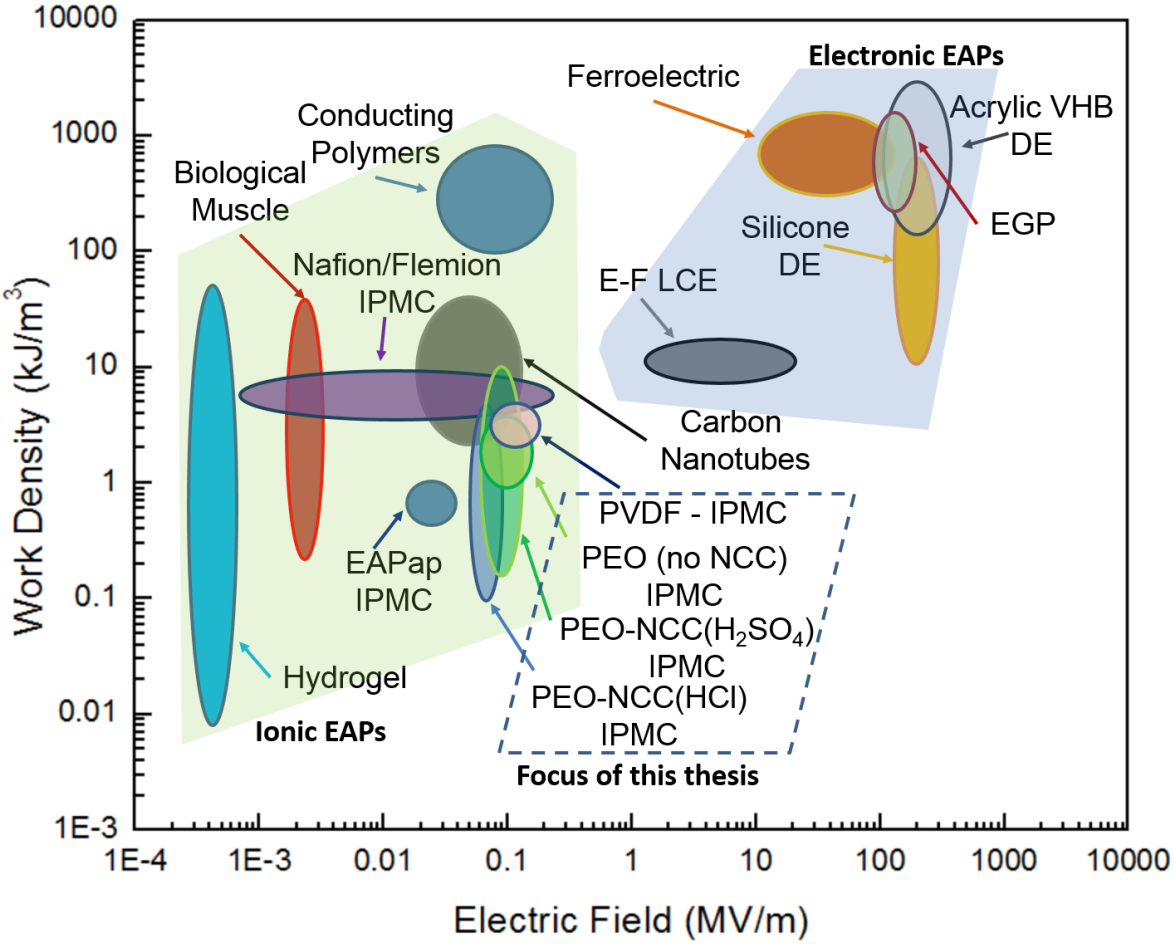

Figure 20: Updated performance comparison for ionic and electronic EAPs, including the results from this report

3.4 Development of Arrhenius-Like Behavior Based Electromechanical Bending Model

This section discusses the results of the Arrhenius-based electromechanical actuation model described in Chapter 1. Specific attention was focused on the PEO-based IPMCs and the majority of the reported results discuss the results of PEO films with varying concentrations of ionic salt and NCC content, as well as testing under various conditions like varying temperature, voltage, and thickness. The simplicity of this model allows for quick analytical results of sample

actuation. It can also be extended to multiple polymer systems. As such, results from synthesized PVDF-based films are also reported here, as well as published results from other researchers for varying EAP systems, such as: IPMCs (Nafion and Flemion) and conducting polymers (polypyrrole).

Through additional inspection of the results shown in **Figure 19**, it was found that during actuation, the sample film response followed an Arrhenius-like behavior. The transitioning parts of the nonlinear actuation behavior of IPMC EAPs can be described as three modes: slow, steady, and saturated. As such, it is found that this response can be modeled as an Arrhenius-like behavior using **Eq. (3.1)**, where time would take the place of Temperature in an ordinary Arrhenius relationship.

$$y = y_{max} e^{-B/t} \tag{3.1}$$

Here, B is a time constant and y can be any of the parameters typically utilized to describe actuator behavior, namely: strain ε, tip-displacement angle θ, and radius of curvature R. This relationship obeys the boundary conditions: as $t \to 0, y \to 0$ and as $t \to \infty, y \to y_{max}$. ε and R are linked through the expression shown in **Eq. (3.2)**.[1]

$$\varepsilon = \frac{h}{2R} \tag{3.2}$$

where, h is the EAP thickness. R and θ can be related if the sample is modeled as a section of constant arc length on a contracting circle, where an initial flat actuator would have an infinite radius of curvature. If described in this way, then their relation is $s = R\theta$, where s is arc length. These relationships make **Eq. (3.1)** a very flexible modeling equation. θ was modeled here since it describes more of a physical representation of how the samples perform compared to displaying strain data. The geometry of the bending IPMCs was shown in **Figure 13** where the tip-displacement angle is the angle subtended by the radius of the time-dependent characteristic circle of the film and its length. The tip-displacement angle can also be represented by the angle of the tip of the actuator with respect to the initial orientation of the film.

As mentioned, **Figure 19** displays the tip-displacement behavior of the PEO-NCC composites under 4 V DC. Values for each sample were averaged from six tests where three films were actuated twice. The fitting function was applied to this experimental data and was found to closely follow the experimental data in all cases, as shown by the solid curve in **Figure 21** (see next section). Of note is that with 1.5 vol.% NCC added to the composites, maximum actuation is

achieved, whereas increased NCC concentrations (7.5 vol.% NCC) provided a lowered performance. The increase in actuation is believed to be due to the addition of sulfate ions to the actuation and swelling process. These ions interact with the hydroxyl groups along the NCC chain during the hydrolysis process[2] and comprise roughly 2.0 wt.% of the final NCC suspension. It is widely known that the moiety of the sulfate groups attached at the NCC surface is rather labile and can readily be removed when submitted to mild alkali conditions,[3] thus their incorporation into the PEO matrix is likely responsible for the added performance. Samples with 5.0 wt.% LP had 30% lower stiffness than 1.0 wt.% samples, but with an increased displacement of 250%. The addition, for the 5.0 wt.% LP samples, composites with 1.5 vol.% yielded both a 20% increase in Young's modulus and a 33% increase in displacement. Using the fitted maximum strain, energy densities were calculated to be 4.3 kJ/m^3 and 12 kJ/m^3 for the 5.0 wt.% samples without NCC and for the 1.5 vol.% NCC composites, using $W = \frac{1}{2} Y \varepsilon_{max}^2$, where Y is the sample's Young's Modulus.[4]

Rearranging **Eq. (3.1)** yields **Eq. (3.3)**:

$$\ln y = -B\left(\frac{1}{t}\right) + \ln y_{max} \tag{3.3}$$

This simple manipulation immediately turns a complex nonlinear curve fit into an easy-to-interpret linear regression, which can be seen in **Figure 21**. The trending of the slope (the time constant *B*) is easy to infer and understand; the slope generally increases with increasing LP concentration which makes sense, intuitively since the 5.0 wt.% samples actuate faster and further than the 1.0 wt.% samples. Therefore, they should reach similar angles earlier in their response time with their maximum strain being their projected y-intercept ($\ln y_{max}$). Interestingly, the 1.5 vol.% NCC samples, though saturating with a higher overall strain, started slower than their non-NCC counterparts. This may be due to some initial impedance caused by the stiff NCC rods. The time constant *B* increased with increasing LP concentration (16 to 28 s); with the NCC, the time constant spiked to 53 s for 1.0 vol.%, then decreased to 39 s for 1.5 vol.%, then finally 34 s for 7.5 vol.%.

The Arrhenius-Based Model described herein, again describes the actuation response of the PEO-based actuators very well. The three-phased behavior of these EAPs (also illustrated in **Figure 7**) the slow, phase [**Figure 7-i)**], constant, steady bending phase [**Figure 7-ii**)], and finally a saturated bending or strain phase [**Figure 7-iii**)] can be attributed to the ionic flux in the matrix outlined in Chapter 1. The Arrhenius-Based Model suits these conditions well, and further study,

as will be discussed in the proceeding sections, will show that this simple model can be extended to PEO-based films under varying experimental testing conditions as well as multiple EAP systems.

3.4.1 Performance of PEO Composites with Sulfuric-Acid Based NCC

As described in Chapter 2, the curve of the sample bending actuation is assumed to follow that of a near-perfect circle, so the films were modeled as a segment of constant arc length on a contracting circle. The strain was found to be a function of the changing radius of curvature, assuming a constant sample thickness, with the strain response calculated using the **Eq. (3.2).**The tip displacement and strain for PEO-NCC composites are showcased in **Figure 19** for various concentrations of ionic salt and NCC in the composite EAPs. From the figure, it is clear that for certain NCC concentrations, namely 1.5 vol.%, that there is a large increase in the actuation response (actuation increased initially with increasing NCC content, then decreased after peaking with 1.5 vol.% NCC). It is reasonable to imagine that further increases in NCC content would reduce the ionic mobility in the composite since NCC has a much more dense structure than PEO, so that the ions may not be able to move within NCC. However, compared with composites without NCC, a higher electromechanical strain is observed in the composites, as shown in **Figure 19**. This indicates that the NCC can have some positive influence on the actuation performance. **Figure 21** shows the nonlinear and linear fitting profiles for the tip-displacement angle data shown in **Figure 19**. It is clear that the nonlinear fitting **Eq. (3.1)** and its linear form **Eq. (3.3)** match well both representations of the experimental data.

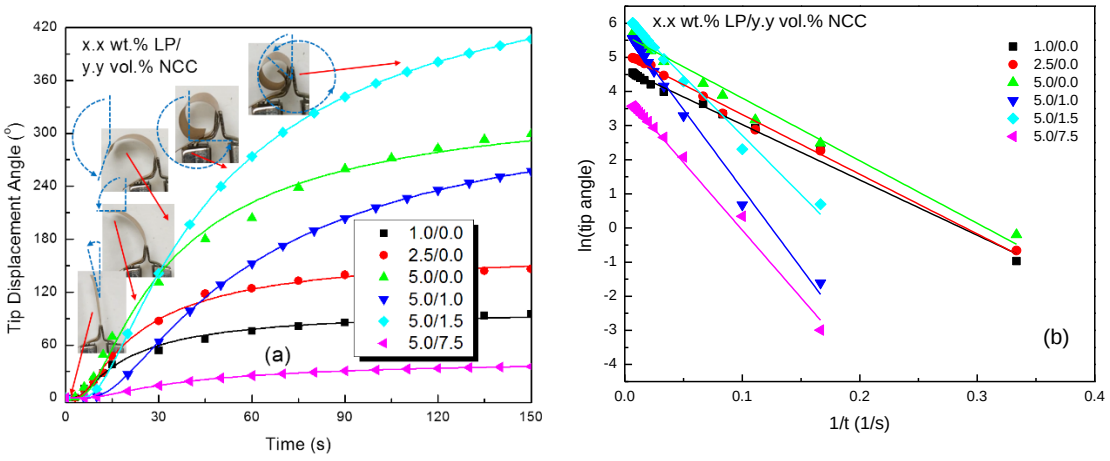

Figure 21: a) Nonlinear and b) linear Arrhenius-Based Model fitting for PEO-NCC composites with varying wt.% and vol.% of LP and NCC

It is well known that NCC interacts with the PEO matrix via hydrogen bonding between the hydroxyl groups present on the NCC surface and the atomic oxygen along the PEO backbone.[5, 6] However, during the sulfuric acid hydrolysis process used in NCC synthesis, the acid interacts with some of these surface hydroxyl groups wherein charged sulfate groups (SO_3^-) are attached to the NCC chain for promoting better dispersion in aqueous solutions, as previously mentioned.[2] A sample of the NCC suspension was dried and it was determined that the sulfur concentration was 0.8 wt%, which translates to roughly 2.0 wt.% SO_3^-. The suspension had been thoroughly dialyzed during the hydrolysis process to remove any free sulfuric acid, indicating that this concentration of sulfates was attached to the NCC chain. It is widely known that the moiety of the sulfate groups attached at the NCC surface is rather labile and can readily be removed when submitted to mild alkali conditions.[3] The increased strain is therefore theorized to be caused by this trait and that the lithium within the PEO matrix (i.e., a solid-polymer electrolyte) disassociates the sulfate groups from the NCC chains and that these freed sulfate ions also contribute to the ionic flux, moving towards the cathode with the perchlorate ions. With the perchlorate and sulfate ions being about the same size, with radii of 240 pm and 258 pm, respectively, the addition of the sulfate contributes approximately 1.31 μg of free, equally-mobile anions per sample (a 0.14% increase in ions for 1.5 vol.% NCC). At low NCC concentrations, the result of this contribution is an increase in strain; however, as the NCC concentration increases further, the added sample stiffness caused by the rigidity of the NCC structure outweighs the effect of the added amount of sulfate ions transiting in the matrix, thus decreasing the overall actuation. That is, there are two factors that determine the influence of NCC on the electromechanical response observed in the composites: one is positive due to the sulfate contribution of NCC and the other is negative due to the dense structure of NCC. Therefore, if the size of NCC can be further reduced, better electromechanical properties should be observed. **Table 3** displays the fitting results for the PEO-based composites with sulfuric-acid hydrolysis based NCC. As mentioned, the addition of small concentrations of NCC can increase actuator performance, but too much NCC will degrade the performance due to increases in film stiffness.

Table 3: Nonlinear and linear fitting parameters for PEO IPMCs with varying concentrations of LP and NCC

PEO-NCC Composites		Eq. (3.1) (nonlinear fitting)			Eq. (3.3) (linear fitting)		
x.x/y.y wt.% Salt/vol.% NCC	V (DC)	B (s)	θ_{max} (°)	s_{max} (%)	B	θ_{max} (°)	s_{max} (%)
1.0/0.0	4.0	16	100	0.31	16	100	0.25
2.5/0.0	4.0	19	170	0.51	17	160	0.40
5.0/0.0	4.0	28	350	0.97	22	320	0.81
5.0/1.0	4.0	52	360	0.91	46	330	0.83
5.0/1.5	4.0	50	530	1.47	36	480	1.2
5.0/7.5	4.0	35	45	0.11	40	40	0.1

3.4.2 PEO with Hydrochloric Acid Hydrolysis-based NCC IPMC Composites

As described, the PEO-NCC composites with the NCC created via a sulfuric acid hydrolysis process resulted in a few of the concentrations resulting in similar, if not better, actuation results, namely, for the 1.5 vol.% NCC samples. This increased actuation response was believed to be due to the addition of the sulfate space charge, a remaining sulfate group from the hydrolysis process, being weakly linked to the NCC chain. Upon excitation, this sulfate group added to the actuation response of the PEO-NCC composites and thus the addition of the NCC to the PEO matrix not only increased the film's stiffness, but was responsible for the increased actuation response for low levels of NCC added.

To prove that the sulfate space charge was likely responsible for the increased actuation response, a suspension of NCC created through a hydrochloric acid hydrolysis process, similar to the sulfuric acid hydrolysis process was conducted. The resulting NCC had no remaining space charges on its structure. Samples were created in a similar manner to the sulfuric-acid-based PEO-NCC composites and tested under 4 V DC for 2.5 min. The resulting time-dependent, tip actuation angle response is shown in **Figure 22**. It is clear, that even with only 1.0 vol.% added suspension that there is a dramatic decrease in actuation response. **Table 4** showcases the fitting parameter for each of the experimental trials. This result lends proof that it is the sulfate space charge present on the sulfuric-acid-based hydrolysis process that causes the increased actuation performance.

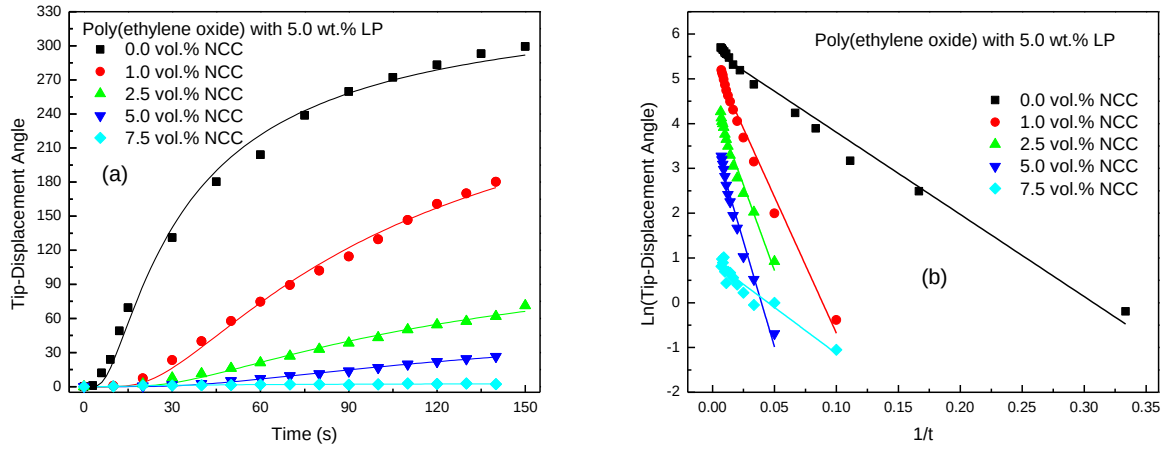

Figure 22: a) Nonlinear and b) linear actuation response for PEO-NCC composites utilizing hydrochloric-acid-hydrolysis based NCC

Table 4: Fitting parameters for PEO-NCC composites utilizing hydrochloric-acid-hydrolysis-based NCC

PEO-NCC Composites		Eq. (3.1) (nonlinear fitting)			Eq. (3.3) (linear fitting)		
x.x/y.y wt.% Salt/vol.% NCC	V (DC)	B (s)	θ_{max} (°)	s_{max} (%)	B	θ_{max} (°)	s_{max} (%)
5.0/0.0	4.0	28.0	350	0.97	18.3	280	0.71
5.0/1.0	4.0	90.7	335	0.84	60.9	224	0.56
5.0/2.5	4.0	114	141	0.35	76.3	93.1	0.23
5.0/5.0	4.0	143	71.9	0.18	94.1	41.1	0.10
5.0/7.5	4.0	30.1	30.3	0.076	20.6	2.53	6.3E-5

3.4.3 Variable-Voltage Testing of PEO-Based IPMCs

The Arrhenius-Based Model was also tested for the PEO-based films under varying voltages. **Figure 23.a-b** shows the nonlinear and linear fitting of a single 5.0 wt.% sample (with no NCC) under 4, 8, and 10 V DC (the PVDF films tended to breakdown at voltages higher than 4 V DC and therefore those results are not shown here). Films were actuated at the target voltage until impeded by the sample holder, then the polarity was reversed in order to straighten the film. The voltage was incremented to the next value and the process was repeated. It is clear that actuation occurs faster with increasing voltage, however, through analysis of **Figure 23**, even though the samples were actuated under differing voltages their maximum displacement was approximately the same. This is an intuitive conclusion since the samples tested were at the same LP concentration and should therefore have very similar final actuation performance. The time

constant was found to decrease with increasing voltage with approximately a 40 s *B* value for 4 V DC and 6.5 s at 10 V DC, indicating a slower response at lower voltages. A separate sample was used for the variable-voltage testing, resulting in fluctuations in the time constant value; this can be attributed to minor differences in the samples during the synthesis process.

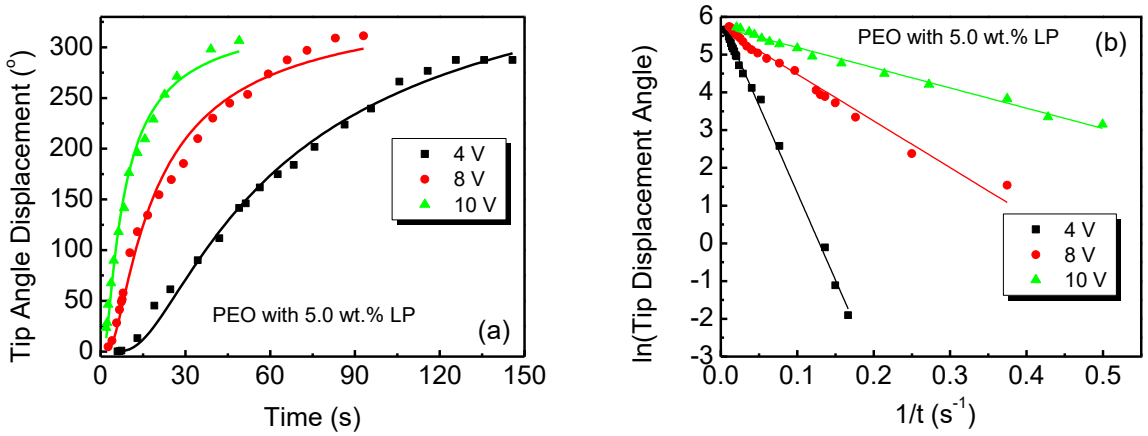

Figure 23: a) Nonlinear and (b) linear regression modeling of PEO-based IPMCs with 5.0 wt.% LP under varying applied DC voltages

In addition to the 5.0 wt.% LP results, samples with 1.0 and 2.5 wt.% LP were also tested under similar variable voltage conditions. **Figure 24.a-b** show the nonlinear and linear fitting results for PEO IPMCs with 2.5 wt.% LP while **Figure 24.c-d** show the fitting results for 1.0 wt.% LP. For these tests, a single IPMC film was actuated with 4 V DC for roughly 2.5 min, then -4 V DC was applied to return the film to its original shape. The external voltage was then increased and the process was repeated. Generally, for these actuators, the rate of actuation increased with increasing voltage. The increasing actuation response was showcased in each type of actuator with near-constant fitted maximum tip-displacement angle when fitted with both **Eq. (3.1)** and its linear counterpart, **Eq. (3.3)**.

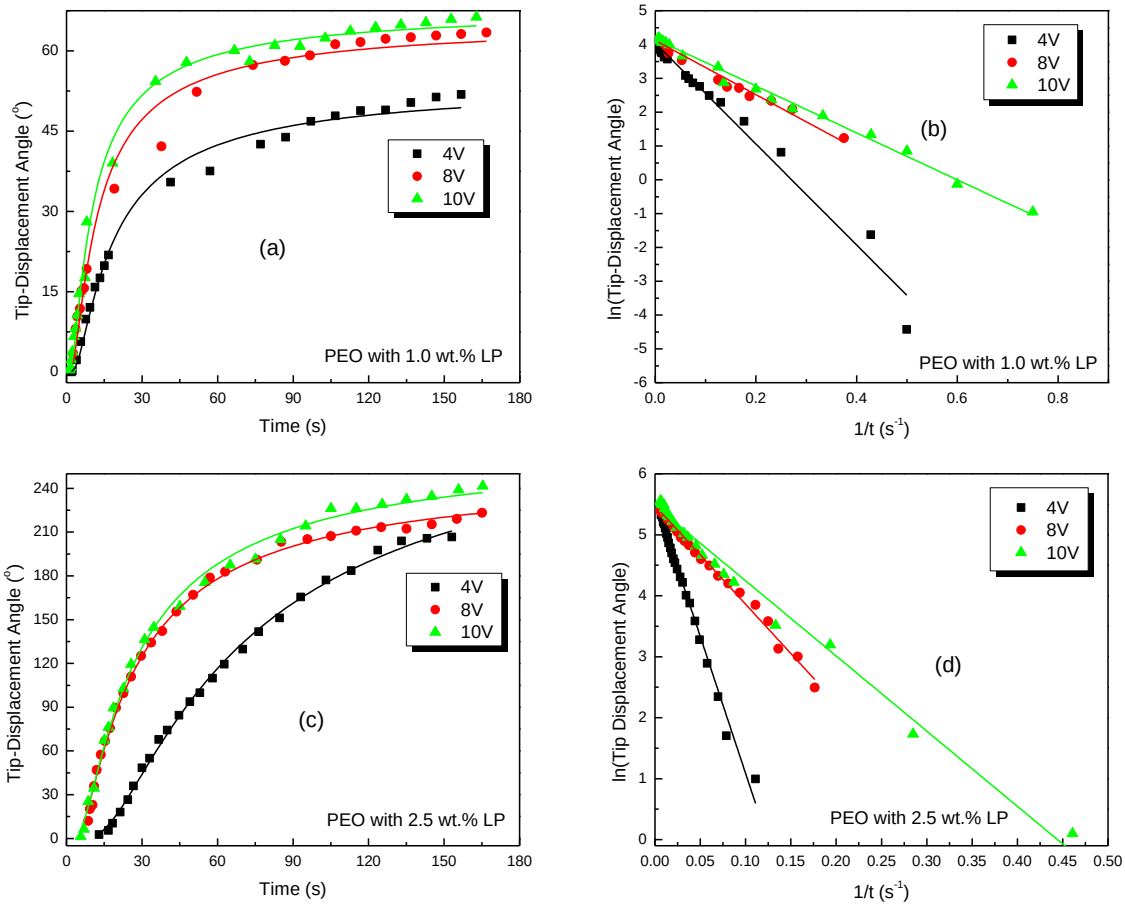

Figure 24: Results for varying voltage testing for 1.0 wt.% LP with (a) nonlinear and (b) fitting results and 2.5 wt.% LP with (c) nonlinear and (d) fitting results

Table 5 shows the fitting results for each of the PEO EAPs tested in this study under varying voltages.

Table 5: Fitting parameters for PEO IPMCs actuated under varying voltages

PEO IPMCs		Eq. (3.1) (nonlinear fitting)			Eq. (3.3) (linear fitting)		
x.x wt.% Salt	V (DC)	B (s)	θ_{max} (°)	s_{max} (%)	B	θ_{max} (°)	s_{max} (%)
1.0 wt.% LP	4.0	15	54	0.17	15	57	0.16
	8.0	10	66	0.21	8	62	0.20
	10	8	68	0.22	7	64	0.21
2.5 wt.% LP	4.0	55	300	0.81	45	260	0.88
	8.0	21	250	0.66	16	240	0.62
	10	20	270	0.70	13	240	0.63
5.0 wt.% LP	4.0	54	410	1.5	46	380	1.3
	8.0	17	350	1.2	12	300	1.0
	10	6.5	340	1.2	5.4	310	1.0

3.4.4 Variable-Temperature Testing of PEO-Based IPMCs

The Arrhenius-Based Model was also tested for the PEO films under varying temperatures. **Figure 25.a-b** show the nonlinear and linear regression behavior of three 2.5 wt.% LP samples (with no NCC), averaged across two runs each for temperatures of 0 ^{o}C, 10 ^{o}C, 20 ^{o}C, 30 ^{o}C, 40 ^{o}C, and 50 ^{o}C under 4 V DC. Films were actuated at the target temperature for 2.5 min, then the polarity was reversed in order to straighten the film. 2.5 wt.% films were selected for this experiment due to their maximum actuation not exceeding ~200^{o} and therefore there was no impedance of actuation by the sample holder and any changes in actuation due to temperature fluctuations would be easy to spot. A wait time of 2 min occurred between successive tests at a given temperature. The temperature was then incremented to the next value, the samples were held at that temperature for 10 min, and the process was repeated. Through analysis of **Figure 25**, it is clear that actuation occurs faster and further with increasing temperature. This is an intuitive conclusion as the matrix expands with increasing temperature and the ions become more readily mobile. The time constant was found to increase with increasing temperature, from 32 s at 0 ^{o}C to 117 s at 20 ^{o}C, then it decreased as the temperature moved to 30 ^{o}C then on to 50 ^{o}C with time constants of 75 s and 25 s, respectively. However, the fitted maximum tip-displacement angle increased continuously with increasing temperature from 2.4^{o} at 0 ^{o}C to 209^{o} at 50 ^{o}C. This interplay between the peaking time constant and continually increasing tip-displacement angle could be a function of ionic mobility and there being some kind of transition point within the IPMC. Once the transition point occurs (between 20 and 30 ^{o}C), the ionic mobility increases and the time constant begins to drop causing translating to an increase in actuation performance. **Table 6** lists all of the fitting parameters for this set of experiments.

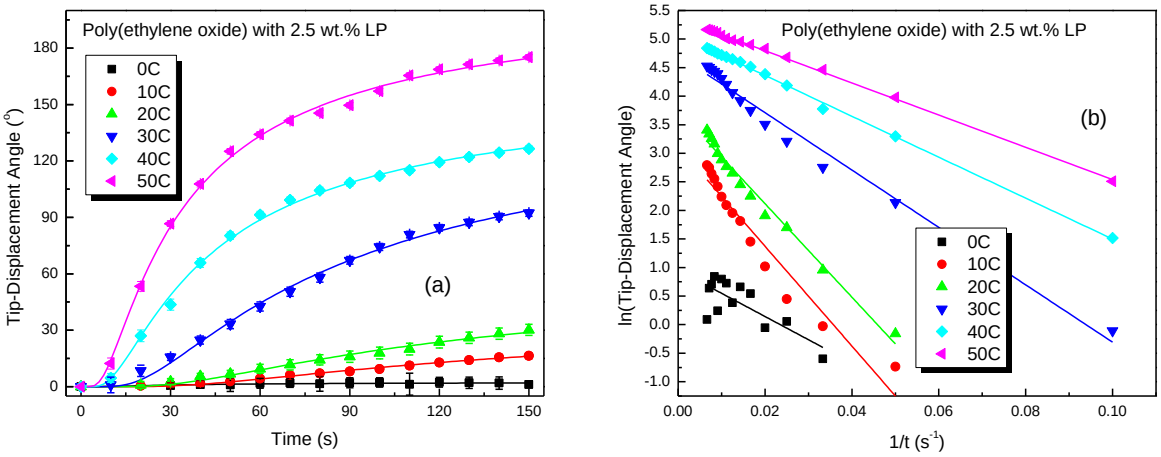

Figure 25: Actuation response for PEO-based IPMCs under various temperatures; (a) nonlinear and (b) linear fitting regressions

Table 6: Fitting parameters for PEO IPMCs actuated under varying temperatures

PEO w/ 2.5 wt.% LP		Eq. (3.1) (nonlinear fitting)			Eq. (3.3) (linear fitting)		
Temperature (^oC)	V (DC)	B (s)	θ_{max} (°)	s_{max} (%)	B	θ_{max} (°)	s_{max} (%)
0	4.0	32	2.4	6.0E-5	40	2.6	6.6E-5
10	4.0	140	40	0.10	87	23	0.06
20	4.0	120	63	0.16	82	43	0.11
30	4.0	75	150	0.38	50	110	0.28
40	4.0	36	160	0.40	36	160	0.40
50	4.0	27	210	0.53	28	210	0.53

3.4.5 Variable-Thickness Testing of PEO-Based IPMCs

To understand the effect of thickness on the IPMC behavior, four sets of samples were prepared under the same conditions and at the same time to ensure as-close-as-possible synthesis procedures were undertaken. PEO EAPs with 2.5 wt.% LP were synthesized from 3 ml, 4 ml, 5 ml, and concentrated 5 ml solutions. The concentrated solution was made by using 10 ml of an initial solution and evaporating 5 ml of the deionized water from it. For the 3 ml, 4 ml, 5 ml, and the concentrated solutions, the resulting film thicknesses from each solution was 31.8 µm, 44.8 µm, 58.5 µm, and 103 µm, respectively. **Figure 26.a-b** show the nonlinear and linear fitting, respectively, using the Arrhenius-Based Model.

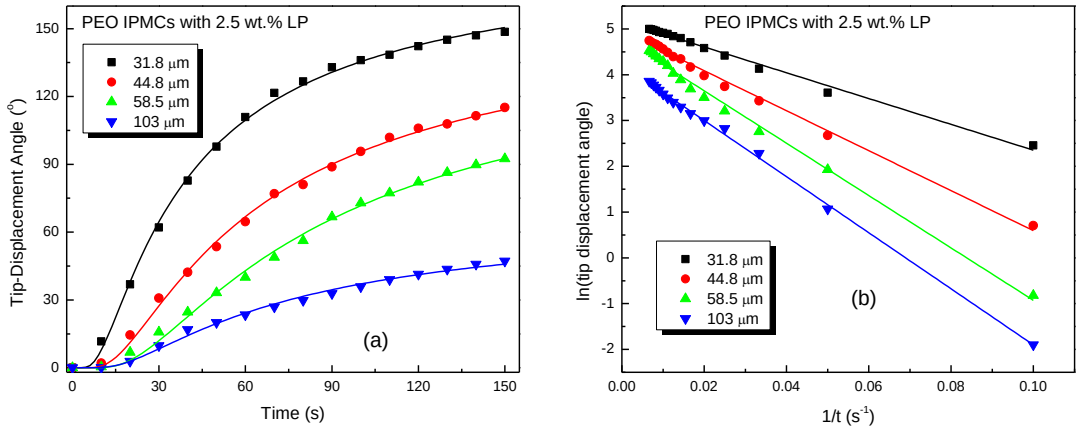

Figure 26: Actuation response for PEO-based IPMCs with various thicknesses; (a) nonlinear and (b) linear fitting regressions

Through inspection of **Table 7**, it can be seen that the general trend for both fittings is that as the thickness increases, there is an increase in the time constant *B*. This would denote a longer response time for the thicker samples, which is consistent with experimental results. Also, though the maximum tip-displacement angle clearly occurs with the 31.8 μm samples, the maximum strain occurred with the 58.5 μm samples. The strain and tip angle sharply decreased with the 103 μm samples. Due to the trading of values between the 31.8 μm 58.5 μm samples' performance, an optimal selection of thickness for these samples therefore becomes an application specific choice instead of an experimentally derived conclusion.

Table 7: Fitting parameters for PEO IPMCs actuated for varying thicknesses

PEO w/ 2.5 wt.% LP		Eq. (3.1) (nonlinear fitting)			Eq. (3.3) (linear fitting)		
Thickness (μm)	V (DC)	B (s)	θ_{max} (°)	s_{max} (%)	B	θ_{max} (°)	s_{max} (%)
31.8	4.0	31.7	190	0.278	28.2	180	0.263
44.8	4.0	53.6	160	0.329	43.7	140	0.288
58.5	4.0	76.8	150	0.403	57.2	120	0.322
103	4.0	63.8	70	0.331	61.3	65	0.307

3.5 PVDF-based IPMC Performance and Analysis

With successful fabrication, testing, and modeling of the PEO-NCC composites, it was of interest to compare these results with a separate EAP system to test the validity of the models obtained. Experimentation has begun with PVDF EAPs to characterize and compare their electromechanical actuation with the PEO-NCC EAPs. Successful actuation at 4 V DC have been

conducted with large actuations achieved, as shown in **Figure 27.a**, with over 180° of tip displacement observed, occurring with a response time of roughly 5-10 s. This fast response makes PVDF EAPs interesting, not just for adding more weight to the proposed electromechanical models, but for real-world application use as well.

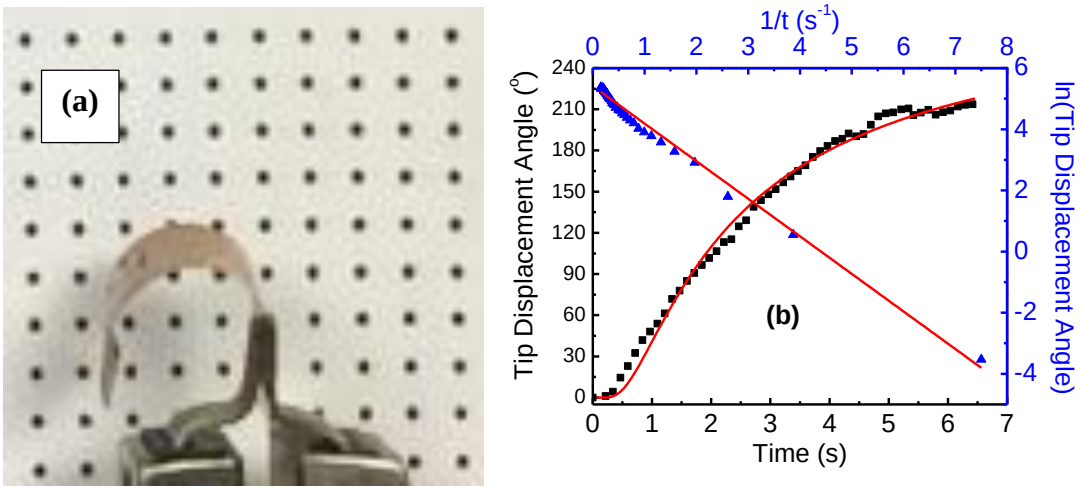

Figure 27: PVDF EAP with 15 wt.% cobalt perchlorate; (a) actuation shown after 5 s under 4 V DC; (b) measured tip-displacement angle data and fitting

Current success for this polymer system was found with adding 15 wt.% CoPH (**Figure 27.b**). Samples actuated with a response time of under 10 s, which is two orders of magnitude faster than the PEO-NCC composites. The nonlinear fitting again closely follows the observed actuation performance and the linear regression again shows how well the nonlinear performance can be translated. The time constant for this film was found to be approximately 2.0 s with an energy density of 3.46 kJ/m^3. **Table 8** contains these values for both fitting regimes.

Table 8: PVDF Arrhenius-Based Model fitting parameters

PVDF		Eq. (3.1) (nonlinear fitting)			Eq. (3.3) (linear fitting)		
wt.% CoPH	V (DC)	B (s)	θ_{max} (°)	s_{max} (%)	B	θ_{max} (°)	s_{max} (%)
10.0	4.0	2.61	16	0.0241	2.02	13	0.0196
12.5	4.0	2.64	80	0.121	1.76	59	0.0889
15.0	4.0	1.98	300	0.452	1.22	220	0.331

Figure 28.a-b shows the nonlinear and linear fittings of PVDF samples with varied CoPH concentration. CoPH was added at 10.0 wt.%, 12.5 wt.%, and 15 wt. %. As anticipated, the films with the most ionic salt concentrations had the largest actuation performance and there is a sizeable increase in performance when moving from 12.5 wt.% to 15 wt.%. Of note is that the Arrhenius-Based Model fits all three concentrations fairly well. Single samples were tested for each

concentration and the films were synthesized during the approximate same timeframe. **Table 8** also contains the fitting parameters for both the nonlinear and linear fittings for the PVDF films with lowered CoPH concentrations. Generally, the time constant decreases with increasing wt.% CoPH while the maximum tip-displacement angle increases with increasing wt.%. This is more evident when examining the linear fitting parameters whereas the time constant decreases, both the maximum tip-displacement angle and maximum strain performance increase.

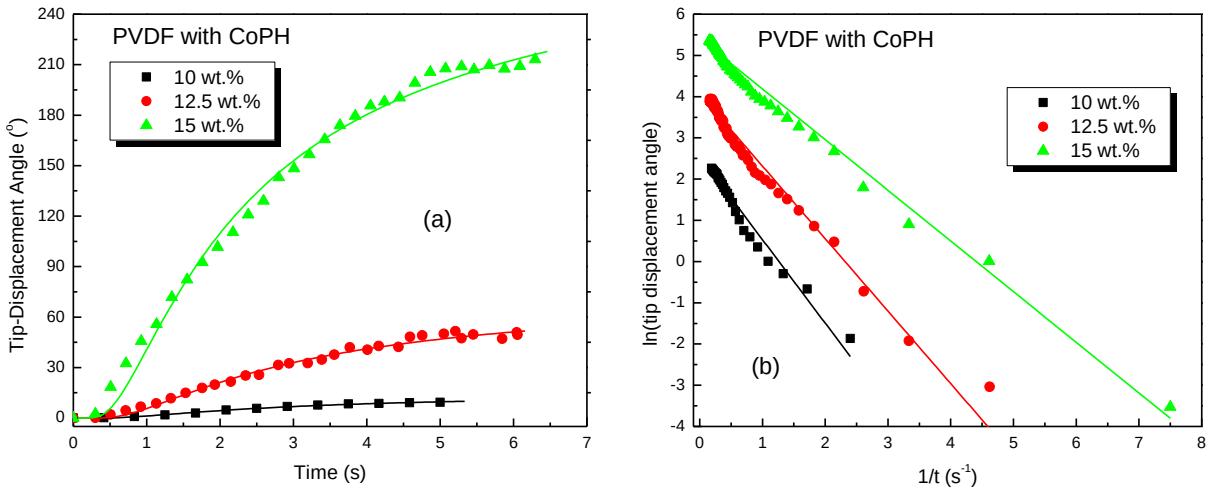

Figure 28: a) Nonlinear and b) linear fittings for PVDF IPMCs with varied CoPH concentrations

3.6 Analysis and Fitting of Published Polymer Systems Electromechanical Performance

With success of having the proposed fitting model accurately describe the motion of PEO and PVDF-based IPMCs, research was aimed at further validating this model by using it to describe the behavior of EAPs whose time-dependent actuation response had been published by other researchers. IPMCs tested include the heavily-studied Nafion and its other commercial-EAP counterpart, Flemion, as well as extending the applicability of this fitting model to non-IPMC EAPs, specifically the conducting polymer, polypyrrole (PPy). The successful incorporation of this model into the characterization of multiple polymer systems yields the potential of this model becoming a powerful, yet simple function which can readily describe the complex EAP behavior across various materials and testing conditions.

The specifics of the synthesis process for the PEO and PVDF-based EAPs discussed herein was described previously and a basic description of their creation will be given here. PEO-based EAPs were developed as a biodegradable alternative to Nafion; samples were created through adding PEO and the ionic salt, lithium perchlorate (LP), into deionized water. The mixture was

then solution cast on glass slides, peeled, and gold was sputtered onto each side of the film to act as electrodes. Final dimensions were 19.1 x 6.35 x 0.0545 mm. PVDF films were similarly synthesized using cobalt perchlorate (CoPH) as the ionic salt and DMF as the solvent. The first set of Nafion data referenced herein did not provide mobile-ion information, but samples were 50 x 10 x 0.28 mm, with Pt electrodes.[7] The researchers in the second set of Nafion data referenced in this report acquired the commercially available Nafion 211 from Ion Power, Inc.,[8] with a thickness of 25 μm and samples were cut into 1 x 6 mm strips and used trifluoromethanesulfonate (Tf^-) as the mobile ion.[9] The referred to Flemion samples were donated to the researchers from Asahi Glass Co. Ltd and had thicknesses of approximately 150-180 μm for dry and wet samples, respectively, with dimensions of 3 x 30 mm and utilized tetrabutylammonium (TBA^+) as the mobile cation.[10] The conducting-polymer, polypyrrole (PPy), EAPs were synthesized by growing 30 μm PPy layers on either side of a gold-coated, non-conducting, 110-μm thick PVDF layer that was infused with lithium triflouromethansulfonimide (Li^+TFSI^-).[11] Upon electric excitation, redox reactions occurred within the PPy and the $TFSI^-$ ions moved toward the positively-charged PPy layer and the Li+ ions moved toward the negatively-charged PPy layer, generating a bending actuation due to the volume expansion/contraction between the PPy layers, similar to how IPMCs actuate. Final PPy-EAP films had dimensions of 20 x 3 x 0.17 mm.

It was also shown that **Eq. (3.1)** could be rewritten, enabling this model to transform the nonlinear actuation response into a linear regression fitting (**Eq. (3.3)**). This flexibility allowed for an intuitive analysis process, where the slope of the line is the *B* parameter, and the *y*-intercept is the targeted performance parameter. **Figure 29.a** shows the nonlinear fitting of PEO samples with increasing concentrations of LP overlaid with the linear regression fitting. From the nonlinear curves, it can be seen that films with more LP had a larger tip-displacement angle, likewise, from the linear curves, samples with more LP also had a larger slope, indicating that these EAPs actuated faster and further than the lower LP samples. These time constants (*B*) are shown in **Table 9** along with their corresponding Tip-displacement angle and strain. The described trend for these actuators can be quantified with the displayed results. The results are similar, the disparity between the nonlinear and linear fitting parameters can be attributed to the level of complexity with fitting each curve. Likewise, the results for the PVDF films are also displayed in **Table 9**.

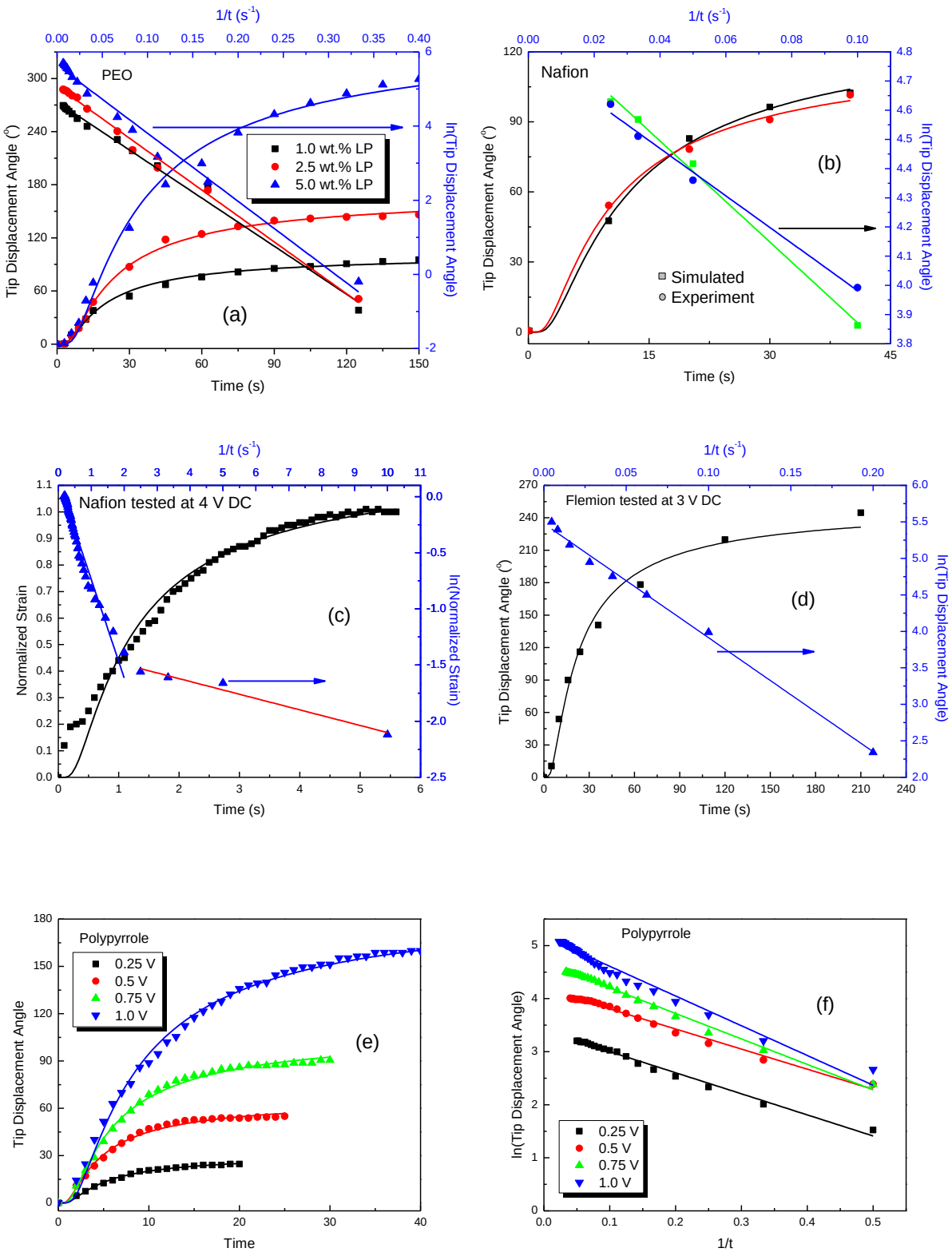

Figure 29: Time-dependent fitted actuation behavior of (a) PEO with varying concentrations of LP at 4.0 V DC, (b) Nafion redrawn from ref[7] at 1.5 V DC, (c) Nafion redrawn from[8, 9] at 4.0 V DC, (d) Flemion redrawn from ref[10] at 3.0 V DC, (e) the nonlinear and (f) linear response of PPy films at various voltages, redrawn from ref[11].

As can be seen, these curves fit the experimental data very well. Through using this model to fit data published by other researchers, it is possible to view this form as a more generalized model through which multiple polymer systems can be described. Two data sets were found publishing the time-dependent nature of Nafion films bending under different excitation conditions. **Figure 29.b** shows data that was extrapolated for this report from both their published experimental actuator position tracking and simulation results.[7] Their simulation results utilized a highly-involved finite-element, gray-box approach which characterized the actuator as undergoing nonlinear beam deformation. As can be seen, their simulation results, though very accurate, are not as closely aligned with their experimental results compared to the fitting proposed herein. *B*-values for the simulated and experimental results are shown in **Table 9**; in comparing them with the PEO samples, the shorter *B*-value indicates a faster response.

In **Figure 29.c**, the versatility of the proposed model is showcased. In this study, researchers published normalized strain data for their Nafion films,[9] represented by the black squares. **Eq. (3.1)** characterizes the time-dependence of this data very well, utilizing strain as the dependent variable. An issue arises when trying to fit the data using **Eq. (3. 3)** (the blue triangles). The model is accurate down to 1 s (blue line) and then there is a transition. This step can also be seen in the nonlinear data and may be due to inaccuracies with their test equipment for areas of small strain or some initial fast-action response, which can also be fitted by **Eq. (3.3)** (red line). The *B*-value for this sample for the nonlinear and linear blue curve is shown in **Table 9**; a *B*-value for the red curve was found to be 0.08 s.

Flemion, though not as commercially popular as Nafion, is also a widely-available commercial IPMC material, and is very similar to Nafion in its structure.[12] The tip-displacement angle data shown in **Figure 29.d** was extracted from a composite image of a Flemion film bending under 3 V DC for 210 s.[10] Again, **Eq. (3.1)** and **Eq. (3.3)** fit the experimental data very closely for both representations of the data. The *B*-value are shown in **Table 9** and is comparable to the PEO films.

Finally, the adaptability of this model is displayed through the fitting results shown in **Figure 29.e-f**. As mentioned, in this study the conducting polymer, PPy, sandwiched an ion-infused PVDF layer and the swelling of the PPy layers, when electrically stimulated, generated a bending actuation.[11] Conducting polymers are defined as a separate type of EAP and thus the ability of **Eq. (3.1)** to fit the prescribed data outlines the flexibility of this model to characterize

bending EAP actuators more generally. The fitted data was obtained from the researchers gray-box simulation results where they tracked the motion of 16 points along the length of the PPy EAP and simulated this motion through a numerical, electro-mechanical optimization technique to measure the whole-body actuation process of the EAPs. The fitted results shown in **Figure 29.e-f** were for the tip of the actuator, but it was found that **Eq. (3.1)** and **Eq. (3.3)** could also fit the data represented by the other 15 points that were tracked. Time constants are shown in **Table 9** and ranged from approximately 4 s for the 0.25 and 0.5 V tests, then 5 s for the 0.75 s test, and finally 7 s for the 1.0 V test, which describes larger actuation responses for the samples with increasing applied voltage.

Table 9: Fitted Parameters for Nonlinear and Linear Regressions

			Eq. (3.1) (nonlinear fitting)			Eq. (3.3) (linear fitting)		
	Salt	V (DC)	B (s)	θ_{max} (°)	s_{max} (%)	B (s)	θ_{max} (°)	s_{max} (%)
PEO	1.0 wt.% LP	4.0	16	102	0.31	16	105	0.31
	2.5 wt.% LP	4.0	19	170	0.51	17	160	0.52
	5.0 wt.% LP	4.0	28	350	0.97	18	280	0.91
PVDF	15 wt.% CoPH	4.0	2.0	290	0.39	1.2	220	0.30
Nafion †*	Simulated	1.5	10	135	--	10	136	--
	Experiment	1.5	8.4	122	--	8.1	121	--
Nafion *	Tf^-	4.0	0.98	--	1.2‡	0.98	--	1.2‡
Flemion *	TBA^+	3.0	19	260	--	12	220	--
PPy *	Li^+TFSI^-	0.25	4.3	31	--	4.0	30	--
		0.5	3.9	66	--	3.8	66	--
		0.75	4.9	110	--	4.8	110	--
		1.0	7.0	190	--	5.6	176	--

†salt not listed, ‡normalized, fitted strain, *data provided was fitted from published actuation data referenced elsewhere in this study

The generalization of a simple, easy to use fitting model for IPMC EAP actuators was conducted in this research. The usability of this model was extended from fitting two IPMCs to four IPMCs and also bridging the potential of the fitting form to other bending EAP actuators, namely the conducting polymer, polypyrrole. The ease through which this equation can be applied to EAP performance makes this a powerful black-box model. Future work is aimed at extending the model to more of a gray box model with comparing physical laws so as to characterize more of the actuators physical parameters, like viscosity, terminal velocity, and diffusion coefficient.

Taking into consideration the dimensions of the films (~54.5±5 μm for 5 ml solution-cast samples and ~32 μm for the 3 ml of solution used for the PVDF samples) and their electromechanical actuation performance, and based on their Young's modulus their corresponding elastic energy density can be calculated using **Eq. (2.10)**. For the composites without NCC this was calculated to be ~1.6 J/kg which is similar with other reports.[13] The composites with 1.5 vol.% NCC exhibit an energy density (~3.5 J/kg) more than two times higher than the composites without NCC. All of these are much higher than the elastic energy density obtained in cellulose-based actuators (0.84 J/kg)[14] and much higher than the energy density obtained in the EAPs made of hydrogels (~0.006 J/kg).[15] It was reported that the net energy density for biological muscle is 0.2 - 40 J/kg.[16] Thus, the energy density observed in the PEO-NCC biodegradable composites is within the requirement for artificial muscle actuators. The calculated energy densities for the EAPs tested in this study are listed in **Table 10**.

Table 1, discussed earlier, lists energy densities for various other EAPs, including values found here; **Figure 20** also contains the performance data from **Table 10** and illustrates the performance of the PEO-based and PVDF actuators created in this study in comparison to other EAPs.

Table 10: Fitted and Calculated Properties for PEO-NCC Composites with Various Concentrations of LP and NCC

	Salt/NCC Content	V (DC)	Y_m (MPa)	s_{max} (%)	W (kJ/m^3)	W $(\sim J/kg)$
PEO	1.0 wt.% LP	4.0	312	0.31	1.31	1.15
	2.5 wt.% LP	4.0	248	0.51	2.36	2.07
	5.0 wt.% LP	4.0	92.9	0.97	4.36	3.83
PEO w/ 5.0 wt.% LP	1.0 vol.% NCC-H_2SO_4	4.0	125	0.91	5.54	4.87
	1.5 vol.% NCC-H_2SO_4	4.0	112	1.47	12.1	10.6
	2.5 vol.% NCC-H_2SO_4	4.0	154	1.06	8.60	7.61
	7.5 vol.% NCC-H_2SO_4	4.0	316	0.11	0.20	0.171
	1.0 vol.% NCC-HCl	4.0	176	0.84	4.72	4.15
	2.5 vol.% NCC-HCl	4.0	339	0.35	0.954	0.838
	5.0 vol.% NCC-HCl	4.0	454	0.18	0.372	0.327
	7.5 vol.% NCC-HCl	4.0	501	0.076	0.090	0.080
PVDF	15 wt.% CoPH	4.0	476	0.39	3.66	2.52

3.7 Comparison of Arrhenius-Based Model with Other Published Models Concerning Previously Published EAP Data

To further confirm the applicability of the Arrhenius-Based Model for general use with EAP actuation, this section will display the Arrhenius-Based Model along with the published models described in Chapter 1 to the previously-published actuation data displayed in the previous section. Again, a lot of models have been proposed to describe the time-dependent nature of ionic EAP bending actuation, but this section will show how the compact form of the model presented in this study, with only two fitting parameters, can accurately describe the three-phased slow, steady, and saturated response of the displayed EAPs better than the other presented models. Published fitting models utilized from Chapter 1 are: Xiao-Bhattacharya, Montazami, Jain, Shi, and an approximated Chen model with a prescribed Arrhenius fitting and linear fitting $F(t)$ (described in Chapter 1). With the data fitted with the Chen model, is that the published report introducing it does not identify exactly the $F(t)$ utilized at the tip of the film to generate the bending actuation within the film. Therefore, a linear and Arrhenius representation of this force was utilized. Thus, through inspection of the fitted results, it can be seen how well and how poorly this particular model is.

Figure 30 displays a recreation of published Nafion actuation data.[8, 9] As can be seen from **Figure 30.a**, except for the linear form of the Chen model, This fitting was interesting, because the Xiao-Bhattacharya, Montazami, Jain, and Shi models fit the steady to saturation data very well, with a correlation very near to the Arrhenius-Based Model presented in this dissertation. However, there is an experimental discontinuity with the recorded experimental data published in the study. For data recorded under about 0.5 s, there is a step in the data that does not seem to flow smoothly with the rest of the data. In an attempt compare the fittings as accurately as possible with the majority of the experimental data, the strain response under 0.5 s was estimated (as shown by the blue circles in **Figure 30**). Upon examination of **Figure 30.b**, it can again be seen that the majority of the models fit the experimental data very well up until the discontinuity. However, with the estimation of the short-interval strain, it can be seen that the Arrhenius-Based Model fits the data the most closely (note: the Arrhenius-Based Model was only fitted against the experimental data; fitting against that and the estimated strain would only make the fitting that much closer). It can be concluded from this that the Arrhenius-Based Model fits the Nafion experimental data most closely.

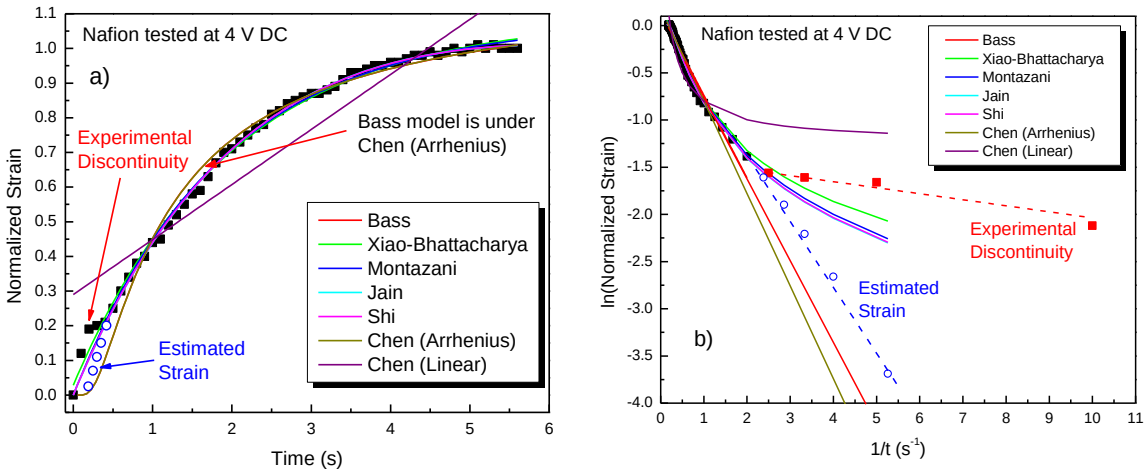

Figure 30: Fitted Nafion EAP actuation data using multiple models

Figure 31 displays a recreation of published Flemion actuation data.[10] Through inspection of **Figure 31.a**, it can be seen that the most of the models generally fit the experimental data very well. However, upon analysis of the linear representation of the actuation data, as shown in **Figure 31.b**, it is very clear that the Arrhenius-Based Model does a better job at portraying the slow, steady, and saturated response of the actuators. The apparent discrepancies between the other models and the slow response, is very clear in **Figure 31.b**.

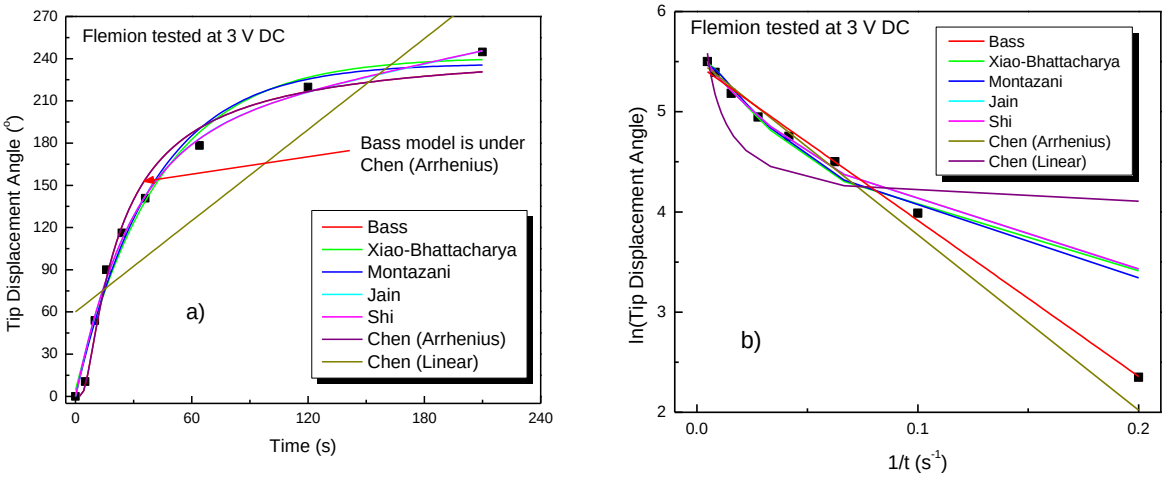

Figure 31: Fitted Flemion EAP actuation data using multiple models

Figure 32 displays a recreation of Polypyrrole actuation data. As with the previous two fittings of published data, the majority of the models fit the steady and saturated actuation response of the conducting-polymer EAP, as illustrated in **Figure 32.a**. However, upon linearizing the data, wherein the slow response is the focus (**Figure 32.b)**, all but the Arrhenius-based model do well with describing the full time-dependence of the actuator response.

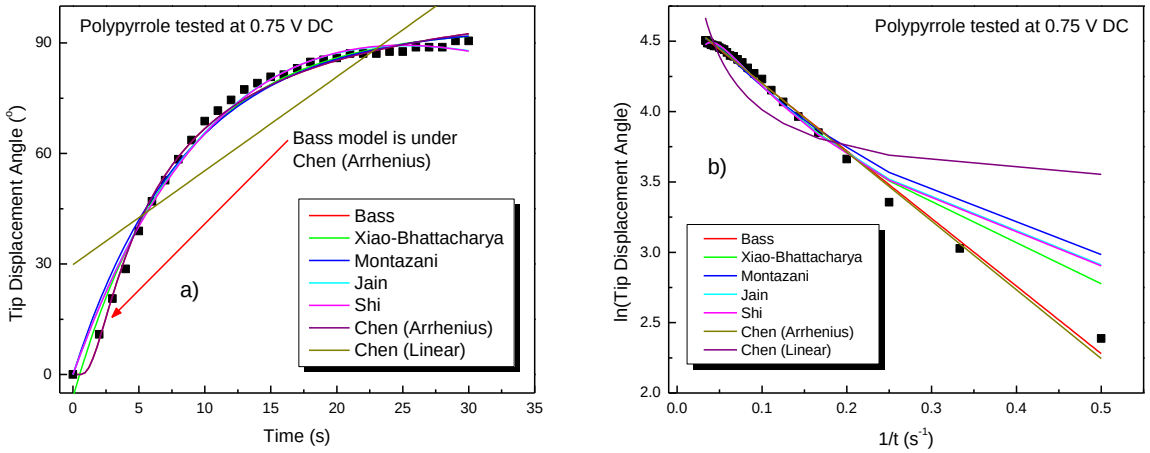

Figure 32: Fitted Polypyrrole EAP actuation data using multiple models

As has been clearly illustrated in this section, the Arrhenius-Based Model presented in this dissertation, does a better job of characterizing the nonlinear: slow, steady, and saturated response of EAP bending actuators. In contrast, the other models presented here can only readily describe the steady and saturated response. This leads to the conclusion that the Arrhenius-Based Model is the better fitting model and it can also be used generally across multiple polymer systems. This, in addition, to the fitting only requiring two fitting parameters makes this a very flexible and versatile fitting form.

3.7.1 Critical Comparative Analysis with Published Models

Experimental results of the prepared PEO-based IPMCs (without NCC) are shown in **Figure 33**, where a voltage of 4 V DC was used for all the samples tested at room temperature. Clearly, the three actuation phases of slow, steady, and saturated are observed and labeled as I, II, and III, respectively, in the figure. However, the time period for each phase is different. These are consistent with the results reported for other *i*-EAPs.[17] The higher the LP concentration, the longer is the phase II process. The results shown in **Figure 33** indicate that the response time increases with increasing LP content.

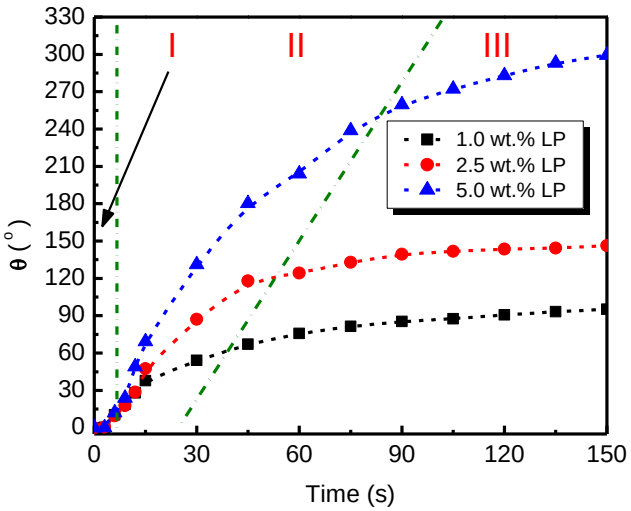

Figure 33: Time dependence of the tip-displacement angle (θ) of PEO-LP actuators at room temperature under 4 V. The content of LP is indicated in figure. The time dependence of the tip-displacement angle shows three phase behavior. Three phases are labeled as I, II, and III.

The experimental results shown in **Figure 33** are fitted using **Eqs. (1) – (3)**, denoting the use of the Montazami [**Eq. (1.6)**], Jain [**Eq. (1.14)**], and Shi [**Eq. (1.15)**] models, respectively, with the time dependence of the tip displacement angle described with a *y* for the IPMCs. It is found that all three models can fit the experimental results as shown in **Figure 34.a**, where the sample with 2.5 wt.% LP is presented as an example. However, it is found that all three models cannot fit the results well at the beginning (i.e. phase I process and earlier phase II process). Clearly, the fitting results for **Eq. (4)** are significantly better for the experimental data in this time.

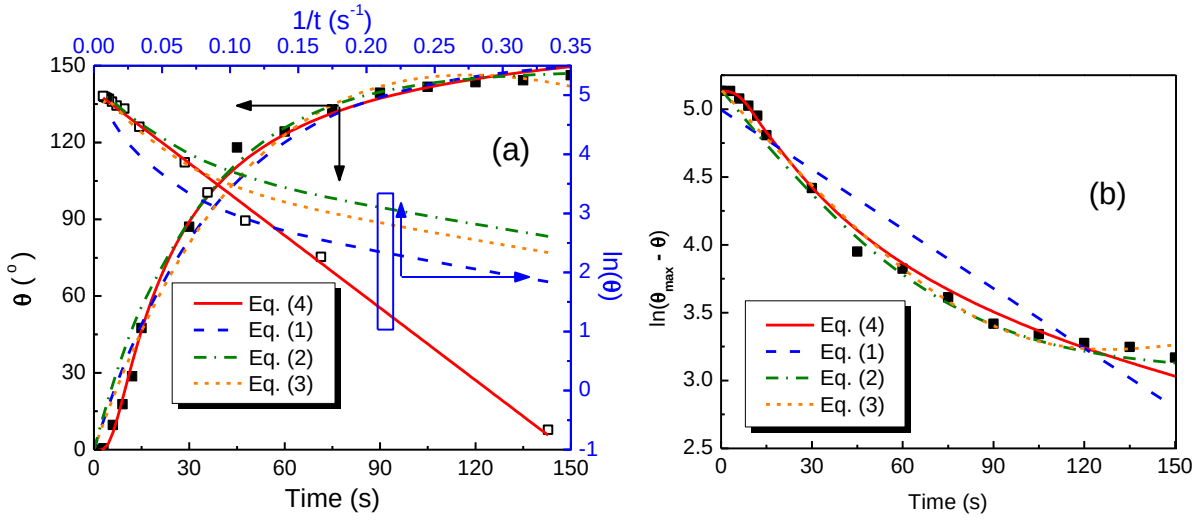

Figure 34: (a) Time dependence of the tip-displacement angle of PEO with 2.5 wt.% LP under 4 V at room temperature with the fitting curves using different equations and the plot of log(θ) vs. 1/t with the fitting curves. (b) The plot of ln(ymax –y) vs. t.

To further analyze the results, the fitting constants for each equation are presented in **Table 11**. By physics, it is expected that the change in the fitting constants should somehow reflect the change in the LP content and the sign of every fitting constant should be the same for all *i*-EAPs. In other words, as the LP content increases, a fitting constant should either decrease or increase, but would not change its sign. For **Eq. (3)**, it is found that *Q* increased with LP content, while *a* and *b* both decreased. However, the sign of fitting constant *b* changes from positive for samples with 1.0 and 2.5 wt% LP to negative for sample with 5.0 wt.% LP, which is against the physics of i-EAPs. For **Eq. (2)**, it is found that the value of *b* increases and, then, decreases with increasing LP content, which is against the physics of *i*-EAP. It is also found that the increase (~1.2 times) in the value of *a* from samples with 2.5 wt% LP to 5.0 wt % LP is three orders lower than that (~$1.2x10^3$ times) from samples with 1.0 wt.% LP to 2.5 wt.% LP, which is unreasonable considering the change in LP content. Additionally, the fitting results from **Eq. (3)** show some reduction in the actuation with time. That is, after 120 s, the fitting response decreases with time, which is against the experimental results and the physics of *i*-EAPs. Actually, both **Eq. (2)** and **(3)** show something contradictory to the physics of *i*-EAPs. For **Eq. (2)**, one can get that the actuation initially increases from zero with time and, then, decreases with time and eventually reaches to zero, which is certainly against the experimental results and physics of *i*-EAPs. **Equation (3)** indicates that the actuation initially increases from zero with time and, then, decreases slightly with time and, finally, increases with time. The final stage from the linear term of **Eq. (3)** results in an infinite actuation, which is again unreasonable by the physics. Therefore, one may conclude that both **Eq. (2)** and **(3)** are invalid to characterize the time dependence of the actuation observed in *i*-EAPs.

Table 11: Fitting constants used in Eqs. (1) – (4) to fit the results shown in Figure 33.

LP content (wt.%)	**Eq. (4)**		**Eq. (1)**		**Eq. (2)**			**Eq. (3)**		
	Y_{max}	τ (s)	Y_{max}	τ (s)	K (°/s)	a (1/s)	b (1/s)	Q (°/s)	a (1/s)	b ($x10^{-3}$)
1.0	104°	14.8	92°	55.7	2.25	$8.80x10^{-6}$	0.023	2.9	0.036	1.50
2.5	169°	19.7	147°	68.5	4.75	$1.09x10^{-5}$	0.032	4.5	0.031	0.16
5.0	345°	22.8	339°	66.0	5.25	$1.27x10^{-2}$	0.0017	5.0	0.011	-2.20

Regarding **Eq. (1)**, the fitting constant shows some irregular change. For example, when the LP content is changed from 1.0 to 2.5 wt.%, the time constant increases from 55.7 to 68.5 seconds. However, when the LP content is changed from 2.5 to 5.0 wt.%, the time constant decreases from 68.5 to 66.0 seconds. That is, the fitting time constant shows some irregular change

with LP content, which is unreasonable by the physics. Therefore, a new relationship/model is needed to characterize the time dependence of the actuation observed in *i*-EAPs. Considering the fact that all current models cannot fit the actuation in the phase I process, a new relationship/model is introduced as:

$$y = y_{max} e^{-\tau/t} \tag{4}$$

where, τ and $y_{\max}$ are the time constant and maximum actuation. Here the tip-displacement angle (θ) is used as the measure of the actuation. [**Eq. (4)** was introduced in this dissertation as **Eq. (3.1)**, but is labeled as **Eq. (4)** here for simplicity] From a physics point of view, **Eq.(4)** follows the expectation: 1) as the time approaches to zero, the actuation is zero; 2) the actuation monotonically increases with time; 3) as the time approaches very long, the actuation reaches its maximum (y_{max}); 4) this relationship reflects the three phase behavior in the actuation. Similar to **Eq. (1)**, there are only two fitting constants.

The results shown in **Figure 33** are fitted using **Eq. (4)**. The fitting constants are presented in **Table 11** and the fitting curve is presented in **Figure 34.a** as an example. From **Figure 34.a**, one can find that the fitting results using **Eq. (4)** is better is than the other three. First of all, the fitting results of **Eq. (4)** reflect the actuation during in phase I process very well. Additionally, the fitting constants shown in **Table 11** indicate that the fitting constants of **Eq. (4)** coordinately change with the LP content. For example, the time constant increases with the LP content, which is consistent with the results shown in **Figure 33**.

To further show the advantage of Eq. (4) over others, the fitting results using both **Eq. (4)** and **(1)** are again compared. **Equation (4)** can be written as

$$\ln y = \ln y_{max} - \tau/t \tag{5}$$

That is, the new model would result in a linear relationship between the logarithm of actuation, ln*y*, and the reciprocal of time, *1/t*. The plot of ln*y* vs. 1/t is shown in **Figure 34.a**. Clearly, the experimental results show a very good linear relationship. However, the tendency of **Eq.(1)** is completely different with the experimental results, especially at large 1/t (i.e. the phase-I process).

Equation (1) can be written as:

$$\ln(y_{max} - y) = \ln y_{max} - t/\tau \tag{6}$$

That is, there would be a linear relationship between the $\ln(y_{max} - y)$ and the time. The experimental results shown in **Figure 33** are plotted as $\ln(y_{max} - y)$ vs. *t*. As shown in **Figure 34.b,** the fitting results of **Eq. (6)** do not represent the tendency of the experimental results at all.

The results shown in **Figure 34** and **Table 11** clearly demonstrate the advantage and correctness of **Eq. (4)** over other models. To further confirm it, both **Eqs. (1)** and **(4)** are used to analyze the electromechanical response of the samples with 2.5 wt.% LP at different temperatures (10, 20, 30, 40, 50^{o}C). Both equations can fit the results obtained at each temperature. However, the fitting using **Eq. (1)** cannot reflect the electromechanical response at the beginning (i.e. the phase I process and earlier phase II process), which is exactly what was observed above in **Figure 34**. Regarding fitting constants using **Eq. (4)**, it is concluded that the saturated actuation (y_{max}) increases with increasing temperature and that the time constant (τ) decreases with increasing temperature. A higher temperature means that the ions in *i*-EAPs have greater mobility, which would result in a fast response or a smaller time constant. For the polymer matrix, the higher is the temperature, the smaller is its elastic modulus. Therefore, for the same ion accumulation in the PEO, a larger actuation would be obtained at a higher temperature. In other words, the fitting results using **Eq. (4)** are consistent with the physics of *i*-EAPs.

To further validate applicability and universality of **Eq. (4)**, the experimental data reported for two other *i*-EAPs are analyzed: one is Flemion and the other is polypyrrole (PPy) actuator.[10, 11] Flemion is a commercial IPMC and has a response time of 10^2 s.[10] PPy is a conducting polymer, representing a different type of i-EAPs, and has a much fast response (i.e. a shorter response time).[11]

The results shown in **Figure 35.a** are the electromechanical response of a Flemion actuator under 3 V DC,[10] while the results shown in **Figure 35.b** are obtained from a PPy actuator under 0.75 V DC.[11] The experimental data shown for the Flemion films was acquired from the still images published in their findings while the PPy data was acquired from a time-dependent figure that displayed changes in tip-displacement angle. Both **Eq. (1)** and **(4)** are used to fit the experimental results. Again both equations can fit the experimental results, but the fitting results using **Eq. (1)** do not reflect the actuation behavior at the beginning. Additionally, both **Eq. (5)** and **(6)** are also used to check the tendency of the electromechanical response. In **Figure 35.a**, the plot of ln(y) vs. $1/t$ is presented, while the plot of ln(y_{max}-y) vs. t is presented in **Figure 35.b**. Again the experimental results show that **Eq. (5)** can well describe the electromechanical response of *i*-EAPs. These results again show the advantage of **Eq. (4)** over **Eq. (1)**.

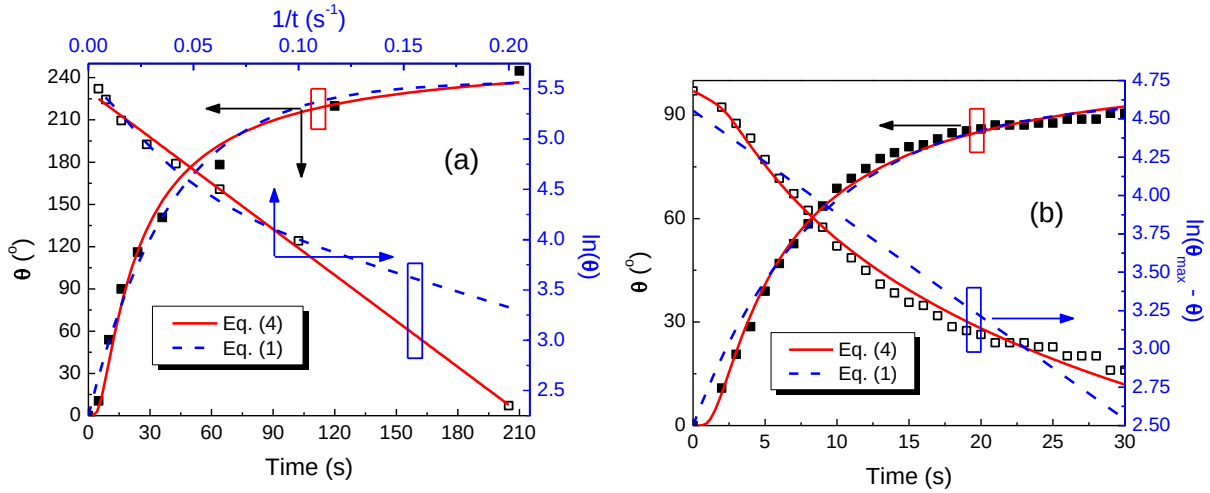

Figure 35: (a) Time dependence of the tip-displacement angle of Flemion, tested at 3 V, with fitting curves using Eq. (1) and (4) and the plot of the log(θ) vs. 1/t. (b) Time dependence of the tip-displacement angle of polypyrrole, tested at 0.75 V, with fitting curves using Eq. (1) and (4) and the plot of ln(y_{max} –y) vs. *t*. The experimental data in (a) is from Ref [10] and the data in (b) is from Ref [11].

It is experimentally found that the electromechanical response of an i-EAP under a constant voltage has three phases: phase-I process – slow; phase-II process – steady increase; phase-III process – saturation. Current models used to describe this electromechanical response are studied using the experimental results obtained in PEO doped with LP with different contents. The shortcomings of all existing models for fitting the experimental results are discussed. Some are physically incorrect. All cannot reflect the electromechanical response at the beginning (i.e. the phase-I and earlier phase-II process). Additionally, the fitting constants are inconsistent with the physics. A new and reasonable model, **Eq. (4)**, is introduced to characterize the electromechanical response of *i*-EAPs. The new relationship also provide an easy way to fit the results: a linear relationship is obtained by plotting the logarithm of the actuation versus the reciprocal of time. The correctness and advantages of the new model are also confirmed using the electromechanical response of the PEO-LP actuators at different temperatures. The applicability and universality of the new model are validated using the reported results from other *i*-EAPs: one is Flemion and the other is PPy.

3.8 Connection of the Arrhenius-Based Model with Stokes-Einstein Model

This section provides a further analysis of the parameters derived from fitting experimental data with the Arrhenius-Based Model and correlating them to physical properties that are otherwise difficult to obtain. To obtain the physical parameters for the time constant *B* in **Eq. (3.1)**, the motion of the ions through the polymer matrix was modeled using the Stokes-Einstein equation

which describes spherical, charged particles traveling through a viscous medium with low Reynolds number.[18] The PEO matrix was assumed to be this viscous medium. With the ClO_4^- ion having a radius three times that of the Li+ (or Co^{2+}), at 240 pm and 76 pm (or 79 pm for Co^{2+}), respectively, it was assumed that the ClO_4^- ion was the slower of the two ions traveling through the matrix. Therefore, the time it would take for this type of ion to traverse the matrix would determine when saturation actuation would occur for the EAP as a whole. **Eq. (3.1)** can be solved for the strain time *t*, as shown by **Eq. (3.4)**; using the fitted *B* value and assuming a 90% actuation condition ($y/y_{max} = 0.90$), the time to reach the saturated strain actuation was found to be approximately 5 min for the 5.0 wt.% LP with 0.0 vol.% NCC samples, which is in agreement with experimental results.

$$t = B \ln \frac{y}{y_{max}} \tag{3.4}$$

To explain this process, it was presumed that one of the last ClO_4^- ions began its motion very close to the negative electrode, when the 4 V DC was initially applied. To contribute to the expansion process at the positive electrode it needed to travel through nearly the entire thickness of the polymer matrix, taking roughly 10 min. Assuming that the ion traveled at a steady-state velocity,[18] the terminal velocity of the ion can be found using **Eq. (3.5)**. The electrostatic force applied to both the Li+ and ClO_4^- ions due to the 4 V DC can be described with **Eq. (3.6)**, where, *z* is the valence number, e_0 is the electrical charge, and *E* is the applied electric field. From here, the effective dynamic viscosity (η) of the PEO matrix can be determined with **Eq. (3.7)**, where, r_{ClO4^-} is the radius of the perchlorate ion. With the values obtained here, the Stokes-Einstein relation (**Eq. (3.8)**) for determining the apparent diffusion coefficient can be used.

$$v_{t_{ClO4^-}} = t_{95} h \tag{3.5}$$

$$F = z e_0 E \tag{3.6}$$

$$\eta = \frac{F}{6\pi v_t r_{ClO4^-}} \tag{3.7}$$

$$D = \frac{k_B T}{6\pi \eta r_{ClO4^-}} \tag{3.8}$$

This new approach for modeling the strain response of the EAPs makes it possible to calculate physical parameters of the EAPs that previously was not possible. These properties can now be compared (

Table 12) across the various PEO and other polymer-based samples.

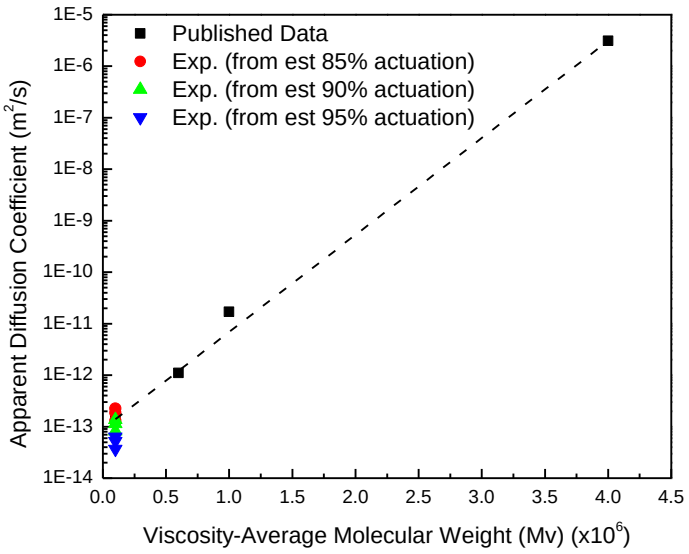

Figure 36: Comparison of apparent diffusion coefficient calculation to published data for PEO systems at varying molecular weights with lithium perchlorate salt added to the matrix

The 90% actuation assumption was decided upon after reviewing the results showcased in **Figure 36**. As seen, solving **Eq. (3.1)** for time results in a natural log function (**Eq. (3.4)**). If **Eq. (3.4)** is solved for a 100% actuation condition, a nearly infinite saturation time will result, so a reasonable actuation performance percentage was chosen which correlated well with the observed experimental results. To find a reasonable actuation percentage, the apparent diffusion coefficients were calculated for the 1.0, 2.5, and 5.0 wt.% PEO films (without NCC) under 4 V DC for assumed actuations of 85%, 90%, and 95% saturation. This data was plotted as a function of viscosity-average molecular weight (M_v) of the PEO samples used. The calculated data was plotted with respect to published data concerning the diffusion coefficient determination of lithium perchlorate in PEO films with M_v ranging from 600k M_v to 4M M_v.[19] The published diffusion coefficients were determined through an impedance analysis[20] and through utilizing Nernst's relationship regarding the diffusion coefficient as a function of ionic mobility, where the ionic mobility was determined to be a function of the interstitial volume between the PEO chains in the matrix. The samples tested in this thesis were 100k M_v. It can be seen that the diffusion coefficient increases exponentially (when considering the log of the diffusion coefficient) with increasing molecular weight of the PEO polymer. The diffusion coefficients determined by the 90% actuation assumption fit reasonably well with the published data for the range of LP concentrations used in this study. Diffusion coefficients for saturation times of 85% and 95% were above and below,

respectively, those calculated for the 90% case. This made the 90% actuation case the selected condition for determining the apparent diffusion coefficients of the actuators.

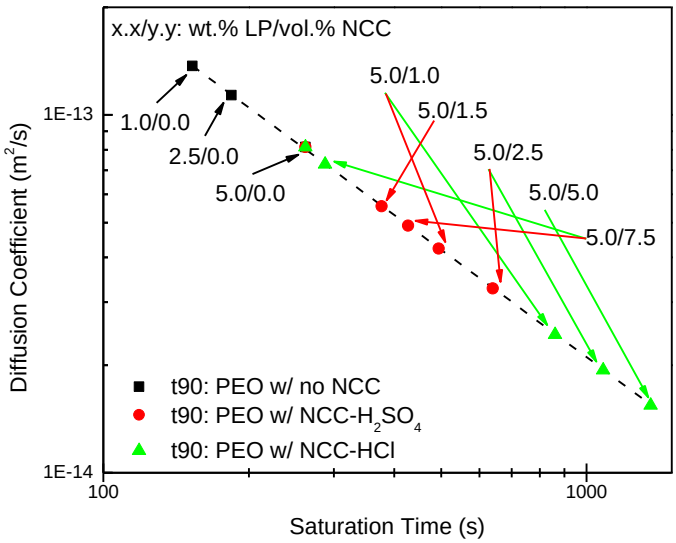

Figure 37: Apparent diffusion coefficient as a function of saturation time for PEO composites with varying concentrations of LP and NCC

While the determined value may not be the exact diffusion coefficient for the diffusing species, it does showcase the connection of the film's mechanical actuation to the flux of ions through the PEO matrix, along with any accompanying additives in the matrix. For PEO films, analysis shows that with increasing LP concentration, that the Diffusion coefficient decreases while the viscosity increases. With increasing NCC concentration, this analysis is a little less straight forward, where the apparent diffusion coefficient fluctuates with increasing NCC content. **Figure 37** shows the calculated apparent diffusion coefficient as a function of saturation time calculated under the 90% actuation condition. This is plotted for PEO composites with increasing LP concentration (without NCC) and for PEO composites with increasing NCC concentrations for both NCC created using a sulfuric-acid hydrolysis (NCC-H_2SO_4) process and NCC created using a hydrochloric-acid hydrolysis (NCC-HCl) process. The linear relationship between saturation time and the diffusion coefficient, for the log-log plot, is quite evident with the parameters related through a power-law fitting. Upon inspection of the data however, there are some peculiarities. As expected, with increasing LP concentration the diffusion coefficient for the PEO films goes down. This correlates to an increase in the viscosity of the polymer and henceforth a softer sample, which is corroborated through the sample synthesis process. However, the parameters seem to fluctuate along this line with increasing concentrations of both types of NCC. For the sulfuric-acid based

NCC there is a dip saturation time for the 1.5 vol.% and 7.5 vol.% samples. As described, the 1.5 vol.% NCC concentration looks to be a sweet spot for NCC addition and resulted in an increased IPMC actuator performance. Whereas, the dip for the 7.5 vol.% concentration relates to the added stiffness of the samples from the addition of the NCC resulting in the samples reaching their maximum actuation at earlier times compared to other samples resulting in a relatively high apparent diffusion coefficient. As a reminder, this early saturation for the 7.5 vol.% samples has the comparatively lowest actuation results for this type of PEO-NCC composite. For the NCC-HCl composites, there is only a dip for the 7.5 vol.% samples, with the results being explained in the same manner as the sulfuric-acid based NCC composites previously mentioned. As such, it can be assumed that the fitting form from **Eq. (3.1)** and the Stoke's Einstein model do not readily take into account the addition of fillers to the polymer matrix, so the accompanying results do not entirely follow the prescribed pattern of behavior as far as these parameters are concerned.

Apparent diffusion coefficients were also calculated for the other EAPs referenced in this study for comparison, namely: Nafion, Flemion, and polypyrrole, as well as for the PVDF films also synthesized in this study.

Table 12 shows the calculated apparent diffusion coefficient and dynamic viscosity, and their corresponding referenced diffusion coefficients. Comparing the PEO diffusion coefficients with those of the PEO films made from the higher M_v PEO polymer, the large increase in recorded diffusion coefficient for the higher M_v PEO samples may make the synthesis of IPMCs at the higher molecular weight be an area of interest. In some cases for polymers in

Table 12, the referenced results used different mobile ions to calculate their results and for the calculated apparent diffusion coefficients, the size of the mobile ion was approximated for some of the polymer systems. That aside, the calculated results are very close to the published data for diffusion coefficients. This result lends weight to the 90% actuation performance assumption as well as to the use of the Stoke's Einstein model for considering the IPMC polymer matrix as an electrolyte. Of note with the displayed values, it was found that the diffusion coefficient increased with increasing voltage (from 8.14E-14 m^2/s at 4 V DC to 1.32E-13 m^2/s at 10 V DC), which is to be expected due to the larger electrostatic driving force applied to the ions under the larger applied voltage. As a reference to the calculated dynamic viscosity values for the PEO-NCC composites, these values place the PEO-NCC films between that of chocolate syrup and ketchup, at around 10 and 50 Pa·s, respectively.[21]

Table 12: Diffusion coefficient comparison for various bending EAPs

	Salt	V (DC)	t_{90} † (s)	D † (m^2/s)	η † $(Pa \cdot s)$
PEO	1.0 wt.% LP	4.0	153	1.37E-13	6.77
(M_v~100k)	2.5 wt.% LP	4.0	184	1.14E-13	8.15
	5.0 wt.% LP	4.0	262	8.14E-14	11.4
PEO w/ 5.0	1.0 vol.% NCC-H_2SO_4	4.0	494	4.23E-14	21.9
wt.% LP	1.5 vol.% NCC-H_2SO_4	4.0	377	5.56E-14	16.7
	2.5 vol.% NCC-H_2SO_4	4.0	640	3.27E-14	28.3
	7.5 vol.% NCC-H_2SO_4	4.0	427	4.90E-14	18.9
	1.0 vol.% NCC-HCl	4.0	861	2.43E-14	38.1
	2.5 vol.% NCC-HCl	4.0	1080	1.93E-14	47.9
	5.0 vol.% NCC-HCl	4.0	1360	1.54E-14	60.1
	7.5 vol.% NCC-HCl	4.0	288	7.28E-14	12.7
PEO[19]	LP	--	--	1.10E-12 ‡	--
(M_v~600k)					
PEO[19]	LP	--	--	1.70E-11 ‡	--
(M_v~1M)					
PEO[19]	LP	--	--	3.10e-6 ‡	--
(M_v~4M)					
PVDF	15 wt.% CoPH	4.0	19.1	3.85E-13	2.41
PVDF[22]	Li^+	--	--	8.06E-12 to 2.12E-10 ‡	--
	F^-	--	--	7.39E-12 to 1.91E-10 ‡	--
Nafion * ‖	Experiment	1.5	79.7	1.88E-11	0.049
	Simulated	1.5	94.9	1.58E-11	0.057
Nafion *	EMI^+Tf^-	4.0	9.30	7.90E-13	1.17
Nafion[8]	Tf^-	--	--	3.86E-12 ‡	--
	EMI^+	--	--	2.73E-12 ‡	--
Flemion *	TBA^+	3.0	147	1.56E-12	0.592
Flemion[23]	Li^+	--	--	1.00E-9 to 1.00E-11 ‡	--
PPy *	Li^+TFSI^-	0.25	40.8	2.53E-12	0.366
		0.5	37.0	1.40E-12	0.664
		0.75	46.5	7.41E-13	1.25
		1.0	66.4	3.89E-13	2.38
PPy[24]	LP	--	--	4.00E-13 to 1.75E-13 ‡	--

†calculated value, ‡reference value, *data provided was fitted from published actuation data referenced elsewhere in this study, ‖no salt information provided

Chapter 3 References

1. Zhang, Q., et al., *An all-organic composite actuator material with a high dielectric constant.* Nature, 2002. **419**(6904): p. 284-287.
2. Hubbe, M.A., et al., *Cellulosic nanocomposites: a review.* BioResources, 2008. **3**(3): p. 929-980.
3. Habibi, Y., H. Chanzy, and M.R. Vignon, *TEMPO-mediated surface oxidation of cellulose whiskers.* Cellulose, 2006. **13**(6): p. 679-687.
4. Ragavan, V., *Materials Science and Engineering–A first course*. 2006, Prentice Hall of India, New Delhi.
5. Mahadeva, S.K., et al., *Effect of poly (ethylene oxide)-poly (ethylene glycol) addition on actuation behavior of cellulose electroactive paper.* Journal of applied polymer science, 2009b. **114**(2): p. 847-852.
6. Azizi Samir, M.A.S., F. Alloin, and A. Dufresne, *Review of recent research into cellulosic whiskers, their properties and their application in nanocomposite field.* Biomacromolecules, 2005. **6**(2): p. 612-626.
7. Yim, W., et al. *Dynamic modeling of segmented ionic polymer metal composite (IPMC) actuator*. in *Intelligent Robots and Systems, 2006 IEEE/RSJ International Conference on*. 2006. IEEE.
8. Liu, Y., et al., *Ion transport and storage of ionic liquids in ionic polymer conductor network composites.* Applied Physics Letters, 2010. **96**(22): p. 223503.
9. Montazami, R., et al., *Thickness dependence of curvature, strain, and response time in ionic electroactive polymer actuators fabricated via layer-by-layer assembly.* Journal of Applied Physics, 2011. **109**(10): p. 104301.
10. Nemat-Nasser, S. and Y. Wu, *Comparative experimental study of ionic polymer–metal composites with different backbone ionomers and in various cation forms.* Journal of Applied Physics, 2003. **93**(9): p. 5255-5267.
11. Mutlu, R., et al., *Electro-mechanical modelling and identification of electroactive polymer actuators as smart robotic manipulators.* Mechatronics, 2014. **24**(3): p. 241-251.
12. Bar-Cohen, Y., et al. *Challenges to the transition of IPMC artificial muscle actuators to practical application*. in *MRS Symposium Proceedings*. 1999. Citeseer.
13. Shahinpoor, M. and K.J. Kim, *Solid-state soft actuator exhibiting large electromechanical effect.* Applied Physics Letters, 2002. **80**(18): p. 3445-3447.
14. Zhang, Y., et al., *Effects of lithium perchlorate on poly (ethylene oxide) spherulite morphology and spherulite growth kinetics.* Journal of Applied Polymer Science, 2012. **123**(4): p. 1935-1943.
15. Ghaffari, M., et al., *Aligned Nano-Porous Microwave Exfoliated Graphite Oxide Ionic Actuators with High Strain and Elastic Energy Density.* Advanced Materials, 2013. **25**(43): p. 6277-6283.
16. Bar-Cohen, Y., *Y. Electroactive Polymer (EAP) Actuators as Artificial Musles: Reality, Potential, and Challenges*. 2004, Bellingham: SPIE Press.
17. Mahadeva, S.K., S. Yun, and J. Kim, *Dry Electroactive Paper Actuator Based on Cellulose/Poly (Ethylene Oxide)—Poly (Ethylene Glycol) MicroComposite.* Journal of Intelligent Material Systems and Structures, 2009a. **20**(10): p. 1141-1146.
18. Tropea, C., A.L. Yarin, and J.F. Foss, *Springer handbook of experimental fluid mechanics*. Vol. 1. 2007: Springer.

19. Nasir, N.H.A., et al. *Ionic conductivity in solutions of poly (ethylene oxide) and lithium perchlorate*. in *Macromolecular Symposia*. 2010. Wiley Online Library.
20. Chan, C. and H. Kammer, *Properties of solid solutions of poly (ethylene oxide)/epoxidized natural rubber blends and LiClO4.* Journal of applied polymer science, 2008. **110**(1): p. 424-432.
21. Bourne, M.C. and M. Rao, *Viscosity measurements of foods.* Instrumental methods for quality assurance of foods, 1991: p. 211-229.
22. Saito, Y., A.M. Stephan, and H. Kataoka, *Ionic conduction mechanisms of lithium gel polymer electrolytes investigated by the conductivity and diffusion coefficient.* Solid State Ionics, 2003. **160**(1): p. 149-153.
23. Saito, M., K. Hayamizu, and T. Okada. *Investigation of Ion and Water Transport Mechanisms in Perfluorosulfonated Ionomer Membranes for Fuel Cells*. in *Proton Conducting Membrane Fuel Cells IV: Proceedings of the International Symposium*. 2006. The Electrochemical Society.
24. Otero, T.F., M. Marquez, and I.J. Suarez, *Polypyrrole: Diffusion coefficients and degradation by overoxidation.* The Journal of Physical Chemistry B, 2004. **108**(39): p. 15429-15433.

Chapter 4: Development of Charge-Distribution Based Actuation Model

4 Overview

In conjunction with the development of the simple Arrhenius-like model used to describe the nonlinear behavior of the IPMC films, a physics-based model is proposed which can characterize how the ionic flux within the EAP matrix translates into the observed bending behavior. This model was based off of the following major assumptions: 1) the electromechanical actuation (characterized by either strain, tip-displacement angle or radius of curvature) is linearly proportional to the charge distribution within the matrix; 2) both the cation and anion are mobile and initially randomly distributed within the IPMC and they will accumulate at their respective electrode upon electric excitation; 3) the drift velocity of the mobile ions is constant[1] and is proportional to valence number and ionic radius; 4) the accumulation of charge at both EAP electrodes causes volumetric expansion on both sides and the observed bending is due to the size disparity between the cation and anion causing one side of the film to have a larger expansion. IPMCs actuate due to the flux of ions within the polymer matrix and the overall accumulation of ions on either surface of the films, therefore, the time-dependent distribution of the charges within the film is directly related to the electromechanical actuation. The application of an electric field across the two electrodes creates an electrostatic force that attracts the mobile ions to their attracting electrodes. Also, IPMC systems consider the polymer matrix as a solid-polymer electrolyte[2, 3] and as such, upon excitation from an external electric field, it can be assumed that the ions traveling through the matrix travel at a steady-state velocity,[1] i.e. the ions travel at a constant drift velocity towards their respective electrodes. As mentioned previously, the Stokes-Einstein model defines the diffusion coefficient of a charged particle traveling through an electrolyte as $D = \mu k_B T$, where μ is the ionic mobility.[1] The ionic mobility can be written as $\mu = v_d/E$, where v_d is the ionic drift velocity and E is the applied electric field. This relationship further extends the third assumption to stating that both the drift velocity of the mobile ions *and* the ionic diffusion coefficients are constant for the charge carriers as they travel through the polymer matrix. The drift velocity, v_d, will be used heavily in the derivation of the ionic-flux-based actuation model.

Typically, IPMC actuation is characterized by stating that the size disparity between the anion and cation cause one side of the EAP to expand and contract, and it is through this process

that the observed bending occurs.[4-6] In this report, the assumption of expansion/contraction is adjusted, resulting in the novel approach where it is proposed that the accumulation of ions causes *both* sides of the EAP to expand. The inherent size differences between the anion and cation causes one side to have a larger expansion and therefore, bending occurs. This idea behind EAP actuation is similar to the way that bimetallic systems bend for a given temperature gradient due to dissimilar coefficients of thermal expansion for the two metals. Bending occurs due to one metal expanding further than the other with changes in temperature.

These broad assumptions led to the initial development of the charge distribution of the ions within the matrix with the governing equations for this motion discussed presently. To reduce confusion with symbols, a *1* will be the suffix used for negative charges and a *2* will be used for positive charges. The equations were established on the consideration that the ionic radius $r_1 > r_2$ (ex: $r_{ClO4-} = 240\ pm, r_{Li+} = 76\ pm$) which resulted in the drift velocities $v_2 > v_1$. As such, the saturation time for the negative charges was longer than that of the positive charges ($t_1^{sat} > t_2^{sat}$), due to the assumption that the larger negative charges traveled slower through the matrix than the positive ions (this further assumes a constant viscosity within the matrix).

4.1 Development of Relationships for Time-Dependent Charge Distribution

The accumulation of charge at the electrode-polymer interface was assumed to occur along a one-dimensional surface (**Figure 38.a**), therefore specific regions were noted for the accumulation region for each ion and the remaining thickness of the polymer matrix (in between the electrode interface and the dotted lines). The total charge within the matrix, for a given type of ion, can be denoted by **Eq. (4.1)**, which describes the amount of charge in the bulk of the polymer and in the accumulation (*delta* δ_i) zone. Once the polymer synthesis is completed, no more ions can be added to the IPMCs, therefore the number of charges present within the polymer remains constant throughout the actuation process regardless of where the charge is located, as described by **Eq. (4.2)**, where the sample thickness $h = h_{total} - (\delta_1 + \delta_2)$ and Q_i represents the total charge of the target ionic species. Finally, saturation time was defined as the time it would take for one ion to start its diffusion process at its repelling electrode and transit the entirety of the polymer matrix at a constant velocity. This is described by **Eq. (4.3)**.

$$q_1^{tot} = q_1^h + q_1^\delta \tag{4.1}$$

$$q_1^{tot} = \frac{Q_1}{h}(h - v_1 t) + Q_1 \frac{t}{t_1^{sat}} = constant \tag{4.2}$$

$$t_1^{sat} = \frac{h}{v_1}, t_2^{sat} = \frac{h}{v_2} \tag{4.3}$$

Due to the larger, negative ions having a slower drift velocity, and therefore longer saturation time, it was assumed that the saturation time for the IPMC as a whole was driven by when all of the negative ions reached the positive electrode, since all of the faster moving positive ions would have already reached the negative electrode. Therefore, the boundary conditions for the charge distribution were based primarily off of the diffusion of the negative ion. In the following derivation, charge, charge-per-unit length, and effective-strain equations will be developed with regards to the negative ion; once derived, the positive-charge analog will be shown and any differences in form will be outlined.

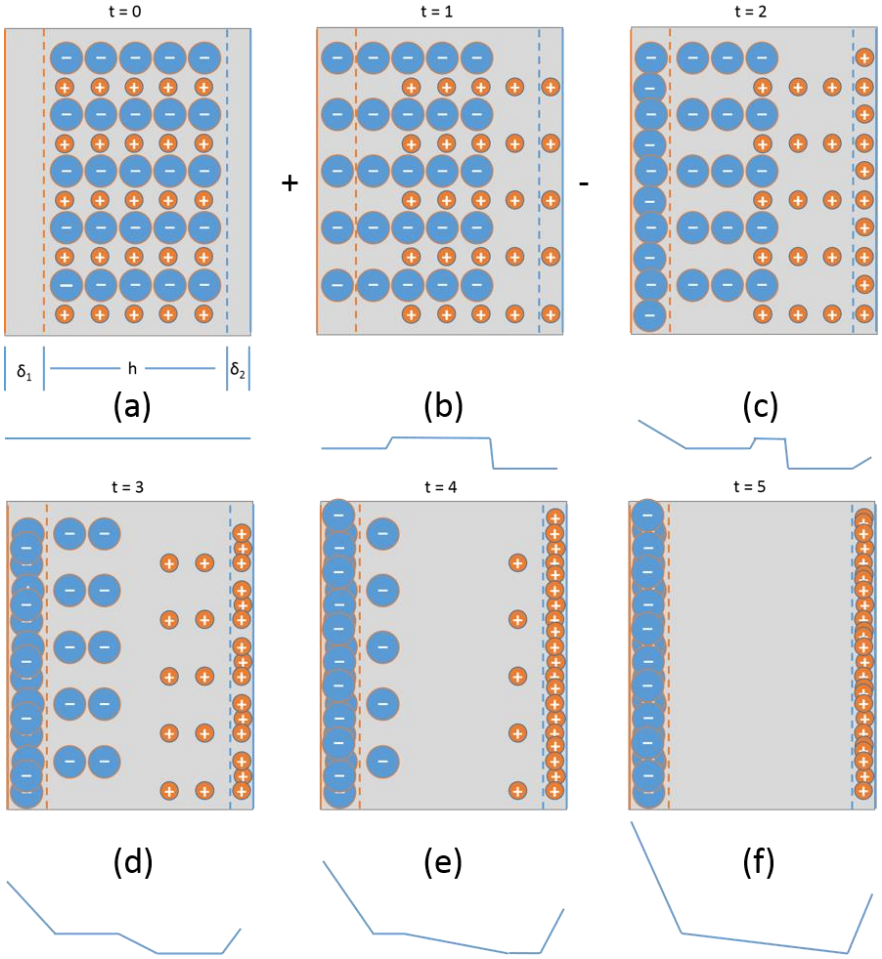

Figure 38: Idealized ionic flux under applied electric field and generalized effective strain profile for: (a) initial distribution of ions in polymer matrix, (b-f) constant flux of ions under an applied electric field

Figure 38 can be used as a visual representation of the processes going on within the IPMC as the charges diffuse through it under the application of an applied electric field. Through

inspection of **Figure 38.a-c**, since the ions are initially randomly distributed within the IPMC, there is overlap between the ions and a weighted cancelling of their contributions to actuator strain. The blue lines below each of the figures represent the generalized effective strain that the redistribution of charge would impose on the IPMC structure. As such, both sides of the film experience expansion wherein one side of the film will strain more, with respect to time, causing the observed bending actuation. **Figure 38.c** marks the point just before the overlap of charges and cancelling of strain behavior. This point is the second boundary condition (**Eq. (4.5-6)**) and the first set of equations relating to charge q and charge per unit length ρ are shown below. (note: the *free* superscript notation denotes the non-overlapped charge). This overlap point is also showcased in **Figure 38.a-b**, where sample data was generated with $v_2 = v_1$ and $v_2 = 4v_1$, respectively. The intersection of the two lines occurs at $\frac{t_1^{sat}}{v_2/v_1+1}$.

$$\boldsymbol{Boundary\ Condition\ 1}: at\ t = 0, q_1^{free} = 0 \tag{4.4}$$

$$\boldsymbol{Boundary\ Condition\ 2}: 0 \leq t \leq \frac{t_1^{sat}}{v_2/v_1 + 1} \tag{4.5}$$

$$q_1^{free} = q_1^{h-free} + q_1^{\delta} \tag{4.6}$$

The amount of negative charge that becomes non-overlapped was found to be dependent on how fast the positively charged ion moved (and vice versa). It was assumed that there was no overlapping of charges when they reached the accumulation zone and reached a maximum value at t_1^{sat}. Substituting this description into **Eq. (4.7)** yields:

$$q_1^{free} = \frac{Q_1 v_2 t}{h} + \frac{Q_1 t}{t_1^{sat}} = \frac{Q_1 v_2 t}{h} + \frac{Q_1 v_1 t}{h} \tag{4.7}$$

Rearranging yields,

$$q_1^{free} = \frac{Q_1}{h}(v_1 t + v_2 t) \tag{4.8}$$

And finally,

$$q_1^{free} = \frac{Q_1}{h}(L_1 + L_2) = \rho_1(L_1 + L_2) \tag{4.9}$$

$$q_2^{free} = \frac{Q_2}{h}(L_1 + L_2) = \rho_2(L_1 + L_2) \tag{4.10}$$

where,

$$L_i = v_i t \tag{4.11}$$

and represents the length of thickness that the furthest ion from its attracting electrode has traveled under electric excitation.

The free charge-per-unit-length equations below extended the charge-based equations by considering the amount of charge located in either the bulk or accumulation zones of the matrix.

$$\rho_1^{free} = \rho_1^{h-free} + \rho_1^{\delta} = \frac{q_1^{h-free}}{v_2 t} + \frac{q_1^{\delta}}{\delta_1} \tag{4.12}$$

$$\rho_1^{free} = \frac{Q_1}{h} + \frac{Q_1}{\delta_1}\frac{t}{t_1^{sat}} \tag{4.13}$$

Manipulating **Eq. (4.13)**, yields:

$$\rho_1^{free} = \frac{Q_1}{h}\left(1 + \frac{h}{\delta_1}\frac{t}{t_1^{sat}}\right) = \rho_1\left(1 + \frac{v_1 t}{\delta_1}\right) \tag{4.14}$$

where, $v_1 = h/t_1^{sat}$. Finally, the charge per unit length for each ionic species, with respect to time, can be represented as (where $\rho_i = Q_i/length$):

$$\rho_1^{free} = \rho_1\left(1 + \frac{L_1}{\delta_1}\right) \tag{4.15}$$

$$\rho_2^{free} = \rho_2\left(1 + \frac{L_2}{\delta_2}\right) \tag{4.16}$$

From here, the behavior of the individual ionic species has to be described utilizing two separate boundary conditions, due to the assumption that they would travel through the matrix at different speeds, so therefore their particular saturation time needs to be taken into account. Starting with the negatively-charged ion, the next boundary condition is below (note: the setup for the non-overlapped charges is the same as before and since there is no overlap, the amount of free charge equals the total negative charge):

$$\textbf{\textit{Boundary Condition 3}}\text{: } \frac{t_1^{sat}}{v_2/v_1 + 1} \leq t < t_1^{sat} \tag{4.17}$$

$$q_1^{free} = q_1^{h-free} + q_1^{\delta} \tag{4.18}$$

$$q_1^{free} = \frac{Q_1}{h}(h - v_1 t) + \frac{Q_1 t}{t_1^{sat}} \tag{4.19}$$

$$q_1^{free} = \frac{Q_1}{h}[(h - v_1 t) + v_1 t] \tag{4.20}$$

$$q_1^{free} = Q_1 \tag{4.21}$$

Similarly, a relationship concerning the charge per unit length can be developed showing the respective time-dependent charge distribution for the matrix and accumulation zone, resulting in **Eq. (4.24)**.

$$\rho_1^{free} = \rho_1^{h-free} + \rho_1^{\delta} = \frac{q_1^{h-free}}{(h - v_1 t)} + \frac{q_1^{\delta}}{\delta_1} \tag{4.22}$$

$$\rho_1^{free} = \frac{Q_1}{h} + \frac{Q_1 t}{\delta_1 t_1^{sat}} = \frac{Q_1}{h}\left(1 + \frac{ht}{\delta_1 t_1^{sat}}\right) = \frac{Q_1}{h}\left(1 + \frac{v_1 t}{\delta_1}\right) \tag{4.23}$$

$$\rho_1^{free} = \rho_1\left(1 + \frac{L_1}{\delta_1}\right) \tag{4.24}$$

The fourth boundary condition concerns the saturation of positive charge carriers. Due to their smaller size, compared to the negative ions, they travel faster through the polymer matrix and likewise, reach the negative electrode sooner than the negative ions reach the positive electrode. Therefore, the saturation time for the cations is shorter, yielding the following relationship for charge per unit length, which is the anion analog for **Eq. (4.24)**. At t_1^{sat} (or t_2^{sat}), since all charges are in their respective accumulation zone, $\rho_i = Q_i/\delta_i$.

$$\textbf{\textit{Boundary Condition 4}}\text{: } \frac{t_1^{sat}}{v_2/v_1 + 1} \leq t < t_2^{sat} \tag{4.25}$$

$$\rho_2^{free} = \rho_2\left(1 + \frac{L_2}{\delta_2}\right) \tag{4.26}$$

With regards to the charges 'canceled out' or overlapped charges towards the center of the polymer matrix, relationships governing the amount of charge in this area can also be created. These equations become important when concerning sample strain in the next section. Before excitation, it is assumed that all of the charges are in the bulk of the polymer and that an inconsequential amount of ions are in their respective accumulation zones. After excitation, but before the limit of the second boundary condition, a region of overlapped charges still exists and therefore, this region counters volumetric strains at the edges of the film (**Figure 38.a-c**). Finally, after the second boundary condition limit is met, there is no more overlap of charges and no more strain cancelling within the polymer matrix (**Figure 38.d-f**). Relationships for the center of the matrix for the second and third boundary conditions are listed below.

$$\textbf{\textit{Boundary Condition 2}}\text{: } 0 \leq t \leq \frac{t_1^{sat}}{v_2/v_1 + 1} \tag{4.27}$$

$$Overlapped\ Region\text{: } q_1^{cancelled} = q_2^{cancelled} = \rho_i[h - (L_1 + L_2)] \tag{4.28}$$

$$Overlapped\ Region: \rho_1^{cancelled} = \rho_2^{cancelled} = \frac{Q_i}{h} = \rho_i \tag{4.29}$$

$$\textbf{Boundary Condition 3}: \frac{t_1^{sat}}{v_2/v_1 + 1} \leq t < t_i^{sat} \tag{4.30}$$

$$Overlapped\ Region: q_1^{cancelled} = q_2^{cancelled} = 0 \tag{4.31}$$

$$Overlapped\ Region: \rho_1^{cancelled} = \rho_2^{cancelled} = 0 \tag{4.32}$$

4.2 Extending Charge Distribution Relationships to Actuator Performance

As mentioned, it is assumed that the strain incurred by the IPMCs resulting in the observed bending actuation of the films is linearly proportional to the distribution of charge within the polymer matrix. The relationships developed in the previous section will now be adjusted to render the equations unitless, resulting in functions that describe the *effective strain s* induced in the actuators by each type of charge carrier. When utilized to describe experimental strain results, a constant of proportionality will be used to deduce the actual strain within the EAP.

Another assumption laid out previously was that the IPMC bending actuation was a result of an, essentially, unbalanced expansion on either side of the film. This leads to there being an effective strain for both the negative and positive ions incurred within the matrix. The general process for this derivation is shown in **Eqs. (4.33-34)**.

$$s_1^{eff} = s_{L1}^{eff} + s_{\delta 1}^{eff} - s_1^{cancelled} \tag{4.33}$$

$$s_2^{eff} = s_{L2}^{eff} + s_{\delta 2}^{eff} - s_1^{cancelled} \tag{4.34}$$

The effective strain relationships were determined by taking the difference of the non-overlapped charge in the matrix and accumulation zone with the charges in the overlapped region while also dividing each term by either the matrix or accumulation zone thickness, then finally multiplying the function by the ionic diameter over the ionic charge. Before excitation, there was no strain in the films, therefore:

$$\textbf{Boundary Condition 1}: t = 0 \tag{4.35}$$

$$s_1^{eff} = s_2^{eff} = 0 \tag{4.36}$$

After electric excitation, combining **Eq. (4.15)** (or **Eq. (4.16)** and **Eq. (4.28)** with **Eq. (4.33)** as described, yields:

$$\textbf{Boundary Condition 2}: 0 \leq t \leq \frac{t_1^{sat}}{v_2/v_1 + 1} \tag{4.37}$$

$$s_1^{eff} = \frac{Q_1}{h}\frac{2r_1}{q}\left[\frac{L_1}{\delta_1} + \frac{1}{h}(L_1 + 2L_2) - 1\right] \tag{4.38}$$

$$s_2^{eff} = \frac{Q_2}{h}\frac{2r_2}{q}\left[\frac{L_2}{\delta_2} + \frac{1}{h}(L_2 + 2L_1) - 1\right] \tag{4.39}$$

Extending these results to the other boundary conditions, yields:

$$\textbf{Boundary Condition 3}: \frac{t_1^{sat}}{v_2/v_1 + 1} \leq t < t_i^{sat} \tag{4.40}$$

$$s_1^{eff} = \frac{Q_1}{h}\frac{2r_1}{q}\left[1 + L_1\left(\frac{1}{\delta_1} - \frac{1}{h}\right)\right] \tag{4.41}$$

$$\textbf{Boundary Condition 4}: \frac{t_1^{sat}}{v_2/v_1 + 1} \leq t < t_2^{sat} \tag{4.42}$$

$$s_2^{eff} = \frac{Q_2}{h}\frac{2r_2}{q}\left[1 + L_2\left(\frac{1}{\delta_2} - \frac{1}{h}\right)\right] \tag{4.43}$$

Since $t_2^{sat} < t_1^{sat}$, a final boundary condition needs to be introduced to reflect the period between the two saturation times. There are no more positive charges within the matrix to accumulate on the negative electrode, so the effective strain is constant.

$$\textbf{Boundary Condition 5}: t_2^{sat} \leq t \leq t_1^{sat} \tag{4.44}$$

$$s_2^{eff} = \frac{Q_2}{\delta_2}\frac{2r_2}{q} \tag{4.45}$$

The effective strain induced by the accumulation of both charges can be combined for calculating the tip-displacement angle of the actuator as the IPMC bends. **Figure 39** describes the geometry for determining this angle. If the IPMC is modeled as a curved trapezoid with a constant thickness, then the area of the trapezoid can be calculated using **Eq. (4.46)**. From there, the tip-displacement angle can be calculated using **Eq. (4.47)**. This relationship enables the translation of the charge distribution within the IPMC to the macro-scale bending actuation.

$$A = \frac{1}{2}\left(s_1^{eff} + s_2^{eff}\right)h_{tot} = 2\pi h_{tot} s_1^{eff} - {h_{tot}}^2\pi\theta \tag{4.46}$$

$$\theta = \frac{\left(s_1^{eff}\delta_1\right)(2\pi - 1/2) - \left(s_2^{eff}\delta_2\right)/2}{\pi h_{tot}} \tag{4.47}$$

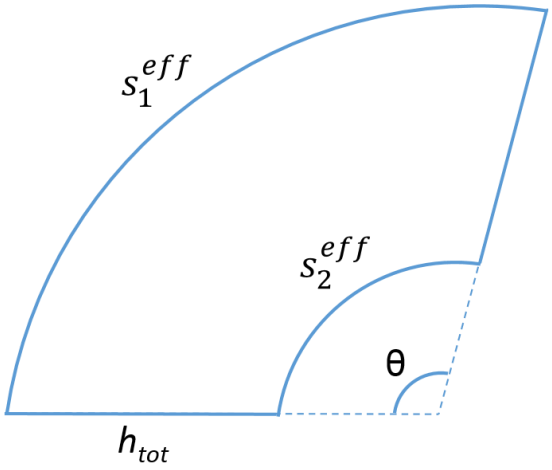

Figure 39: Tip-displacement angle determination for ionic-flux model

To test the effective strain and tip-displacement angle equations, a set of simulation data was created and the values used are shown in **Table 13**. A size coefficient of three was used in the table to more accurately mirror experimental results for LP in PEO since $r_{ClO4-} \cong 3r_{Li+}$. **Figure 40.a** shows the time-dependent effective strain for the individual ionic species. **Figure 40.b** shows the nonlinear and linear fitting results using **Eq. (3.1)** and **Eq. (3.3)** for changes in the tip-displacement angle. As can be seen, the fitting results follow the data fairly well, however, they do not describe the saturation mode observed with the IPMCs when all or most of the ions have accumulated at their electrodes. Therefore, the effective strain relationships developed need to be adjusted to account for this phenomena, as will be discussed in the proceeding section.

Table 13: Ionic Model Simulation Data

Total Charge - 1	Q_1	25 C
Total Charge - 2	Q_2	25 C
Individual Charge	q	1 C
Drift Velocity - 1	$v_1 = v_1^{ini}$	1 dia/s
Drift Velocity - 2	$v_2 = v_2^{ini}$	3 dia/s
Film Thickness	h	5 dia
Edge Thickness - 1	δ_1	1 dia
Edge Thickness - 2	δ_2	0.333 dia
Ionic Radius - 1	r_1	0.5 dia
Ionic Radius - 2	r_2	0.167 dia
Saturation Time - 1	t_1^{sat}	5 s
Saturation Time - 2	t_2^{sat}	1.67 s
Scaling Coefficient	size coef.	3
Redistribution Velocity Parameter – 1	$\frac{v_1^{ini}}{v_1^r \Delta t}$	0.580 s^{-1}
Redistribution Velocity Parameter - 2	$\frac{v_2^{ini}}{v_2^r \Delta t}$	0.193 s^{-1}

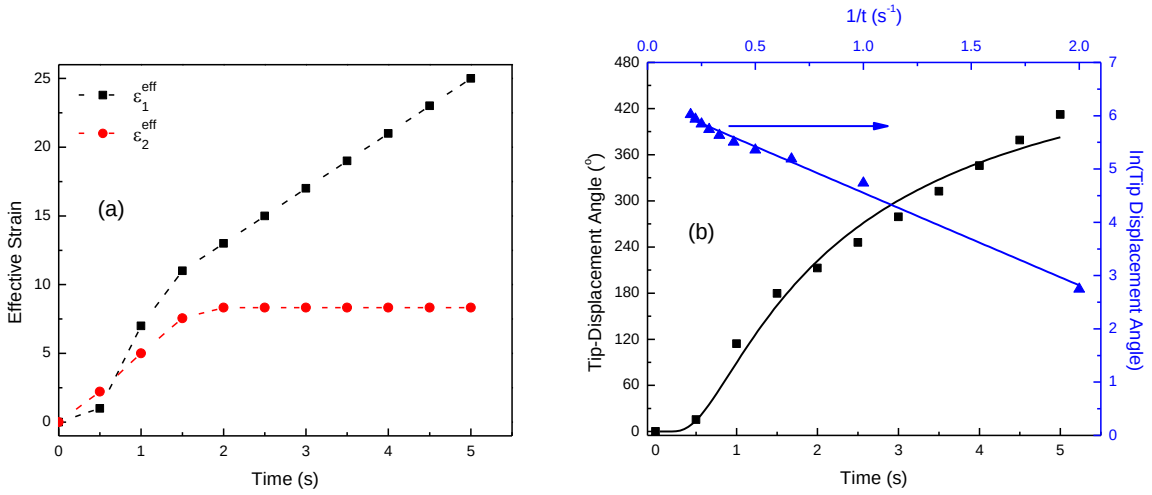

Figure 40: (a) Time-dependent effective strain for the distribution of the individual charges without saturation condition and (b) resulting calculated tip-displacement angle

4.3 Accounting for the Redistribution of Charges at the Polymer-Electrode Interface

To account for the saturation behavior observed in the IPMC bending, the interactions with the ions at the polymer-electrode interface was examined. This interaction was modeled as a change-in-momentum for the ions. Charges moving through the solid-polymer electrolyte and encountering the electrode would come to a halt; the time to go from the particles drift velocity to zero is assumed to be constant (shown in **Eq. (4.48)**)

$$F_d = \frac{\Delta p}{\Delta t} = \frac{m\left(v_i^{fin} - v_i^{ini}\right)}{\Delta t} \rightarrow F_d = -\frac{mv_i^{ini}}{\Delta t} = constant, where\ v_i^{ini} = v_i \tag{4.48}$$

At the polymer-electrode interface, the charges are redistributed across the interface; the assumption is that the ions will have an initial velocity of zero and then reach some redistribution velocity v_i^r, with the redistribution force required to do this decreasing as time goes on. Also, it is theorized that the ions have more mobility at the interface, resulting in higher velocities achieved during redistribution.

$$F_r = \frac{\Delta p}{\Delta t} = \frac{m\left(v_i^r - v_r^{ini}\right)}{\Delta t} \rightarrow F_r = \frac{mv_i^r}{t} \neq constant \tag{4.49}$$

To maintain the saturation conditions as a unitless parameter and to remove the need to know the mass of the ion, a ratio of the described drift force to the redistribution force was conducted. This ratio was subtracted from the s_i^{eff} relationships. It was found that through taking the square of this ratio that the negative from the F_d equation was nulled and that, while staying within the saturation time, the results of adding this parameter provided results that very closely resembled those seen by the actuators.

$$s_i^{eff} = s_i^{eff} - \left(\frac{F_d}{F_r}\right)^2 = s_i^{eff} - \left(\frac{-v_i^{ini}t}{v_i^r \Delta t}\right)^2 \tag{4.50}$$

Of note is that neither v_r^{fin} or the Δt for determining the time it takes for the charges in the electrolyte to come to a halt at the electrode interface were assumed to be known. When incorporated into the test data, it was assumed that the product of these two parameters was some constant. Adjusting this product yields that v_r^{fin} is more than likely greater than v_i^{ini}, which could be explained through reasoning that the charges have a little more freedom to move near the electrode than in the polymer matrix.

$$\textbf{Boundary Condition 1}: t = 0 \tag{4.51}$$

$$s_1^{eff} = s_2^{eff} = 0 \tag{4.52}$$

$$\textbf{Boundary Condition 2}: 0 \leq t \leq \frac{t_1^{sat}}{v_2/v_1 + 1} \tag{4.53}$$

$$s_1^{eff} = \frac{Q_1}{h}\frac{2r_1}{q}\left[\frac{L_1}{\delta_1} + \frac{1}{h}(L_1 + 2L_2) - 1\right] - \left(\frac{-v_1^{ini}t}{v_r^{fin}\Delta t}\right)^2 \tag{4.54}$$

$$s_2^{eff} = \left\{\frac{Q_2}{h}\frac{2r_2}{q}\left[\frac{L_2}{\delta_2} + \frac{1}{h}(L_2 + 2L_1) - 1\right] - \left(\frac{-v_2^{ini}t}{v_r^{fin}\Delta t}\right)^2\right\} * \frac{r_2}{r_1} \tag{4.55}$$

$$\textbf{Boundary Condition 3}: \frac{t_1^{sat}}{v_2/v_1 + 1} \leq t < t_i^{sat} \tag{4.56}$$

$$s_1^{eff} = \frac{Q_1}{h}\frac{2r_1}{q}\left[1 + L_1\left(\frac{1}{\delta_1} - \frac{1}{h}\right)\right] - \left(\frac{-v_1^{ini}t}{v_1^r\Delta t}\right)^2 \tag{4.57}$$

$$\textbf{Boundary Condition 4}: \frac{t_1^{sat}}{v_2/v_1 + 1} \leq t < t_2^{sat} \tag{4.58}$$

$$s_2^{eff} = \left\{\frac{Q_2}{h}\frac{2r_2}{q}\left[1 + L_2\left(\frac{1}{\delta_2} - \frac{1}{h}\right)\right] - \left(\frac{-v_2^{ini}t}{v_2^r\Delta t}\right)^2\right\} * \frac{r_2}{r_1} \tag{4.59}$$

$$\textbf{Boundary Condition 5}: t_2^{sat} \leq t \leq t_1^{sat} \tag{4.60}$$

$$s_2^{eff} = \left[\frac{Q_2}{\delta_2}\frac{2r_2}{q} - \left(\frac{-v_2^{ini}t}{v_2^r\Delta t}\right)^2\right] * \frac{r_2}{r_1} \tag{4.61}$$

Eqs. (4.51-61) showcase the final effective strain relationships utilized for characterizing the charge distribution of ions within the polymer matrix and their contribution to the observed actuation response, with a scaling factor attributed to the ε_2^{eff} functions. **Figure 41.a-b** show the nonlinear and linear fitting results (using **Eq. (3.1)** and **Eq. (3.3)**, respectively) using the simulation data provided in **Table 13**. With v_r^{fin} and Δt unknown for the redistribution, it was determined that this would be an empirically derived term and is therefore lumped into the redistribution velocity parameter, as shown in the table. The ability for both the Arrhenius-based and the charge-distribution models to marry one another with this simulated data lends credence to both models. As such, their use with experimental data will prove to make for these being very powerful fitting forms.

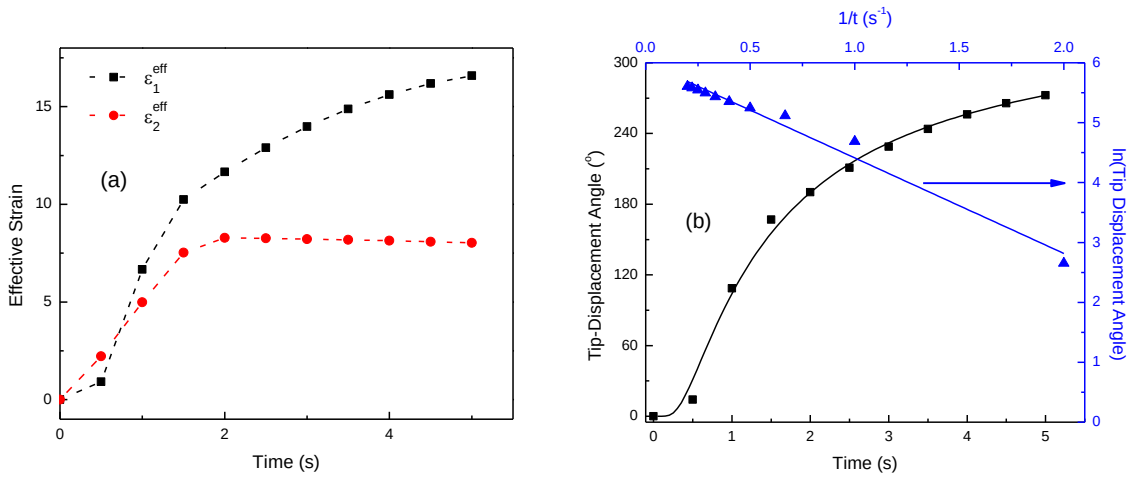

Figure 41: (a) Time-dependent effective strain for the distribution of the individual charges with saturation condition and (b) resulting calculated tip-displacement angle

4.4 Fitting Experimental Results

With the demonstrated ability of the charge-distribution model to generate data that can effectively describe the nonlinear behavior observed by the bending IPMC actuators using an idealized set of simulation data, as with the Arrhenius-like model, effort was placed with translating the charge-distribution model into one that could also fit the gathered experimental data. In doing so, more validity will be added to the ability of the charge distribution model to describe the processes going on within the IPMC actuators that result in bending. Specifically, the fitting of experimental data validates the novel assumption that both sides of the film expand under electric excitation, which is counter to the accepted theory that one side expands while the other contracts, as stated earlier. This section will showcase the ability of the charge-distribution model to simulate the actuation performance of various polymer systems, including: PEO, PVDF, Nafion, Flemion, and Polypyrrole. **Figure 42** illustrates the modeling of PEO-NCC composites with 5 wt.% LP and 1.5 vol.% NCC. It can be seen that both the Arrhenius-based and charge-distribution model fit the experimental data very closely, both with the linear and nonlinear fitting. The figure also provides inserts of the actual composite and its time-dependent displacement at various time steps during actuation. The drift velocities utilized in the charge-distribution model were taken from the fitted Arrhenius-based model. Saturation time was calculated from that fitting and used, with the sample thickness, to estimate the ionic drift velocity for the larger anion. The amount of

charge within the polymer matrix was calculated from the wt.% ionic salt used per sample and the sample dimensions.

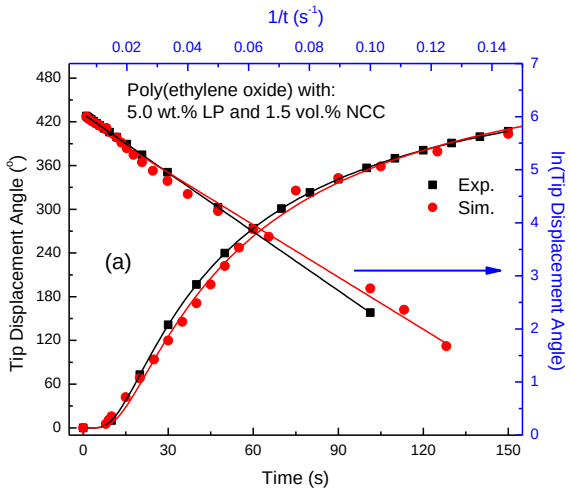

Figure 42: Experimental Results of PEO-NCC composite with 5.0 wt.% LP and 1.5 vol.% NCC, simulated with the charge-distribution model and fitted with Arrhenius-based model; inserts show observed IPMC performance during actuation

4.4.1 PEO-Based IPMC Results

As described in previous sections, the Arrhenius-based model does well with fitting the nonlinear, time-dependent response of the IPMC EAPs. Here, the results of utilizing the charge-distribution model is overlaid onto the experimental results for multiple PEO-based results. As will be seen, the fitting results for both models represent the experimental data very well. **Figure 43.a-c** illustrate the fitting results for the non-NCC PEO film at various LP wt.%.

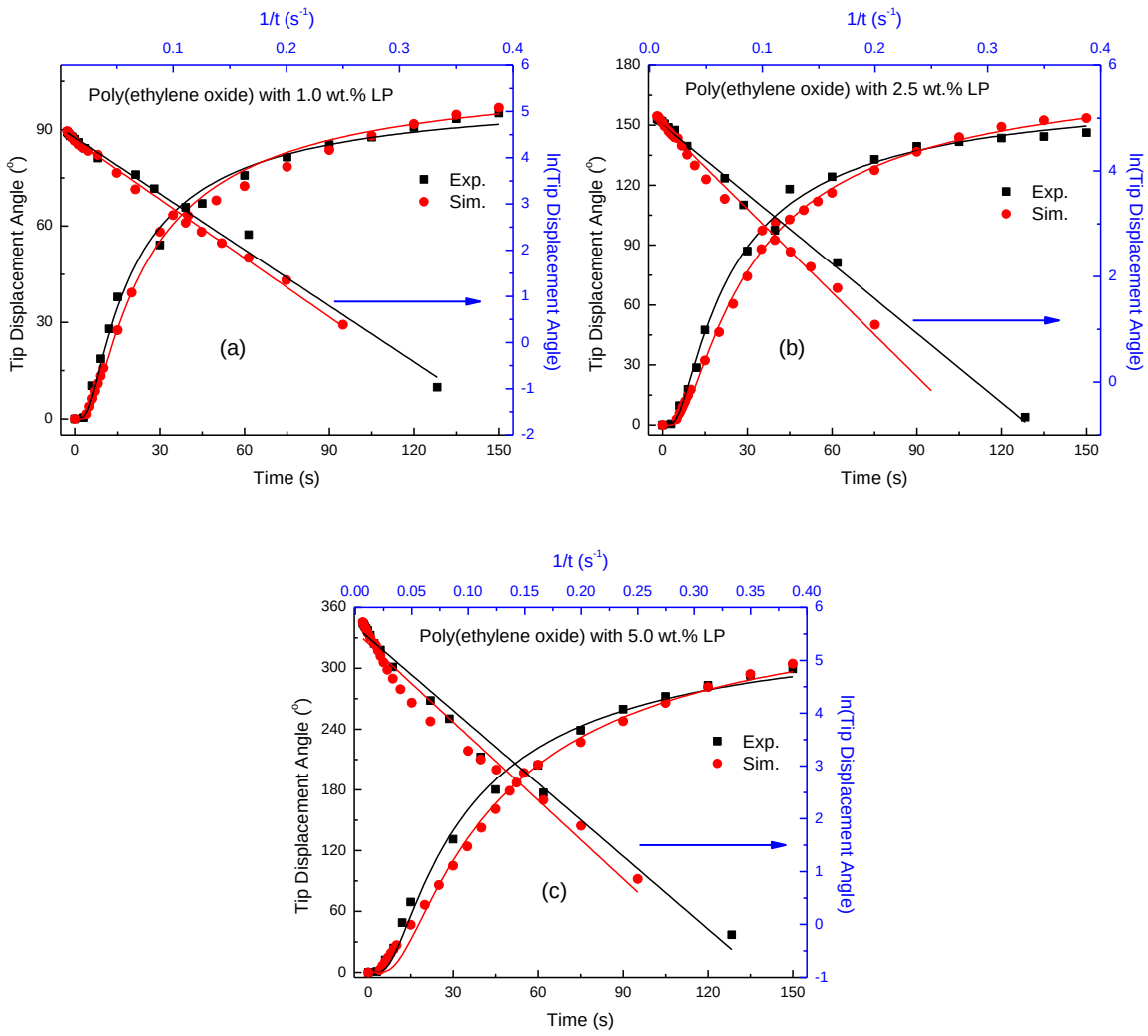

Figure 43: Fitting of both the Arrhenius-based model (solid line) and charge-distribution model (red points) for PEO with experimental data (black points): (a) 1.0 wt.% LP, (b) 2.5 wt.% LP, and (c) 5.0 wt.% LP

Figure 44.a-b illustrate the results for utilizing both fitting models for PEO-NCC composites with 5.0 wt.% LP and varying concentrations of LP.

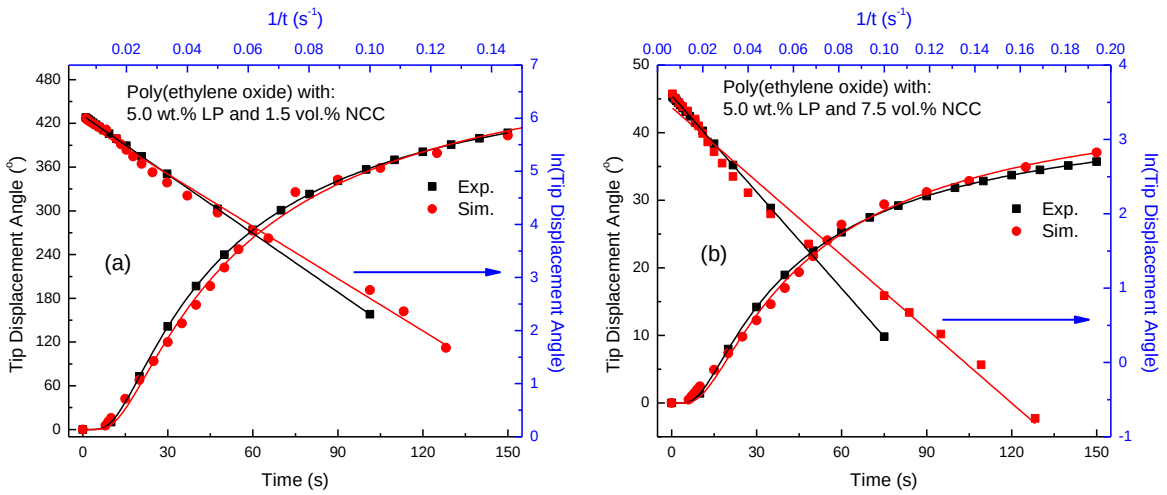

Figure 44: Fitting results for PEO with vol.% NCC concentrations of (a) 1.5 and (b) 7.5 vol.%

Figure 45.a-b illustrate the results for utilizing both fitting models for non-NCC PEO-based films which were subjected to testing under varying voltages.

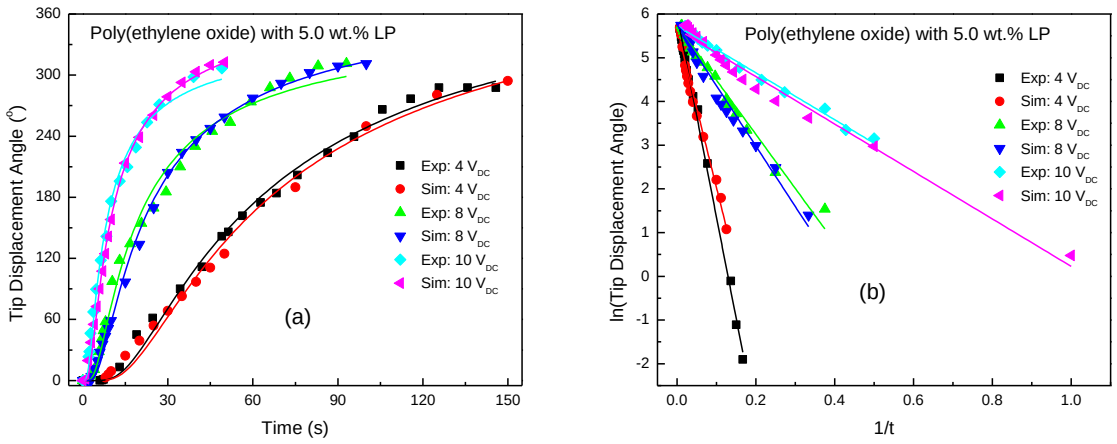

Figure 45: Fitting results for non-NCC PEO films under varying applied voltages

As can be seen by all of the figures, the two developed actuation models represent the observed actuation phenomena very well and under various conditions. **Figure 46** shows a compilation of PEO-based composites and their representative Arrhenius-Based Model and Charge-Distribution model fittings for samples with increasing wt.% LP and increasing vol.% NCC. The insets describe the actuation performance commensurate with the data points. It is clear that the Charge-Distribution model can accurately represent the experimental data as closely and precisely as the Arrhenius-Based Model. This result makes for both models being able to readily describe the time-dependent actuation performance of the PEO-based IPMCs.

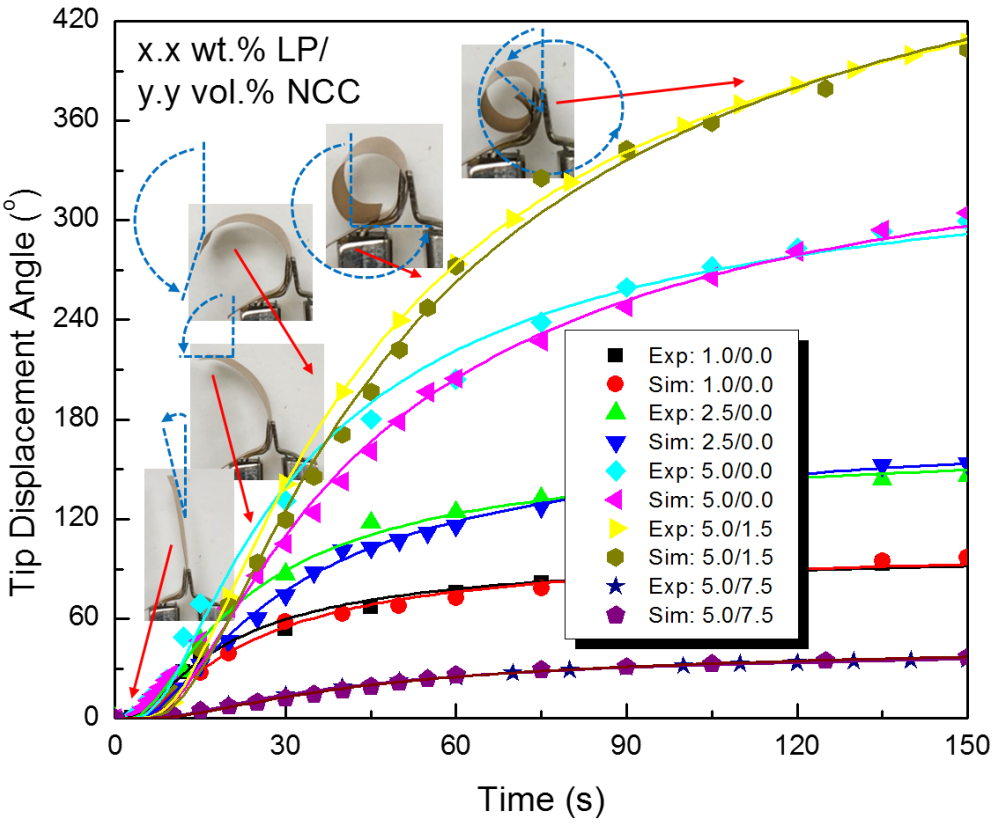

Figure 46: Charge-Distribution and Arrhenius-Based Model fitting of experimental data for PEO-based IPMCs

4.4.2 Results for Other Polymer-Based Systems

Similar to the PEO-based IPMCs, the Arrhenius-based model does well with fitting the nonlinear, time-dependent response of other polymer systems; including both IPMC and conducting-polymer bending actuators. Here, the results of utilizing the charge-distribution model is overlaid onto the experimental results for multiple polymer systems. Experimental results were obtained for the PVDF films whereas information on Nafion, Flemion and the conducting polymer, PPy were obtained and redrawn from previously published worked, as mentioned. As will be seen, the fitting results for both models represent the experimental data very well. **Figure 47** illustrates the fitting results for the PVDF with 15 wt.% CoPH. Of note is that the nonlinear simulation tracks the experimental data fairly well, but tends to lag behind the empirical results, which is more readily inferred from the linear regression. This could be due to the short timeframe through which actuation occurred or the fact that there were twice as many perchlorate ions to cobalt ions in the matrix (Co^{2+} versus ClO_4^-).

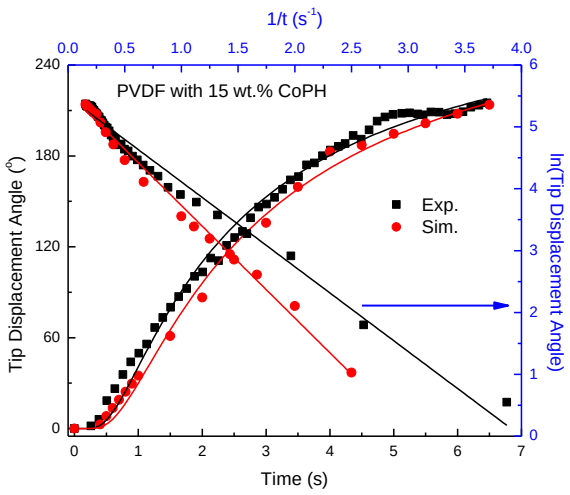

Figure 47: Fitting results for PVDF IPMC with 15 wt.% CoPH

The remainder of the figures shown in this section deal with experimental data pulled from published literature and are redrawn here for the purpose of displaying the adaptability and functionality of the two fitting forms, specifically in this case the charge-distribution model. As such, the data pulled from the publications is not perfect due in part to the error involved with obtaining the data from the published figures and with those authors posting data that was concerning phenomenon specific to their research and not necessarily for the study of the time-dependent nature of the film's actuation behavior. Therefore, refinements in sample data that may have otherwise been examined or added as to how well it describes the actual observed EAP response may not have been conducted and thus the larger disparity between their results and the simulated fitting results. In addition, liberties were taken with estimating the number of charge carriers within the polymer matrix as no information on ionic concentration within the final films was mentioned. Accurately estimating the amount of free charge carriers for the given sample thickness was essential for utilizing the charge-distribution models for the following fitting results.

Figure 48 displays the recreated experimental data and fitting results for a study on Nafion films.[7, 8] The simulated charge-distribution model follows along the experimental data fairly well as with the fitted Arrhenius-model curve. Of note is for results shown for under about 0.75 s. Here there is a reported step in the data, of which was not explained in the report. This step is likely due to sensitivity issues with their actuation recording device and not actual sample data.

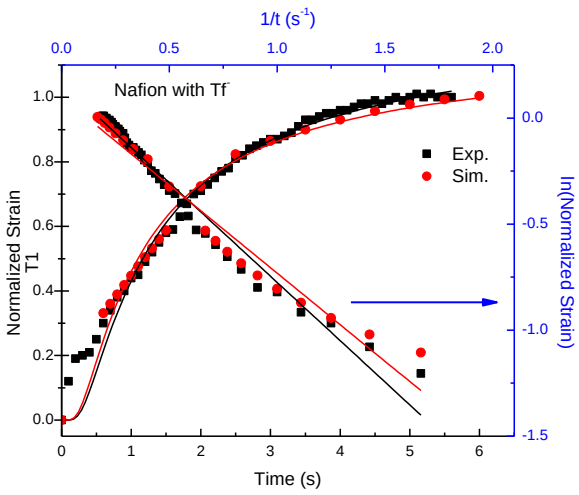

Figure 48: Fitting results for Nafion IPMCs; experimental data redrawn from ref[7, 8]

Figure 49 displays the fitting results for experimental data extracted from a study on Flemion EAPs utilizing TBA^+ as the mobile ion.[9] Data was pulled from a set of images showing the time-dependent actuation response of the actuators across eight compiled images. Tip-displacement angles were extracted from these angles and used for the fitting results. As can be seen, the charge distribution closely aligns with the experimental results, but undershoots them at small time intervals.

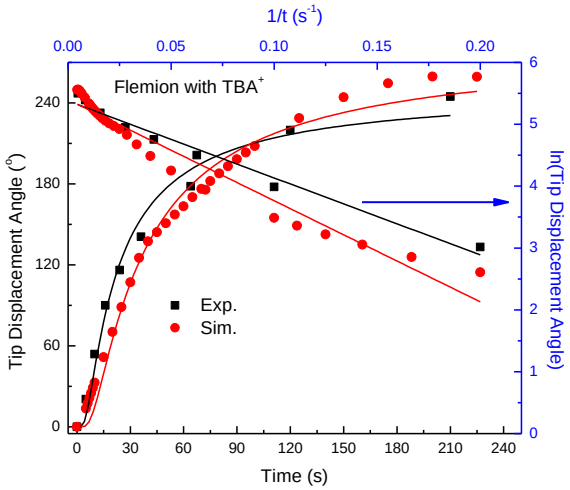

Figure 49: Fitting results from Flemion IPMCs; experimental data redrawn from ref[9]

Figure 50 illustrates how both the Arrhenius-based model and the charge-distribution model can be extended from use with IPMC EAP bending actuators to other types of EAPs, namely the conducting polymers, polypyrrole. Here, experimental data from a study on

polypyrrole bending actuators was redrawn.[10] Data was extracted from time-dependent tip-displacement curves for the actuators. The researchers tracked 16 points across the films and the data in the figure represents those at the tip of the figure, though the fitting was found to be valid for each of the 16 points along the actuator. As such, a very good fitting results for both the Arrhenius-based and charge distribution models.

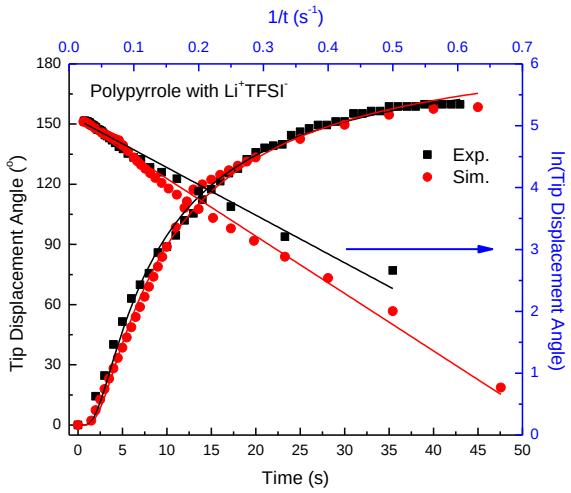

Figure 50: Fitting results from the conducting polymer, PPy; experimental data redrawn from ref[10]

4.5 Fitting Parameter Results

Table 14 displays the fitting parameters used in applying the charge distribution model to the experimental data shown in the preceding set of figures. h is the sample thickness, and δ_1 and δ_2 are the respective accumulation zone thicknesses for the anion and cation, respectively. The $v_i^{ini}/v_i^r \Delta t$ parameter can be described as a redistribution parameter for the ions as they reach their respective electrode-matrix interface. And finally, it was mentioned as one of the assumptions of the charge distribution model that the actuation performance (i.e., the tip-displacement angle) was linearly proportional to the modeled ionic redistribution. Therefore, m_i and b_i represent the scaling factors for the effective strain response of the anion and cation, respectively, for the calculation of the tip-displacement angle. Of note is that b_2, for the cation, was set to zero; in trying to determine a usable value for this parameter, from dataset to dataset, the results were always very small, so this parameter was assumed to be zero.

Through inspection of the accumulation zone data, it can be seen this zone decreased with increasing wt.% LP for the PEO samples, but then nearly doubles with the addition of NCC. This may be the result of some of the transiting ions being impeded by the cellulose structure. The

accumulation zones were also seen to increase with increasing applied voltage. These results indicate that the actuation performance may also be inherent to the behavior of the PEO matrix itself in response to the increased electric field and not just solely on volumetric expansion generated by the accumulated ions at the matrix-electrode interface. A larger applied electric field would result in a faster moving ion, effecting a more widespread area in a shorter period of time, creating a larger effective accumulation zone and faster actuation response. The actuation response of IPMCs would thus be comprised of two responses; 1) volumetric expansion on either side of the IPMC due to the accumulation of ions and 2) a reactionary matrix response due to the incident ions on the polymer chains within the matrix. While 1) is an intuitive response, evidence of 2) can be seen by the relaxation response that can be seen in some IPMC actuators, like Nafion.[11] This relaxation was also evident in the PVDF films tested in this study. After the initial actuation response, which is the focus of their study in this report, the films can relax up to 50% of their initial performance while still under an applied voltage and can even recoil back to their original position in under 30 s when the external excitation is removed. The variation in the described accumulation zones therefore works as a way to begin to quantify this two pronged actuation response of IPMC actuators.

Also of interest concerning the accumulation zone parameter is its temperature influence. For the 2.5 wt.% PEO IPMCs, there was an initial increase from 0 ^{o}C up to 30 ^{o}C and then a decrease in the parameter with increasing temperature thereafter, while when compared to **Figure 25**, there is a constant increase in actuation performance. This could be due to an increased flexibility of the PEO chains to move with respect to one another. The other parameters in **Table 14** mirror the behavior of the accumulation zone parameter, but this specific parameter identifies more of the physical process at work within the IPMC and was therefore the focus. Results for PVDF samples and fitted results for external work is also included in the table and show the viability of the charge distribution model across a wide array of EAPs.

Table 14: Charge-Distribution Model fitted parameters

	Salt/NCC Content	V (DC)	Ionic Radii Ratio	h (μm)	δ_1 (μm)	δ_2 (μm)	$\frac{v_1^{ini}}{v_1^r \Delta t}$ (s^{-1})	$\frac{v_2^{ini}}{v_2^r \Delta t}$ (s^{-1})	m_1	m_2	b_1	b_2
PEO w/ LP	1.0 wt.%	4.0	3.16	50.3	10.4	3.28	0.069	2.19E-2	1.80E-2	5.70E-3	0.82	0
	2.5 wt.%	4.0	3.16	56.4	6.00	1.90	0.110	3.48E-2	3.20E-2	1.01E-2	1.70	0
	5.0 wt.%	4.0	3.16	54.5	4.36	1.38	0.100	3.17E-2	6.80E-2	2.15E-2	4.50	0
PEO w/ 5.0 wt.% LP NCC-H_2SO_4	1.5 vol.% NCC	4.0	3.16	56.5	9.81	3.11	0.040	1.27E-2	6.50E-2	2.06E-2	5.00	0
	7.5 vol.% NCC	4.0	3.16	55.2	8.18	2.59	0.055	1.74E-2	6.50E-3	2.06E-3	0.50	0
PEO w/ LP Variable Voltage	2.5 wt.%	4.0	3.16	56.4	6.77	2.14	0.065	2.06E-2	5.60E-2	1.77E-2	2.50	0
	2.5 wt.%	8.0	3.16	56.4	9.02	2.86	0.090	2.85E-2	4.00E-2	1.27E-2	2.00	0
	2.5 wt.%	10	3.16	56.4	10.2	3.21	0.078	2.47E-2	3.50E-2	1.11E-2	1.60	0
PEO w/ LP Variable Voltage	5.0 wt.%	4.0	3.16	54.5	4.36	1.38	0.071	2.25E-2	1.00E-1	3.17E-2	6.50	0
	5.0 wt.%	8.0	3.16	54.5	5.18	1.64	0.170	5.38E-2	7.00E-2	2.22E-2	4.50	0
	5.0 wt.%	10	3.16	54.5	6.54	2.07	0.330	1.05E-1	5.50E-2	1.74E-2	4.00	0
PEO w/ 2.5 wt.% LP Variable Temp.	0 °C	4.0	3.16	56.4	0.56	0.18	0.300	9.50E-2	1.00E-3	3.17E-4	0.00	0
	10 °C	4.0	3.16	56.4	1.69	0.54	0.055	1.74E-2	2.00E-2	6.33E-3	0.25	0
	20 °C	4.0	3.16	56.4	3.10	0.98	0.058	1.83E-2	2.80E-2	8.87E-3	1.00	0
	30 °C	4.0	3.16	56.4	3.38	1.07	0.095	3.01E-2	6.80E-2	2.15E-2	3.20	0
	40 °C	4.0	3.16	56.4	5.64	1.79	0.085	2.69E-2	3.80E-2	1.20E-2	2.00	0
	50 °C	4.0	3.16	56.4	7.9	2.50	0.080	2.53E-2	3.70E-2	1.17E-2	2.00	0
PEO w/ 2.5 wt.% LP – Variable Thickness	2.5 wt.%	4.0	3.16	31.8	2.07	0.66	0.165	5.22E-2	2.80E-2	8.87E-3	1.00	0
	2.5 wt.%	4.0	3.16	44.8	2.82	0.89	0.095	3.00E-2	4.20E-2	1.33E-2	1.90	0
	2.5 wt.%	4.0	3.16	58.5	2.93	0.93	0.093	2.94E-2	6.50E-2	2.06E-2	1.90	0
	2.5 wt.%	4.0	3.16	103	0.82	0.26	0.240	7.60E-2	5.00E-3	1.58E-3	0.90	0
PVDF	15 wt.% CoPH	4.0	3.22	32.0	3.20	0.99	2.500	7.76E-1	1.80E-2	5.59E-3	3.50	0
Nafion †‡	Tf^-	4.0	3.16*	25.0	2.75	0.87	1.500	4.75E-1	3.80E-4	1.20E-4	0.03	0
Flemion †‡	TBA^+	3.0	3.16*	160	17.6	5.57	0.085	2.69E-2	5.00E-2	1.58E-2	3.00	0
PPy †‡	Li^+TFSI^-	1.0	3.16*	60.0	5.40	1.71	0.355	1.12E-1	5.20E-2	1.65E-2	2.50	0

†salt radii not listed – estimated as the same ratio as the LP samples, ‡ data provided was fitted from published actuation data referenced elsewhere in this study, *assumed ionic ratio

Table 15 displays the resulting linear fit of the Arrhenius-Based Model (**Eq. (3.3)**) for the experimental data as well as for the data generated by the charge distribution model. Through inspection of the fitted maximum tip-displacement angle, it can be seen that the performance simulated through the charge-distribution model generally aligns with that of the experimental results, with an average percent difference of 6.4% across all of the fitted data with 76% of the results below that average. The accuracy between the fitted parameters for the experimental and simulated charge-distribution model data provide validity for the assumptions and equations utilized for this model. The table references results for the majority of the PEO samples, the PVDF

films, as well as an excerpt of data for the externally published data spanning all of the described EAP systems (Nafion, Flemion, and PPy). Similar comparisons can be made across the time constant, *B*, and % strain data shown with average percent differences being as low as 5.8% when comparing strain data, but rising to 11% for comparing time constants. As this table comprises linear fitting results as opposed to the nonlinear fitting form for the Arrhenius response model (**Eq. (3.3)**), which results in more closely aligned fitting curves to the experimental data due to different weighting of the fitted parameters, a time constant that is *reasonably* close should suffice for this percent difference when considered in conjunction with how well the other parameters compare.

Table 15: Fitted parameters utilizing the Arrhenius-Based Model on the experimental data and the simulated data generated from the Charge-Distribution Model

		B_{exp} (s)	B_{sim} (s)	θ_{max}^{exp} (°)	θ_{max}^{sim} (°)	s_{max}^{exp} (%)	s_{max}^{sim} (%)	R_{exp}^2	R_{sim}^2
PEO w/ LP	1.0 wt.%	16.2	17.0	105	99	0.26	0.25	0.992	0.996
	2.5 wt.%	17.5	20.5	160	159	0.40	0.40	0.995	0.995
	5.0 wt.%	18.3	20.2	282	272	0.70	0.68	0.986	0.972
PEO w/ 5.0 wt.% LP (NCC-H_2SO_4)	1.5 vol.% NCC	39.7	37.3	530	499	1.32	1.24	1.000	0.983
	7.5 vol.% NCC	34.6	31.5	45	42	0.11	0.11	1.000	0.973
PEO w/ 2.5 wt.% LP	4 V DC	39.5	48	234	304	0.60	0.78	0.983	0.991
	8 V DC	24.3	24	281	275	0.72	0.71	0.977	0.997
	10 V DC	27.1	28	260	274	0.67	0.71	0.966	0.993
PEO w/ 5.0 wt.% LP	4 V DC	46.2	38.0	388	303	0.97	0.75	0.997	0.986
	8 V DC	12.3	13.8	300	310	0.75	0.77	0.981	0.982
	10 V DC	5.37	7.29	307	342	0.76	0.85	0.990	0.985
PEO w/ 2.5 wt.% LP – Variable Temp.	0 °C	40.6	39	2.6	2.6	0.01	0.01	0.587	0.991
	10 °C	112	110	31	32	0.08	0.08	0.979	0.997
	20 °C	90.4	95	47	55	0.12	0.14	0.979	0.996
	30 °C	50.2	47	112	112	0.29	0.29	0.983	0.992
	40 °C	35.8	36	162	159	0.42	0.41	0.999	0.988
	50 °C	28.2	28	213	213	0.55	0.55	0.999	0.989
PEO w/ 2.5 wt.% LP – Variable Thickness	31.8 µm	32.8	41.0	190	200	0.27	0.29	0.997	0.998
	44.8 µm	51.4	55.2	160	170	0.32	0.35	0.993	0.001
	58.5 µm	69.1	61.2	140	130	0.38	0.35	0.988	0.993
	103 µm	57.5	59.9	65.2	73.7	0.031	0.035	0.9871	0.997
PVDF	15 wt.% CoPH	1.35	1.84	238	265	0.35	0.39	0.978	0.992
Nafion †‡	Tf^-	1.12	1.03	--	--	125	120	0.994	0.996
Flemion †‡	TBA^+	12.4	17.2	216	219	1.01	1.02	0.976	0.967
PPy †‡	Li^+TFSI^-	5.61	6.88	176	180	0.46	0.47	0.978	0.970

†salt radii not listed – estimated as the same ratio as the LP samples, ‡ data provided was fitted from published actuation data referenced elsewhere in this study

The end result of all of these fitting parameters is the emergence of a gray-box fitting model that can accurately describe the electromechanical actuation response across several different types of electroactive polymers, for both IPMCs and conducting polymers. In contrast to the Arrhenius-Based Model, which had two fitting parameters, *s* for describing strain, tip-actuation angle or radius of curvature and *B*, the time constant, with one fitting form equation that was valid for the entirety of the actuation response; the more detailed Charge-Distribution Model utilizes four independent fitting parameters (the accumulation zone width δ_i, the redistribution parameter $v_i^{ini}/v_i^r \Delta t$, the linearly related sizing coefficient *m*, and the linear related adjustment factor *b*) with the ionic velocities coming from the experimental fitting results utilizing the Arrhenius-Based Model. These parameters span five separate boundary conditions and describe how the distribution of ions in the polymer matrix affect the overall bending actuation response. The success of the Charge-Distribution Model with fitting the dielectric data validates the assumptions made with putting the series of relationships together. The result is two viable models, the Arrhenius-Based and Charge-Distribution model, that can be used for describing the highly nonlinear bending response of IPMC EAPs, with one being very compact (the Arrhenius-Based Model) and easy to use for quick analysis and the other providing an insight into the inner workings of the actuators (the Charge-Distribution Model).

Chapter 4 References

1. Tropea, C., A.L. Yarin, and J.F. Foss, *Springer handbook of experimental fluid mechanics*. Vol. 1. 2007: Springer.
2. Oguro, K., et al. *Polymer electrolyte actuator with gold electrodes*. in *1999 Symposium on Smart Structures and Materials*. 1999. International Society for Optics and Photonics.
3. Bennett, M.D. and D.J. Leo, *Ionic liquids as stable solvents for ionic polymer transducers.* Sensors and Actuators A: Physical, 2004. **115**(1): p. 79-90.
4. Anton, M., et al., *Towards a biomimetic EAP robot.* Proc. of TAROS, 2004: p. 6-8.
5. Diab, M.O., et al. *Electromechanical model of IPMC artificial muscle*. in *Computer Applications & Research (WSCAR), 2014 World Symposium on*. 2014. IEEE.
6. Carpi, F., et al., *Electroactive polymer actuators as artificial muscles: are they ready for bioinspired applications?* Bioinspiration & biomimetics, 2011. **6**(4): p. 045006.
7. Liu, Y., et al., *Ion transport and storage of ionic liquids in ionic polymer conductor network composites.* Applied Physics Letters, 2010. **96**(22): p. 223503.
8. Montazami, R., et al., *Thickness dependence of curvature, strain, and response time in ionic electroactive polymer actuators fabricated via layer-by-layer assembly.* Journal of Applied Physics, 2011. **109**(10): p. 104301.

9. Nemat-Nasser, S. and Y. Wu, *Comparative experimental study of ionic polymer–metal composites with different backbone ionomers and in various cation forms.* Journal of Applied Physics, 2003. **93**(9): p. 5255-5267.
10. Mutlu, R., et al., *Electro-mechanical modelling and identification of electroactive polymer actuators as smart robotic manipulators.* Mechatronics, 2014. **24**(3): p. 241-251.
11. Shahinpoor, M., *Mechanoelectrical phenomena in ionic polymers.* Mathematics and Mechanics of Solids, 2003. **8**(3): p. 281-288.

Chapter 5: Dielectric Analysis and Development of Dielectric Monitoring Model

5 Overview

In this chapter, an analysis of the dielectric properties of PEO-based films will be conducted. Concentration will be focused on the frequency and temperature dependence with how these materials respond to an alternating electric field. In addition, this analysis will be extended, introducing a novel approach to monitoring the PEO-based IPMC actuation process wherein the time-dependent dielectric response was monitored under an applied 4 V DC. This new methodology opens up the opportunity to remotely monitor actuation performance through direct feedback from the films themselves without the need for an external optical monitoring system. The end result of this is that for applications where weight is concerned, that the electromechanical response of these actuators could be sensed using AC dielectric readings as the films are driven under a larger DC load to determine the near-real time performance of the film.

5.1 General Dielectric Analysis

This section describes the frequency-dependent dielectric characteristics and response of PEO-based IPMCs without any externally applied DC electric field. Essentially, in this section the electromechanical actuation response of PEO-based IPMCs will not be discussed and focus will be on the film's dielectric properties. These films were analyzed using two types of impedance analyzers and AC frequencies were ranged from either 0.1 Hz to 1 MHz or from 100 Hz to 1 MHz, unless otherwise specified. Films with varying concentrations of LP and NCC were submitted to temperatures ranging from -40 ^{o}C to 60 ^{o}C.

Figure 51.a shows the general dielectric response from 100 to 1 kHz of a PEO sample with no LP or NCC in its matrix (three samples tested and averaged). Concerning electromechanical performance, since no LP is present within the PEO matrix there was not actuation response from this sample, as expected. Though the PEO polymer is a well-studied material in its own right,[1] further analysis of this material will be conducted in the following sections with how it compares to PEO samples with varying concentrations of LP and NCC. By inspection of the figure, it looks as though the low frequency, DC, real permittivity could be estimated to be 50 while the high frequency value looks to flatten to around 5. The 1 kHz real permittivity value for this film is 18.1. As previously illustrated in Chapter 2, there is a rapid increase in the real permittivity value for the PEO film below 100 Hz. An in-depth analysis of this process will be conducted in the next section.

Figure 51.b shows the dielectric response for a free standing sulfuric-acid-based NCC film with a thickness of approximately 45 µm. It was made by air drying 10 ml of NCC suspension at 35 mg/ml at room temperature in an aluminum pan. It can be seen that the loss for this material is relatively low and that the real dielectric constant has a weak frequency dependence and varies between 3 and 5 for the given frequency range. The 1 kHz real permittivity value for this film is 3.82.

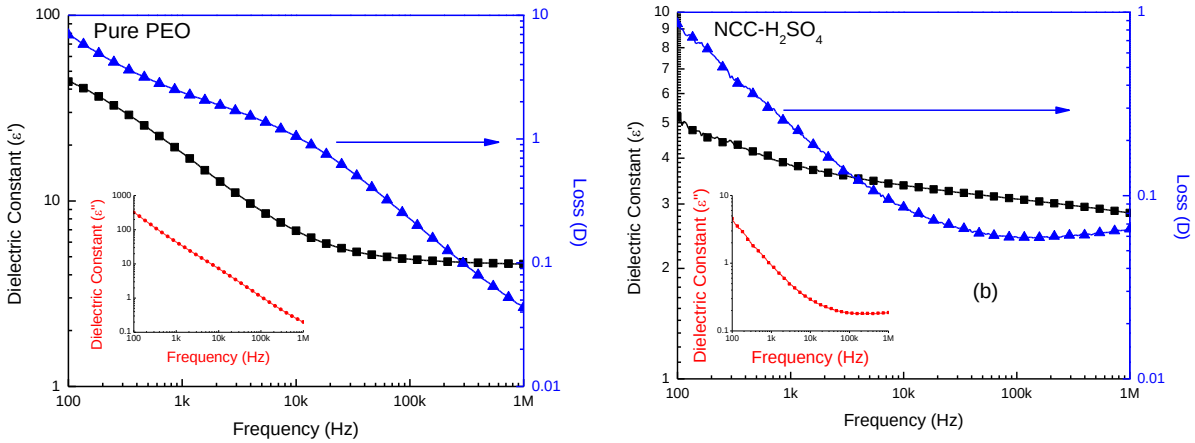

Figure 51: Dielectric behavior for a) a pure PEO film and b) sulfuric acid hydrolysis based NCC film

5.1.1 Low-Frequency Dielectric Analysis

Figure 52.a-d show the low-frequency (0.1 Hz to 1 MHz) real permittivity, imaginary permittivity, dielectric loss, and Cole-Cole plot, respectively, for films with LP concentrations of 0.0, 1.0, 2.5, and 5.0 wt.% (one sample tested). It is clear that all of these parameters increase with increasing LP content. It is also evident that a loss peak is generated with the addition of LP to the matrix and that this peak shifts to higher frequencies with increasing LP content. This peak is a relaxation peak and represents the frequency where the mobile ions within the matrix can no longer oscillate at the applied AC frequency.[2] **Table 16** lists the real permittivity, imaginary permittivity, dielectric loss, and conductivity at the low (~DC frequency) and high (~infinite frequency) frequencies, as well as the values for these parameters where the loss peak is present.

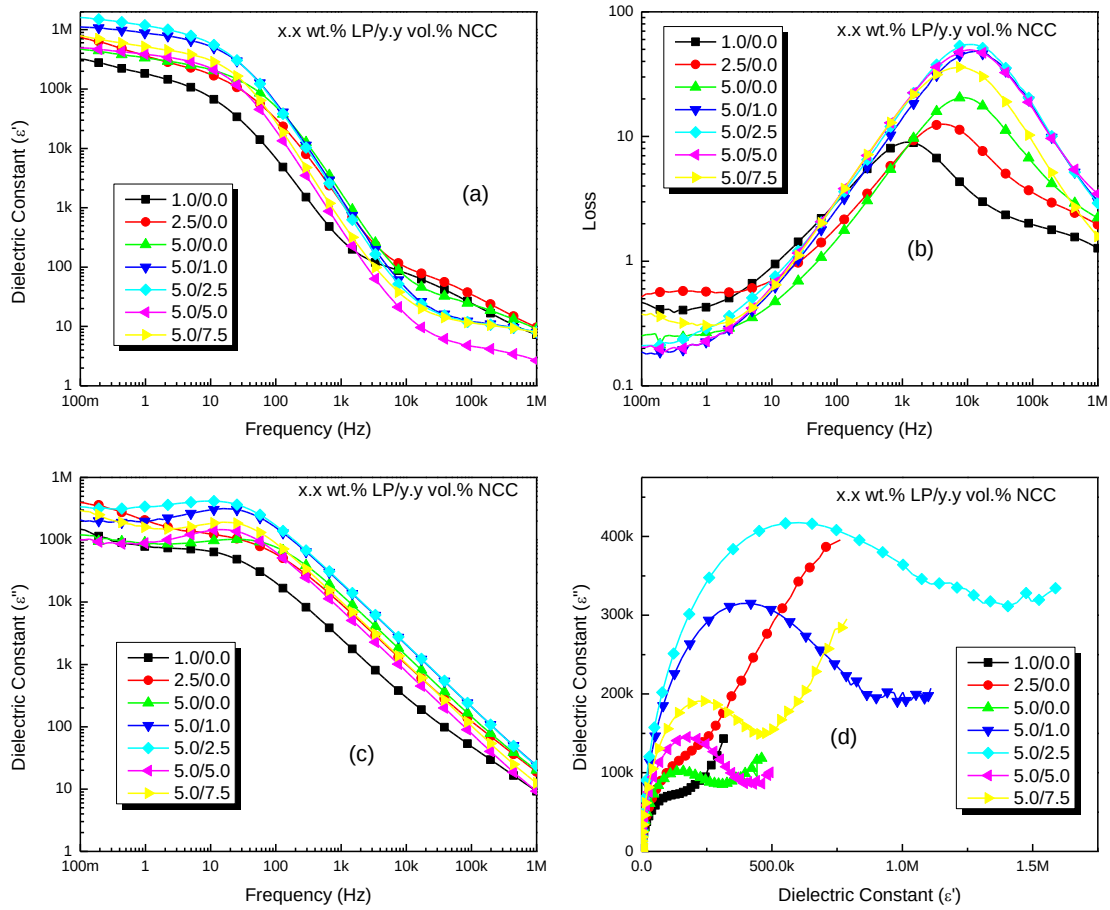

Figure 52: Low-frequency testing of PEO films with varying LP and NCC concentrations for a) real permittivity, b) dielectric loss, c) imaginary dielectric constant, and d) Cole-Cole plot

As can be seen from the table, the general trend for the real permittivity at both 0.1 Hz (the approximated DC permittivity) and at 1 MHz (the approximated permittivity at an infinite applied AC frequency) is that there is an initial increase in permittivity with increasing wt.% LP. Once at 5.0 wt.%, the permittivities continue to increase up to around 2.5 vol.% NCC, then decrease at 5.0 wt.% NCC, then finally increase again at 7.5 wt.% NCC. The initial increase with increasing LP concentrations is due to the increased conductive filler content boosting the dielectric constant.[3] With increasing NCC concentrations, the initial increase is likely due to the increase of mobile space charges donated by the NCC chains; the decrease could be explained as a the rigid NCC fibers beginning to inhibit the vibration of the ions; the final increase is likely due to effects from the NCC. The loss at 0.1 Hz follows this same trend while the dielectric loss at 1 MHz behaves in the opposite way where it gets larger, then smaller with increasing NCC content.

Table 16: Low-frequency dielectric data for PEO-based IPMC EAPs

		Approximate Values				At Loss Peak Frequency				
wt.% LP	vol.% NCC	ε'_{DC} (.1 Hz)	D (.1 Hz)	ε'_{∞} (1 MHz)	D (1 MHz)	f (kHz)	ε'	D	ε''	σ (S/cm)
1.0	0.0	3.18E5	0.466	7.26	1.27	1.26	229	9.01	2070	1.43E-6
2.5	0.0	7.62E5	0.519	9.65	1.96	4.64	169	12.5	2120	5.72e-6
5.0	0.0	4.73E5	0.252	9.03	2.23	7.56	89.1	20.5	1820	5.82e-6
5.0	1.0	1.11E6	0.187	7.91	3.03	10.5	41.5	47.5	1970	8.86e-6
5.0	2.5	1.63E6	0.210	8.06	2.92	12.3	31.2	54.6	1700	7.37e-6
5.0	5.0	4.89E5	0.204	2.66	3.48	14.5	11.0	48.3	530	4.35e-6
5.0	7.5	7.88E5	0.374	7.91	1.58	7.56	22.2	36.0	1370	4.77e-6

5.1.2 Variable-Temperature Dielectric Analysis

Figure 53.a-e show the real permittivity, imaginary permittivity, dielectric loss, Cole-Cole plot, and conductivity, respectively, for films with LP concentrations of 1.0 wt.% LP for temperatures from -60 ºC to 60 ºC at 10 ºC intervals from 100 Hz to 1 MHz (one sample tested). Similar figures can be constructed for 2.5 and 5.0 wt.% samples, so this series of plots acts as an example for the other films as well. **Figure 54.a** showcases the 1 kHz values for all of the films tested under varying temperatures while **Figure 54.b** displays the dielectric information for how the loss peak and frequency of the relaxation peak change with increasing temperature. For this particular set of figures, there is an increase in the real and imaginary permittivities with increasing temperature, but the real permittivity drops when the temperature increases above 30 ºC. The melting temperature of PEO is ~65 ºC[1] and this decrease in permittivity could be attributed to the polymer matrix beginning to break down. Compared to the 1.0 wt.% samples, the 2.5 wt.% films have a larger maximum real permittivity, a comparable imaginary permittivity, comparable conductivities, and comparable loss peak values. Compared to the other two concentrations of LP, the 5.0 wt.% samples have a larger maximum real permittivity and loss peak value, and a comparable imaginary permittivity and conductivity compared to the other two concentrations.

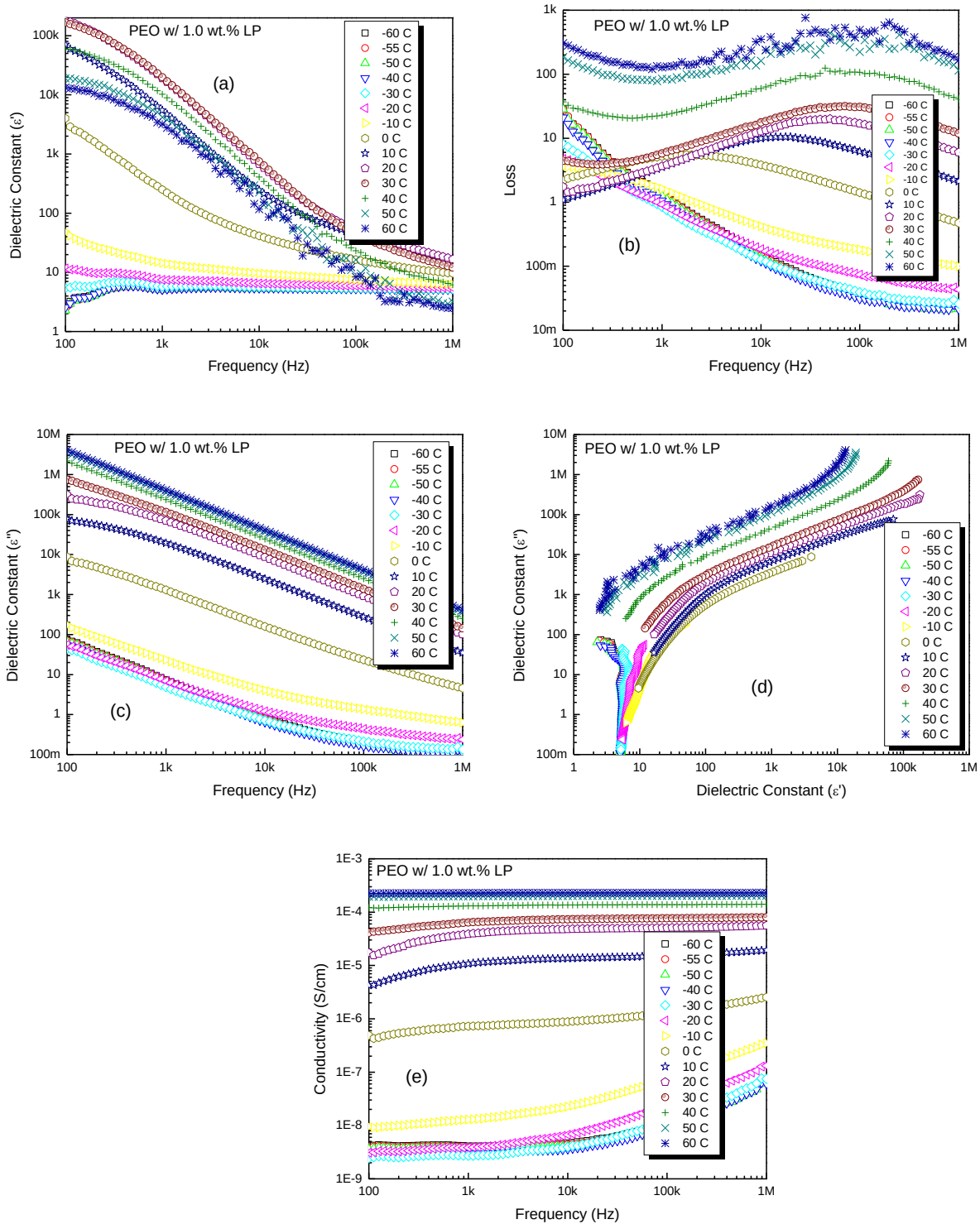

Figure 53: Temperature-dependent response of PEO films with 1.0 wt.% LP for a) real permittivity, b) dielectric loss, c) imaginary permittivity, d) Cole-Cole plot, and e) conductivity

Again, **Figure 54.a** tracks the real permittivity and dielectric loss at 1 kHz for each of the wt.% with how they change with respect to temperature. **Figure 54.b** tracks the imaginary permittivity and conductivity at 1 kHz with respect to increasing temperature. As can be seen in figure a, the real permittivity increases with increasing temperature, then peaks at around 20-30 ^{o}C, then decreases as the temperature approaches the melting temperature. The loss however, shows a low temperature dependence until about 20-30 ^{o}C, then increases sharply, making room temperature the optimal operating temperature for these films. Figure b shows how the imaginary permittivity and film conductivity mirror each other with respect to temperature; there is a low temperature dependence from -60 ^{o}C to -30 ^{o}C, followed by a sharp increase in value until around 20 ^{o}C where again the temperature dependence drops for both of these parameters. As will be discussed in further detail in later chapters, based on how the conductivity is defined with relation to the imaginary dielectric response, it should mirror the imaginary permittivity.

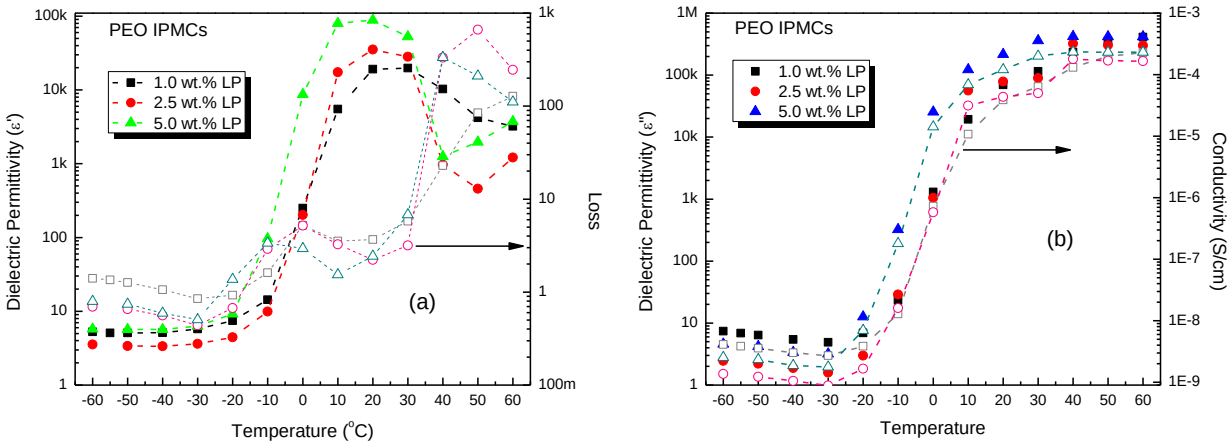

Figure 54: Temperature dependent changes in dielectric response of PEO-LP IPMCs for a) the real permittivity and loss and b) the imaginary permittivity and conductivity

Figure 55 shows how the dielectric loss varies with increasing temperature. From the figure, it can be seen that the loss values with increasing wt.% LP are very similar, indicating that this behavior is independent of salt concentration and directly related to temperature, and the data also displays a near linear behavior when considering the log of the loss versus linear time. The difference between the samples comes when considering the frequency with which the loss peak occurs from sample to sample. For the 1.0 wt.% sample, the loss peak appears to occur at a continually increasing temperature while both the 2.5 wt.% and 5.0 wt.% samples both have an initial increase in loss-peak frequency, then they have decreasing frequency locations of the loss peak.

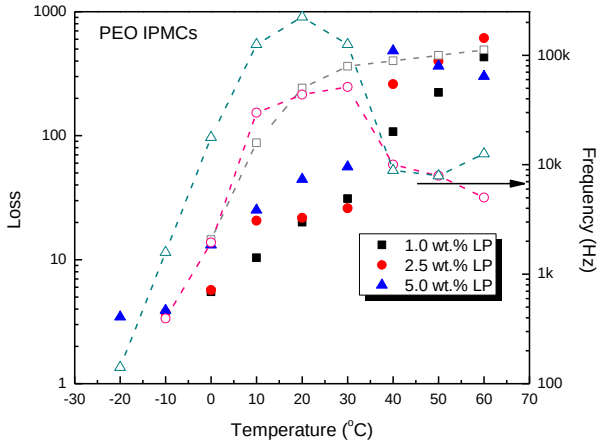

Figure 55: Temperature dependence of loss peak and its frequency location for PEO IPMCs with LP

5.2 In-Depth Frequency and Temperature Dielectric Analysis

This section will further explore the dielectric properties of the PEO-based films presented in this study wherein an analysis of both the frequency and temperature dependence of these films will be conducted in conjunction to one another. An effort will be made to connect the resulting parameters to the processes described previously when these materials are used as IPMCs. Calculations outline in Chapter 2 will be utilized here for determination of parameters such as relaxation time and AC conductivity.

5.2.1 Real and Imaginary Permittivity

Here, an in-depth analysis of the real and imaginary permittivity will be conducted. Of note, is that PEO-NCC composites, containing 5.0 wt.% LP, had a dielectric response similar to that of the PEO-based films with 5.0 wt.% LP, but with no NCC. Therefore, the raw data from those tests will not be presented here. However, the analysis of the effects that NCC has on these films will be included.

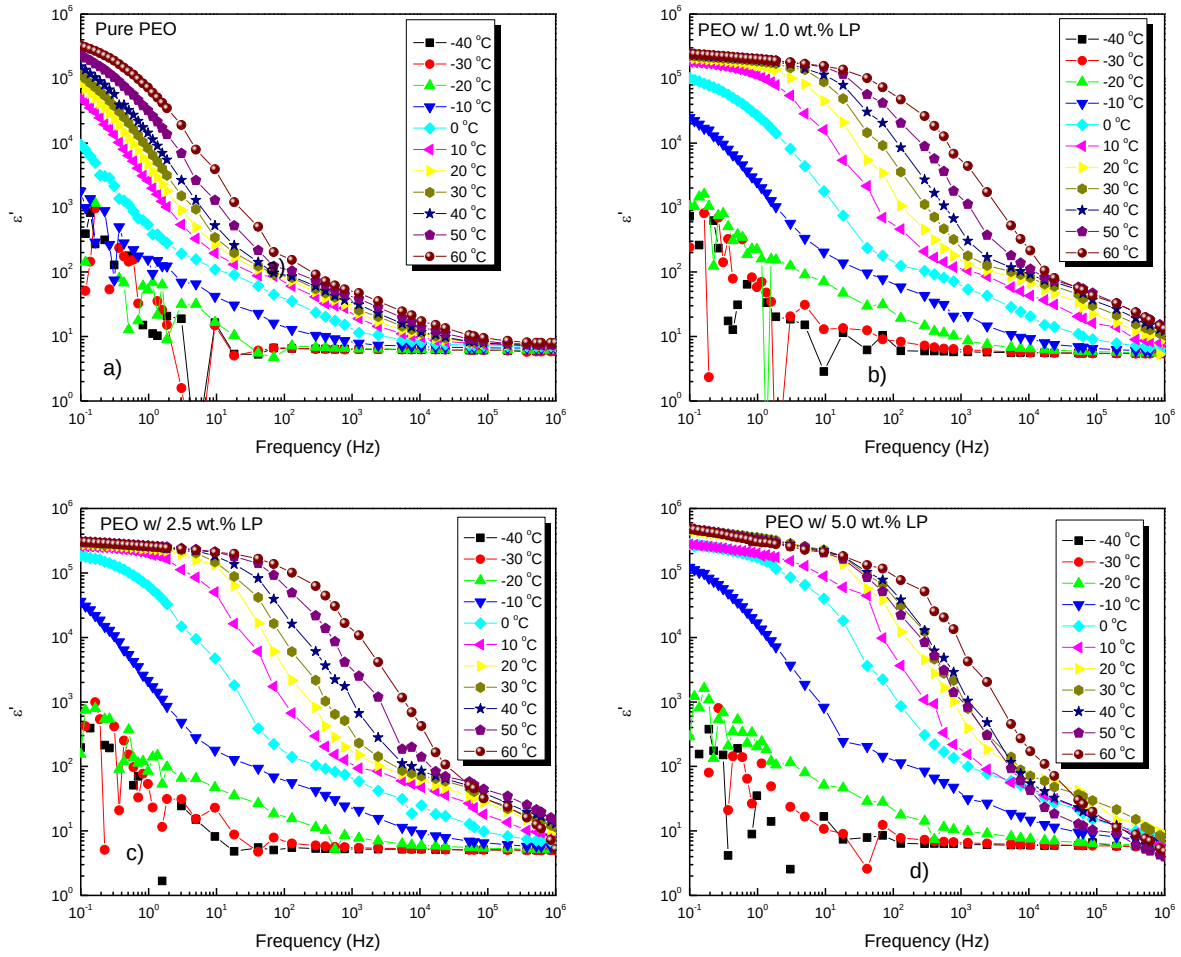

Figure 56: Temperature dependence of the real permittivity response of PEO-based films containing a) 0.0, b) 1.0, c) 2.5, and d) 5.0 wt.% LP

Figure 56.a-d show the temperature-dependence of the real permittivity for PEO-based films with varying wt.% LP. In all cases, there is an initial, large permittivity response, followed by a drop in permittivity spanning approximately four orders of magnitude of increasing AC frequency, and then the permittivity begins to level out at high frequencies. It is clear that even with small additions of LP, that the drop in permittivity behavior is spread across higher frequency ranges, compared to the non-LP film. This is a direct result of the ionic mobility with the matrix influencing the applied electric field. Further inspection reveals that the real permittivity decreases with decreasing temperature across all frequencies and LP concentrations. This is due to the inability of the dipoles within the material to reorient under a rapidly changing AC electric field as the temperature drops and ionic mobility within the polymer matrix being constricted.[4]

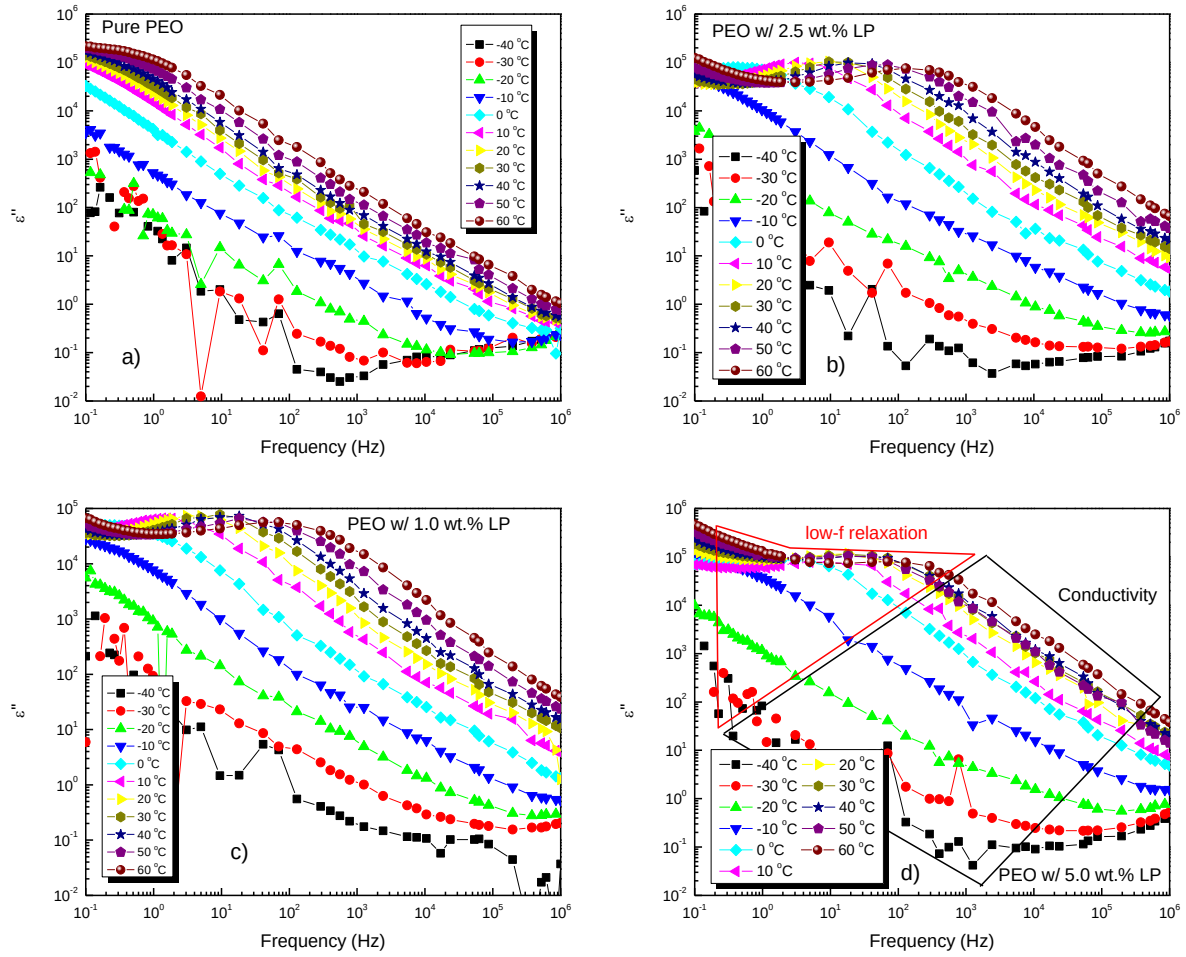

Figure 57: Temperature dependence of the imaginary permittivity response for PEO-based films containing a) 0.0, b) 1.0, c) 2.5, and d) 5.0 wt.% LP

Figure 57.a-d show the temperature dependence of the imaginary permittivity for PEO-based films with varying concentrations of LP. Here it can be seen that there is a low-frequency relaxation process occurring within the samples containing LP, as is represented by the peak. This peak shifts to higher frequencies with increasing temperatures for all polymers. This process corresponds to a structural rearrangement within the polymer matrix.[5] An example of the identification of the low-frequency relaxation and the conductivity dominant regions for these films is shown in **Figure 57.d**. An interpretation of the slopes of the conductive region is given below.

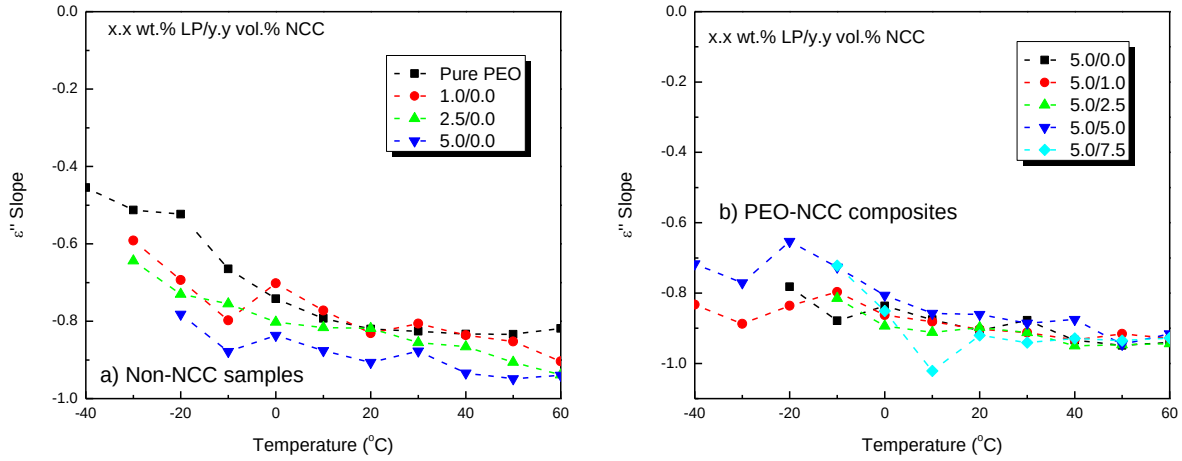

Figure 58: Temperature-dependent slope determination of the imaginary permittivity of PEO-based composites with increasing a) LP and b) NCC concentrations

Figure 58.a-b display the slope of the imaginary permittivity for PEO-based films with and without NCC added to them. It can be seen that the slope of the films increases with increasing temperature. This means that as the temperature increases, the conductive response of the films increases.[6] Also of note, is that the higher wt.% LP films in **Figure 58.a** reach steeper slopes at lower temperatures. This result is intuitive, since there are a larger amount of LP ions within the PEO matrix, which translates to a larger conductive response. For **Figure 58.b**, the change in slope values follow generally the same pattern. By inspection, it can be seen that the higher vol.% NCC composites lag somewhat behind their lower NCC concentration counterparts. This result will be described further, shortly, and is likely due to the larger activation energy required for ionic conduction in these films.

In analyzing the real permittivity from the **Figure 52, Figure 56, Figure 57**, and **Table 16,** the universal model for relaxation in ideal dielectric materials was considered.[7] There are three criteria for satisfying this model of which, two of the criteria can be easily analyzed with respect to the experimental data. The conditions, with respect to the angular frequency ω are listed as **Eqs. (5.1-3)** and are below along with their boundary conditions. The constants n and m concern the sudden hopping transition of a charge or dipole and the flip-flop transitions of an oscillating charge or dipole, respectively.

1. $\varepsilon'(\omega) = \varepsilon"(\omega)\tan(n\pi/2) \propto \omega^{n-1}$, where $0 < n < 1$ $\zeta \gg \omega \gg \omega_p$ (5.1)

2 $\varepsilon(\omega) \propto \left(1 + \frac{i\omega}{\omega_p}\right)^{-1}$, where ω_p is the loss peak frequency $\omega \cong \omega_p$ (5.2)

3 $\varepsilon(0) - \varepsilon'(\omega) \propto \varepsilon"(\omega) \propto \omega^m$, where $0 < m < 1$ $\omega \ll \omega_p$ (5.3)

Condition 1 essentially states that at very high frequencies ($\zeta \cong 10^{12}\ Hz$), the real permitty resolves to some final permittivity and that can be readily described by manipulating and fitting the imaginary permittivity or angular frequency to the data. The agreement of this condition with the experimental results can be seen through the inspection of **Figure 52** or **Figure 56,** where the real permittivity looks to converge at some value greater than 1 at high frequencies.

Further application of this condition was conducted and an example of how Condition 1 applies to the PEO dielectric data is shown in **Figure 59.a**. This figure displays a sample set of real permittivity data at 30 ^{o}C for a PEO sample with 5.0 wt.% LP. The high-frequency convergence of $\varepsilon''\tan(n\pi/2)$ and ω^{n-1} can be seen for frequencies over 1 MHz. The close fitting of this condition, for both proportionalities, was found by using an *n* value of 0.2. The result of this is that for this case, the PEO films satisfy Jonscher's universal law for relaxation in ideal dielectrics. An *n* value of 0 indicates that charges within the system are essentially free, with minimal impediments, while an *n* value of 1 indicates that the charges are immobile and unable to follow changes in the applied electric potential.[7] The low *n* value indicates that the ions traveling within the matrix are relatively free to vibrate in the presence of an AC electric field. Furthermore, through inspection on **Figure 56**, it can be seen that the high-frequency response of the PEO film appears roughly the same for temperatures above -20 ^{o}C, indicating that the *n* value for this material is independent of temperature.

Condition 2 relates the behavior of the complex permittivity (real and imaginary) at around the frequency where the dielectric loss peak occurs. This parameter cannot be easily applied to the current dataset and is therefore not considered in this comparison.

Condition 3 essentially means that as the frequency lowers to near the DC condition [$\varepsilon(0)$] that both the difference between it and the real permittivity approaches zero and likewise, for low frequencies, for an ideal dielectric the imaginary permittivity experience a peak and will also approach zero. Upon inspection of the imaginary permittivity plots (**Figure 52.c**), there is the shoulder of a peak at around 30 Hz and then the permittivity increases again. This is believed to be due to the conductive component for the films. Therefore, with the current measured data, the

imaginary permittivity does not approach zero with decreasing frequency. The universal law describes the behavior of near perfect dielectrics that have an imaginary permittivity peak and a low conductivity response. Therefore, initial examination of the PEO-based composites would conclude that they do not follow this condition due to their conductive properties.

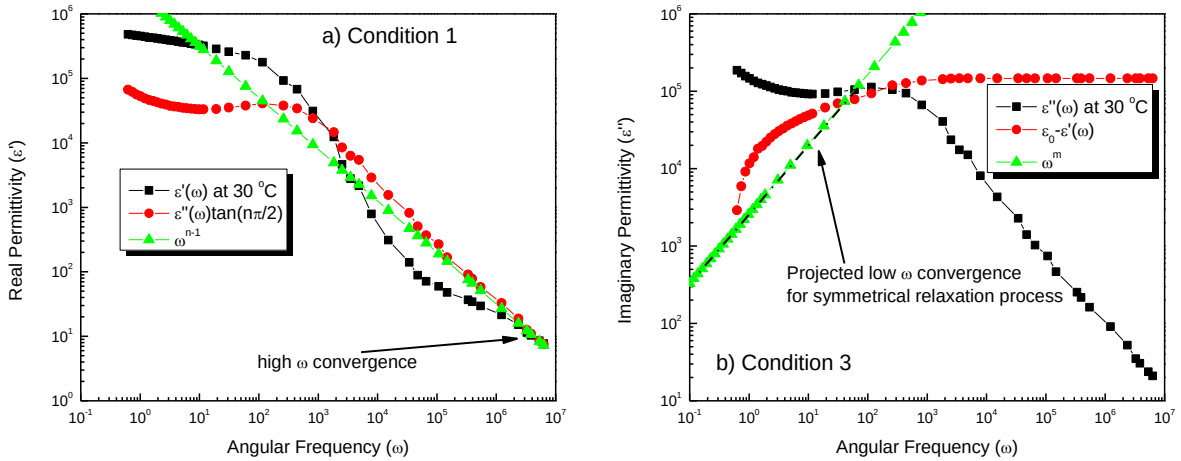

Figure 59: Satisfying of universal dielectric relaxation model for experimental dielectric data from a PEO-based EAP with 5.0 wt.% LP; a) meeting of Condition 1 for high frequencies, b) meeting of Condition 3 for low frequencies

A further examination of the imaginary permittivity, however, yields that the PEO-based films do adhere to the third condition of Jonscher's universal law. **Figure 59.b** displays the imaginary permittivity data at 30 °C for the same PEO film. Here, it is clear that there is not a peak present, again due to the ionic conductivity of the sample. However, the satisfaction of the Jonscher's third condition can be approximated by assuming that the low-frequency side of the imaginary permittivity peak is symmetrical with the high-frequency side (dotted line). By doing this, it was found that the ω^m proportionality, with an *m* value of 0.9, condition can be met (green line). Unfortunately, it was not possible to manipulate the $\varepsilon'(0) - \varepsilon'(\omega)$ proportionality to have it be in line with the imaginary low-frequency projection. This is most likely due to the conductive response of the film. The *m* value corresponds to the 'flip-flop' transitions of dipoles or charge carriers within a dielectric under an applied AC external field.[7] A value of 1 indicates that all of the dipoles within a material alternate at once as the electric field switches polarity, with total correlation, while a value of 0 translates to uncorrelated transitions. With a determined value of 0.9 obtained for the PEO-based films, it can be concluded that the LP ions within the matrix show good correlation with the switching AC field. Additionally, since the ω^m proportionality accurately represents this curve, it can be assumed that the PEO films also satisfy this condition. Furthermore, as described in the analysis of **Figure 58.a**, the slope of the imaginary permittivity

curve gets steeper with increasing temperature. A less steep slope would therefore necessitate a lower *m* value to fit the projected peak data. This indicates that for low temperatures, the 'flip-flop' response of the dipoles within the matrix are less correlated and more randomized than when temperatures are higher. The satisfaction of Condition 3, in conjunction with Condition 1 being met, means that the dielectric response of the PEO-based films can be accurately fitted by Jonscher's universal model of dielectric relaxation.

5.2.2 Dielectric Loss

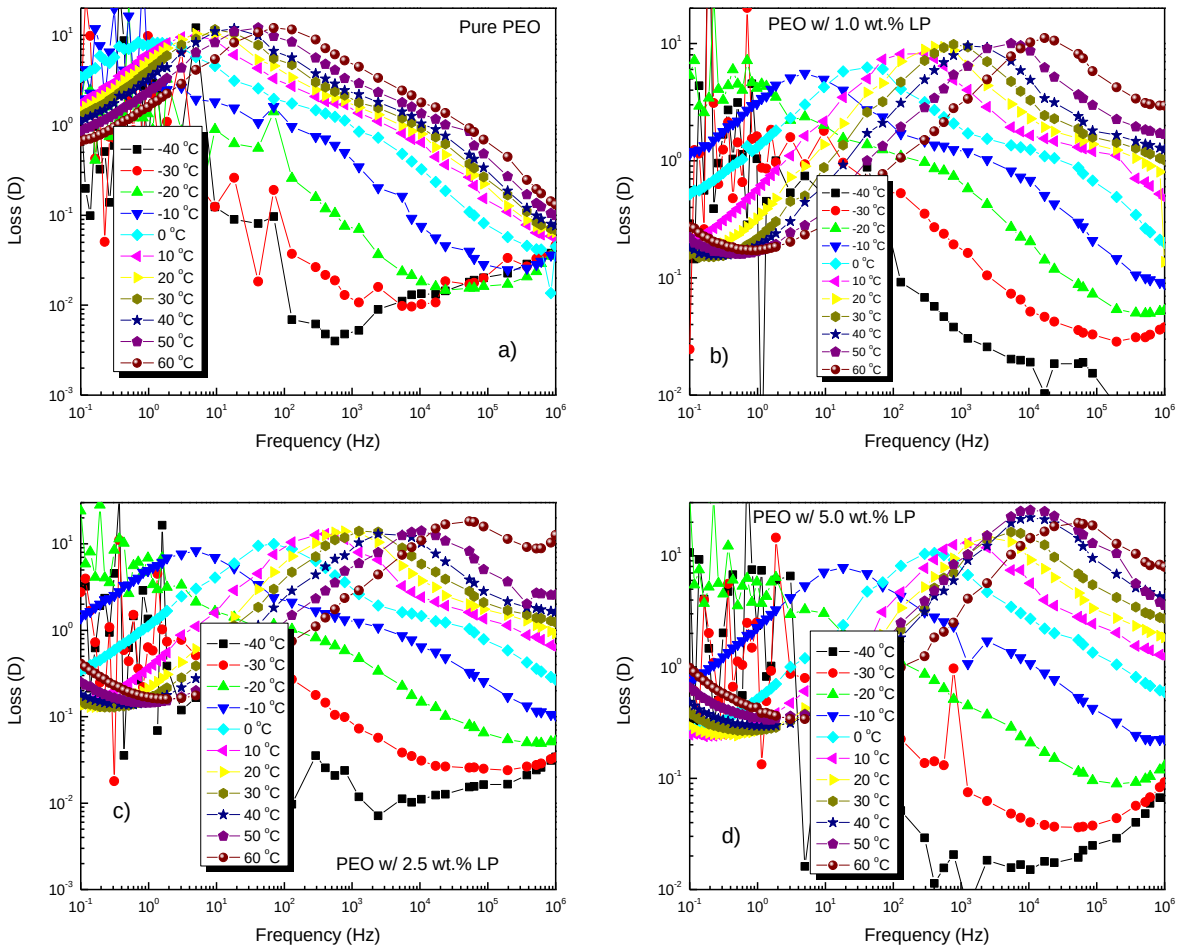

Figure 60: Temperature dependence of dielectric loss peak location in PEO-based films containing a) 0.0, b) 1.0, c) 2.5, and d) 5.0 wt.% LP

Figure 60.a-d show the temperature-dependence of the dielectric loss for PEO-based films with varying wt.% LP. The low frequency relaxation peak of the PEO film without any added LP is assumed to be attributed to any water remaining in the sample after solution casting. There is a sizeable jump in the frequency location of the loss peaks when LP is added to the PEO matrix, resulting in the conclusion that these loss peaks are due to the added LP in the system. It can be

readily seen in all figures, that the frequency location of the loss peak increases with increasing temperature. This is likely related to increased ionic mobility within the films enabling the LP ions to more easily vibrate at higher AC frequencies.

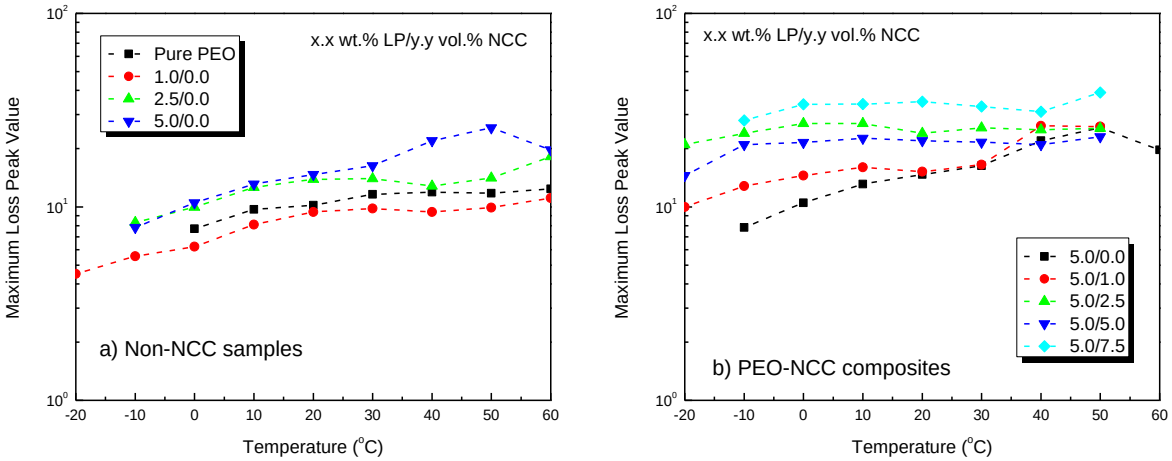

Figure 61: Temperature-dependence of maximum loss peak values for PEO-based composites with increasing a) LP and b) NCC concentrations

Figure 61.a-b show the changes in relaxation peak values for PEO EAPs with varying concentrations of LP and NCC. In **Figure 61.a**, it is found that with increasing LP content, there is an increase in loss peak value. Likewise, in **Figure 61.b**, there is a steady increase in loss peak values with increasing concentrations of NCC. This infers, that the material becomes more lossy or energy dissipative with increasing salt and NCC content.

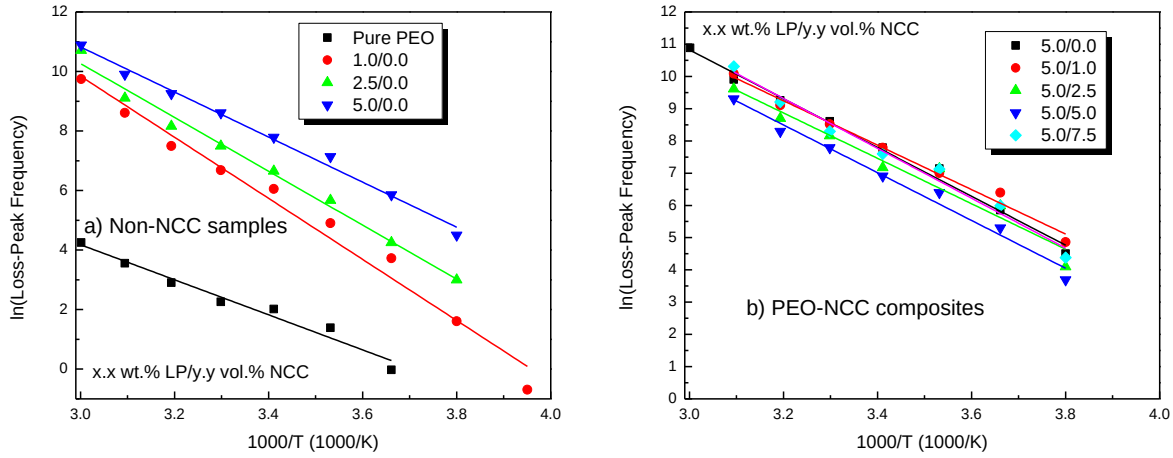

Figure 62: Fitting of temperature-dependent frequency locations of loss peaks for PEO-based films with increasing a) LP and) NCC concentrations

Figure 62.a-b show the frequency location of the loss peaks for PEO-based films with varying concentrations of LP and NCC added to them. The temperature dependence of the peak location can be fitted by utilizing the Arrhenius relationship described by **Eq. (5.4)**.[8, 9]

$$f = f_{max} e^{-Q/k_B T} \tag{5.4}$$

Here, f is the frequency location of the loss peak, f_{max} is the fitted location of the loss peak at very high temperatures, Q is the activation energy for ionic migration, and k_B is the Boltzmann constant ($1.38 \cdot 10^{-23} J/K$). This relationship can be represented in the linear form shown below and is what was used to fit the data in the figure.

$$\ln f = (-Q/k_B)\frac{1}{T} + \ln f_{max} \tag{5.5}$$

The activation energy can be determined by multiplying the fitted Q/k_B value by the Boltzmann constant and then converting the value into electron volts eV ($1\,J = 6.242 \cdot 10^{18}\ eV$). The resulting activation energies are shown in **Table 17**. Their trend is shown in **Figure 63** and is plotted against film LP wt.% and NCC vol.%, respectively. Interestingly, it was found that activation energy decreased linearly with increasing wt.% LP at a rate of 0.0598 eV per wt.% LP. Upon creating PEO-NCC composites, there is an initial drop in activation energy, followed by a linear increase in activation energy with increasing NCC content. This result makes sense, in that the increased rigidity within the sample for high concentrations of NCC would result in decreased ionic mobility, making them require more energy in order to move under an applied field. The rate of increase in activation energy for NCC-based composites was found to be 0.0114 eV per vol.% NCC. Additionally, this initial decrease in activation energy for PEO-NCC composites could be directly linked to the increased performance of PEO-NCC actuators, as shown and described in Chapter 3. Therefore, additional study of these composites could yield an optimized ratio of LP and NCC that would create the maximum EAP performance. Of note, for the pure PEO film, it is assumed that the dielectric loss peak is due to the vibration of water molecules remaining in the polymer matrix after the film was solution cast. As such, the corresponding activation energy is also included in **Table 17** and in **Figure 63**.

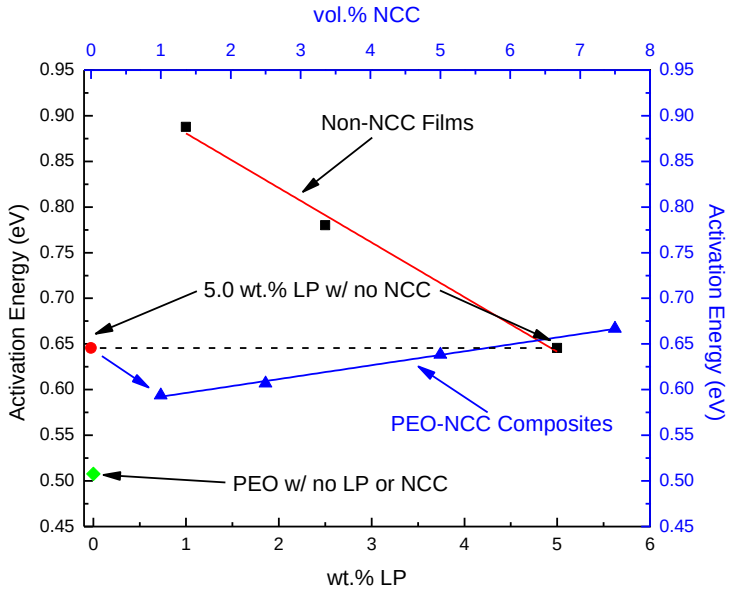

Figure 63: Activation energy trending for PEO-based films with increasing a) LP and b) NCC concentrations

Solving **Eq. (6.2)** for when the fitting crosses the x-axis of **Figure 58.a-b** yields the glass-transition temperature T_g of the films.[10] The values for the PEO-based films tested in this study are shown in **Table 17**. It can be seen that there is a rapid decrease in T_g when LP is added to the films. This is likely due to the softening effect of LP to the PEO matrix, causing the shift to lower temperatures. Upon adding NCC to the PEO matrix, there is a calculated increase in T_g.

Table 17: Activation energy determination for PEO-based films

			Loss Peak			Relaxation Time	
	wt.% LP	vol.% NCC	Q/k_B (kK)	Q (eV)	T_g $(°C)$	Q/k_B (kK)	Q (eV)
PEO	0.0	0.0	5.89	0.508	-3.58	--	--
	1.0	0.0	10.30	0.888	-20.6	8.79	0.758
	2.5	0.0	9.05	0.780	-31.3	8.55	0.736
	5.0	0.0	7.49	0.646	-47.4	8.04	0.693
PEO-NCC	5.0	1.0	6.89	0.594	-53.0	--	--
	5.0	2.5	7.04	0.607	-48.9	--	--
	5.0	5.0	7.41	0.639	-41.3	--	--
	5.0	7.5	7.74	0.667	-46.1	--	--

5.2.3 Cole-Cole Plot Analysis

The real and imaginary dielectric data for PEO-based films with varying concentrations of LP are plotted against each other in the commonly used Cole-Cole plot, as shown in **Figure 64.a-d** (analysis described in Chapter 2). Here, it can be seen, that for neat PEO films, there is relatively

no temperature dependence concerning the ε_∞ and ε_s behavior of the film, and thus there is no variation in the film's relaxation time with changes in temperature. With no ionic charges present within the matrix, this conclusion makes sense. For **Figure 64.b-d**, there is a clear temperature dependence and corresponding lossy tail. Fitted semicircles, as described in Chapter 2, are fitted against all data.

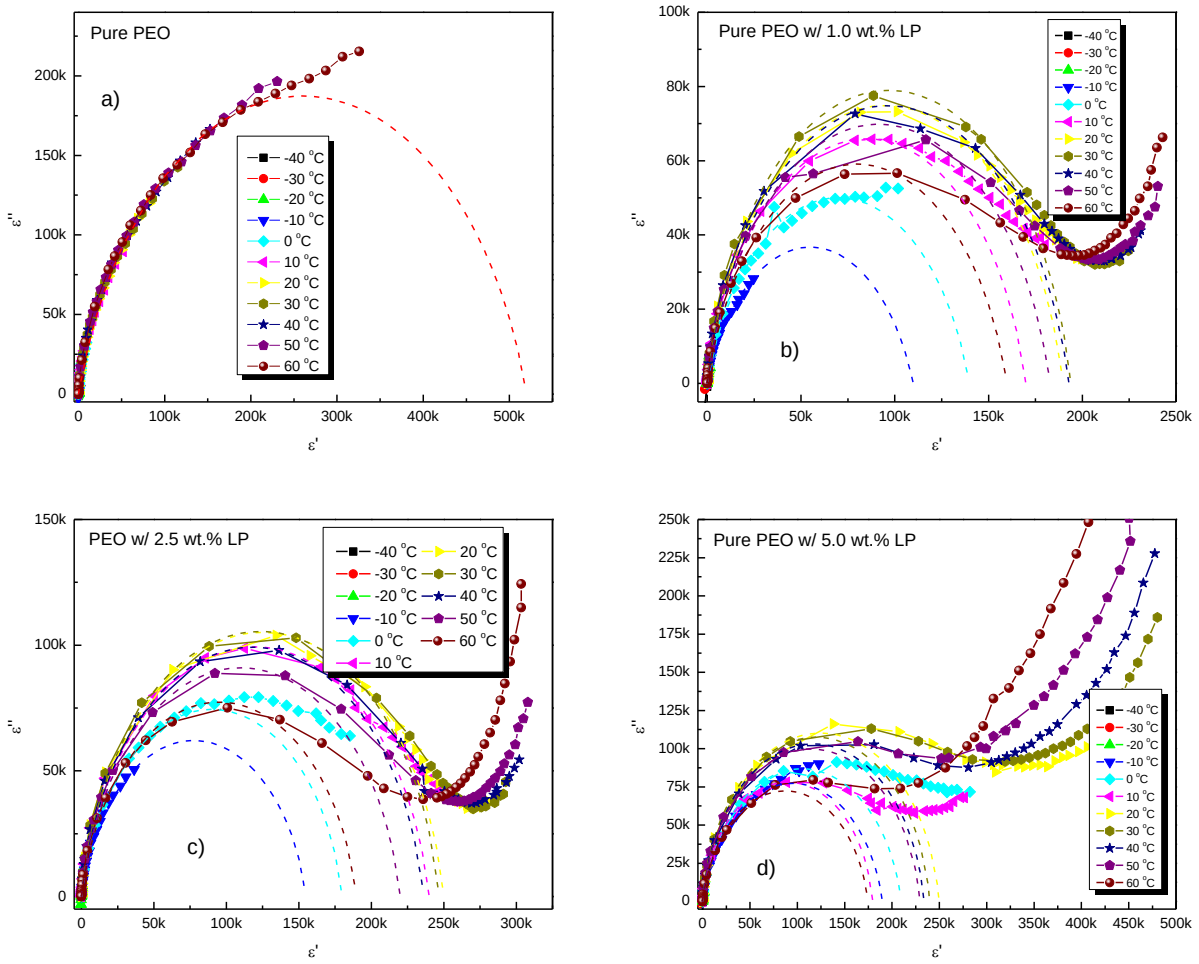

Figure 64: Temperature dependence of the Cole-Cole plots for PEO-based films with a) 0.0, b) 1.0, c) 2.5, and d) 5.0 wt.% LP

The resulting parameters of a Cole-Cole fitting of the Cole-Cole plots shown in **Figure 64.a-d** are illustrated in **Figure 65.a-b**. Here, their temperature dependence can be clearly seen. It was found that the α parameter in the Cole-Cole equation showed an initial increase in all LP concentrations for PEO samples, with all concentrations reaching a maximum α parameter at 30 ^{o}C, and followed by a decreasing α value (**Figure 65.a**). This denotes a possible physical change occurring within the sample. In reviewing the Cole-Cole plots, it can be seen that the semi-circle

like features expand with temperature increasing up to 30 ^{o}C, then contracting with increasing temperatures. The relaxation time for these films can be calculated, as prescribed in Chapter 2. The results for PEO films with varying LP concentrations are shown in **Figure 65.b**. Here, it was found that relaxation time increased with increasing temperature. This is an intuitive conclusion, as increased temperatures result in increased ionic mobility, so they would logically experience a longer time to return to a randomized state if the applied electric field were removed. Further inspection of this figure resulted in fitting it with an Arrhenius relationship, similar to **Eq. (6.2)**, but in this case relaxation time was used as the independent variable. This also yields a measure for calculating activation energy. The results utilizing this method track closely with those found using the changes in loss-peak frequency, as shown in **Table 17**. However, due to fluctuations in relaxation time found at high temperatures for 5.0 wt.% LP samples, the process of utilizing the loss peaks for determining activation energy was deemed the more appropriate analysis method for this EAP material.

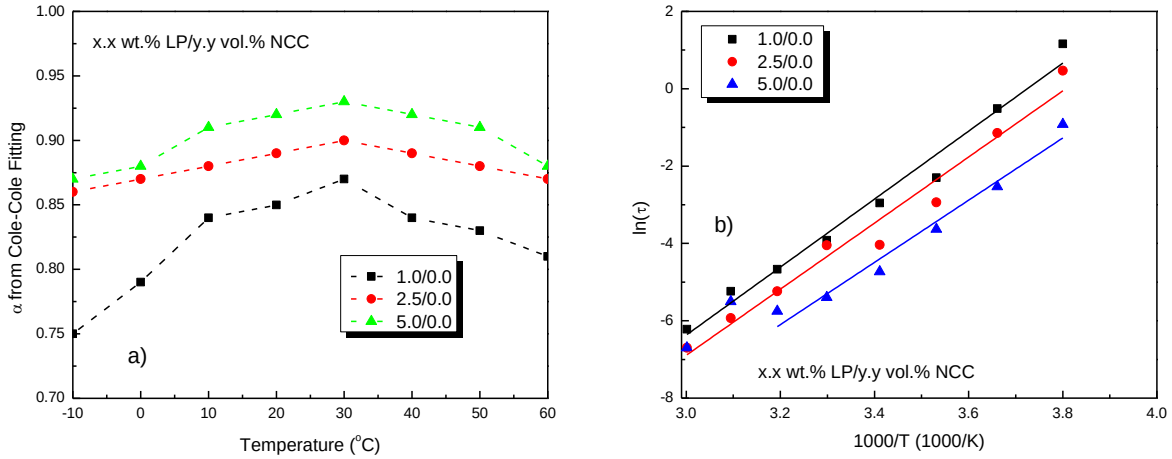

Figure 65: Trending of Cole-Cole fitting parameters for PEO-based films with increasing LP concentration; a) α parameter b) relaxation time fitting

The fitted values for the Cole-Cole relationship are displayed in **Table 18**. Here, it was assumed that the high-frequency dielectric constant was roughly 5.7 for films. This value was taken from the low-temperature permittivity measurements. Low-frequency real permittivities were approximated during the fitting process so as to fit the experimental data as accurately as possible. However, this process was challenging, due to the high-loss tail or very-low frequency data for the films preventing or not being present so as to get a precise semicircle fitting. Due to this approximation process, activation energies shown in **Figure 63.a-b** were again drawn from the loss-peak transitions.

Table 18: Cole-Cole Fitting Parameters

Temp.	ε_s	1.0 wt.%		2.5 wt.%		5.0 wt.%	
		ε_∞ (10^4)	τ (s)	ε_∞ (10^6)	τ (s)	ε_∞ (10^6)	τ (s)
-10	5.7	5.50	3.18	0.790	1.59	0.900	0.398
0	5.7	6.82	0.599	1.00	0.318	1.05	0.0796
10	5.7	8.78	0.0100	1.20	0.0531	0.950	0.0265
20	5.7	10.1	0.0521	1.23	0.0177	1.25	0.00884
30	5.7	9.70	0.0199	1.23	0.0175	1.20	0.00454
40	5.7	9.30	0.00936	1.20	0.00531	1.19	0.00318
50	5.7	9.10	0.00531	1.10	0.00265	1.15	0.00408
60	5.7	8.00	0.00199	0.950	0.00123	0.870	0.00123

5.2.4 Conductivity

Figure 66.a-d show the temperature dependence of the AC conductivity for PEO-based films with varying concentrations of LP. For all samples, there are three well-defined regions that can be identified through visual inspection of these plots which are dependent on both frequency and temperature. For low frequencies, the conductivity increases with increasing frequency and temperature, which follows a power-law fitting. This is followed by a plateaued region of the conductivity, where it is more-or-less independent of frequency, but increases with temperature. This denotes that this region is dominated by the DC conductivity. Finally, it can be just discerned with the lower-temperature tracks, that a high-frequency, power-law region exists. Evaluation of the conductive response can be conducted through use of **Eq. (5.6)**.[11]

$$\sigma(\omega) = \sigma_{DC} + A\omega^k \tag{5.6}$$

Here, σ_{DC} is the DC conductivity, A is a constant, and k is a fractional exponent with a value between zero and one. The *k* parameter is used to better understand the conductive mechanisms within the film.[12] Of note, is that the frequency dependence of this function, with the *k* value, is defined for high-frequency conductivity response, but here, it will be used for the low-frequency power-law behavior, as represented in **Figure 66.a-d**.

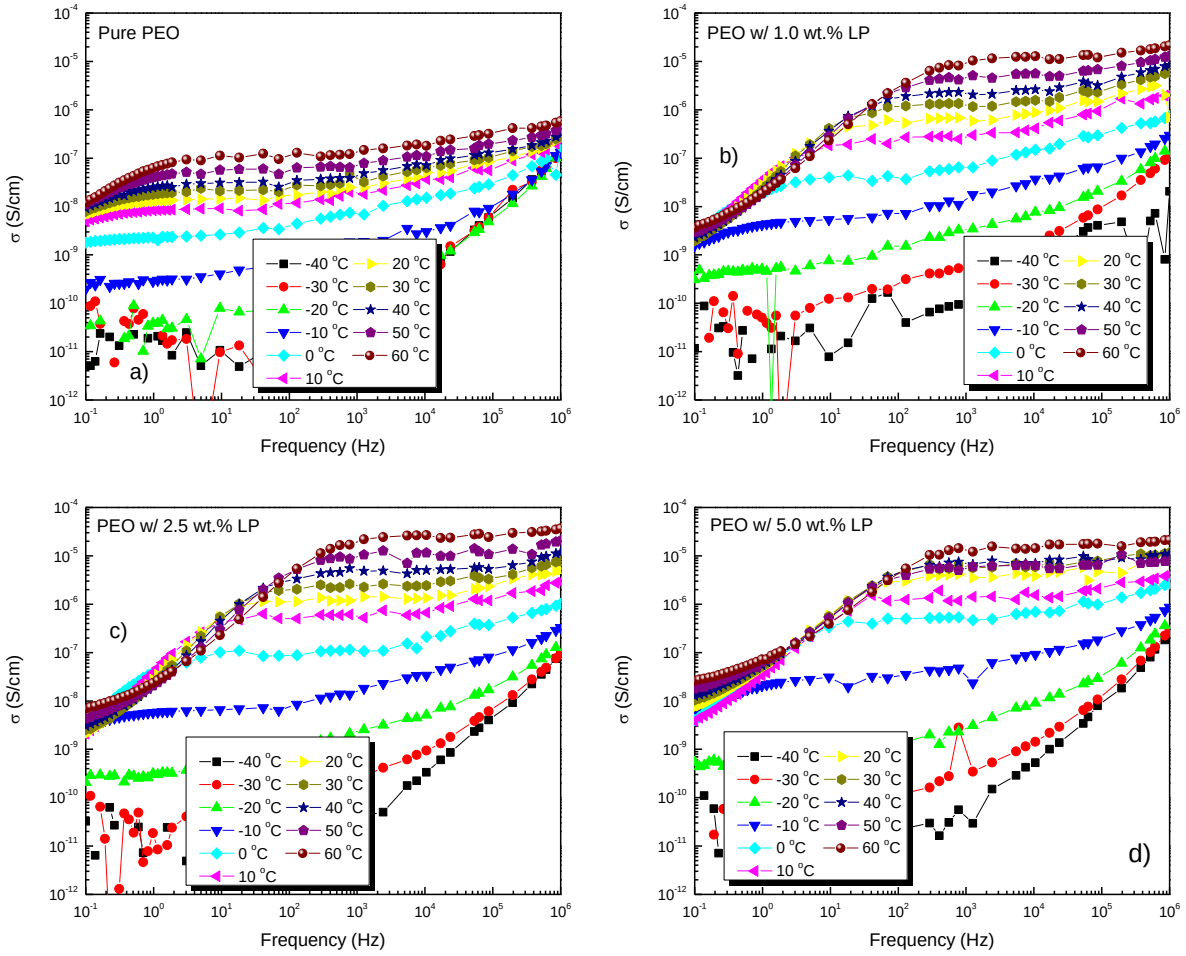

Figure 66: Temperature dependence of the AC conductivity response for PEO-based films with a) 0.0, b) 1.0, c) 2.5, and d) 5.0 wt.% LP

Figure 67.a shows the DC conductivity for PEO-based samples with varying concentrations of LP and NCC. It can be seen that the conductivity increases for all samples with increasing temperature, resulting in an increased ionic mobility within the samples. Of note, is that the 2.5 wt.% samples have a higher high-temperature DC conductivity, but the 5.0 wt.% samples have a higher room-temperature conductivity. **Figure 67.b** shows the power-law fitting, *k* value and how it changes with time and PEO film composition. It is readily apparent that this value is higher than one, contrary to how the fitting parameter is defined. It is important to note that **Eq. (6.3)** is for high-frequency power-law fitting and that this fitting is done for the film's low-frequency conductivity response. Since fitting for this region is not currently defined, the values obtained can at least be relatively compared here. There is a considerable dip when moving from 2.5 wt.% to 5.0 wt.% LP samples. However, comparative values are again reached for 5.0 wt.%

samples when NCC is added, indicating a conductivity contribution, likely due to the freed sulfate ions discussed in Chapter 3.

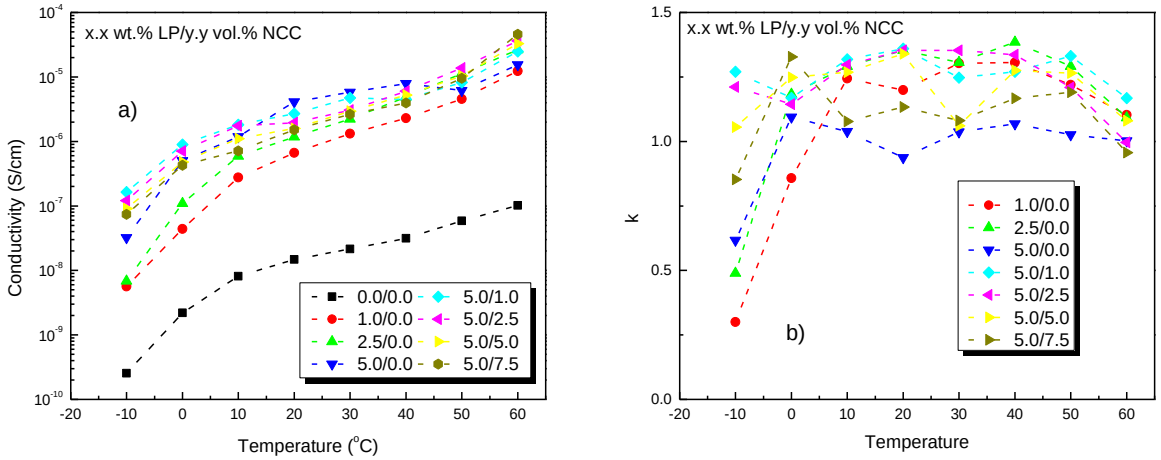

Figure 67: Temperature-dependent parameters for PEO-based films; a) DC conductivity, b) power-law k-value fitting

5.2.5 Universal Dielectric Curve for PEO Films

Comparison of the dielectric data from all of the PEO-based films presented here leads to a striking result; that outside of frequency shifts due to temperature or minor increases or decreases with varying the wt.% LP, all of the dielectric measurements quite similar. Part of this conclusion is intuitvive, being that the polymer system does not change, however, the consistency of the results across the films, including those of the pure PEO matrix, is very interesting. The presented data spans an AC frequency application of 0.1 Hz to 1 MHz. The common nature of response across the films enables the creation of a universal set of dielectric curves across an even broader frequency range. **Figure 68.a-d** display these universal curves and their dielectric response from 0.1 Hz to 10 GHz. These curves were generated based off of the 1.0 wt.% PEO samples. The bulk of the displayed data is from the 40 ^{o}C measurements, spanning from 0.1 Hz to 1 MHz. The high frequency data was copied from the -20 ^{o}C measurements across the 30 Hz to 1 MHz spectrum and shifted to blend with the 40 ^{o}C data. The result is the characteristic dielectric curves of PEO-based films containing LP, as shown in **Figure 68**. These curves provide a way of extending and evaluating the PEO's dielectric behavior even when the experimental equipment reaches its limits.

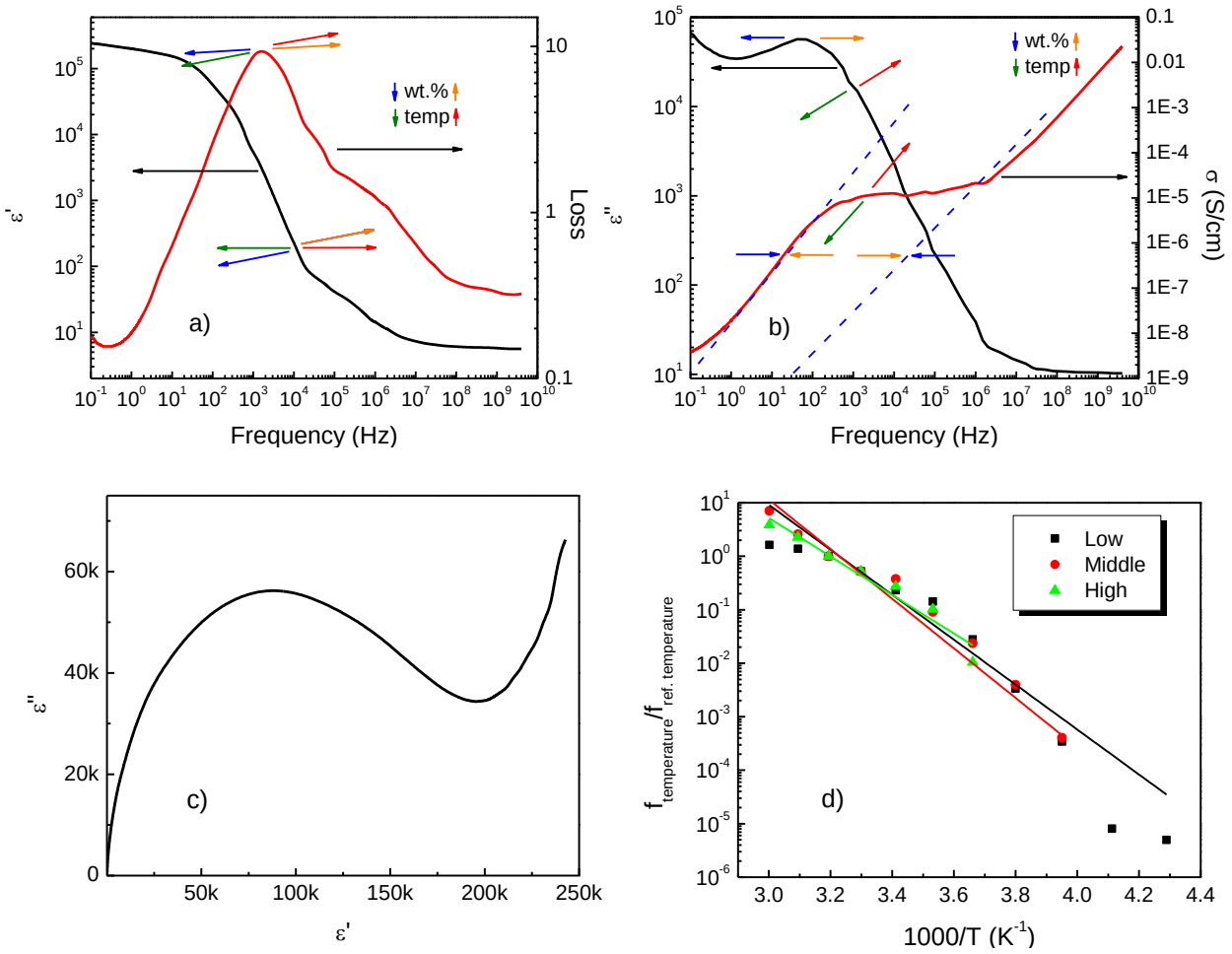

Figure 68: Universal dielectric curves for PEO films with LP ionic salt. Based off of 1.0 wt.% LP PEO samples. Frequency dependent dielectric response includes: a) real permittiivty and loss, b) imaginary permittivity and conductivity, c) Cole-Cole plot, and d) for a arbitrary low, middle, and high real permittivity value, the ratio of the corresponding frequency to a reference frequency

The arrows in **Figure 68** depict how these curves would behave under different conditions. The real permittivity (black curve) and dielectric loss (red curve) are displayed in **Figure 68.a**. Concerning the real permittivity, with increasing temperatures, the response of the films is a general frequency shift of the recorded data from higher to lower frequencies while for changes in wt.% LP variations, the frequency shift is accompanied by an increase in the real permittivity readings with increases in LP. A similar response occurs with the loss. Of note is the loss data from 10^5 Hz to 10^7 Hz. This 'hump' signifies a secondary relaxation response within the film, likely due to the anion and cation found in the LP.

Figure 68.b displays the universal imaginary permittivity and conductivity response of the films. The imaginary permittivity response is comparative real permittivity response in **Figure 68.a**. The conductivity response is a little more interesting. As can be seen, the sample conductivity

increases linearly across the *log log* representation of the data. Then from approximately 300 Hz to 1 MHz there is a flat, frequency independent conductive response. The conductive response then again increases linearly for higher frequencies. The cause of this behavior may be either attributed to an ionic response and a polymer matrix response for the high and low frequency conductivity responses, accompanied by a balanced response between the two at middle frequencies. This 'flat' spot shifts to higher conductivities with increasing temperature and its frequency range expands with increasing salt concentration. This makes for a highly tunable conductive material. This trait lends to PEO's study as an energy storage device, however, since the conductivity only reaches levels of 1E-5 S/cm when the films are heated to 40 oC or above, at this point they are not ready for electronics application which need roughly 1E-3 S/cm for operation.[13]

For **Figure 68.c** displays the characteristic Cole-Cole plot for the PEO-based films. As can be seen, when reading the data as the low-frequency measurements starting at the right and moving left, the high-frequency response displays a semi-circular result commensurate with dielectric materials. However, there is the aforementioned conductivity response for the low-frequency measurements. Increases in wt.% LP act to increase the radius of the circle, while increases in temperature have an initial increase in radius from -20 ^{o}C to 40 ^{o}C where the radius begins to shrink. This shrinkage is likely due to the response of the PEO matrix itself since the temperature is approaching PEO's melting temperature of 65 ^{o}C.

Finally, **Figure 68.d** displays the temperature dependence of the frequency location for the real permittivity data taken at a specific temperature to the frequency location of the same real permittivity value at a reference temperature (40 ^{o}C). The frequency and permittivity data are taken from **Figure 56.b**. **Figure 68.d** is a normalized representation of how far the universal dielectric curve would have to be shifted in order to represent the material response for a given temperature. Plotted as $log\ f_{temp}/f_{ref.\ temp}$ *vs. 1/T* yields the linear representation of the data, as shown. Fitting this data using an exponential relationship similar to that used in section 5.2.2, the activation energy of the films can be generated. After determining the frequency locations for an arbitrarily selected low, middle, and high permittivity value, the activation energy was calculated to be 0.927 eV, 0.833 eV, and 0.714 eV, respectively. Taking the average of these value yields an activation energy for the 1.0 wt.% LP in PEO films of 0.825 eV. This value has a percent difference of 7.37% compared to the activation energy value calculated when tracking the loss peak locations in section

5.2.2. This result verifies the determined activation energy for this particular film and forms a solid baseline for using the universal curve for calculating the activation energy of the other wt.% LP films as well as representing the dielectric response of wt.% LP concentrations within and not reported in this dissertation.

5.3 Time-Dependent Dielectric Analysis and Modeling

As previously described, there is a clear time-dependent dielectric response of the EAP films as they progress through their actuation. The predictable nature of this dielectric response for these actuators, viewed in conjunction with the mechanical actuation, made its analysis the focus for finding a new method for monitoring actuation without optical devices. Electromechanical actuation occurs in these actuators via electrostatic pressure differences, generating volume changes on either side of the EAPs due to the size disparity of the mobile ions. For the LP samples, with its ionic radius being three times as large as the Li^+, it was assumed that the ClO_4^- ion dominated the actuation. This assumption was paralleled with the dielectric response, with the recorded AC dielectric readings being a combination of the responses from the Li^+ and ClO_4^- ions. By further inspection of **Figure 16.a**, there can be seen a definitive high and low frequency response from the film and, as can be inferred from the figure, as time goes on, the high frequency portion of the figure begins to extend and dominate response. It was assumed that this portion governs the dielectric response during EAP actuation, so the attention was centered here. **Figure 16.b** suggests that there are two relaxation processes occurring, with these individual responses becoming more evident with increased time, as shown by the disassociation of the primary relaxation peak into two, more broadened peaks.

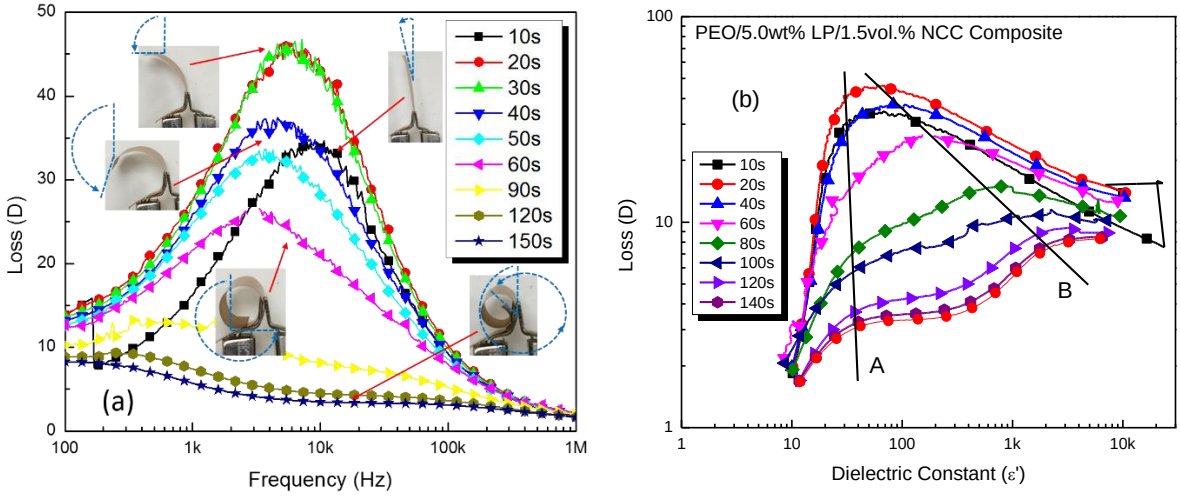

Figure 69: a) Loss vs. frequency and b) the complex plane plot for PEO-NCC composites with 5.0 wt.% LP and 1.5 vol.% NCC

Unfortunately, this time-dependent response for the dielectric data can be difficult to interpret with regards to clearly separating the relaxation responses. Tracking the relaxation processes found in the loss data serves as a way to do so. **Figure 69.a** again displays the loss versus frequency to show the time dependence of how this particular dielectric parameter changes with respect to time as the film performs its electromechanical actuation. The insets show the film performance for a given dielectric reading. The 1.5 vol.%, 5.0 wt.% LP film was chosen due to it generating the largest actuation performance of the PEO IPMCs. Again, to more readily visualize the multiple relaxation processes, plotting a complex plane plot, which is the dielectric loss *D* versus the real dielectric constant (**Figure 69.b)**, accentuates the two relaxation processes. A clear dissociation of the peaks becomes evident along with the connection between the peaks, as time progresses. The processes were labeled as *A* and *B* in the figure and their dielectric progression can be connected through the various readings, as denoted by the straight black lines in the figure.

Through inspection it was determined that the peak locations between successive measured time intervals change as a function of time and could be connected, as shown by the straight lines in **Figure 69.b**. These were labeled *A* and *B* for the low and high frequency responses, respectively, since it was not possible to discern which relaxation response was attributed Li^+ or $ClO4^-$ ions. The high-frequency response (*A*) is stable and its location is almost time-independent, with respect to the real dielectric constant, compared to the low-frequency (*B*) response. The location of these points and their progression with time is important for splitting the data into the responses associated with the high and low frequency regimes. The straight lines indicate that the relaxation peaks can be traced from the final data set to the beginning of the experiment, thus contributing the fact that there are two compiled relaxation responses. The trace of the frequency locations for these peaks can be applied to the dielectric response and it is possible to see how the two ionic responses contribute to the overall dielectric readings.

As an aside, the dielectric analysis was confined to the 5.0 wt.% LP PEO-based samples. Efforts for conducting the same analysis on the 1.0 wt.% LP and 2.5 wt.% LP samples were not possible due to the relaxation peaks of the lower wt.% samples trending towards frequencies falling to frequencies below the range used for the experiment. In addition, the loss peaks did not readily dissociate into the two independent relaxation processes as with the 5.0 wt.% LP samples. Therefore, this dielectric analysis is confined to the 5.0 wt.% LP samples. **Figure 70.a-e** show the complex plane plots of the composites tested where the two relaxation processes were identified.

The films for each composite figure contained 5.0 wt.% LP and concentrations of sulfuric-acid based NCC of 0.0, 1.0, 2.5, and 7.5 vol.% NCC. As can been seen from the figures, each set of dielectric sweeps contains relaxation responses that dissociate into two separate peaks.

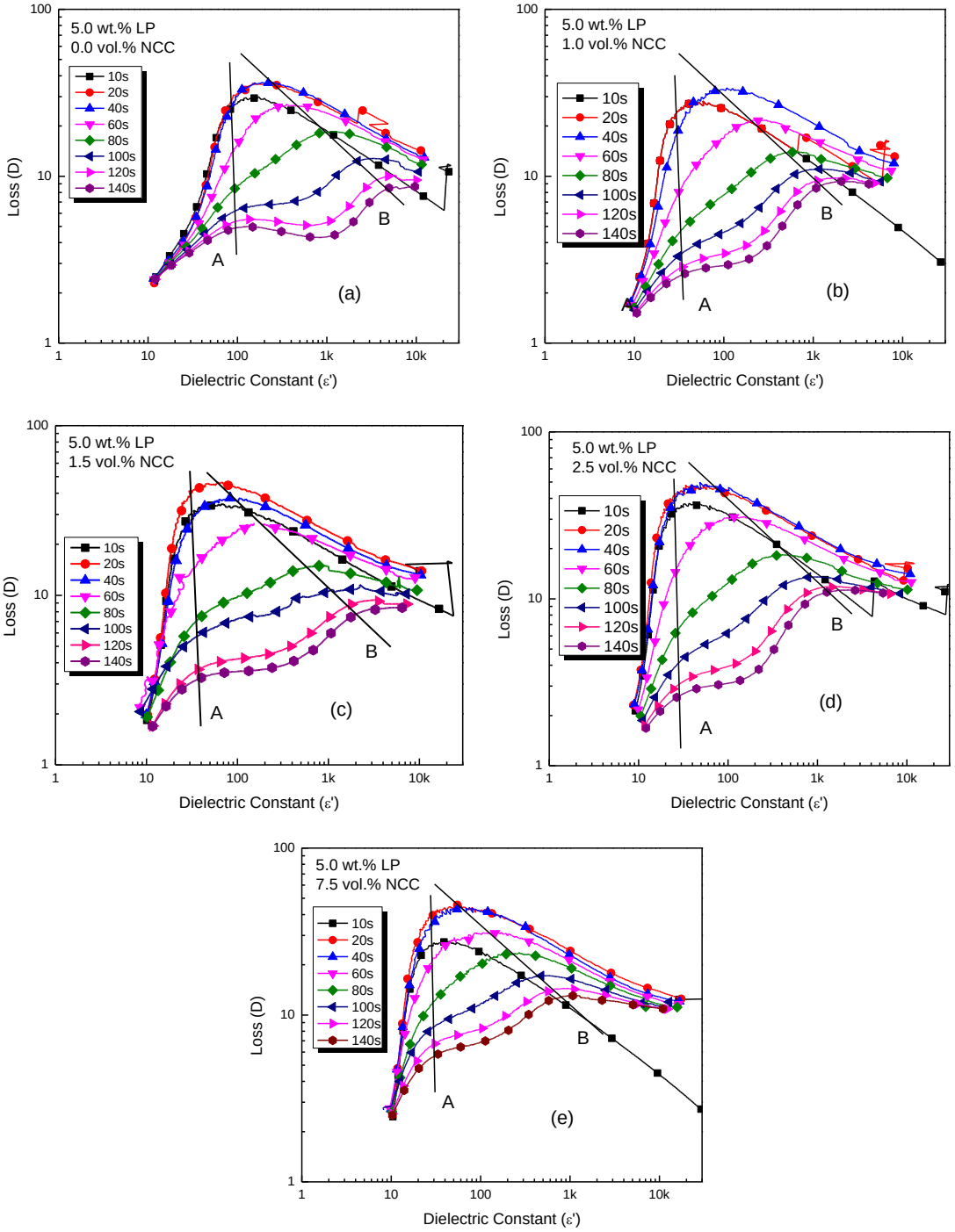

Figure 70: Complex plane plots for PEO-NCC composites with a) 0.0, b) 1.0, c) 1.5, d) 2.5, and d) 7.5 vol.% NCC

5.3.1 Application of the Cole-Cole Model

To analyze the time-dependent dielectric processes of the PEO-based composites the well-studied Cole-Cole model was used. This model was created to measure the dielectric response of a system of non-interacting dipoles subjected to an AC electric field.[14, 15] In this application, the Li^+ and ClO_4^- ions are substituted as the non-interacting dipoles. The equation for the model is:

$$\varepsilon^*(\omega) = \varepsilon_\infty + \frac{\varepsilon_0 - \varepsilon_\infty}{1 + (i\omega\tau_0)^{1-\alpha}} \tag{5.7}$$

where, $\varepsilon(\omega)^*$ is the frequency-dependent complex permittivity, ε_∞ and ε_0 are the high and low-frequency permittivities, respectively, α is representative of the width of the relaxation peak, ω is the angular frequency, and τ_0 is the relaxation time (the time it takes the ions to reach a randomly oriented position once the applied electric field is removed). The complex permittivity can be split into its real and imaginary components with **Eq. (5.8)** describing the real permittivity, where $n = 1 - \alpha$.

$$\varepsilon' = \varepsilon_\infty + (\varepsilon_0 - \varepsilon_\infty)\frac{\cos(\theta)}{[1 + 2(\omega\tau_0)^n \cos(\pi n/2) + (\omega\tau_0)^{2n}]^{1/2}} \tag{5.8}$$

$$\text{where, } \theta = \tan^{-1}\left\{\frac{(\omega\tau_0)^n \sin(\pi n/2)}{1 + (\omega\tau_0)^n \cos(\pi n/2)}\right\} \tag{5.9}$$

However, this model can only be used for a single relaxation response, and so it was necessary to develop a process for splitting the data between the two ionic responses and focusing on applying the model to the changing, high-frequency response. This was done through using the data obtained from **Figure 16.a**, where the real permittivity value for the relaxation peak location at each time step was recorded. The time-dependent shift of these two relaxation process can be seen in **Figure 71.a-b** where the separate processes are highlighted in green.

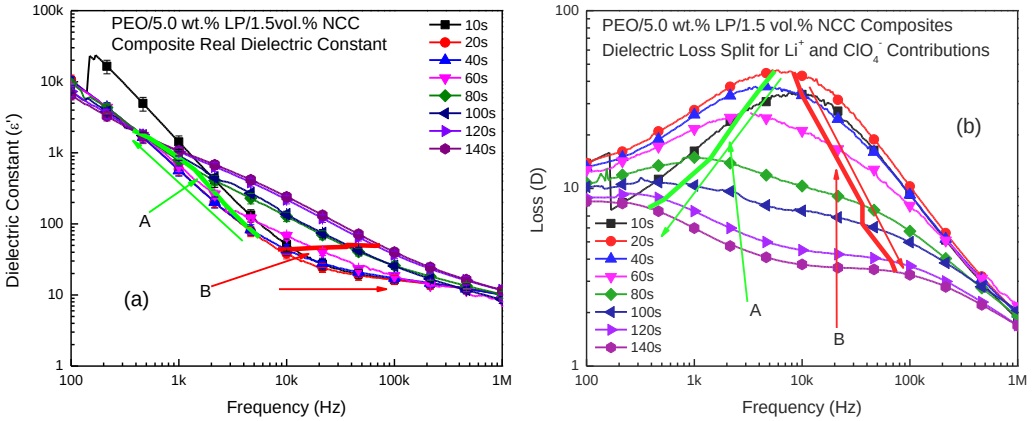

Figure 71: Tracking the time-dependent relaxation processes for the a) real permittivity and b) dielectric loss for PEO-NCC composites with 5.0 wt.% LP and 1.5 vol.% NCC

To split the data so that the high-frequency region could be fitted with the Cole-Cole model, the following assumptions were made:

$$\varepsilon_0 = A - B \tag{5.10}$$

$$\varepsilon_\infty \cong \varepsilon_{\infty_{pure\ PEO}} \tag{5.11}$$

$$f_{cut} = \frac{f_A - f_B}{2} \tag{5.12}$$

where, $f_A - f_B$ are the frequency locations of *A* and *B* for each time step and f_{cut} is the frequency where the low-frequency data is stripped away. These assumptions enabled the isolation of the high-frequency region without encompassing any of the overlap area between the two relaxation processes. As can be seen by **Figure 72**, for samples with 5.0 wt.% LP and 1.5 vol.% NCC, the Cole-Cole model fits the high-frequency real permittivity data with close correlation, validating the assumptions used (the open shapes are the experimental data and the dashed lines are the fitting data).

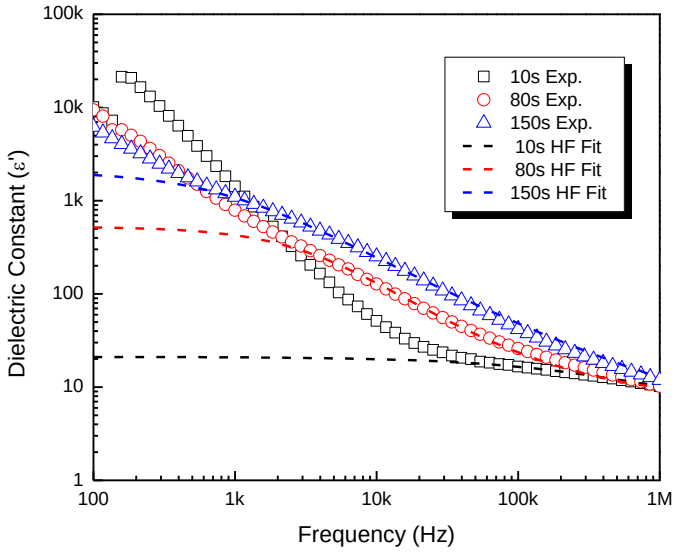

Figure 72: High-frequency (HF) dielectric fitting for a sample of the time-dependent dielectric response of PEO-NCC composites with 5.0 wt.% LP and 1.5 vol.% NCC

Tracking the fitted relaxation time value for each time step returns the behavior shown in **Figure 73**. When plotted with log-scale time, the relaxation time has a similar Arrhenius behavior to that of the strain and can be explained by a similar physical process; the ions can return to randomly disbursed positions relatively quickly in the short time after their initial acceleration, but as they continue to move through the matrix this time steadily increases until the majority of the ions are at the electrode interface wherein, the relaxation time levels out. The fitting form for **Figure 73** is **Eq. (5.14)** (described in the next section), where the relaxation response can be described as a function of the Arrhenius-Based Model utilized for the electromechanical response of the films. This fitting directly links the dielectric processes the observed bending actuation.

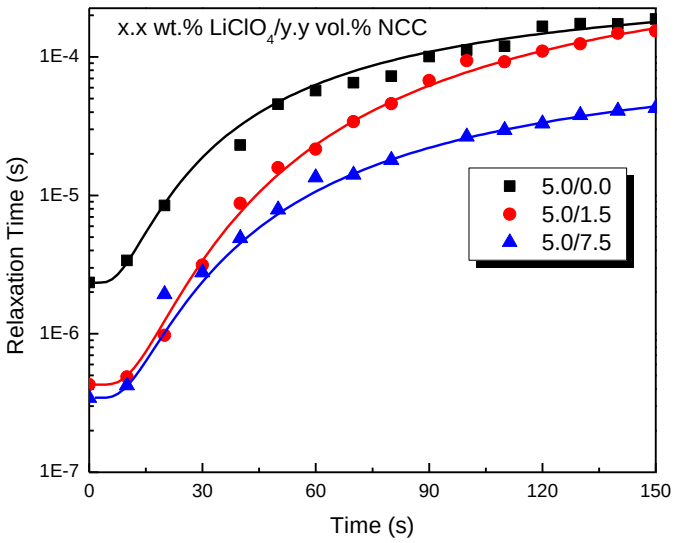

Figure 73: Sample of relaxation time tracking and Dielectric Model fitting for PEO-NCC composites with various NCC concentrations

5.3.2 Dielectric Response Modeling and Linking to Electromechanical Behavior

Plotting strain as a function of relaxation time yields a direct relationship between the two, as shown in **Figure 74**. It was found that this can be described using the below model:

$$s(\tau) = s_{max}\frac{\ln(\tau/\tau_0)}{C} \tag{5.13}$$

where, τ/τ_0 is the ratio of the relaxation time for a given time step to the starting relaxation time and *C* is a constant of integration, likely related to the sample's conductivity, but whose physical components are, as of yet, undetermined. Likewise, **Eq. (5.13)** and **Eq. (3.1)** can be combined to describe the fitting curve of **Figure 73** with the relation:

$$\frac{d\tau}{dt} = \frac{d\tau}{ds}\frac{ds}{dt} \rightarrow \tau(t) = \tau_0 e^{Ce^{-\frac{B}{t}}} \tag{5.14}$$

With this clear relationship between the mechanical strain response and the dielectric relaxation time, it is possible to predict and to monitor the bending actuation of the EAP without the need for external optical equipment, once the strain profile is known. This methodology extends the testing and evaluation process for these actuations to real-world applications where device actuation can be monitored through analyzing dielectric measurements. As mentioned earlier, EAP films with various ionic salt and NCC concentrations have been synthesized; currently, only PEO-based films with 5.0 wt.% LP have been found to exhibit the separation of dielectric relaxations, as identified in this chapter. Further research into this phenomenon with other polymer films may prove this to be a more universal model. As of now, it acts as a starting point for an exciting area of IPMC EAP researcher and one that can lead to many interesting applications.

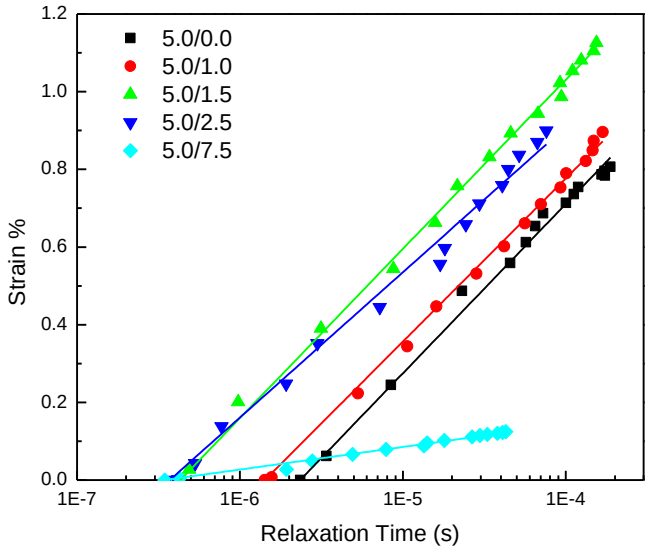

Figure 74: Strain % as a function of relaxation time for PEO-NCC composites with various concentrations of NCC

Table 19 showcases the relaxation times and fitting parameters generated from this dielectric study. The fitted parameters include the Arrhenius-Based Model's maximum mechanical strain s_{max} and the time constant *B*. In addition are the linked Dielectric Model parameters, which are the relaxation time τ_0, and integration constant *C*. Surprisingly enough, both of these complex nonlinear behaviors can be linked and described utilizing only these four parameters; making for a very compact and easy to use set of models for IPMC performance. As was shown in Chapter 3, the electromechanical model was able to be fitted against multiple sets of actuation data for samples created in this study, as well as those published from other researchers. The direct fitting ability of the Arrhenius-Based Model to that data suggests that the Dielectric Model presented in this chapter should have a similar applicability. Through inspection of the table, it can be seen that the relaxation time decreases with increasing vol.% NCC while the integration constant peaks at 2.5 vol.% NCC then drops with the 7.5 vol.% NCC. This peak behavior can also be seen with the maximum strain where maximum strain occurs in the range of 1.5-2.5 vol.% NCC, then dips dramatically when the vol.% increases to 7.5 vol.%.

Table 19: Electromechanical and dielectric fitting parameters

wt.% LP	vol.% NCC	s_{max} (%)	B (s)	τ_0 (s)	C
5.0	0.0	0.97	27.5	2.34E-6	5.92
5.0	1.0	0.91	52.2	1.42E-6	6.90
5.0	1.5	1.47	50.0	4.30E-7	7.78
5.0	2.5	1.10	67.4	3.71E-7	8.88
5.0	7.5	0.11	34.6	3.44E-7	5.94

5.4 Additional Thoughts: Conductivity's Influence on Real Permittivity

The equations describing and defining the dielectric properties of materials have been widely accepted, studied, and utilized. Dielectric materials are described as those that are electrical insulators which have the ability to be polarized under an applied electric field.[16] This polarization is due to the formation of an electronic dipole arising from the distortion and displacement of an electron cloud surrounding its positively charged nucleus in the direction of an external electric field. The ease with which these dipoles can be formed and manipulated generates varying levels of energy storage capacity, depending on the dielectric medium under investigation. Dielectric materials and are used for a wide variety of applications, such as capacitors, microwave communications, filters, and antennas.[17] Under an applied DC electric field, a materials' permittivity (or dielectric constant) can be calculated by solving **Eq. (1.1)** for ε_r or relative permittivity. For a given material, there are generally three kinds of electric dipoles, wherein one side is negatively charged and the other is positively charged.[18] They can either be polar molecules that are oriented in such a way that there is an imbalance of charge. Water is a polar molecule where the covalent bonding between the oxygen and hydrogen atoms results in the two hydrogen atoms being grouped on one side of the molecule, creating a net positive charge, while the oxygen atom has a net negative charge on the other side. Cations and anions have inherently opposite charges and under an electric field, they will attempt to migrate to their attracting electrode. Dipoles can also be formed from materials that have filled electron shells. The negative charge of the electron cloud surrounding the positive nucleus shifts with respect to the applied field faster than the nucleus can creating a separation of positive and negative charges between the two. Each of these types of electric dipoles will try to orient themselves in the direction of the applied electric field.

A material's permittivity indicates an intrinsic measure of a material's susceptibility to electronic polarization with how it affects and is affected by an applied external electric field.[16] Under an applied AC electric field, ε_r becomes a complex quantity where its behavior can be expressed by a real and imaginary part, as shown in **Eq. (6.9)**. The result is that when the AC field is applied to the dielectric material, the dipoles within the structure rotate and orient themselves to the polarity of the field. When the polarity of the electric field switches, the dipole then rotates again to maintain alignment with the field. This rotation requires energy, which is lost to heat due to friction and to the acceleration and deceleration of the dipoles as they rotate. Losses are incurred

with respect to the level with which the rotating dipole is out of phase with the AC field. The larger the losses, the larger the imaginary portion of the dielectric constant, which increases with increasing frequency. The applied electric field can be described by $E = E_0 e^{i\omega t}$, where ω is the angular frequency of the field that the dielectric material oscillates with respect to. As such, the real portion can still be calculated using **Eq. (1.1)**, while the imaginary portion of the dielectric constant is defined, through manipulations of the time-dependent Maxwell's equations,[18] as shown in **Eq. (5.16)**, where, σ is the conductivity and $\omega = 2\pi f$ is again the angular frequency and is directly proportional to the frequency *f* of the applied AC field. This definition of conductivity is independent of the real portion of the permittivity. Therefore, if the conductivity of a material were controlled through the addition of charge carriers (in this case, concentrations of LP for the PEO films and concentrations of CoPH for the PVDF films), then increases in conductivity should only effect the imaginary permittivity and not the real permittivity. Also, through measuring the dielectric loss *D* (the ratio between the imaginary and real permittivity, **Eq. (5.17)**, which represents the level of heat lost by the material due to the dipole oscillations), it is possible to calculate the imaginary permittivity and thus the material's frequency-dependent conductivity.

$$\varepsilon_r^* = \varepsilon' - j\varepsilon'' \tag{5.15}$$

$$\varepsilon'' = \frac{\sigma}{\omega \varepsilon_0} \tag{5.16}$$

$$D = \tan\delta = \frac{\varepsilon''}{\varepsilon'} = \frac{\sigma}{\omega \varepsilon_0 \varepsilon'} \rightarrow \sigma(\omega) = \omega \varepsilon_0 \varepsilon' \tan\delta \tag{5.17}$$

In this report, EAPs were synthesized with various concentrations of ionic salts added to the polymer matrix. In doing this, it was found that there were upwards of 3-4 orders of magnitude increase in the low-frequency values found for the real permittivity compared to those measured from the polymer matrix without any ionic salts added. The addition of the ionic salts was found to have a direct influence on both the calculated real and imaginary permittivities and the conductivity for the EAPs, with larger salt concentrations correlating to larger conductivities. This also lent to increased actuation performance due to the larger number of charge carriers transiting through the polymer matrix. With the marked increase in real permittivity as the conductivity increased, the observed results beg the question with whether the two properties are linked in some way that is independent of calculations based off of contributions from the imaginary permittivity.

To date, there are little to no publications breaching this topic, which could be due in part to the pervasiveness of the accepted models, arising from **Eqs. (5.15-17)**. However, as will be

analyzed during the data-gathering process of this initiative, there is evidence of some relationship between the real portion of a material's permittivity and its conductivity, which is independent of the imaginary permittivity. As such, the final objective in this report seeks to find, and possibly link, evidence of an underlying relationship between the real dielectric permittivity and the material's conductivity. This research is being conducted as a fundamental study of the dielectric properties of materials independent of with whether or not the results can be linked to the study of EAPs. If a relationship can be established, then this process can open up new areas of dielectric research and provide a better understanding the laws governing a material's dielectric response. This report aims to breach the topic possibly reinvestigating and reevaluating the structure of the Maxwell equations and the process through which the conductivity is defined for dielectric materials.

As stated, traditional analysis of a material's conductivity, as it is connected to the material's permittivity, stems from the imaginary portion of the complex dielectric constant (as shown in **Eqs. (5.15-17)**). The derivation of those equations through the manipulation of the time-harmonic Maxwell equations does not account for any dependence of the real portion of the dielectric constant and as such, is not annotated in illustrated in the aforementioned equations. A more detailed derivation of the imaginary permittivity from the Maxwell relationships is as follows.[18] The derivation begins with the time-harmonic Maxwell relationship, as shown in **Eq. (5.18)**. Here, *H* is the magnetic field strength, *J* is the electric current density, ω is the angular AC frequency, and *D* is the electronic displacement.

$$\nabla \times \bar{H} = \bar{J} + j\omega\bar{D} \tag{5.18}$$

The current density can be split into two parts where $\bar{J_c}$represents the conduction part of the current density which describes the flow of electrons and $\bar{J_\iota}$represents an excitation current density due to the application of an external electric field. This is represented by **Eq. (5.19)**. $\bar{J_c}$can be further defined by **Eq. (5.20)**, where $\sigma_s$is the conductivity of the material and $\bar{E}$ is the applied electric field. The electric displacement can also be defined in terms of the material's complex permittivity and the applied electric field, as shown in **Eq. (5.21)**.

$$\nabla \times \bar{H} = \bar{J_\iota} + \bar{J_c} + j\omega\bar{D} \tag{5.18}$$

$$\bar{J_c} = \sigma_s\bar{E} \tag{5.19}$$

$$\bar{D} = \varepsilon\bar{E} \tag{5.20}$$

Substituting the current density and dielectric displacement equations, along with the definition of the complex permittivity, $\varepsilon = \varepsilon' - j\varepsilon''$, into **Eq. (5.18)** yields **Eq. (5.21)**, below.

$$\nabla \times \bar{H} = \bar{J}_i + \sigma_s \bar{E} + j\omega\left(\varepsilon' - j\varepsilon''\right)\bar{E} \tag{5.21}$$

Grouping the imaginary and real portions of **Eq. (5.21)** yields **Eq. (5.22)**,

$$\nabla \times \bar{H} = \bar{J}_i + (\sigma_s + \omega\varepsilon'')\bar{E} + j\omega\varepsilon'\bar{E} \tag{5.22}$$

The effective conductivity can be defined as **Eq. (5.23)** and thus, rearranging the terms yields the material's conductivity solely defined in terms of the imaginary permittivity, as seen in both **Eq. (5.24)** (where, $\sigma = \sigma_e - \sigma_s$) and **Eq. (5.15)**. As will be seen from the experimental data, this definition for conductivity may be due to be updated.

$$\sigma_e = \sigma_s + \omega\varepsilon'' \tag{5.23}$$

$$\varepsilon'' = \frac{\sigma_e - \sigma_s}{\omega} \tag{5.24}$$

From the dielectric analysis of PEO-NCC composites and PVDF films, an investigation into a possible direct connection between the real permittivity and conductivity has been undertaken. Though concrete connections have yet to be made on this topic, the work presented here represents a fundamental analysis on the topic that, if anything, can act as a springboard to future scientists embarking on a similar journey. **Figure 75** and **Figure 76** show the real permittivity, imaginary permittivity, dielectric loss, and conductivity for PEO-NCC composites and PVDF films, respectively. **Figure 75** displays the results for PEO-NCC composites with increasing LP salt wt. %. It is clearly evident that with increasing salt concentration, there is a 2-3 orders of magnitude increase in the real and imaginary permittivities and the conductivity over the polymer matrix without any salt or filler. There is also a loss peak that emerges with increasing salt concentration, indicating that the response of the salt ions dominates over the matrix material. The presence of the ionic salt is responsible for the increased response of the materials' properties and is the driving force behind the increase in sample conductivity. It is clear that there is a definite link between the conductivity and the different permittivities that is to be explored in this analysis.

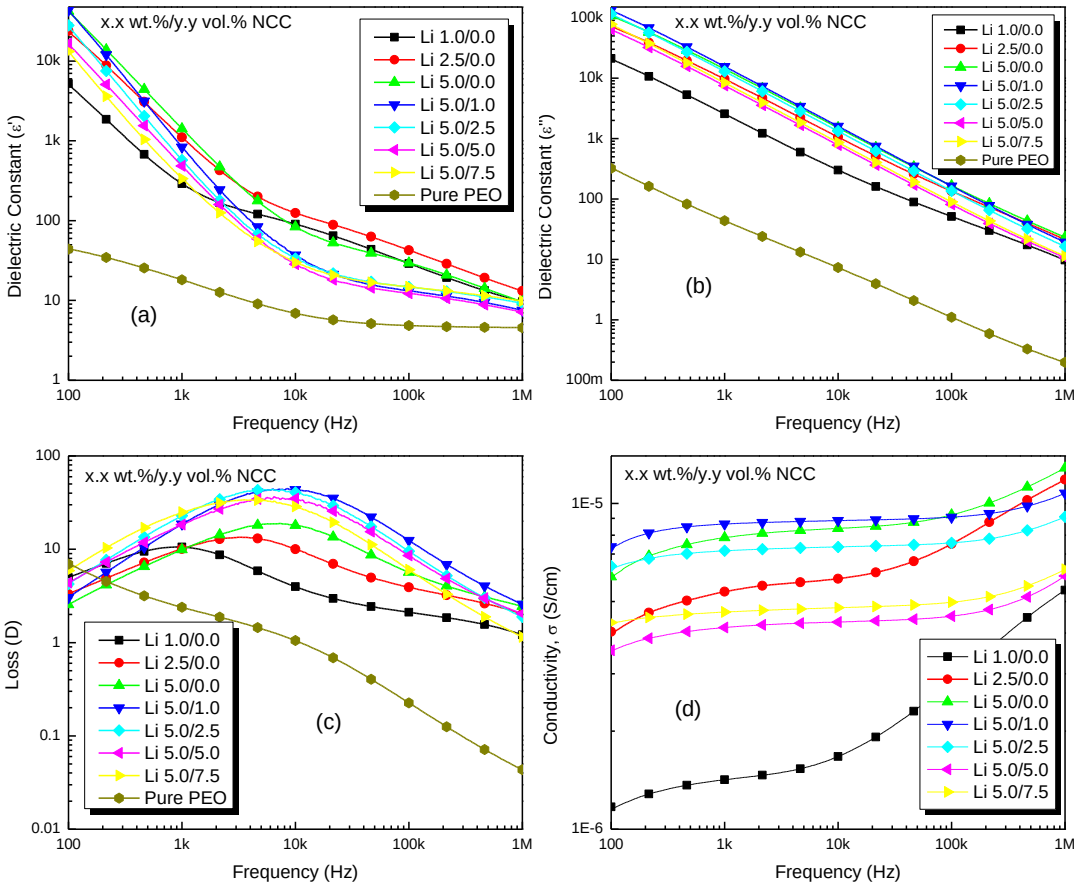

Figure 75: Dielectric response of PEO-NCC composites with various concentrations of LP

Figure 76 shows the results for PVDF films with increasing CoPH salt wt.%. It is also clearly evident that the salt concentration has a large effect on the dielectric properties and the conductivity, with a much larger transformation with increasing salt concentration. This again lends credence to a link between the conductivity and the real permittivity. It is also more apparent as to the transformation that takes place from a more matrix dominated response, to the salt dominated response, with upwards of 6 orders of magnitude increase for the permittivity and 5 orders of magnitude for the conductivity. This top-view of how the real permittivity can be affected by changes in conductivity provides evidence that these two properties are explicitly related and that new models should be developed which incorporate the conductivity into the definition of the real permittivity and not to have it be solely related to the imaginary permittivity.

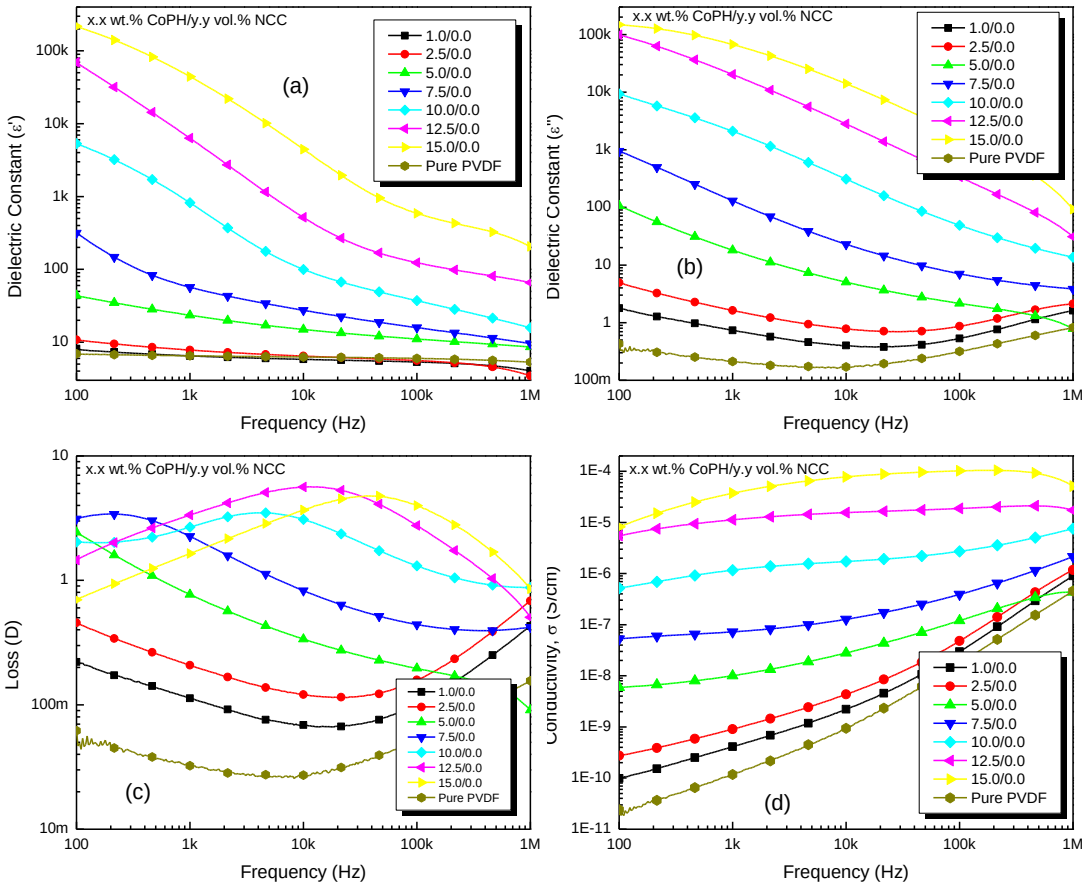

Figure 76: Dielectric response of PVDF films with varying concentrations of CoPH

Table 20 displays the real permittivity, imaginary permittivity, loss, and conductivity at 1 kHz for both the PEO and PVDF data presented in this section. It can readily be seen that increasing the number of charge carriers, which increases the material's conductivity, also has a strong influence on the film's real permittivity where it also increases as the amount of ionic salt is increased. Of note with the PEO films is that when the NCC is added, there is an initial increase in conductivity, around 1.0 vol.%, then a decrease as NCC concentration increases further. This signifies a decreased mobility for the charge carriers in the film and also mirrors the observation of larger actuation performance for low-NCC content samples compared to that of films without any NCC. The correlation between increases in ionic salt (i.e., sample conductivity) and real permittivity confirms that there is a link between the two parameters. Henceforth, the need for further study into this area.

Table 20: Permittivity and conductivity data for PEO and PVDF-based composites at 1 kHz

Polymer	wt.% LP	vol.% NCC	ε'	D	ε''	σ (S/cm)
PEO	0.0	0.0	18.3	2.39	43.7	2.43E-8
	1.0	0.0	290	10.5	2550	1.42E-6
	2.5	0.0	1110	10.1	9640	5.36E-6
	5.0	0.0	1420	9.92	14100	7.86E-6
	5.0	1.0	835	18.6	15600	8.65E-6
	5.0	2.5	574	22.9	12900	7.16E-6
	5.0	5.0	485	18.3	7480	4.16E-6
	5.0	7.5	336	24.9	8350	4.64E-6
PVDF	0.0	0.0	6.45	0.032	0.211	1.18E-10
	1.0	0.0	6.49	0.112	0.736	4.10E-10
	2.5	0.0	7.80	0.208	1.63	9.06E-10
	5.0	0.0	23.5	0.770	18.1	1.01E-8
	7.5	0.0	56.8	2.26	130	7.25E-8
	10	0.0	821	2.68	2100	1.17E-6
	12.5	0.0	6310	3.35	20300	1.27E-5
	15	0.0	4440	1.64	67000	3.73E-5

Chapter 5 References

1. Bailey, F.J., *Poly (ethylene oxide)*. 2012: Elsevier.
2. Gupta, S., *Krishan's Engineering Physics Vol-2*. Krishna Prakashan Media.
3. Zhang, L., P. Bass, and Z.-Y. Cheng, *Physical aspects of 0-3 dielectric composites.* Journal of Advanced Dielectrics, 2015: p. 1550012.
4. Sakthivel, S., et al., *Structure, dielectric, AC and DC conduction properties of acid doped polyaniline films.* European polymer journal, 1997. **33**(10): p. 1747-1752.
5. Chan, R., K. Pathmanathan, and G. Johari, *Dielectric relaxations in the liquid and glassy states of glucose and its water mixtures.* The Journal of Physical Chemistry, 1986. **90**(23): p. 6358-6362.
6. NACEUR, H., A. MEGRICHE, and M. EL MAAOUI, *Frequency-dependant dielectric characteristics and conductivity behavior of Sr1− x (Na0. 5Bi0. 5) xBi2Nb2O9 (x= 0.0, 0.2, 0.5, 0.8 and 1.0) ceramics.* Oriental Journal of Chemistry, 2013. **29**(3): p. 937-944.
7. Jonscher, A., *Dielectric relaxation in solids. 1983.* Chelsea Dielectric, London, 1983.
8. Sundarakannan, B., K. Kakimoto, and H. Ohsato, *Frequency and temperature dependent dielectric and conductivity behavior of KNbO3 ceramics.* Journal of applied physics, 2003. **94**(8): p. 5182-5187.
9. Hou, J., et al., *Dielectric relaxation and electrical conductivity in Bi 5 NbO 10 oxygen ion conductors prepared by a modified sol–gel process.* Journal of Power Sources, 2010. **195**(9): p. 2613-2618.
10. Maceiras, A., et al., *Dielectric relaxation dynamics of high-temperature piezoelectric polyimide copolymers.* Applied Physics A: p. 1-13.
11. Jonscher, A.K., *Theuniversal'dielectric response.* Nature, 1977. **267**: p. 673-679.

12. Deligöz, H., et al., *Electrical properties of conventional polyimide films: effects of chemical structure and water uptake.* Journal of applied polymer science, 2006. **100**(1): p. 810-818.
13. Fergus, J.W., *Ceramic and polymeric solid electrolytes for lithium-ion batteries.* Journal of Power Sources, 2010. **195**(15): p. 4554-4569.
14. Debye, P., *Zur theorie der spezifischen wärmen.* Annalen der Physik, 1912. **344**(14): p. 789-839.
15. Havriliak, S. and S. Negami, *A complex plane representation of dielectric and mechanical relaxation processes in some polymers.* Polymer, 1967. **8**: p. 161-210.
16. Hummel, R.E., *Electronic properties of materials*. 2011: Springer.
17. Fiedziuszko, S.J., et al., *Dielectric materials, devices, and circuits.* Microwave Theory and Techniques, IEEE Transactions on, 2002. **50**(3): p. 706-720.
18. Balanis, C.A., *Advanced engineering electromagnetics*. Vol. 20. 1989: Wiley New York.

Chapter 6: Development of Ionic Conductive Material as an Energy Storage Device

6 Overview

As has been described throughout this report, the composition of IPMCs is generally that of a parallel-plate capacitor, wherein a dielectric, polymeric matrix is metallized on either surface. The difference with capacitors being that there are mobile cations transiting through the matrix in addition to the dipole response from the polymer matrix in response to an applied external electric field. This chapter will examine PEO-based IPMCs as a candidate for an energy storage device. It will be shown that these materials exhibit properties of both a capacitor and a battery, making it a unique and interesting device.

6.1 Use of PEO in Energy Storage Devices

The use of PEO in energy storage devices is not new as PEO has been extensively studied for use as a lithium-ion conducting electrolyte.[1] This is due to PEO's ability to dissolve ionic salts within its matrix, acting as a solid-polymer electrolyte (SPE), which was first introduced by Fenton et al, in 1973.[2] SPEs play an important role in the development of lithium-ion batteries; they can act as a physical separator between the anode and cathode in a battery system and thus reduce the likelihood of a short and they provide for the transportation of ionic charge during cell operations.[3] Ionic motion through the PEO matrix was found to occur mostly through the amorphous regions due to the segmental motion of the polymer chains with minimal amounts occurring in the crystalline region, where the polymer chains are stiffly bonded together.[4, 5] This segmental motion allows the mobile ions to transition from coordination site to coordination site in the matrix; the conductivity of the matrix is a function of ionic motion, and is a consequence of the rate with which new coordination sites or free space can be generated by the movement of the polymer chains. Therefore, research has been conducted to reduce the crystallinity of the PEO matrix to increase the material's conductivity. PEO's inherent crystallinity results in a poor room-temperature conductivity (up to around 1E-4 S/cm when electronics/energy storage devices typically require at least 1E-3 S/cm)[1] and therefore needs additives, such as plasticizers like succinonitrile,[6] polysquarate[7] or other materials to increase the conductivity by reducing the crystallinity level within the matrix. Room temperature conductivities for PEO with lithium bis(trifluoromethanesulfonimidate) LiTFSI salt were found to range from ~5E-8 S/cm[8] to 1E-4 S/cm,[9] depending on the concentration of LiTFSI. Reported room temperature conductivities for PEO with LP were found to range from ~5E-8 S/cm[5] to 5E-5 S/cm.[10] With the addition of a

plasticizer, the reported room temperature conductivities for PEO electrolytes was found to be from 1E-4 S/cm[11] (PEO with polysquarate) to 5E-3 S/cm[12] (PEO with poly(methyl methacrylate), making the latter a suitable prospect for room-temperature battery applications. Conductivity for the PEO electrolytes has been found to reach the desired levels at elevated temperatures, around 70 ^{o}C, but this is around the melting temperature for PEO and thus is not a conducive operating temperature for the films. Therefore, the focus with PEO being utilized in energy storage devices has been to increase its room temperature conductivity. As this is still a heavily researched topic, the push to PEO as a membrane material for lithium-ion batteries is an ongoing study.

The novelty with respect to this report for the use of PEO as an energy storage device is with its intended use and synthesis as an IPMC. This process has imparted properties of both a capacitor and battery in the material, which can open up new applications. These films are flexible, easily synthesized, and can be fabricated into almost any shape. They offer a large, fast capacitive discharge response followed by a long-lasting battery-like discharge. The one drawback found so far for these films is that they have been found to show a leakage current during their charging cycle. For commercial applications, this leakage current could be a negative characteristic if long-term energy storage was critical. The leakage current is due to the PEO IPMCs not being perfect insulators; as such, even after maximum actuation is achieved, and the majority of the mobile ions have transited to their respective electrodes, there is still the diffusion of some ions within the matrix which enables a current to pass through the device. Though not specifically stated for PEO-based lithium-ion batteries (as research is still being conducted on their room temperature conductivity), solutions for overcoming this leakage current would be to thicken the polymer matrix,[13] lower the salt concentration, increase the resistance of the membrane,[14] or place a non-conducting polymer layer between the PEO matrix and the electrode interface.[15]

Thickening the polymer matrix would allow for a larger possibility of a rogue diffusing ion to be inhibited and stopped by the polymer matrix itself and therefore not contribute to the current. The lowering of the salt concentration is a result found through this study. For the PEO films, based on the amount of LP added to the polymer matrix, there are around 2.12E18 LP molecules added for a 5.0 wt.% LP film, leading to a total possible charge for either the Li^{+} or ClO_4^{-} ions of 339 mC. However, **Table 21** will show that the total calculated charge accumulated on the films, when evaluated as a parallel plate capacitor, and based on the low frequency dielectric constant

and applied voltage is 623 μC, which is a three order of magnitude difference from the ionic charge calculated for being in the matrix. Thus, reducing the LP concentration should reduce the leakage current. This however has an impact on the IPMC's electromechanical performance and also the film's conductivity, but a tradeoff is necessary. For the PVDF films, the results are similar; based on the film synthesis, there should be around 1.39E18 molecules of CoPH in each 15 wt.% sample for a total possible charge of 222 mC. The calculated charge based on the applied voltage and the low frequency dielectric constant yields a charge of 33.4 μC. Increasing the resistance of the polymer matrix falls in line with thickening the film; if the ions are inhibited to flow, then they will not add to the current. The addition of high concentrations of NCC could be a possible solution for this, again at the cost of electromechanical actuation performance. However, based on conductivity data shown in this report, there is a drop in conductivity (increase in resistivity) for films with high NCC content compared to the non-NCC composites. Finally, the addition of a non-conductive polymer layer to either side of the PEO matrix should act to block the ions from traveling from the PEO to the electrode and generating a current. This, again may come at the cost of electromechanical actuation, if these films are still to be used as EAPs and the dielectric properties will change. However, this looks to be another possibility. In all, the increase in resistance of the PEO matrix should have a positive impact on the leakage current seen in the films. Increasing the molecular weight of the PEO could also increase the matrix resistance; ionic motion in the matrix is a result of the segmental motion of the polymer chains and increasing the molecular weight (or length) of the chains creates an environment where the chains are more likely to "knot up" and therefore restrict their movement in the creation of coordination sites.[16] If the chains cannot move, then they will not be able to enable the diffusion of the mobile ions at the same rate as they would if the chains were more mobile.

6.1.1 Typical Capacitor and Battery Charge-Discharge Profiles

The charging profile for batteries generally follows a three-phase process.[17] First a constant current is applied until the battery reaches a set voltage limit; this is called bulk charging. Under a constant current, the potential difference across the battery tends to increase linearly with time, according to Ohm's law, as the internal resistance increases. This stage will typically charge a battery to 80-90% of its total charge. When the target voltage is obtained, the second stage, or absorption charge, begins and the current begins to drop as the battery reaches its saturation voltage. The current will decrease, as internal resistance again rises, until the battery is fully

charged. The second stage will charge the battery up to roughly 95% total charge. The third stage of battery charging involves dropping the applied voltage to a lower level to charge the battery to 100% and to maintain the state-of-charge condition, “top off” charging. The discharging of batteries will have a somewhat linear drop in cell voltage vs. time.

Figure 77.a shows the general first two stages of the battery charging profile (bulk charging and absorption charging) for a lithium-ion battery, which are the stages of interest for this report.[17] Here, there is an initial constant current to bring the cell voltage to the target value; once there, the current drops as the charge builds up within the battery. **Figure 77.b** shows the full, nonlinear charge profile for a series of Texas Instrument lithium ion batteries,[18] where the full ramp up of the cell voltage can be seen. The later stages of charging are shown wherein the battery can be “topped off” and obtain 100% charge. **Figure 77.c** displays the charging profile of a lithium-iron-phosphate battery versus “state of charge”[19] (this term is synonymous with time and so is relevant here). Note, the flattened area where the voltage and current are constant for a significant amount of the charge time; this charging profile is similar to the charging profile of the PEO films in the next section.

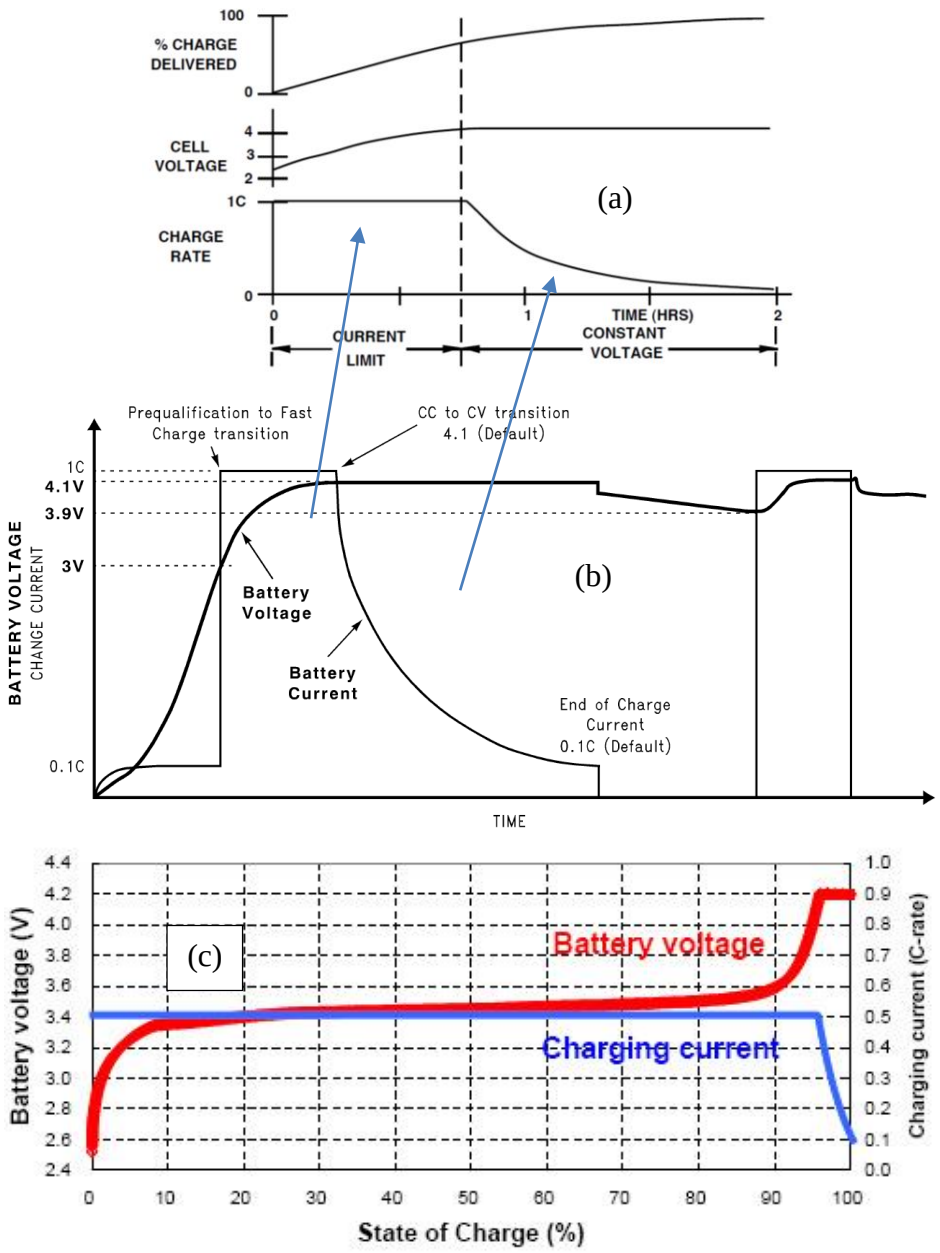

Figure 77: a) General (courtesy of [17]) and b) more detailed charging profiles (courtesy of [18]) for lithium-ion batteries and c) charge profile for a $LiFePO_4$ battery (courtesy of [19])

As for the discharging properties of lithium-ion batteries, their profiles are generally linear for a given amount of discharge and then drop off rapidly. **Figure 78** shows the recreated discharge profile for various applied current draws of an Orbtronic-18650 2900 mAh lithium-ion battery,[20, 21] which is used for flashlights. Note, for small applied current loads, the discharge voltage drops off linearly for a long period of time. For the higher applied current loads, at a certain level, the discharge voltage drops rapidly to zero. This general linear reduction will be used to designate the

battery-like discharge profile of the PEO and PVDF samples in the proceeding sections compared to the rapid capacitive discharge response.

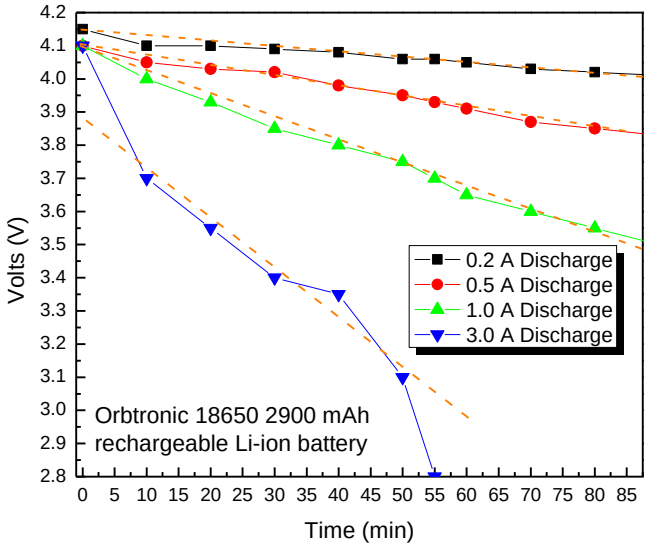

Figure 78: Discharge profile for an Orbtronic-18650 Li-Ion Battery (recreated from [20, 21])

Capacitors, on the other hand, have a much more predictable charge/discharge response; both utilize an exponential response to the application/removal of an external voltage. The inset equations in **Figure 79** are the charging/discharging functions developed for a capacitor in an RC circuit, where $\tau_0 = RC$. Both involve a quick charge and discharge response.

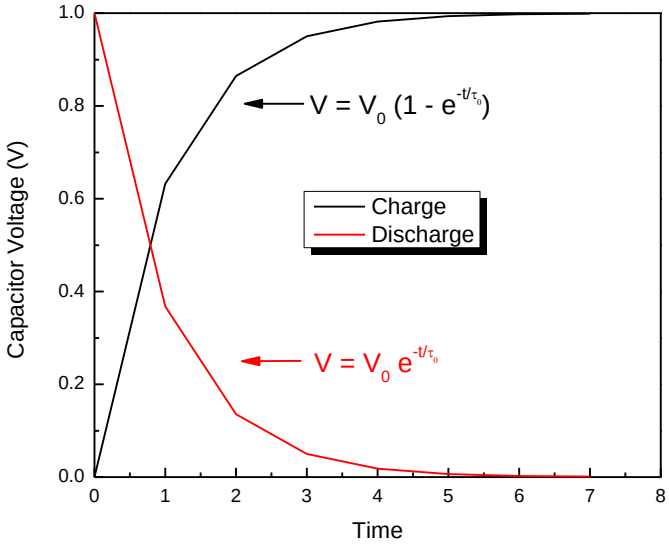

Figure 79: Capacitor charge/discharge profile

6.1.2 Performance and Analysis for PEO-Based Films

As alluded to in the introduction of this chapter and in Chapter 1, the PEO films tested in this experiment displayed properties of both capacitors and batteries for their charge/discharge

cycles. The information displayed in this section concerns the charge/discharge properties of PEO samples with 5.0 wt.% LP. Samples with lower concentrations of LP and those with NCC were not tested for this part of the study. This section serves as a fundamental thought and introduction to further study of PEO-based IPMCs as a potential energy storage material.

The setup for the experiment is as follows: a PEO sample was placed in series with a 10 kΩ resistor; an Agilent E2612A DC power supply, with a digital voltmeter, was connected. Additionally, a multimeter was connected across the resistor, as shown in **Figure 80**.

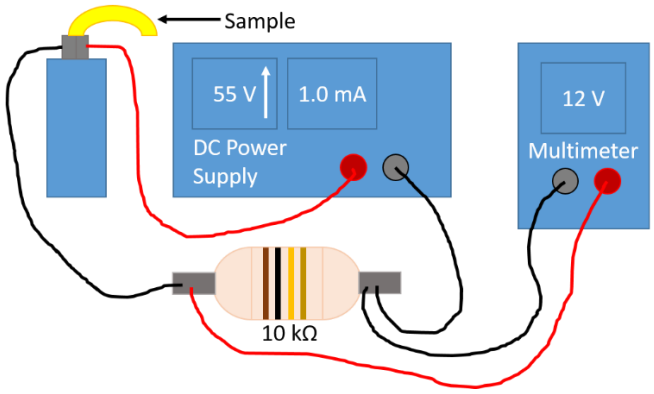

Figure 80: Energy storage experimental setup

Figure 81.a displays the voltage read by the power supply (*V1*) and the voltage read across the resistor (*V2*). The difference between the two is the potential difference across the PEO film. As can be seen, *V1* has a profile that is similar to the battery charging profile in the previous section. *V2* was used as a way to measure how the current traveling through the circuit changed with time. **Figure 81.b** shows the current in the system.

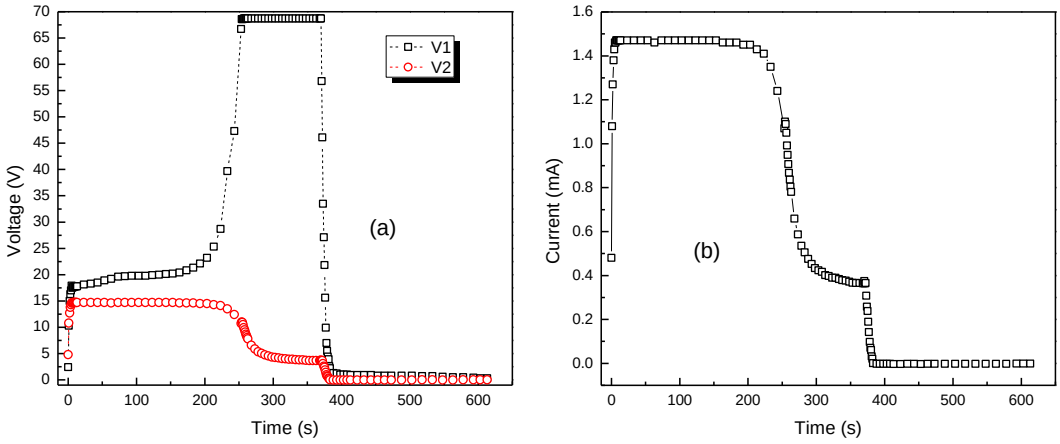

Figure 81: a) Circuit (*V1*) and resistor (*V2*) voltage and b) circuit current time-dependent profiles for a PEO film with 5.0 wt.% LP

Figure 82 displays the charge/discharge profile of a single PEO sample with 5.0 wt.% LP. This figure displays the voltage drop across the film (*V1-V2*) as well as the current profile for the circuit, which is replicated from **Figure 81.b**. Four such samples were tested, with various amounts of time that the films were subjected to a constant voltage, but the profiles and discharge responses of all films were very similar. Therefore, the analysis will be focused on this singular sample. As stated, there are three parts of the battery charging profile; bulk, absorption, and "top off" charging. Here, two are presented, since analyzing long-term charge storage was not a concern during this test. As can be seen, there is a quick ramp up in voltage to about 4.5 V DC across the film. This voltage is maintained for an extended period of time. Of note, is that as this voltage is maintained, the film undergoes its electromechanical bending actuation process. Once this actuation process finishes, and it is assumed that the majority of the ions within the matrix have reached their intended electrode, the voltage begins to increase again as internal resistance begins to build within the film. For this data, the threshold voltage was set at 70 V DC; films had been tested before and allowed to reach their maximum value, around 93 V DC, but the films began to melt, so a lower maximum value was selected. At this constant voltage, it can be seen that the current drops to some minimum level. In an ideal battery or capacitor, the current would reach zero, but this sample has some electrical leakage and therefore there is a non-zero remnant current in the circuit.

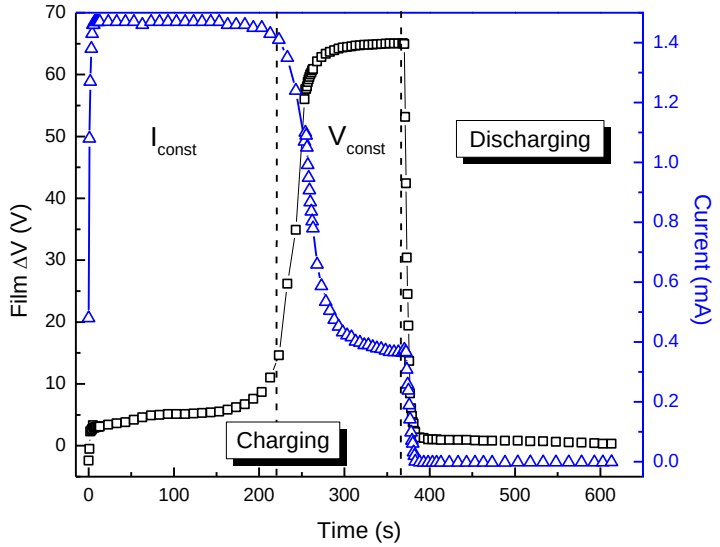

Figure 82: Charge/discharge *ΔV = V1-V2* profile across the PEO film with 5.0 wt.% LP along with the circuit current

Again, the charging profile of the PEO films is similar to that of batteries, however, it was found that the discharge profile of the films had a quick discharge portion, which is more in line with capacitors, and a longer duration voltage drop that is more commensurate with batteries.

Figure 83 displays the voltage drop across the film with respect to time. Represented in log-log scale, there are clearly two steps in the discharge process. It was found that the higher voltage step could be fitted with the general equation for discharging capacitors, as displayed by **Eq. (6.1)**.

$$V = V_0 e^{-t/\tau_0} \tag{6.1}$$

For the lower voltage step, the drop in voltage became linear, with respect to time, which is generally in line with the lithium-ion battery described in the previous section.

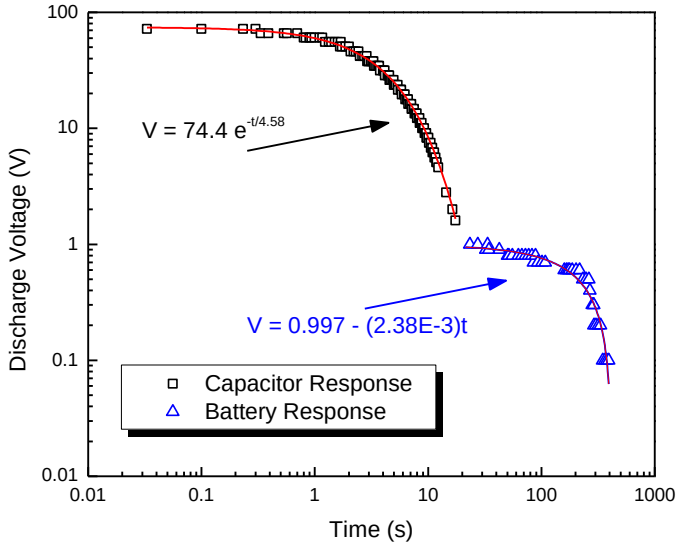

Figure 83: Two-step log-log scale discharge response for PEO film with 5.0 wt.% LP

Zooming in on the "flat" region of the discharge curve from **Figure 82** yields **Figure 84.a**. Here, it can be seen that the voltage drops linearly with a linearly decreasing current. In the referenced lithium-ion battery test in the previous section, the draw on lithium ion batteries generates a linearly decreasing voltage discharge profile. In that case, there was an assumed constant current draw, which is different than in this case, but it still showcases the similarities between the two devices. The current in this figure is negative because it flows opposite the direction of the current released during the capacitor discharge region. To directly compare the capacitive current and the battery-like currents, the absolute battery-like discharge current was plotted with the capacitive current in the log-log scale as shown in **Figure 84.b**. As with the voltage behavior in **Figure 83**, there is a clear two step discharge current process; a fast current release during the high voltage drop and a slow release (in the opposite direction). This slow release can also be attributed to the redistribution of ions within the matrix. The insets in **Figure 84.b** show the bend of the PEO film at the end of the capacitive release portion of the discharge and at the

end of the battery-discharge time. The relaxation of the films is again likely due to the redistribution of the ions within the polymer matrix.

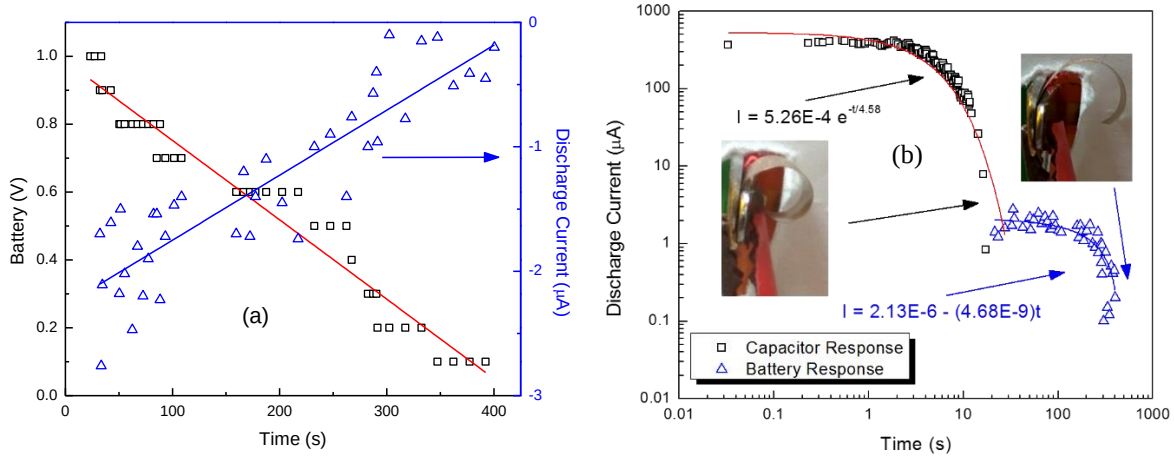

Figure 84: Current discharge profiles for a) battery region and b) both the capacitive region and the absolute value of the battery-like region

Table 21 displays the calculated capacitance values for the PEO film. This value was calculated from the low-frequency dielectric constant displayed in **Table 16** and the dimensions of the film (19 mm x 6.1 mm x 54.5 μm). Of note is the time constant for the fitted voltage drop and its corresponding capacitance value. This value is two orders of magnitude higher than that of the calculated value. This indicates an effective capacitance for the films during the first few seconds of discharge and may be of interest for further study. The other fitting parameters for the PEO film are also shown in the table and in addition to the values for the PVDF samples described in the next section. The conclusion to this section is that PEO-based IPMCs offer a unique and interesting material for further study as an energy storage device since it has properties of both capacitors and batteries.

Table 21: Discharge fitted parameters for PEO and PVDF-based films

	10 $k\Omega$ Series Resistor					Capacitor-Like Discharge				Battery-Like Discharge		
	I_{app} (mA)	ε'_{DC} (10^5)	C_{calc} (μF)	Q_{film} (mC)	E_{calc} (J)	V_0 (V)	τ_0 (s)	C_{eff} (μF)	Q_{cap} (μC)	I_0 (μA)	B_I (nA/s)	Q_{cap} (mAs)
PEO	1	4.73	8.91	340	21.8 m	74.4	4.58	458	623	2.13	-4.68	0.427
PVDF	6	2.17	6.92	220	80.7 μ	53.7	1.16	116	33.4	2.94	-34.9	0.0573
	4	2.17	6.92	220	61.6 μ	38.3	1.12	112	29.2	2.41	-20.9	0.0957
	2	2.17	6.92	220	47.3 μ	23.7	1.10	110	25.6	2.41	-25.4	0.0787
	1	2.17	6.92	220	41.1 μ	8.99	1.00	100	23.9	2.70	-28.3	0.0707

6.1.3 Isolated Circuit Analysis for PEO-Based Films

This section will briefly analyze how the PEO-based films respond when the DC Power supply is taken out of the film-resistor circuit during discharge. This process isolates the PEO film with the resistor, so when discharge occurs, there is no contribution from the power supply and all current passing across the resistor is from the film. A comparative study of four films was conducted, with results shown in **Figure 85.a-d**. All samples tested were 5.0 wt.% LP, charged with an initial constant current of roughly 1 mA, then held at a constant 70 V DC for the second phase of charging, as described in previous sections. These figures show the absolute value of the current produced during discharge.

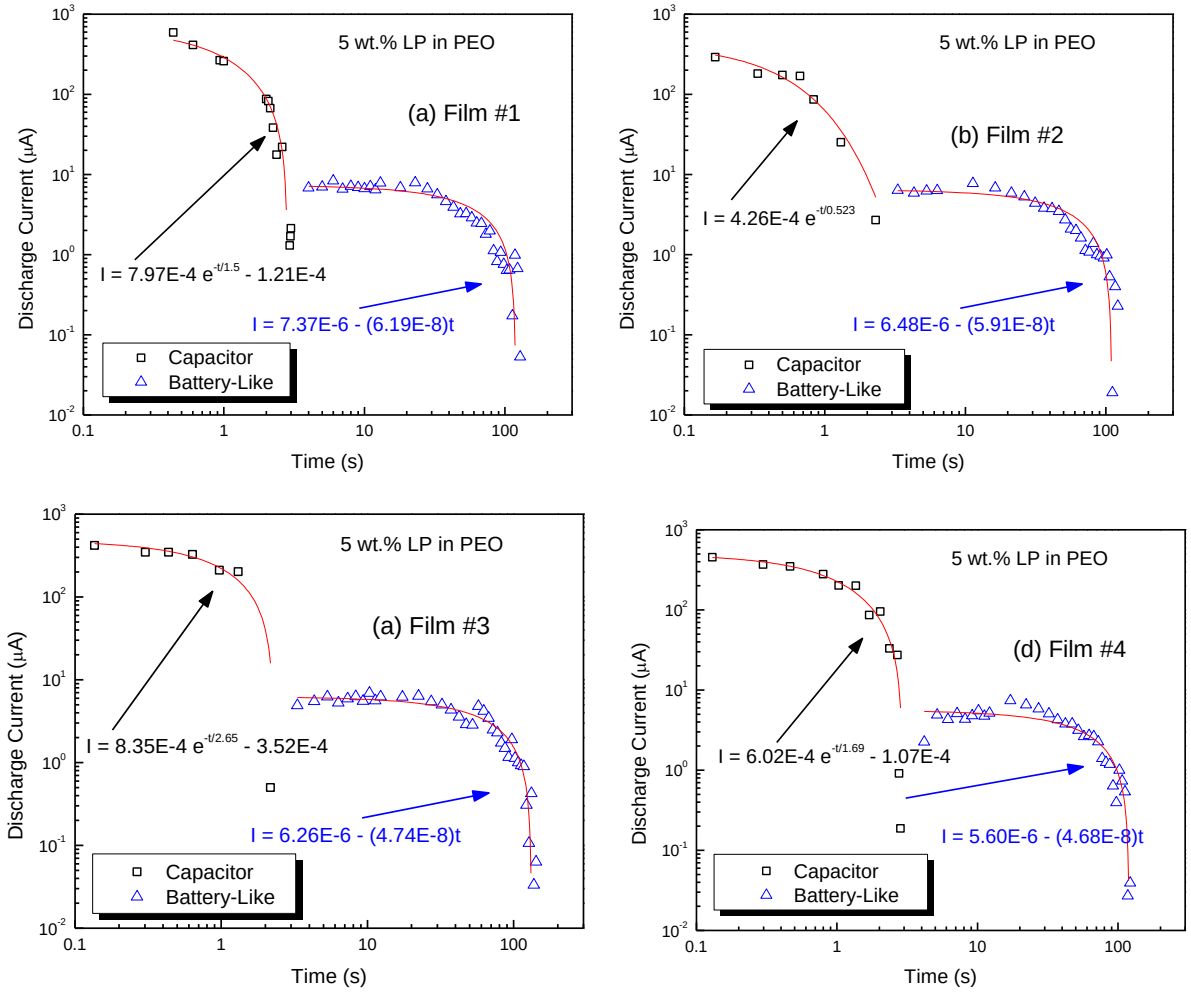

Figure 85: Absolute value of the discharge currents generated for four PEO-based films

Through inspection of **Figure 85**, it can readily seen that there is a step response for the current passing across the resistor that is very similar to that seen for PEO films in the previous section (**Figure 84.b**). Therefore, it can be concluded that both the quick capacitive-like response

and the longer battery-like response are both generated from the PEO film. This result solidifies the proposal of there being a two-phased energy-storage response for these materials. The prospect of this conclusion opens up new doors for energy storage research.

Table 22 shows the calculated parameters of the capacitor-like and battery-like discharging for the four films tested. Comparing these results to **Table 21**, the 10 $k\Omega$ section remains the same, due to the same charging parameters utilized for these films as with the samples tested in the previous section. Initial current was used in the capacitor-like discharge section due to the isolation of the circuit preventing voltage measurements across the film. However, it can be seen that the time constant, τ_0, in **Table 22** is less than those in **Table 21**, indicating a faster discharge response without the DC power supply present. Likewise, the effective capacitance, C_{eff}, and initial charge, Q_0, were also significantly reduced, indicating an influence on the films due to the DC power supply, even though it was effectively turned off during discharge. Finally, in the battery-like discharge section, there is a larger initial current, I_0, and steeper current drop off rate, B_I, in **Table 22** versus **Table 21**, indicating that even though this section of the discharge is extended, compared to the capacitive discharge, the movement of charge when the film is isolated is much more rapid. Interestingly, even with the circuit being isolated for this test, the final charge capacity, Q_{cap}, shown for the PEO film displayed in **Table 21** is comparable to those found in **Table 22**. It is higher than three of the tested films, but on par with film #1. This result shows that even though the circuit is somewhat different between tests, the long-duration discharge or battery-like results of the PEO-based films remains consistent.

Table 22: Discharge fitted parameters for PEO-based films with 5.0 wt.% LP in an isolated circuit

	10 $k\Omega$ Series Resistor					Capacitor-Like Discharge				Battery-Like Discharge		
Film #	I_{app} (mA)	ε'_{DC} (10^5)	C_{calc} (μF)	Q_{film} (mC)	E_{calc} (mJ)	I_0 (μA)	τ_0 (s)	C_{eff} (μF)	Q_0 (mC)	I_0 (μA)	B_I (nA/s)	Q_{cap} (mAs)
1	1	4.73	8.91	623	21.8	796	1.5	150	105	7.37	-61.9	0.438
2	1	4.73	8.91	623	21.8	425	0.523	52.3	36.6	6.48	-59.1	0.339
3	1	4.73	8.91	623	21.8	835	2.65	26.5	18.6	6.26	-47.4	0.326
4	1	4.73	8.91	623	21.8	602	1.69	16.9	11.8	5.60	-46.8	0.297

6.2 Comparative PVDF Energy-Storage Study

With the multitude of PVDF samples with CoPH synthesized for this dissertation, a comparative energy storage study was conducted for PVDF films with 15.0 wt.% CoPH. Compared to the PEO films, the PVDF films did not display the characteristic battery-charging

profile and resembled more of capacitors for their charging profile. However, on discharge, they again had both a quick capacitive response and slow battery-like response with a current opposite that to the capacitive discharge. Since the PVDF films did not have the same charging profile as the PEO films, emphasis was focused on quick charging under varying currents and determining the effects on the films discharge performance. Constant currents of 6 mA, 4 mA, 2 mA, and 1 mA were applied to a single PVDF film and held for 30 s. At the 30 s point, the current was turned off and the discharge time was monitored. **Figure 86.a** shows the DC power supply voltage (*V1*) under the varying currents. **Figure 86.b** shows the resulting circuit current for each applied current. Again, since the PVDF samples did not charge in the same respect as the PEO films, the current profile thus mirrors the potential difference plot. It was found that the higher currents caused a higher circuit voltage and thus a larger potential difference across the PVDF films.

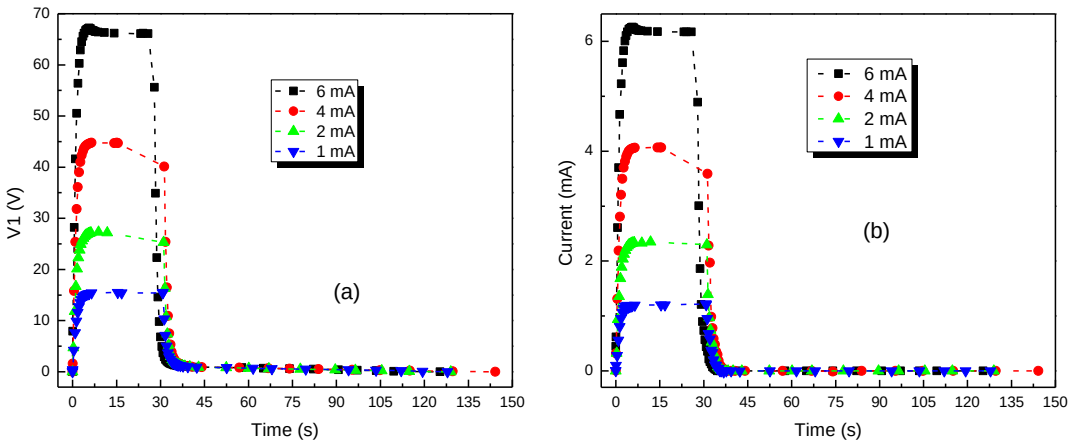

Figure 86: a) V1 and b) circuit current for PVDF films with 15.0 wt.% CoPH at varying applied constant charging currents

Figure 87.a shows the potential difference across the films for the varying applied currents. Again, the larger the current, the larger the potential difference across the samples. The difference between the film potential is due to the small difference between the circuit and resistor potentials, as shown in **Figure 87.b**.

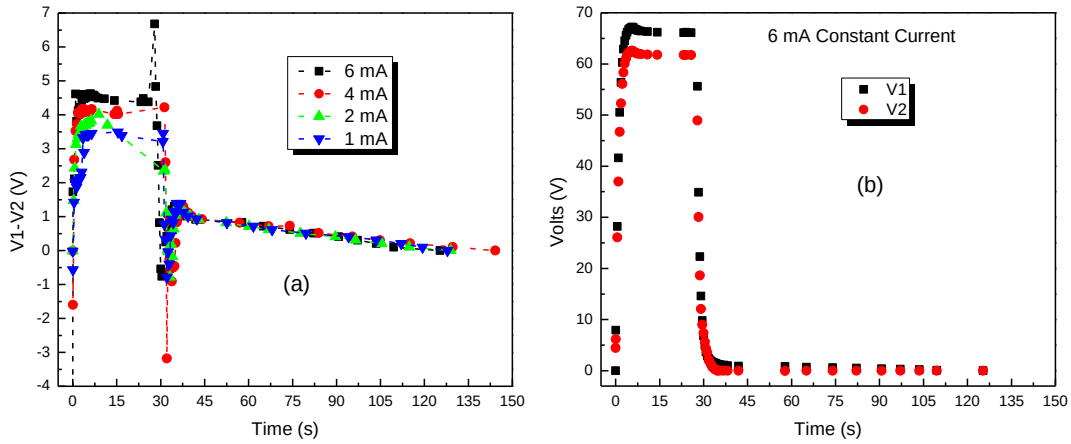

Figure 87: a) Film potential difference *ΔV = V1-V2* and b) circuit and resistor potential differences for PVDF films with 15.0 wt.% CoPH at varying applied constant charging currents

As stated, though the charging profile of the PVDF films more closely represents capacitors versus the battery profile seen with the PEO films, the discharge profile of the PVDF films mirrors the PEO films. There is the same quick voltage drop, signifying a large capacitive section, followed by a slow linear battery-like discharge with the current flowing in the opposite direction of the capacitive discharge, as with the PEO films. **Figure 88.a** displays the voltage drop across the films and as can be seen, there is a sharper drop in voltage for the films with the higher applied constant current. Both are fitted with the general formula for capacitor discharge. For the battery-discharge profile, as with the PEO films, since the battery-discharge current is in the opposite direction compared to the capacitive region, the absolute value for this portion of the discharge is shown in **Figure 88.b**. Interestingly enough, even though the films had different capacitive responses, their battery-discharge performance is very similar.

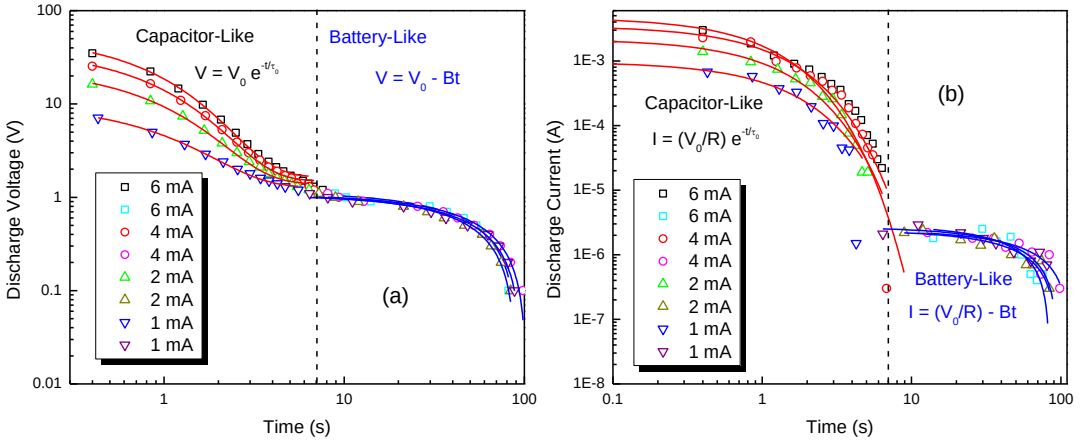

Figure 88: Discharge profiles concerning a) voltage drop across the film and b) the absolute value of the current drop across the circuit for PVDF films with 15.0 wt.% CoPH at varying constant-current charging currents

Zooming in on the "flat" portion of the discharge portion of **Figure 86.a** yields **Figure 89** with the corresponding drop in output voltage for the PVDF films tested under varying applied constant charging currents. As can be seen, this battery portion of the discharge has a voltage drop and discharge current that are again similar across the board for the films, and also similar to the PEO battery-discharge profile (**Figure 84.a**). This result says that though the fast capacitive response is different for the films, due to the higher charging current enabling a larger charge build up on the films, that the battery-like behavior is more or less constant, owing to a more uniform ionic redistribution response for the CoPH within the sample. **Table 21** shows the fitting results and confirms this conclusion.

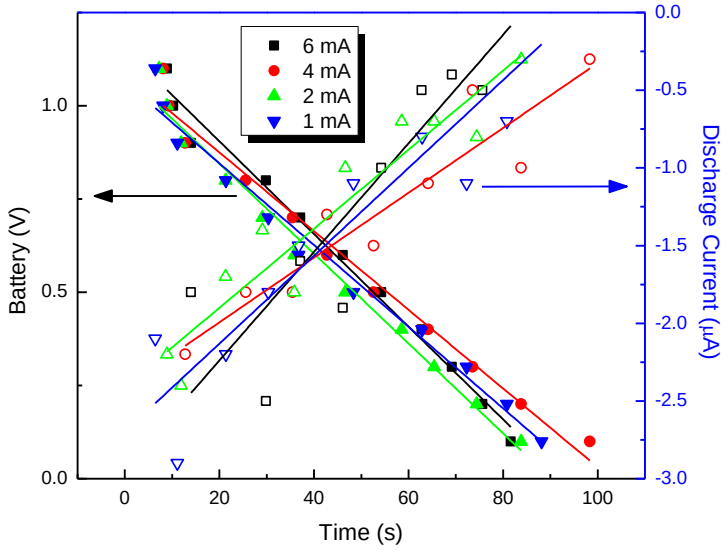

Figure 89: Battery discharge profile for PVDF films with 15.0 wt.% CoPH

Chapter 6 References

1. Fergus, J.W., *Ceramic and polymeric solid electrolytes for lithium-ion batteries.* Journal of Power Sources, 2010. **195**(15): p. 4554-4569.
2. Fenton, D., J. Parker, and P. Wright, *Complexes of alkali metal ions with poly (ethylene oxide).* Polymer, 1973. **14**(11): p. 589.
3. Mittal, V., *Polymers for Energy Storage and Conversion*. 2013: John Wiley & Sons.
4. Osaka, T. and M. Datta, *Energy storage systems in electronics*. 2000: CRC Press.
5. Shen, C., et al., *Physicochemical properties of poly (ethylene oxide)-based composite polymer electrolytes with a silane-modified mesoporous silica SBA-15.* Electrochimica Acta, 2009. **54**(12): p. 3490-3494.
6. Fan, L.-Z., et al., *Enhanced ionic conductivities in composite polymer electrolytes by using succinonitrile as a plasticizer.* Solid State Ionics, 2008. **179**(27): p. 1772-1775.
7. Itoh, T., et al., *Solid polymer electrolytes based on squaric acid structure.* Ionics, 2008. **14**(1): p. 1-6.

8. Itoh, T., et al., *Solid polymer electrolytes composed of polyanionic lithium salts and polyethers.* Journal of Power Sources, 2009. **189**(1): p. 531-535.
9. Marzantowicz, M., et al., *Star-branched poly (ethylene oxide) LiN (CF 3 SO 2) 2: a promising polymer electrolyte.* Journal of Power Sources, 2009. **194**(1): p. 51-57.
10. An, S.Y., et al., *Effect of additives in PEO/PAA/PMAA composite solid polymer electrolytes on the ionic conductivity and Li ion battery performance.* Journal of applied electrochemistry, 2009. **39**(9): p. 1573-1578.
11. Itoh, T., et al., *Solid polymer electrolytes based on poly (lithium carboxylate) salts.* Ionics, 2009. **15**(1): p. 27-33.
12. Ghosh, A. and P. Kofinas, *Nanostructured block copolymer dry electrolyte.* Journal of the Electrochemical Society, 2008. **155**(6): p. A428-A431.
13. Iglesias, L., et al., *Development of electrostatic supercapacitors by atomic layer deposition on nanoporous anodic aluminum oxides for energy harvesting applications.* Frontiers in Physics, 2015. **3**: p. 12.
14. Carlson, T., *Load carrying composites for electrical energy storage*, in *Department of Materials and Manufacturing Technology*. 2007, Chalmers University of Technology: Researchgate. p. 86.
15. Gowda, S.R., et al., *Building energy storage device on a single nanowire.* Nano letters, 2011. **11**(8): p. 3329-3333.
16. Barkema, G. and H. Krenzlin, *Long-time dynamics of de Gennes' model for reptation.* The Journal of chemical physics, 1998. **109**(15): p. 6486-6489.
17. Simpson, C., *Battery Charging*, in *www.ti.com*, N. Semiconductor, Editor. 2011, Texas Instruments: Texas Instruments.
18. Semiconductor, N., *LP3945/LP3946 Battery Charge Management System*, in *www.national.com*, N. Semiconductor, Editor. 2003, National Semiconductor: www.national.com.
19. Technology, P. *How to charge lithium iron phosphate rechargeable lithium ion batteries*. 2015 2 Aug 15; Available from: www.powerstream.com/LLLF.htm.
20. Orbtronic, *IMR 18650 2900mAh Li-ion Battery PD2900 3.7V Button top*. 2015, Orbtronic: www.orbtronic.com.
21. HKJ. *Test/Review: Orbtronic 18650 2900 mAh (Black)*. 2012; Available from: http://budgetlightforum.com/node/10248.

Chapter 7: Discovery of a Completely New Electromechanical Coupling Effect

7.1 Overview

As mentioned in the introduction of this report, electroactive polymers generally fall into two areas: electronic and ionic EAPs. The behavior for materials like PVDF used in ferroelectric, electronic EAPs generates a linear actuation response due to conformal changes along the polymer backbone, wherein a predominantly cis-trans polymer chain reorients into a predominantly trans-trans chain as a response to an applied electric field like that shown in **Figure 90**.[1, 2] The electric dipole polarization of this polymer is reversible and can be changed under an applied electric field. The performance for PVDF films is a linear piezoelectric response. For PVDF, in real materials, the lattice parameter along the c-axis (the polymer backbone direction) for the crystalline structure of the α and β phases was found to be 4.62 Å and 5.12 Å, respectively,[3] for a four carbon-carbon bond lengths along the chain. This disparity between the two phases leads to a 11.1% linear increase in length along the polymer chain direction when the PVDF is excited from the α to β phases.

For an idealized length of PVDF, this 11.1% linear extension between the phases can also be calculated. The distance between successive carbon atoms along the polymer backbone is 1.54 Å.[4] For the cis-trans or α phase of PVDF (**Figure 90.a**), there is a 60^{o} bend in the polymer chain[4, 5] when transitioning from cis- to trans- segments along the chain. In the trans-trans or β phase of PVDF (**Figure 90.b**), the angle made between three successive carbon atoms is 112^{o}[4, 5] (there are two other phases of PVDF with a conformation somewhere between α and β,[4] but the two pure cases mentioned are the ones of interest). Calculating the length of four carbon-carbon bond lengths along a single chain of PVDF for both the α and β phases yields a length of 4.62 Å and 5.12 Å, respectively. This disparity in lengths returns an increase in length of 11.1%, assuming a 100% conversion rate of α to β under an applied electric field. Electric fields needed to generate this linear response are approximately 13-150 MV/m.[6-8] The range of linear actuation for PVDF under an applied electric field presents many possible applications for this film.

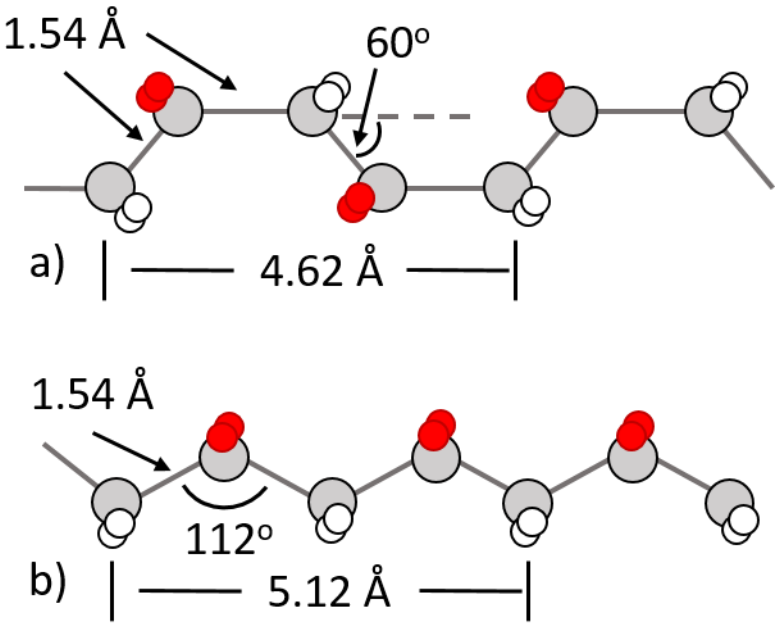

Figure 90: PVDF structure for a) α and b) β phases

On the other hand, as clearly represented throughout the rest of this report, ionic EAPs, specifically ionic-metallic polymer composites, generate a nonlinear, bending actuation response under an applied electric field due to the flux of both cations and anions within the parent polymer matrix and their accumulation at their respective electrodes. Applied fields on the order of 0.057-0.133 MV/m can generate tip deflections of over 360°.

This chapter will introduce and discuss how the electrostrictive, linear response of ferroelectric EAPs can be combined with the bending, nonlinear response of ionic EAPs to form a new area of EAP research and study. As a conceptual study this chapter will act to showcase a new material response and to introduce this new field of study for future research and examination.

7.2 Two-Phase Actuation in PVDF EAPs

In addition to the PEO films, which have been studied extensively in this report, PVDF-based EAPs were also produced for comparison and study. Interestingly, it was found through this study that ferroelectric PVDF films can be forced to generate both the linear and nonlinear, bending actuation responses, resulting in a new area of EAP response and research. 4 V DC were applied to PVDF films containing 15 wt.% CoPH with a thickness of ~30 μm.

To describe how this two-phased actuation phenomenon works, a hinged device was drawn to illustrate the varying actuation mechanisms. **Figure 91.a-c** exemplifies how a linear actuation response can occur utilizing an assembly of pinned hinges where successive expansion of the

hinges results in a linear extension. **Figure 92.a-c** shows how this same device can undergo a bending profile where the hinge expansion occurs on only one side, effectively creating a pivot point and resulting in a curl. **Figure 93.a-c** shows how the bending profile of **Figure 92** can evolve into the linear actuation profile of **Figure 91** as the curled device begins a linear expansion from the last set of hinges back to the base of the device. In reality, for each of these three sets of figures, the actuation process would be continuous instead of being shown with discrete steps, but representing the process in this manner enables a direct and quick intuitive understanding of how each mechanism occurs.

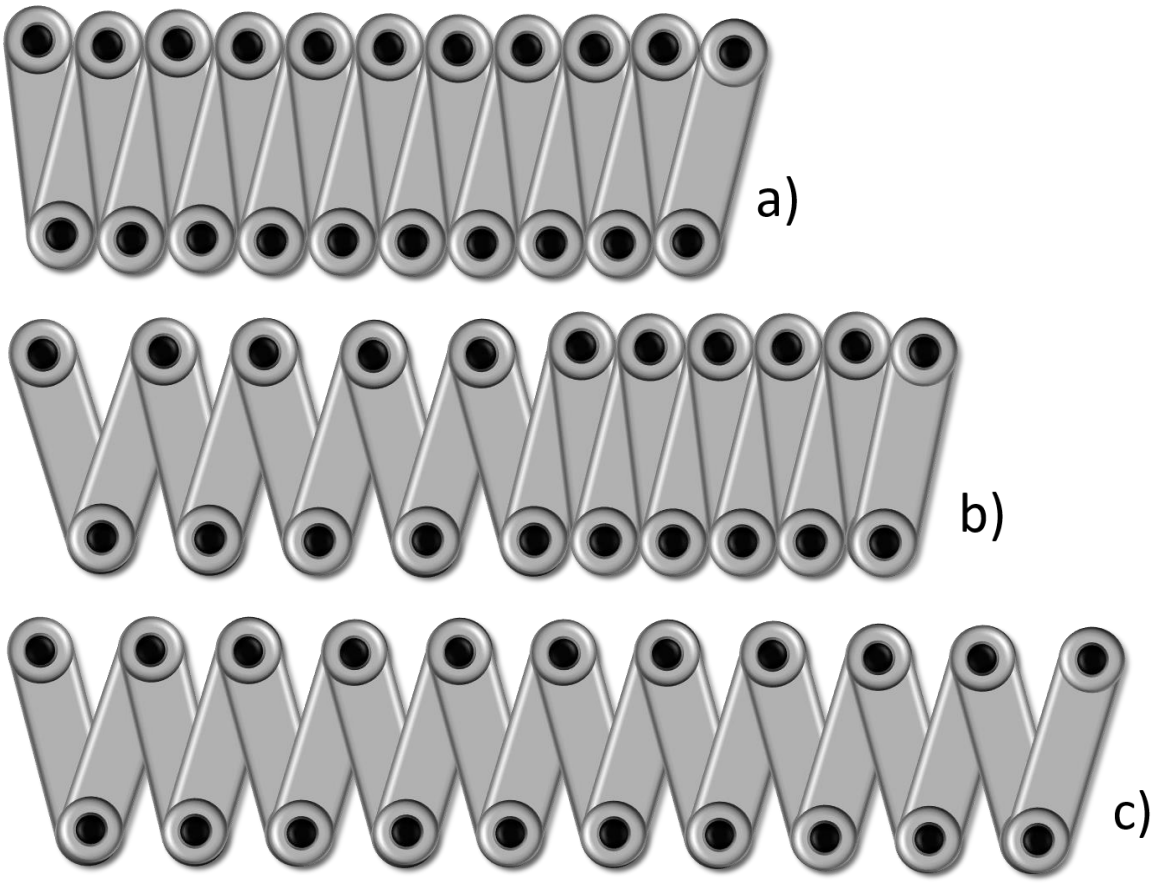

Figure 91: Linear actuation of a hinged device from an a) initial and b) intermediate state to a c) final extended state

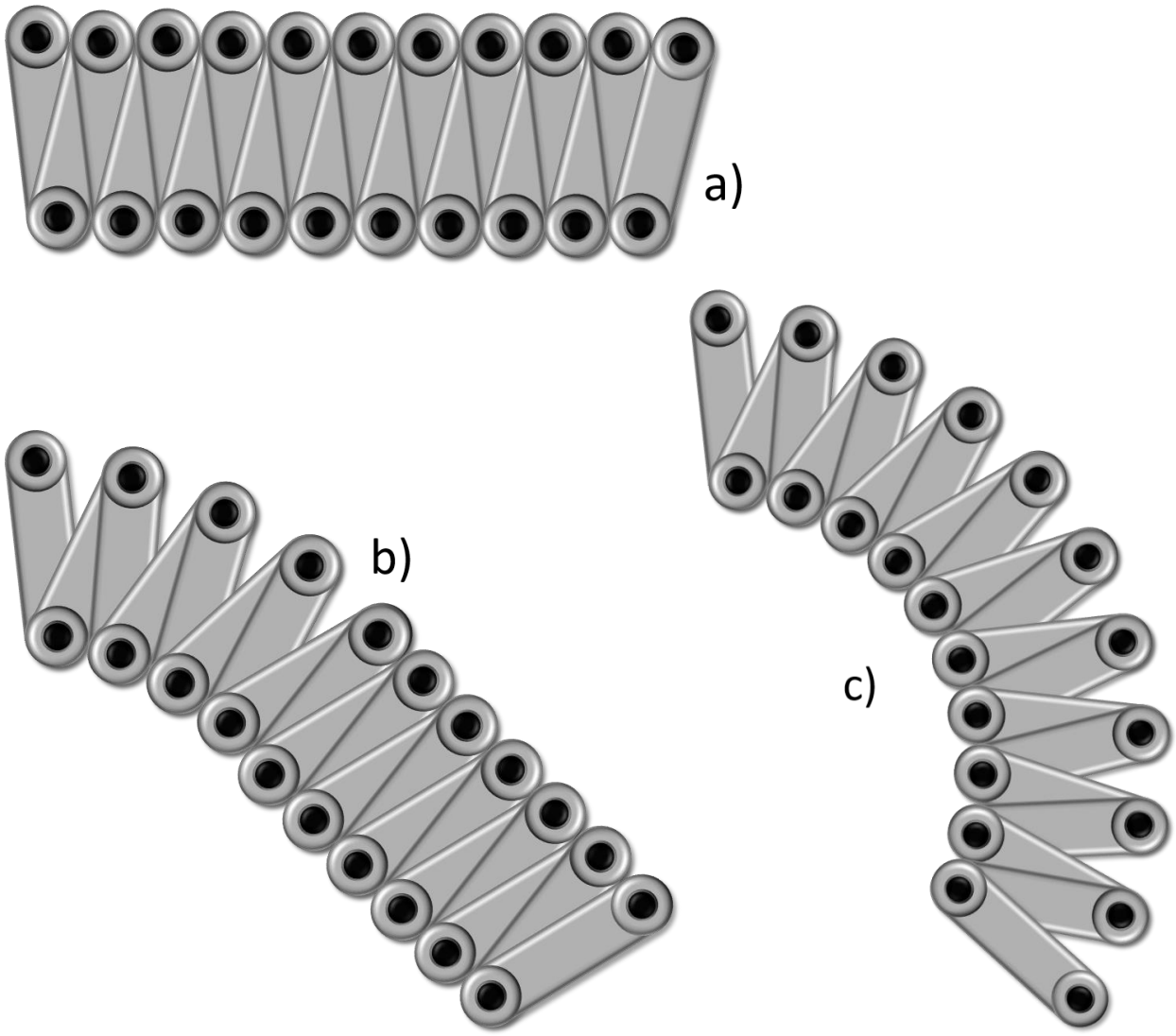

Figure 92: Nonlinear actuation of a hinged device from an a) initial and b) intermediate state to a c) final bended state

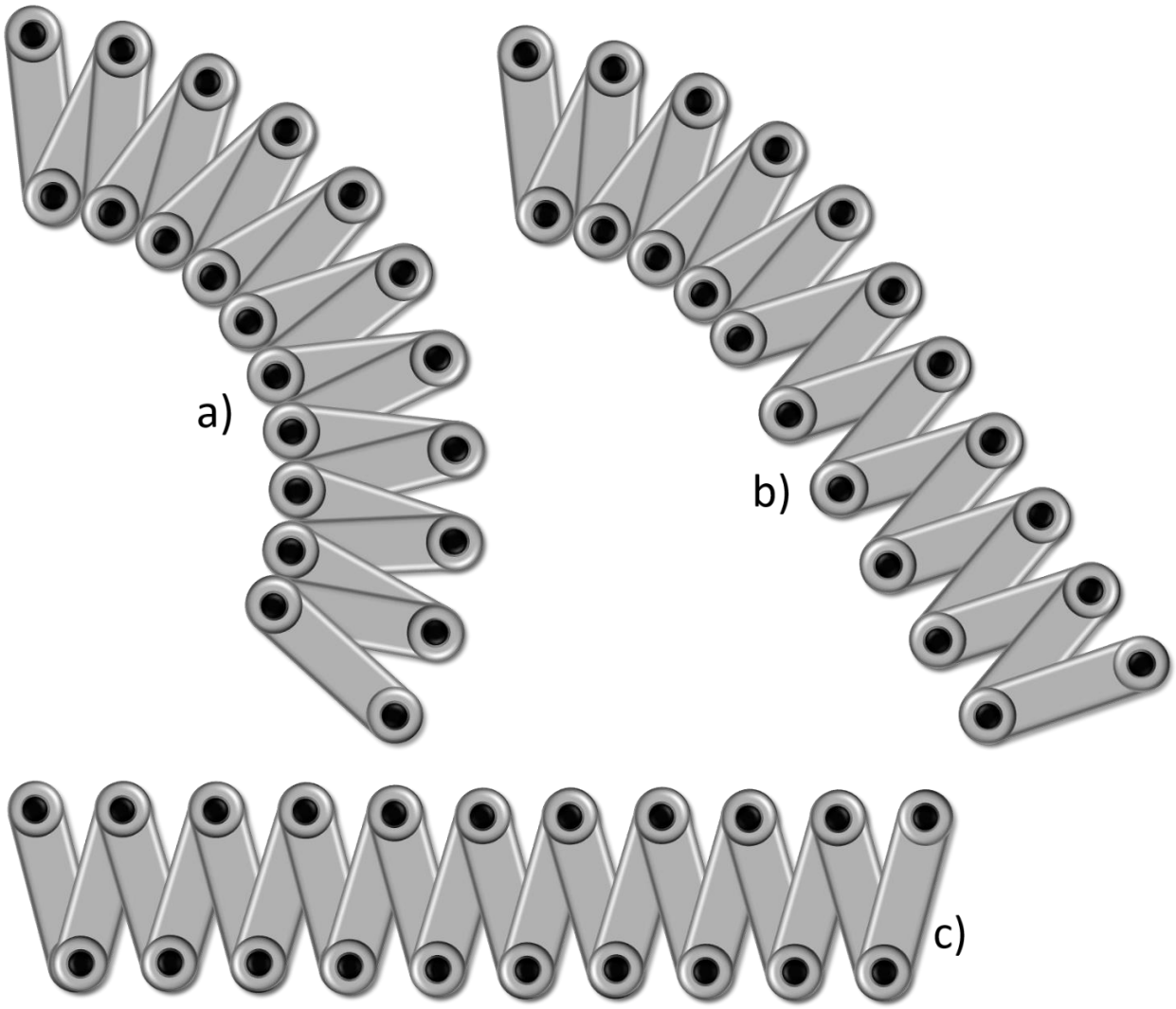

Figure 93: Secondary actuation process of a hinged device from an a) bent orientation actuation to an b) intermediate state, and finally to an c) extended linear actuation state

It is this transition that has been observed in the PVDF actuators. As discussed in previous sections, it was found that PVDF films infused with cobalt perchlorate will perform a large bending actuation with a response time of roughly 5 s under 4 V DC. These results were readily fitted with both the Arrhenius-Based Model and the Charge-Distribution Model outlined. However, if the 4 V DC were maintained and held on the PVDF films, it was observed that the films would begin to bend back towards their original state, indicating a secondary process occurring within the EAPs. It is surmised that the first stage of actuation, where bending occurs, is due to the electrostatic force within the matrix, created by the applied field, predominantly affecting the flux of cobalt perchlorate ions through the matrix. This generates the bending mechanism illustrated in **Figure 92** whereas the second phase of motion is driven by the same electrostatic force generating the

electrostrictive linear actuation phenomenon showcased in **Figure 91**. This two-phase response occurring within one continuous material and produced under a constant driving voltage is a new response observed in electroactive polymers and may lead to new potential applications.

The behavior of the PVDF-based EAPs developed in this study were less predictable and repeatable in their performance compared to the heavily studied PEO-based films showcased for the majority of this report. Therefore, **Figure 94.a-c** display this two-phased response for three separate films, each with 15 wt.% CoPH and tested under 4 V DC. In each of the films, the initial curling actuation response of the film is due to the flux of the cobalt and perchlorate ions traversing the PVDF matrix and accumulating at the positive and negative electrodes. Once this process terminates, there is a recoil-like process that occurs wherein the films begin to bend back towards their original orientation. This secondary process again exemplifies the linear response in the films due to the realignment of the fluorine and hydrogen atoms along the PVDF backbone. The first film (**Figure 94.a**) had an initial bending actuation that covered roughly 210^{o}, then recoiled approximately 90^{o} for 43% linear extension recoil. The latter two films (**Figure 94.b,c**) had initial bending actuations that covered roughly 90^{o} and 120^{o}, respectively, followed by a respective secondary linear recoil response of 45^{o} and 30^{o} from their maximum actuated position. These measurements represent a 50% and 25% linear extension recoil response from the films. As seen, for the samples tested, the maximum recovery during the linear actuation response period was 50%. Finally, upon release of the applied field, the films were seen to recover to almost their initial starting position arising from an elastic response within the films. Of note, is that the films generally have a flat bending response versus the curled response of the PEO films. This could signify a concentrated electric field at the base of the films. This concentrated field at either the base of the film or in other localized regions could yield electric fields high enough to cause the secondary linear response observed in the films. These results are very interesting and again represent a fundamental, preliminary investigation into this phenomenon. Further research may pave the way for a new area of study which should be followed up on and that could lend itself to future, more dynamic EAP applications.

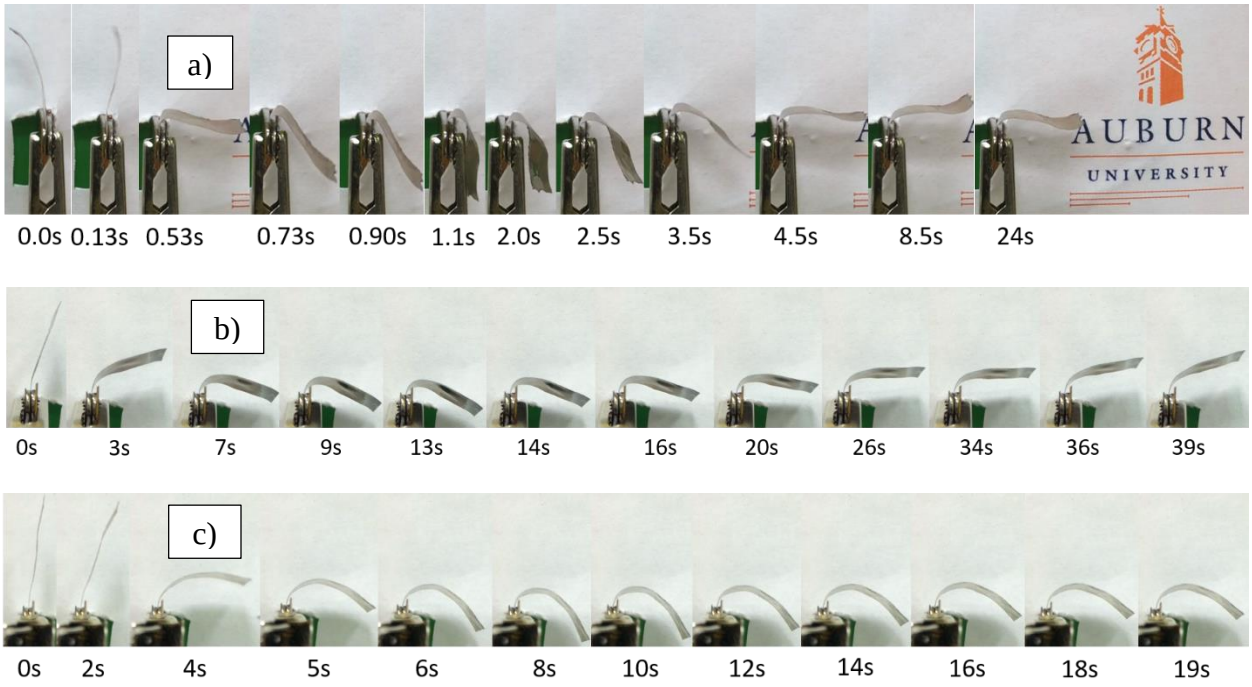

Figure 94: Two-phase actuation phenomenon for PVDF EAPs with 15 wt.% CoPH with 4 V DC applied

7.3 Examples of Two-Phased Motion in Nature and in Industry

The two-phased process showcased with the PVDF films is not a unique process, but is one that has also evolved in nature and that has also been mimicked with industrial robots. However, as stated, it is the encompassment of this two-phased behavior in one continuous medium which makes it a unique material requiring further research. The best example of something having this dual aspect of motion in nature would be the trunk of an elephant.[9, 10] Elephant trunks are highly evolved, having roughly 150,000 muscles and making them capable to articulate in almost any direction. **Figure 95** shows a cross section of an elephant's trunk. They have longitudinal muscles on the top and bottom of their trunk which allows them to make back and forth motions; transverse muscles which enable them to move side to side, and radial muscles which allow them to expand and contract the enclosed nasal cavities. The refined nature of the elephant's trunk enables it to hold/transport up to two gallons of water and it can pick up grass and other food. Elephants have even been trained to use their trunks to throw darts and to delicately hold and use a paint brush.[11]

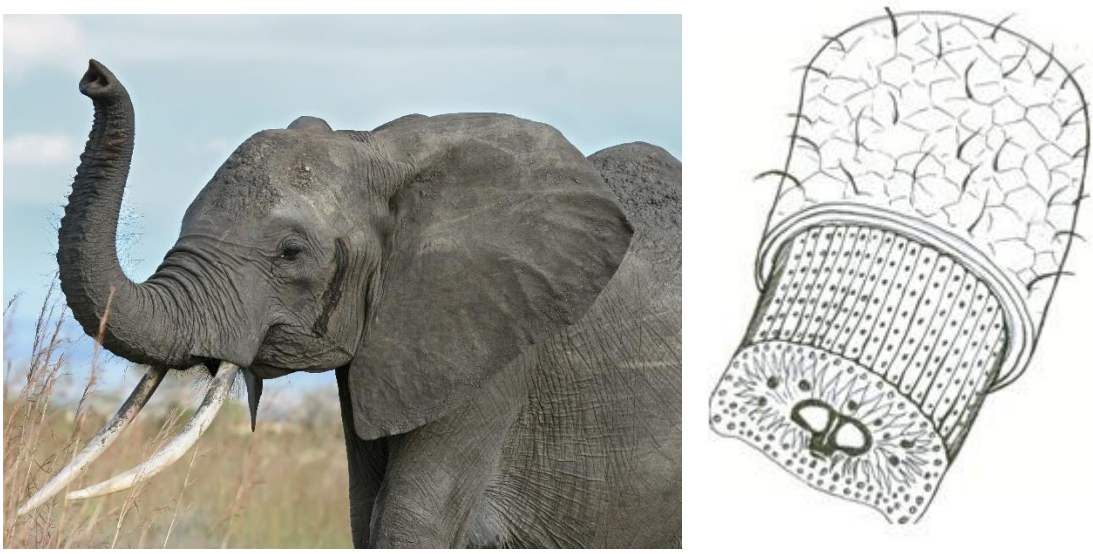

Figure 95: An elephant and the cross-section of an elephant's tusk (copied from ref[9, 10])

The closest mimic to the functionality of the elephant trunk is the Bionic Handling Assistant (BHA), made by the German-based company, Festo.[12-14] The BHA is shown in **Figure 96**. The BHA operates by controlling the flow of compressed air throughout its structure. The construction of the BHA is broken down into four areas, including three segments that make up the 'trunk' and a gripper hand at the end, along with a chassis system enclosing the compressed-air system and electronics. In each segment there are three tubes connected in a triangular structure, with ten air chambers for each tube, in each of the three segments. The amount of air in each chamber is controlled by piezoelectric valves and the BHA's position determined by a series of potentiometers along the 'trunk.' The BHA is made mostly from polyamide, so it is flexible, which enables the arm to extend linearly, as well as nonlinear angular displacement with articulation across 11 degrees of freedom. The three-pronged gripper hand enables it to pick up objects similarly to how an elephant picks up grass. The operation of the BHA requires several systems working in conjunction to achieve its dynamic results.

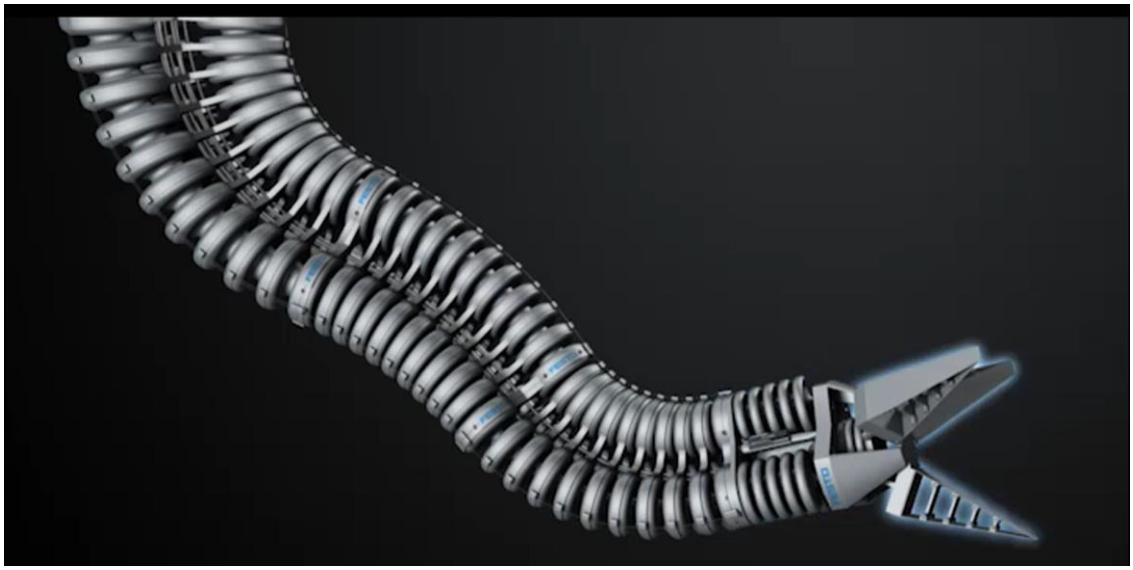

Figure 96: Bionic Handling Assistant industrial robot (copied from ref [12])

Aside from the BHA device, more common industrial robots like the Kuka KR 60-3 (**Figure 97**) have been developed with nearly the same degree of freedom for motion and articulation with the ability to achieve linear and nonlinear actuation performance. The mobility of these robots enable them to quickly and precisely perform operations specific to the automotive, welding, painting, and assembling industries. The Kuka KR 60-3 is a medium payload industrial robot capable of lifting 35 kg with six axes of freedom and operates via a hydraulic system.[15]

Figure 97: Kuka KR 60-3 industrial robot (copied from ref[15])

Both the Kuka KR 60-3 and the BHA do an excellent job of articulating to extreme angles, however they are immobile and require a complex actuation system in order to operate. Though

not as robust as the industrial robots, the PVDF EAP films described in this chapter are capable of exhibiting both the linear and nonlinear behavior similar to that of robots and that of the elephant's trunk. More work in this area is clearly necessary, but the introduction of this phenomenon paves the way for this new area of research.

Chapter 7 References

1. Carpi, F., et al., *Electroactive polymer actuators as artificial muscles: are they ready for bioinspired applications?* Bioinspiration & biomimetics, 2011. **6**(4): p. 045006.
2. Cheng, Z. and Q. Zhang, *Field-activated electroactive polymers.* MRS bulletin, 2008. **33**(03): p. 183-187.
3. Nalwa, H.S., *Ferroelectric Polymers: Chemistry: Physics, and Applications*. 1995: CRC Press.
4. Lando, J., H. Olf, and A. Peterlin, *Nuclear magnetic resonance and x-ray determination of the structure of poly (vinylidene fluoride).* Journal of Polymer Science Part A-1: Polymer Chemistry, 1966. **4**(4): p. 941-951.
5. Hasegawa, R., et al., *Crystal structures of three crystalline forms of poly (vinylidene fluoride).* Polymer Journal, 1972. **3**(5): p. 600-610.
6. Cheng, Z.-Y., et al. *P (VDF-TrFE)-based electrostrictive co/ter-polymers and their device performance*. in *SPIE's 8th Annual International Symposium on Smart Structures and Materials*. 2001. International Society for Optics and Photonics.
7. Cheng, Z.-Y., et al., *Electrostrictive poly (vinylidene fluoride-trifluoroethylene) copolymers.* Sensors and Actuators A: Physical, 2001. **90**(1): p. 138-147.
8. Xia, F., et al. *Poly (vinylidene-fluoride-trifluoroethylene) based high-performance electroactive polymers*. in *Smart Structures and Materials*. 2003. International Society for Optics and Photonics.
9. Redmond, I., *Eyewitness: Elephant*. DK Eyewitness Books. 2000: DK Children. 64.
10. Haynes, G., *Mammoths, mastodonts, and elephants: biology, behavior and the fossil record*. 1993: Cambridge University Press.
11. Channel, N.G. *Inside Nature's Giants: Elephants*. 2015.
12. Grzesiak, A., R. Becker, and A. Verl, *The Bionic Handling Assistant: a success story of additive manufacturing.* Assembly Automation, 2011. **31**(4): p. 329-333.
13. Mahl, T., A. Hildebrandt, and O. Sawodny, *A variable curvature continuum kinematics for kinematic control of the bionic handling assistant.* Robotics, IEEE Transactions on, 2014. **30**(4): p. 935-949.
14. Festo. *Bionic Handling Assistant: Safe human-machine interaction*. 2015.
15. Corp., K.R. *KR 60-3*. 2015.

Chapter 8: Conclusions Future Work, and Acknowledgements

8 Conclusions

The work included herein provided a parametric study on the characteristics and behavior of IPMC EAPs, namely, PEO-based composites. These composites were synthesized to be a biodegradable, green alternative to the commercially available IPMCs, like Nafion and Flemion, that are comprised of, or utilize caustic chemicals during their synthesis which are not biodegradable or recyclable. The PEO IPMCs were characterized based on changes in levels of ionic salt (LP) employed within its matrix and concentrations of NCC (the green additive and stiffening agent) during the synthesis process, and through testing the effects of sample thickness, temperature, and applied electric field levels during experimentation. Through monitoring of the bending actuation performed by the actuators under these conditions, several models were generated to describe the observed behavior of the EAPs. First, a simple Arrhenius-Based Model was developed that could quickly and easily fit the slow, steady, saturated actuation response observed within the films. This model utilizes only two fitting parameters, but is able to accurately describe the entirety of the sample's electromechanical response. Spawning from this model was the Charge-Distribution Model, which aimed at better understanding the physics behind the IPMC bending response. It was assumed that both the anions and cations moved within the matrix at a constant drift velocity and from there it was proposed that IPMC actuation arises not from an expansion and contraction on either side of the film, but that both sides of the film expand as the charge carriers accumulate near the electrode-matrix interface. The observed electromechanical response is thus a result of one side of the film expanding faster than the other side, not unlike bimetallic alloys with different coefficients of expansion.

Both the Arrhenius-Based and Charge-Distribution models require some type of optical monitoring equipment (i.e., photographs or video) to record the films actuation response. This requirement can be cumbersome and costly depending on the desired application; therefore a third model was detailed concerning the frequency and time dependence of the dielectric behavior of the PEO films. An impedance analyzer was used which added a small, sensing AC electric field to the larger driving DC electric field. Through sweeping the frequency through a set range it was found that the electromechanical actuation response, namely the sample's strain, could be linked to changes in its dielectric relaxation time. This discovery creates the possibility of being able to

remotely monitor the samples actuation response without having to require any type of viewing equipment. This model could enable more of the intended lightweight applications for IPMCs.

Finally, an introductory study of the PEO-based IPMCs as possible energy storage devices was conducted. PEO samples with 5.0 wt.% LP were concentrated on and it was found that the samples behaved both like a capacitor (with a fast discharge response) and like a battery (due to its charging profile). This novel study aims to view these materials as possible lightweight energy sources for low-power applications.

In all, this project answered some questions regarding IPMC behavior and opened up new questions in the process. These are exciting materials and I found myself lucky to have had the chance to work with them. It has been a rewarding experience and this dissertation is the culmination of all of that hard work and it is something that I am greatly proud of.

8.1 Future Work

There is great potential for future work that can spawn from the research presented in this study. Further master's and PhD-level-research would be easily warranted for any one or combination of topics discussed herein. IPMCs are amazing materials, but there are still many mysteries, even within the chapters laid out in this investigation, to uncover and solve for the behavior and characterization of IPMCs. The following will name a few areas of possible future focus from each of the chapters laid out in this dissertation: 1) To explore other biodegradable IPMCs such as poly(ε-caprolactone) and to build a portfolio of green alternatives for smart material research; 2) for the Arrhenius-Based Model, to test more polymer systems to encapsulate how general the applicability of this simple actuation model is; 3) conduct a more comprehensive study on the possible physics behind the time constant B within the model; 4) for the Charge-Distribution Model, to also test its applicability to more polymer systems; 5) hone in on the intricacies presented by the model for early time intervals for the possible development of an additional boundary condition to better encompass the physical behavior as the ions are accelerated from rest to inevitably reaching their drift velocity; 6) to investigate more into the idea behind accumulation zones for varying experimental conditions; 7) for the Dielectric-Monitoring Model, to again survey more polymer systems and to find systems that have loss peaks that dissociate similarly to the 5.0 wt.% LP PEO-based IPMC composites within a usable frequency range; 8) to delve further into the possibility of using IPMCs as hybrid capacitor-battery energy storage devices. Exploring any

of these topics would greatly increase our understanding of IPMCS with how they function and for what types of applications they would best be suited.

8.2 Acknowledgements

I would like to first express my great appreciation to my wife, Liz, for always keeping me motivated. Without her constant support, this journey would not have been possible. I would also like to thank my advisors, Drs. Zhongyang Cheng, and Maobing Tu, for continually pushing me and keeping me focused. Thank you committee members, Dr. Barton Prorok, Dr. DongJoo Kim, and Dr. Majid Beidaghi, for all of your ideas. Thank you Dr. Auad for helping me with reading through this dissertation. A great thanks also goes to my family and to all of my friends and coworkers for always being there and helping me along the way, namely, Lauchlin Blue (your ingenuity, hard work, and dedication saved years of my life), Ethan Hofer, Dr. Lin Zhang, Dr. Zhizhi Sheng, Dr. Naved Siddqui, Steve Moore, MariAnne Sullivan, Matthew Baltzell, Adonias Barreto de Pavia, Tong Yang, Wenya Du, Dr. Shin Hirokawa, Dr. Mario Eden, Brennen Reece, and Dr. Yating Chai. The author also gratefully acknowledges the financial support provided by the National Science Foundation through the Auburn University IGERT on Integrated Biorefining (Award #1069004). This work was also partially funded through an IGP grant at Auburn University.